centro de educación continua
división de estudios de posgrado
facultad de ingeniería unam

PERCEPCION REMOTA

DESARROLLO HISTORIO DE SATELITE TERRESTRES.

DR.HANS PETER BAHR.

Marzo, 1980.

Palacio de Minería Calle de Tacuba 5 primer piso México 1, D. F. Tel: 521-40-20

Zusammenstellung bisheriger und geplanter Erdsatelliten-Missionen

Desarollo histórico de satelitos terrestres

Man unterscheidet folgende Erdsatelliten-Typen:

Tipos

1. Wettersatelliten — s. metereológicos
2. Nachrichtensatelliten — s. de telecomunicación
3. Navigationssatelliten — s. de navigación
4. Aufklärungssatelliten — s. militares
5. Geophysikalische Satelliten — s. geofisicales
6. Erderkundungssatelliten — s. por la percepción remota

Im Zusammenhang mit einer Kartierung der Erdoberfläche interessieren nur die Typen 1, 4 und 6; hinzu kommen noch bemannte Weltraumplattformen. In den Tabellen 7a bis d sind die bisherigen Missionen mit diesen Satellitentypen zusammengestellt.

nombre / Name	nación / Land	tiempo / Zeit	resolución / Auflösung
Tiros 1-10	USA	1960-1965 h = 700 km	3,5 km Vidicon (sichtbar)
ESSA 1-9	USA	1966-1969 h = 1500 km	3,5 km Vidicon (sichtbar), APT
NOAA 1-	USA	1970 h = 1500 km	0,9 km (sichtbar & thermal APT)
KOSMOS 1-92	UdSSR	1959-1965 h = 250 km	Filmkapsel
KOSMOS -226	UdSSR	1965-1969 h = 600 km	Vidicon & IR
METEOR 1 →	UdSSR	1970 →	Vidicon, IR & APT
GEOS METEOSAT JAPAN	USA ESA GMS	GARP 1978	

Wettersatelliten — s. meteorológicos → operacional

Name	Land	Zeit	Auflösung
NIMBUS 1-6	USA	1964 ⟶ h = 1000 km	Vidicon 1 km IR-Scanner 8 km
ATS 1-4	USA	1966-68 h = 36 000 km	Farbe
⇒ LANDSAT 1-2	USA	1972 ⟶	Bildelement am Boden 80 m 4 Kanäle
LANDSAT 3	USA	1978 ⟶	Bildelement am Boden 80 m 4 Kanäle oder Bildelement am Boden 40 m 1 Kanal
SEASAT 1	USA	1978	Bildelement am Boden 25 m Radar-X-Band

s. experiment.

Erdbeobachtungssatelliten — s. per la percepción remota

Name	Land	Zeit	Auflösung
SAMOS 1-80	USA	1962-1972	15 m Kameras c = 90 cm Filmrücktransport
MIDAS	USA	1967 ⟶ h = 3000 km geostationär	c = 90 cm IR,UV sichtbarer Bereich
BIG BIRD	USA	1973 ⟶ h = 150 km	1-2 m c = 1,8 m Kameras Filmrücktransport

Aufklärungssatelliten — s. militares

Mission	Jahr	Kamera	H	c	Format	Auflösung	Bodenauflösung
Misión	Año	Cámara	Altura	Distancia focal	Tamaño	Resolución	R. terrestre
GEMINI 4-7	1965	MK 70 Hasselblad C.Zeiss-Optik	200 km	80 mm	5,7 x 5,7 cm	20 Lp/mm	125 mm
GEMINI 10-12	1966	Maurer	200 km	80 mm	5,7 x 5,7 cm	20 Lp/mm	125 mm
APOLLO 7	1968	R220 Maurer	225-420 km	80 mm	5,7 x 5,7 cm	35 Lp/mm	70 m
APOLLO 9	1969	Hasselblad C.Zeiss-Optik	192-496 km	80 mm	5,7 x 5,7 cm	35 Lp/mm	70 m
SKYLAB (S190A)	1973	ITEK	435 km	152 mm	5,7 x 5,7 cm	29 Lp/mm	99 m
SKYLAB (S190B)	1973	ETC Acton	435 km	360 mm	11,5 x 11,5 cm	25 Lp/mm	38 m
SOJUZ 22-30	seit 1976	MKF-6 Jena	250 km	125 km	5,5 x 8,1 cm	80 Lp/mm	25 m

Bemannte Weltraumplattformen   Plataformas espaciales con tripulación

Die geplanten Weltraummissionen sind im folgenden zusammengestellt, und zwar geordnet nach Aktivitäten der USA, anderer Länder sowie der ESA.

Programas espaciales

Weltraum-Fernerkundungsprogramme der USA

de los Estados Unidos

A. Vorgegebene Entwicklungen desarollos terminados

1. Space-Shuttle — Wiederverwendbarer Transporter
2. T.D.R.S.S. — Weltweites Empfangssystem über geostationäre Satelliten
3. Multimodular-Satelliten — Genormte Satelliten

B. Systeme im Bau en construcción

1. LANDSAT - D 1982 — Thematic Mapper:
   - 6 Bänder: 0,42-2,35 µm, Bildelementgröße am Boden 30 m
   - 1 Band: 10-12,5 µm, Bildelementgröße am Boden 120 m
   - 85 M bits/s Datenrate über T.D.R.S.S.

   Scanner

2. Shuttle Experimente (O.F.T.)
   - a) Großformat-Kamera (ITEK) "LFC" — c = 30 cm, 23 x 36 cm Format, 4000 Aufnahmen, Palette
   - b) SEASAT Radar — (X & L Band)

Sistemas proyectados

C. Geplante Systeme

1. MAPSAT (U.S.G.S.) — 1 Band, Bildelement am Boden 30-40 m; 2 Bänder, Bildelement am Boden 60-90 m; 15 Mbit/s Datenrate; h = 900 km
2. STEREOSAT (J.P.L.) — Diodenzeilen (konvergent); Bildelement am Boden 15 m

   Scanner

3. MULTIMODULAR SATELLITEN & GROSSFORMAT-KAMERA

   Lebensdauer 6-9 Monate
   Parkumlaufbahn 900 km
   Missionsumlaufbahn 250 km

   Camara

Weltraum-Fernerkundungsprogramme anderer Länder

Otras naciones

UdSSR - INTERCOSMOS

Soyuz	MKF-6	in Betrieb	cámaras

FRANKREICH Francia

SPOT auf ARIANE	im Bau

20 m Bildelement , 2 Bänder
10 m Bildelement [illegible]
250 Bilder speicherbar [illegible]

JAPAN

MOS (Marine Observation Satellite)	im Bau und geplant	
50 m Bildelement, sichtbar und thermal	1983	} [illegible]
LOS (Land Observation Satellite)	1987	
30 m Bildelement		

VOLKSREPUBLIK CHINA

Programm des Jen Hsi-Min Raumfahrttechnologieinstituts	geplant	proyectado

Weltraum-Fernerkundungsprogramme der ESA

"European Space Agency"

A. Vorgegebene Entwicklungen [desarollos terminados]

1) Bau von SPACELAB (E.R.N.O.) → Bremen
   zur Mehrzwecknutzung im wiederverwendbaren NASA Raumtransporter SPACE-SHUTTLE

2) Bau der europäischen Trägerrakte ARIANE   Cohete europeo

B. Systeme im Bau [en construcción]

1) SPACELAB-1 Experiment
   Photogrammetrische Kamera "metric camera"
   Zeiß RMK 30/23, 3 Filme = 1650 Aufnahmen
   Missionsdauer 1 Woche
   Start: 18.4.1982

2) SPACELAB-1 Experiment
   Mikrowellenerkundung   Micro[illegible]

   in 3 Betriebsarten:
   a) Mikrowellenscatterometer
   b) Passiver Thermalsensor
   c) Bildflugradar im X-Band   [illegible]
      25 m Bildelem.
      Bildbreite 9 km

ESA
(continuación)

1) SPACELAB-KAMERA-MISSION

RMK 30/23 cámara [illegible]

h = 250 km, Bahn 57° Inklin., 8 Tagemission

3 Filme (Filmtests DFVLR/CNES-IGN) evaluación de películas:
[illegible]

Auswertung: IGN, CNES (Frankreich) S/W
IFAG, DFVLR (BR Deutschland) IR Falschfarbe
Universität Mailand (Italien)
Universität Hannover (BR Deutschland)

Automat. Auslösung der Aufnahmefolge

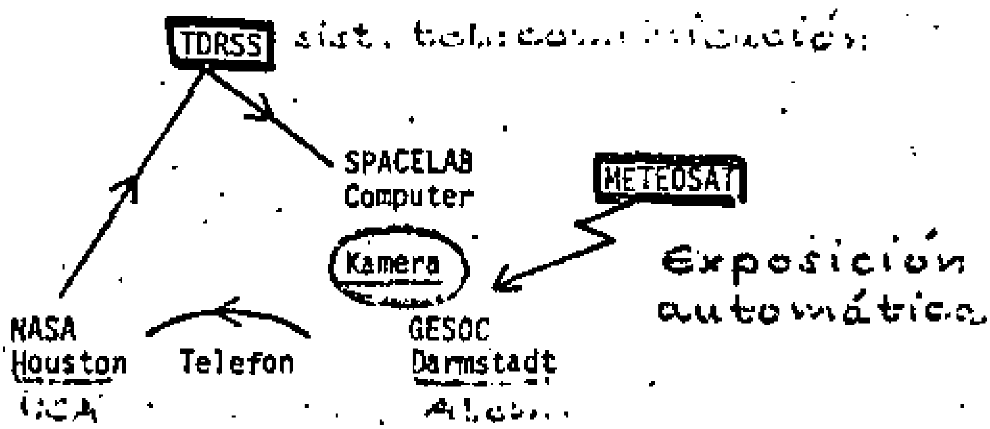

Beschränkungen Limitaciones:

1. Film (3 Magazine) película
2. Energie 1,5 kWh energía, peso
3. Andere Experimente (Ausrichtung erdorientiert) otros experimentos
4. Sonnenstand > 15° altura del sol
5. Wetter tiempo (atmósfera)

2) MICROWELLEN EXPERIMENT

1. SPACELAB MISSION

im Bau [en construcción]

von Dornier & DFVLR

Synthetisches Apertur Radar — Radar satélite (caro)

X-Band	9,6 GH_z
Abstrahlungswinkel	45°
Empfindlichkeit	1 db
dynam. Bereich	-30 db bis + 10 db
Auflösung (resolución)	100 x 100 m gewünscht 25 x 25 m

E.S.A. PLANUNG FÜR ERDERKUNDUNGSSATELLITEN

c. Planung [Proyectos]

1. LASS — Land Applications Satellite System

a. 30 m Pixel Zeilendiode (6 Kanäle)

b. 60 m Pixel Abtaster (refl. IR) (2 Kanäle)

c. 120 m Pixel Thermalabtaster (2 Kanäle)

d. 100 m Pixel Synthet. Aperturradar

2. COMSS — Coastal Ocean Monitoring Satellite System

a. Ozeanfarbabtaster (7 Kanäle, engbandig f. Chlorophyll)

b. Synthet. Apertur Radar, 30 m Pixel

c. Mikrowellenradiometer

centro de educación continua
división de estudios de posgrado
facultad de ingeniería unam

PERCEPCION REMOTA

ANEXO 1

DR. ING. HANS PETER BAHR

MARZO, 1980

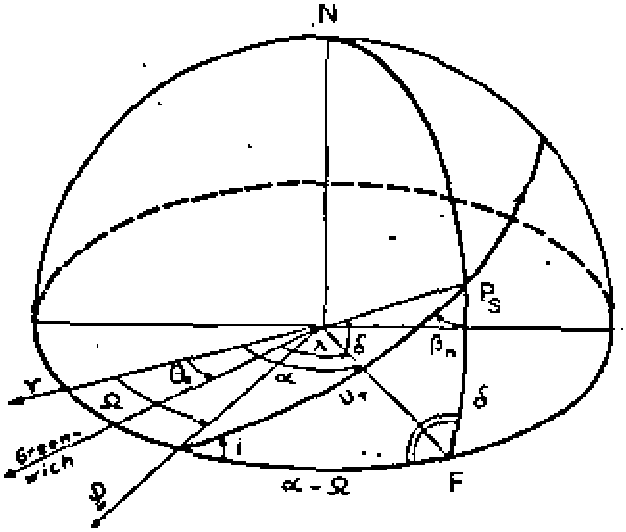

Berechnung geographischer Bahnkoordinaten

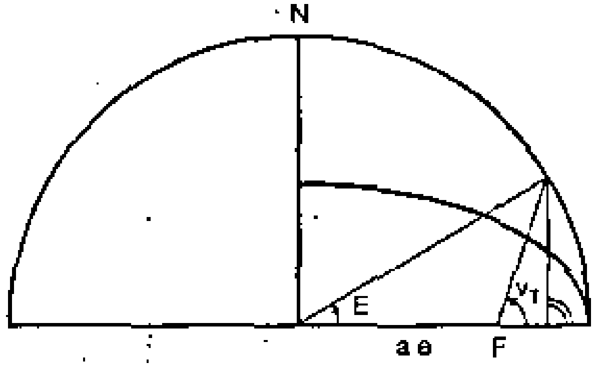

Wahre Anomalie v_T und exzentrische Anomalie E

$\sin \delta_T = \sin u_T \sin i$; $\tan (\alpha - \Omega)_T = \tan u_T \cos i$

$\cot \beta_n = \cos u_T \tan i = \frac{\sqrt{\sin^2 i - \sin^2 \delta}}{\cos i}$

$v_T = \frac{2\pi (T - T_{pe})}{U}$ (für $e = 0$)

$M_T = E - e \sin E$

$v_T = \text{Arctan} \left(\frac{\sqrt{1 - e^2} \sin E}{(\cos E - e)} \right)$

$v_T = M_T + 2e \sin M_T + \frac{5}{4} e^2 \sin 2M_T + \ldots$

(ARNOLD / /; BROUWER, CLEMENCE / /)

$\tan B = \tan \delta / (1 - e_G^2)$

$B \sim \delta + 0{,}^\circ 1926 \sin 2\delta$; e_G^2 (Erde) $\sim 0{,}00667437$

$\lambda_T \sim (\Omega - \Theta_o) + (\alpha - \Omega)_T - 0{,}^\circ 2507 (T - T_o)$

(T in Minuteneinheiten)

centro de educación continua
división de estudios de posgrado
facultad de ingeniería unam

PERCEPCION REMOTA

ANEXO 2

DR. ING. HANS PETER BAHR

MARZO , 1980

<u>INTERFEROMETRISCHES SIDE-SCAN-SONAR</u>

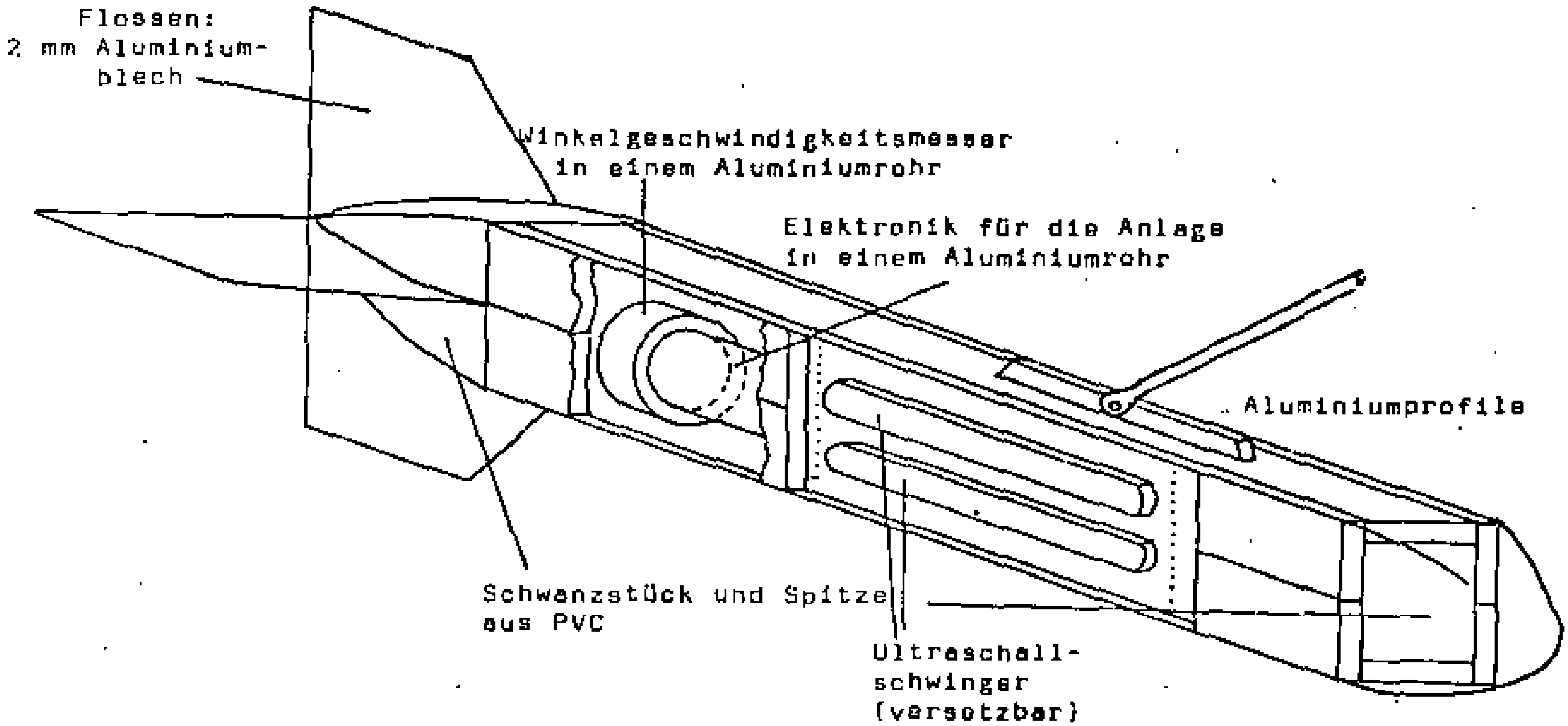

centro de educación continua
división de estudios de posgrado
facultad de ingeniería unam

PERCEPCION REMOTA

APLICACIONES A ZONAS COSTERAS

DR. ING. HANS PETER BAHR

MARZO, 1980

Satellite photograph:

Laguna Madre de Tamaulipas, Mexico and Gulf of Mexico

Flight information data:

Mission: *NASA – APOLLO 7*
Date: *12. Oct. 1968*
Photograph: colour
Magazine: *5* *frame no. 1633*
Camera: *Hasselblad 500 C*
70 mm photography
Lens: *Zeiss Planar f/2,8; 80 mm*
Film: *Kodak Aerial Ektachrome*
Filter: *Wratten 2a*
Altitude above mean sea level: *123 naut. miles*
Geographical position of the principal point:
latitude: *24 degrees 45 min. N*
longitude: *97 degrees 30 min. W*
Chart: *ONC – WAC code H – 23 and H – 24, J – 24 and J – 25*
Local observation time: *12.00*
Sun azimuth: *180°*
Sun elevation: *60°*
Photograph viewing mode: *vertical*
Cloud cover: *30 % cumulus, altocumulus*
Scale of the printed picture: *1 : 800 000*
(section of satellite photograph)
Colours of the printed picture (Munsell scale):
The colours of the printed photograph occur more yellowish and greenish yellow in comparison to the colours of the NASA copy, which shows up less yellowish, but more bluish and purplish tint.

Laguna Madre de Tamaulipas, Mexico and Gulf of Mexico

Interpretation map, from NASA satellite colour photograph

APOLLO mission 7, no. 5–1633

Interpreter H. G. Gierloff-Emden, 1975

Legend of topographic and hydrographic features classified in zones with selected documented objects (generalized: no differentiation of distinct water levels on this small scale map)
Scale approximately 1 : 800 000

I above High Water level: terrestrial
mainland on the map as white area
1 barrier island with dunes and beach (sand) with some beach ridges
2 sand ridges and wash-over fans (sand and loam), partly with vegetation, on the lagoonal side of the barrier island (1 and 2: coastal barrier complex)

II between High and Low Water level: inter-tidal zone
3 flats, temporarily exposed at low water (caused by tidal streams and wind driven currents) partly wind-tidal flats

III below Low Water level: lagoonal and marine
4 flat areas of lagoonal bottom covered with water (0,3 – 1 m deep), mostly turbid water
5 turbid water masses, partly in motion
6 boundaries of water masses in motion (streamlines, torrents and eddies)

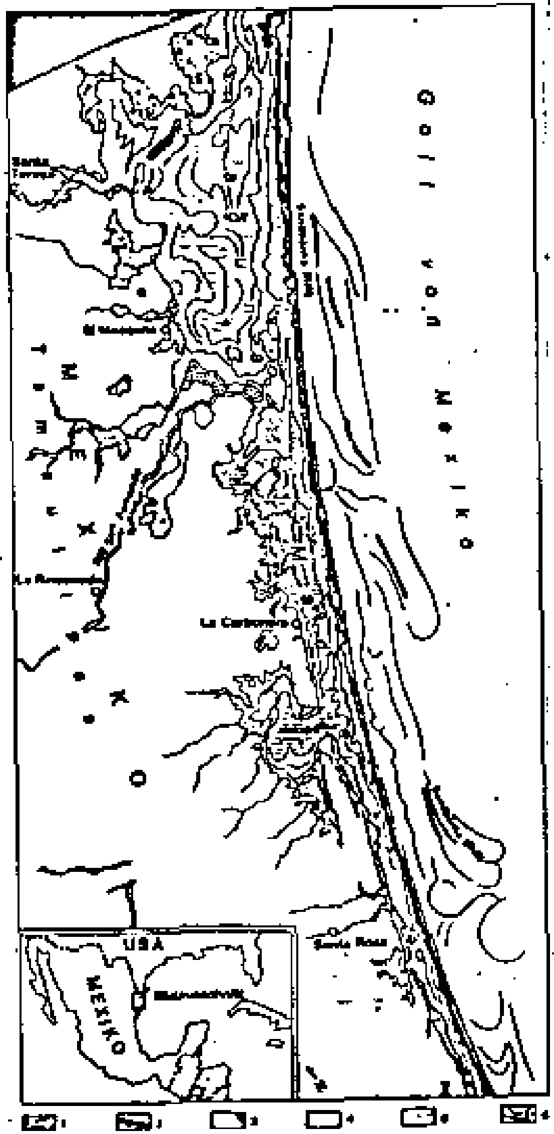

Laguna de Terminos and Campeche Bay, Gulf of Mexico

Interpretation map, from NASA satellite colour photograph

GEMINI mission 5, no. MSC-S-65-45765

Interpreter H. G. Gierloff-Emden, 1975

Legend of topographic and hydrographic features classified in zones with selected documented objects (generalized: no differentiation of distinct water levels on this small-scale map)
Scale approximately 1 : 600 000

I above High Water level: terrestrial
mainland on the map as white area
1 barrier island with dunes and beach (sand), sand ridges
2 inner lagoonal shore (beach)
3 beach ridges
4 salt marshes and marshes

II between High and Low Water level: inter-tidal zone
(4) (compare I) partly mangrove swamp
5 sand bars (bars), for instance delta in the lagoon mouth of Canal Puerto Real, "tidal delta" partly temporarily exposed or covered
6 swamps, for instance in Rio Palizada area
(12) (compare III)

III below Low Water level: lagoonal and marine
7 water bodies of estuaries of rivers, which discharge into Laguna de Terminos
8 debris laden water mass of Laguna del Este
9 water masses of inner lagoon, near river estuaries, brackish
10a sediment laden, lagoonal water mass, with sand and silt and material in suspension
10b water mass, pouring out of Laguna de Terminos channels into Campeche Bay during ebb tide stream
11 boundaries of water masses in motion, partly stream lines, torrents and eddies (different water masses, as described in the map; arrows as symbols for general current direction)
12 sand bars and shoals
13 sandy reefs of the foreshore zone, nearshore circulation (surf belt) with longshore current
14 marine water masses as described on the map
5 and 12 appear in categories II and III, both as a geomorphologic phenomenon of both levels.
The coastal water mass between beach and "Gulf offshore clearwater" includes 10a, 10b and 13.
8, 10a and 10b are hydrographic features, but occur on the satellite photograph in the same colour and tone as 11, a topographic feature: light grey and greyish blue.

Satellite photograph:

Laguna de Terminos, Campeche Bay and Gulf of Mexico

Flight information data:

Mission: *NASA GEMINI 5*
Date: *22. Aug. 1965*
Photograph: colour
Magazine: *MSC – S 65* *frame no. 45765*
Camera: *Hasselblad 500 C*
70 mm photography
Lens: *Zeiss Planar f/2,8; 80 mm*
Film: *Ektachrome MS*
Altitude above mean sea level: *100–200 naut. miles (solution)*
Geographical position of the principal point:
latitude: *18 degrees 45 min. N*
longitude: *91 degrees 35 min. W*
Chart: *ONC – WAC code J – 25*
Local observation time: *14.00*
Sun azimuth: *270°*
Sun elevation: *65°*
Photograph viewing mode: *slightly oblique*
Cloud cover: *10 % alto cumulus*
Scale of the printed picture: *1 : 600 000*

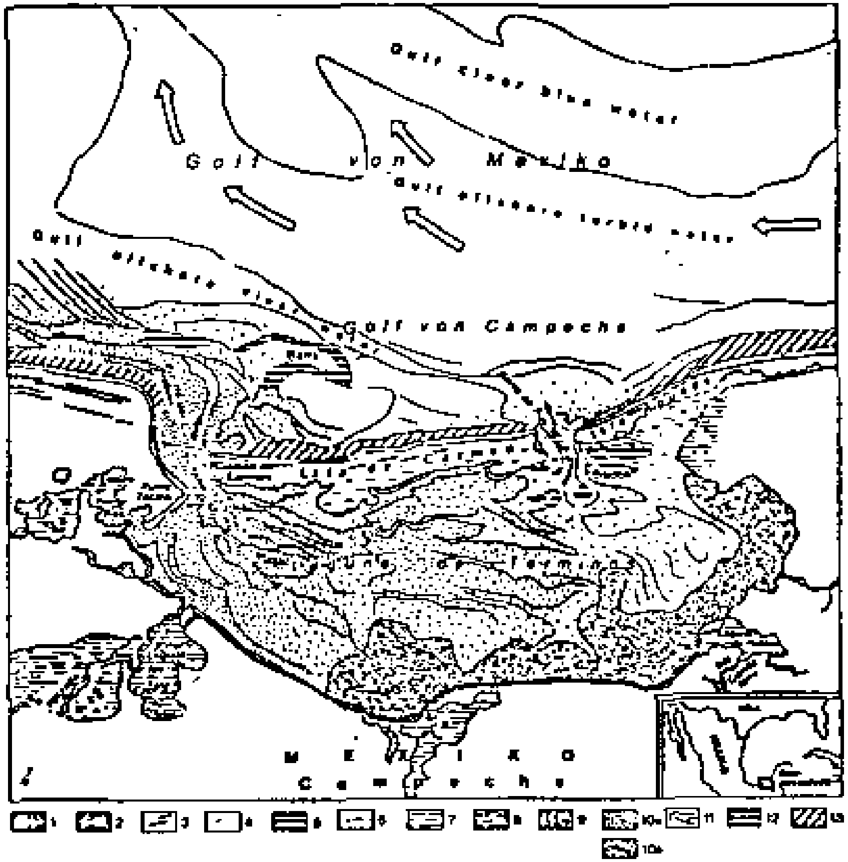

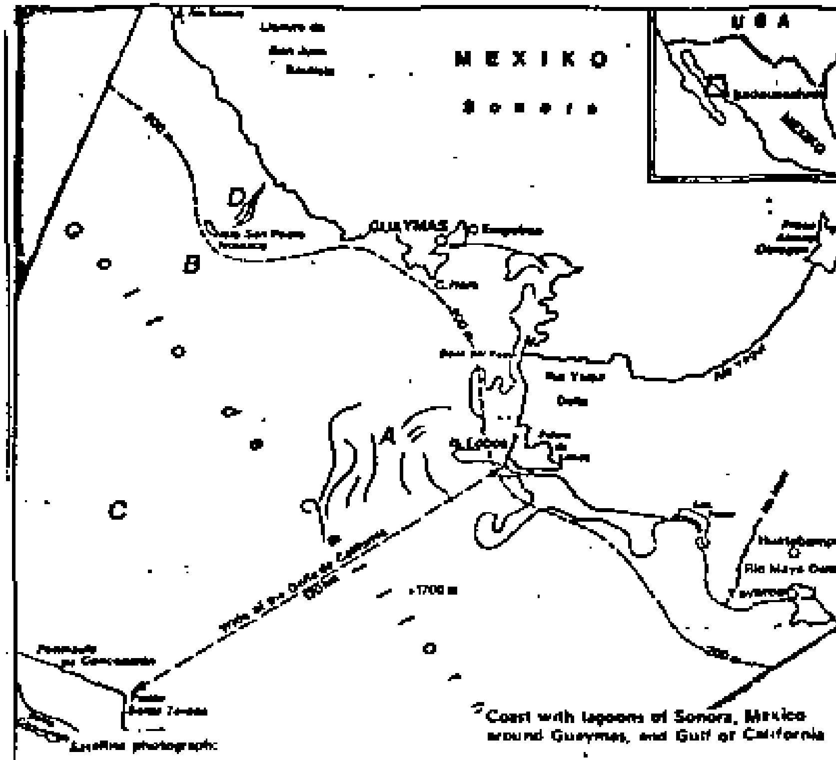

Coast with lagoons of Sonora, Mexico around Guaymas, and Gulf of California

Satellite photograph:

Coast with Lagoons of Sonora, Mexico, around Guaymas and Gulf of California

Sketch within frame of facing NASA satellite colour photograph

APOLLO mission 7, no. 5-1652

Flight information data:

Mission: *NASA – APOLLO 7*

Date: *13. Oct. 1968*

Photograph: colour

Magazine 5 *frame no. 1652*

Camera: *Hasselblad 500 C*
70 mm photography

Lens: *Zeiss Planar f/2,8; 80 mm*

Film: *Kodak aerial Ektachrome*

Filter: *Wratten 2 A*

Altitude above mean sea level: *122 naut. miles*

Geographical position of the principal point:
latitude: *27 degrees 30 min. N*
longitude *111 degrees 00 min. W*

Chart: *ONC – WAC code H – 22*

Local observation time: *12.34*

Sun azimuth: *180°*

Sun elevation: *55°*
sun glint (reflection) in the southern part of the photograph

Photograph viewing mode: *oblique exposure axis to 135°*

Cloud cover: *2 % and fog*

Scale of the printed picture: *variable*

Orientation of the printed photograph: *north is above. To regard the oblique photograph in direction of the camera axis turn the photograph 180° around.*

Legend of topographic and hydrographic features with selected documentated objects

Scale varies due to oblique photograph

Submarine topographic features in shallow water regions of the foreshore region and especially of the coastal lagoons of Sonora, and hydrographic features as distribution of outflowing lagoonal water masses in the Gulf of California can be identified on the photograph.

A sinuous tongues of discoloured water, south of Guaymas, interpreted to be phytoplankton blooms, red tide (biological activity) indicating curvilinear features as slicks on the surface of the sea

B rough sea state and cloud lines

C calm sea state, sea-surface state may be determined from the photographs by means of tone and texture changes which are responses to areas of rough and calm water; details are not as clearly oceanic in nature nor are they definitely of atmospheric character

D probable standing waves near Isla San Pedro Nolasco were recognized which are attributed to either the effects of local current circulation or strong north – south movements of water in the Gulf of California

Detection and interpretation of A, B, C, D from van der Haar et al., 1973, *Photogrammetria*, 29.

PERCEPCION REMOTA

TRANSFORMACIONES NUMERICAS DE UNA IMAGEN ARQUITECTURAL

DR. ING. HANS PETER BAHR

MARZO, 1980

Transformaciones numéricas de una imagen arquitectural

Resumen de cámaras especiales

Firma	Carl Zeiss		Jenoptik			WILD			IPI Hannover
Kamera	TAF	SMK 120	TAN	UMK	SMK 120	P30	P31	C120	[illegible]-kamera*
Typ	Einzel-kamera	Stereo-kamera	Einzel-kameras			Einzel-kameras		Stereo-kamera	Einzel-kamera
Brennweite (mm)	160	60	190	89	56	165	100	64	56
Aufnahmeformat (mm)	130 x 180	90 x 120	130 x 180	130 x 180	90 x 90	100 x 150	100 x 130	65 x 90	60 x 60
Bildwinkel horizontal [g]	63	75	52	68	79	50	68	73	67
Bildwinkel vertikal [g]	45	88	39	68	79	32	63	55	62
Fokussierung auf (m)	∞	5-∞	∞	3-∞	5-∞		2,5-∞	5-30	3-∞

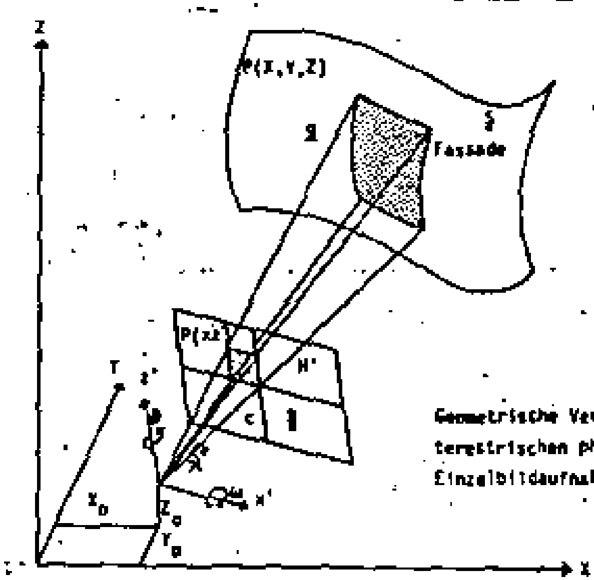

Condiciones geométricas generales

Geometrische Verhältnisse bei der terestrischen photographischen Einzelbildaufnahme

$$S = f_s(X,Y,Z) \qquad \mathfrak{g} = f_g(X,Y,Z)$$

$$g_1 = \begin{pmatrix} X \\ Y \\ Z \end{pmatrix}_1 = \lambda_1 D_{\phi,\omega,\kappa} \begin{pmatrix} x' \\ c \\ z' \end{pmatrix}_1 + \begin{pmatrix} X_0 \\ Y_0 \\ Z_0 \end{pmatrix}$$

Rotaciones

1. Drehung um ϕ

$$D_\phi = \begin{pmatrix} \cos\phi & \sin\phi & 0 \\ -\sin\phi & \cos\phi & 0 \\ 0 & 0 & 1 \end{pmatrix}$$

2. Drehung um ω

$$D_\omega = \begin{pmatrix} 1 & 0 & 0 \\ 0 & \cos\omega & \sin\omega \\ 0 & -\sin\omega & \cos\omega \end{pmatrix}$$

3. Drehung um κ

$$D_\kappa = \begin{pmatrix} \cos\kappa & 0 & \sin\kappa \\ 0 & 1 & 0 \\ \sin\kappa & 0 & \cos\kappa \end{pmatrix}$$

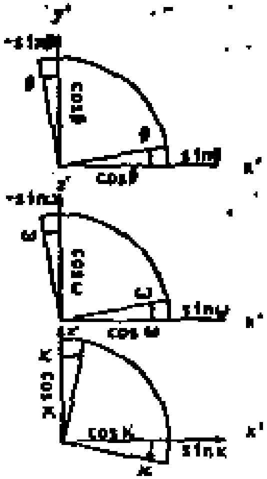

Die Resultierende ergibt sich aus dem Matrizenprodukt

$$D_{\phi,\omega,\kappa} = D_\kappa D_\omega D_\phi \quad \text{La resultada}$$

$$\mathfrak{g} = \begin{pmatrix} X \\ Y \\ Z \end{pmatrix} = \lambda D_{\phi,\omega,\kappa} \begin{pmatrix} x' \\ c \\ z' \end{pmatrix} + \begin{pmatrix} X_0 \\ Y_0 \\ Z_0 \end{pmatrix} \quad \text{Ecuación de Colinearidad}$$

$$D_{\phi,\omega,\kappa} = \begin{pmatrix} \cos\kappa\cos\phi - \sin\kappa\sin\omega\sin\phi & \cos\kappa\sin\phi + \sin\kappa\sin\omega\cos\phi & -\sin\kappa\cos\omega \\ -\cos\omega\sin\phi & \cos\omega\cos\phi & \sin\omega \\ \sin\kappa\cos\phi + \cos\kappa\sin\omega\sin\phi & \sin\kappa\sin\phi - \cos\kappa\sin\omega\cos\phi & \cos\kappa\cos\omega \end{pmatrix}$$

$$S = b_{11}X^2 + b_{22}Y^2 + b_{33}Z^2 + b_{12}XY + 2b_{23}YZ + 2b_{31}ZX + 2b_{14}X + 2b_{24}Y + 2b_{34}Z + b_{44} = 0$$

Ecuación general de una superficie de segundo grado

→ intersección

$$P(X,Y,Z) = f_p(x_i', z_i', c, X_0, Y_0, Z_0, \phi, \omega, \kappa, b_{12} \ldots b_{44})$$

$$b_{33} = b_{23} = b_{31} = b_{34} = b_{12} = 0 \quad \text{und } b_{11} = b_{22}$$

$$b_{11} = 1,\ b_{14} = -X_M,\ b_{24} = -Y_M,\ b_{44} = X_M^2 + Y_M^2 - R^2$$

$$S = (X - X_M)^2 + (Y - Y_M)^2 = R^2$$

Simplificaciones

$$X = \lambda(x'\cos\phi + c\sin\phi)$$
$$Y = \lambda(-x'\sin\phi + c\cos\phi)$$
$$Z = \lambda z'$$

$$\lambda = \frac{(x'\cos\phi + c\sin\phi)X_M + (c\cos\phi - x'\sin\phi)Y_M - \sqrt{((x'\cos\phi + c\sin\phi)X_M + (c\cos\phi - x'\sin\phi)Y_M)^2 - (x'^2 + c^2)(X_M^2 + Y_M^2 - R^2)}}{x'^2 + c^2}$$

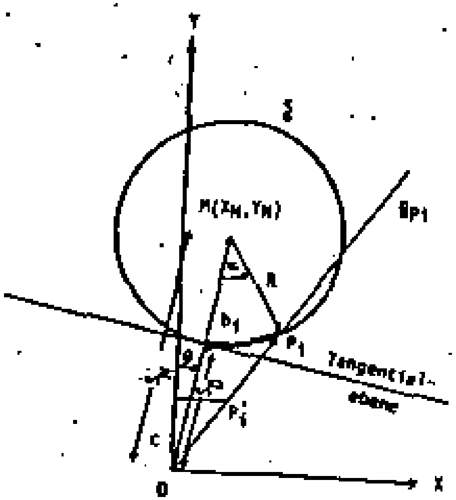

Después de simplificaciones

Fassadenoberfläche S und Aufnahmestrahl g in der X/Y-Ebene nach Einführung von Vereinfachungen

$b_1 = R\alpha$ arco

$$b_1 = R\left(\arcsin \frac{(X_1 - X_M)}{R} + \beta\right)$$

Distancias en el resultado:

$$\bar{x}_1 = R\,\frac{c}{S_D}\left(\arcsin \frac{(X_1 - X_M)}{R} + \beta\right)$$

$$\bar{z}_1 = z_1\,\frac{c}{S_D}$$

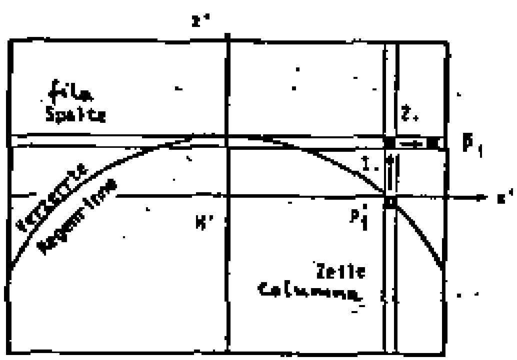

Transformación numérica

Digitale geometrische Transformation in zwei getrennten Schritten

Puntos de apoyo en el original

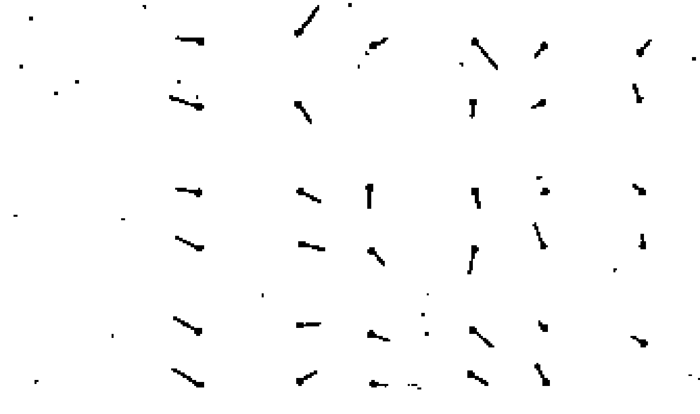

Tratamiento riguroso

Differenz zwischen Paßpunktkoordinaten und Koordinaten des transformierten Bildes (2.2.-IX) nach Helmerttransformation
⟼: entspricht 10 c
Differenz

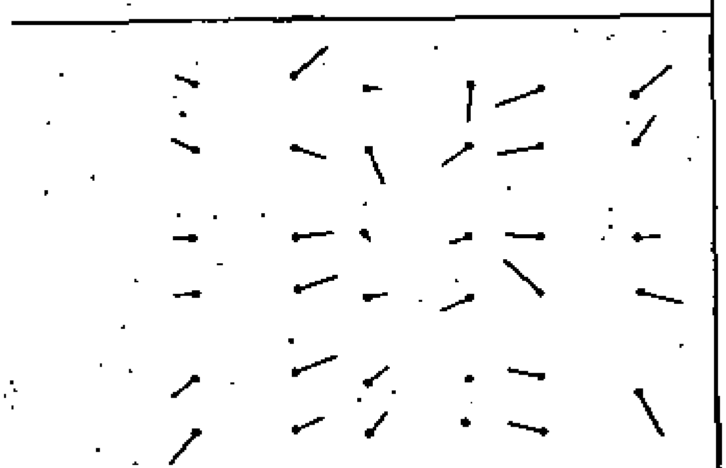

Tratamiento por Polinomios

Differenz zwischen Paßpunktkoordinaten und Koordinaten des mit Po
nomen transformierten Bildes (2.2.-XI) nach Helmerttransformation
⟼: entspricht 10 c
Differenz

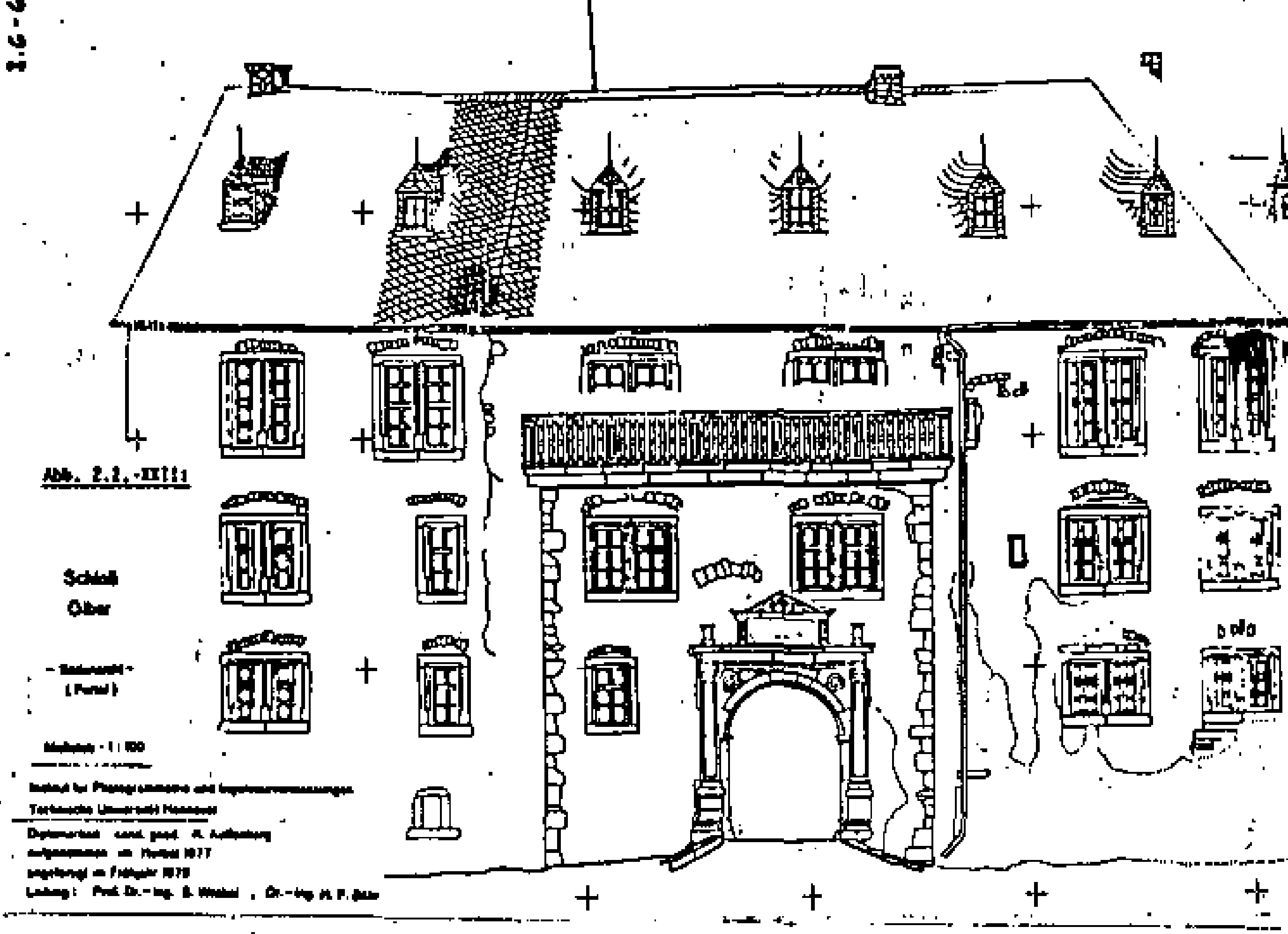

Efecte de errores:

Auswirkung von Fehlern

$m_R = \pm 10$ cm

$m_{XH} = \pm 10$ cm

$m_{YH} = \pm 10$ cm

$m_\beta = \pm 1^0$ por la coord. X

auf die X-Koordinate in Abhängigkeit von x' für

R = 15 m

XH = 0,5 m

YH = 32,9 m

β = 1,7°

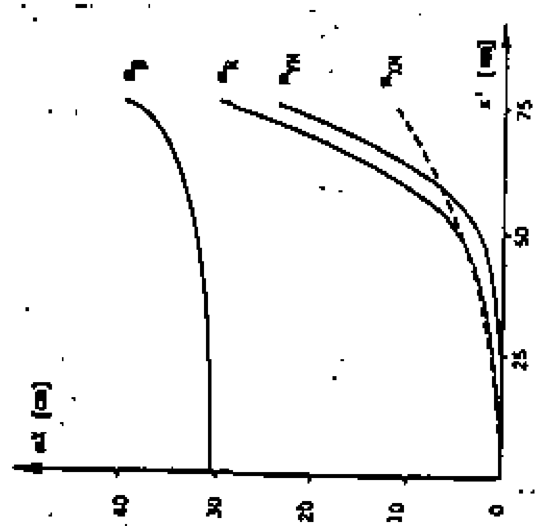

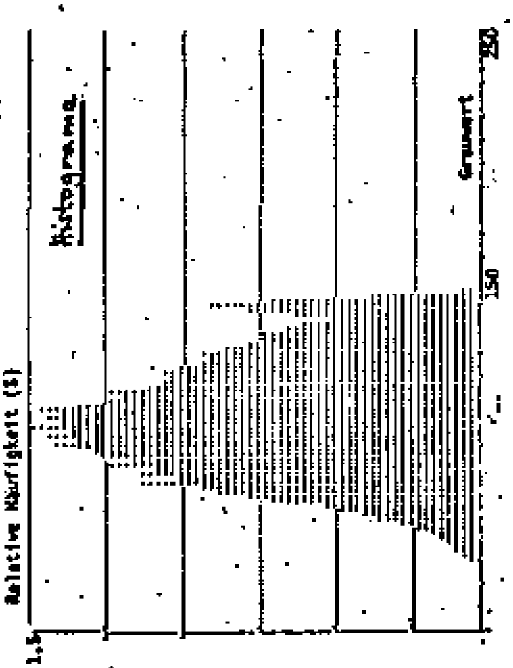

centro de educación continua
división de estudios de posgrado
facultad de ingeniería unam

PERCEPCION REMOTA

INDICE DE INSTITUCIONES QUE TRABAJAN EN EL CAMPO DE LA PERCEPCION REMOTA DE ALEMANIA Y E.E.U.U.

DR. ING. HANS PETER BAHR

MARZO, 1980

Namen der beteiligten Wissenschaftler

Prof. Dr. G. Konecny; Prof. Dr. B. Wrobel; Dr. H.P. Bähr; Dr. G. Dowideit; Dipl.-Math. E. Ennert-Möller; Dipl.-Ing. D. Kolouch; Dipl.-Ing. P. Lohmann; Dipl.-Ing. H. Rödenauer; Dipl.-Ing. W. Schuhr

Verfügbare Ausrüstung

a) Bildinterpretation

Bildanalysator ISI 15o

b) Bildverarbeitung

Optronics P 17oo in Verbindung mit Cyber 73/76
Log-Eletronics IV-C

c) Meßgeräte

Stereokomparator PSK-Zeiss (2 Geräte); Stereoplanigraph C-8-Zeiss (2 Geräte); Stereoautograph A 8 - Wild; Analytischer Plotter AP/C-3 mit IBM 113o.

d) Sonstiges

Orthophoto-Projektor Zeiss OP-3; Colenta-Automat f. Farbentwicklung; Durst Farbvergrößerungsgerät; Entzerrungsgeräte Zeiss SEG V, SEG IV; diverse Geräte für den photogrammetrischen Lehrbetrieb (Wild B-8, Multiplex/8Projektoren; Kleinautograph v. Zeiss; Zeiss-Orel Stereoautograph; Phototheodolite; Stereotop; Stereopret (4 Geräte); Radialtriangulator)

Hasselblad MK 7o

Zusammenarbeit mit anderen Institutionen

Wasser- und Schiffahrtsamt Wilhelmshaven;
Wasserwirtschaftsamt Wilhelmshaven;
Senckenberg Institut Wilhelmshaven;
Bundesanstalt für Geowissenschaften und Rohstoffe, Hannover;
Institut für Meereskunde, Kiel
Rijkswaterstaat, Den Haag.

Fachrichtung: Photogrammetrie

Stand: ....

Karteibogen - Fernerkundung

Institut/Firma Amt	Adresse	Austauschpartner
Institut für Photogrammetrie und Ingenieurvermessungen	Nienburger Str. 1 3000 Hannover	

Einzelvorhaben, die ganz oder teilweise mit den Mitteln der Fernerkundung durchgeführt werden	Status *)
Stichwortartige Darstellung: (evt. Publikationen)	
1. Programmentwicklungen	
- Bildverarbeitungsprogramm "SONARDAT" zur Verarbeitung von Magnetbändern und deren Ausgabe auf Optronics P 17oo	2
- Entzerrungsprogramm für Magnetbanddaten und deren Ausgabe auf Optronics P 17oo (auf Basis v. Kollinearitätsgl. und DGM)	2
- Klassifizierungsprogramm für multispektrale Daten auf Magnetband	1
- Abtastung digitaler Geländemodelle am Analyt.-Plotter	2
2. Anwendungen der Fernerkundung	
- Sedimenttransport im Jadebereich	4
- Gewässerverschmutzung im Jadebereich	4
- Wattkartierung mit Klassifizierungsmethoden	4
3. Untersuchungen	
- Geometrische Analyse für Radaraufnahmen	5
- Geometr. Analyse für Satellitenscanneraufnahmen	5
- Geometr. Analyse für Sonaraufnahmen	5
- Geometr. Analyse für Multispektralscanneraufnahmen vom Flugzeug	4

*)
1 = Experimentell
2 = direkte Anwendung
3 = geplant
4 = laufende Untersuchung
5 = abgeschlossene Untersuchung
6 = Ort der Untersuchung

Fachrichtung: Photogrammetrie

Stand: ....

Karteibogen - Fernerkundung

Institut/Firma Amt	Adresse	Austauschpartner
Institut für Photogrammetrie und Topographie der Univ. (TH)	Englerstraße 7 Postfach 638o 75oo Karlsruhe	--

Einzelvorhaben, die ganz oder teilweise mit den Mitteln der Fernerkundung durchgeführt werden	Status *)

Stichwortartige Darstellung:
(evt. Publikationen)

1. Geometrische Entzerrung und Überlagerung von Abtasterdaten (1,4)
2. Auswertung der Daten multispektraler Abtaster, insbesondere Klassifizierungsverfahren (1,4)
3. Bildverbesserung und Vorverarbeitung (1,4)
4. Digitale Korrelation zur automatischen Auswertung von Stereobildpaaren (5)
5. Digitale Erzeugung eines Orthophotos (3)

*)
1 - Experimentell
2 - direkte Anwendung
3 - geplant
4 - laufende Untersuchung
5 - abgeschlossene Untersuchung
6 - der Untersuchung

Namen der beteiligten Wissenschaftler

Prof. Dr.-Ing. W. Hofmann
Dr. F. Quiel
Dipl.-Ing. J. Wiesel

Verfügbare Ausrüstung

a) Bildinterpretation

8 Spiegelstereoskope

b) Bildverarbeitung

Univac 11o8 des RZ der Univ. Karlsruhe

c) Meßgeräte

Zeiss PSK 2; Zeiss Stereoplanigraph C 8;
Wild A 8; Wild B 8; Jenoptik Topocart m. Orthophot

d) Sonstiges

--

Zusammenarbeit mit anderen Institutionen

Zentralstelle für Geo-Photogrammetrie und Fernerkundung der DFG, München (Prof. Bodechtel;
Institut für Forsteinrichtung und forstl. Betriebswirtschaft Univ. Freiburg, (Prof. Hildebrandt);
Forschungsinstitut für Informationsverarbeitung und Mustererkennung, Karlsruhe (Dr. Bargel);
DFVLR, Institut für Nachrichtentechnik (Dr. Kritikos)

Fachrichtung: Photogrammetrie

Stand: ....

Karteibogen - Fernerkundung

Institut/Firma Amt	Adresse	Austauschpartner
Institut für Angewandte Geodäsie (Bundesforschungseinrichtung)	Richard-Strauß-Allee 11 6000 Frankfurt a.M. 70	

Einzelvorhaben, die ganz oder teilweise mit den Mitteln der Fernerkundung durchgeführt werden	Status*) (s. Angaben in Klammern)
Stichwortartige Darstellung: (evt. Publikationen)	
1. Gewinnen von Informationen für die Fortführung der amtlichen topographischen und chorographischen Kartenwerke der Bundesrepublik Deutschland in den Maßstäben kleiner 1:100 000	(4) +(2)
1.1 Mitwirkung an "Multidisciplinary Geoscientific Experiments in Central Europe" NASA-SR No. 328 (1974)	(5)
1.2 Mitwirkung am Spacelab-Erderkundungsprogramm (1. Mission) ESA, NASA. Die Testgebiete umfassen die Landschaftsstrukturen Küste/Flachland, Mittelgebirge, Hochgebirge.	(4)
2. Herstellen von topographischen und chorographischen Bildkarten (Photokarten) zur Aktualisierung unserer Kartenwerke. Bereitstellen dieser Technologien für Entwicklungsländer / UN-Wirtschafts- und Sozialrat.	(4) +(1)
3. Untersuchungen über die Informationsübertragungskette beim Erstellen von Bildaufzeichnungen; Bildqualität/OEEPE.	(4)
4. Grundlegende Untersuchungen und Entwicklung von Methoden zur analogen und digitalen Bildverarbeitung.	(4)

*)
1 = Experimentell
2 = direkte Anwendung
3 = geplant
4 = laufende Untersuchung
5 = abgeschlossene Untersuchung
6 = Ort der Untersuchung

Namen der beteiligten Wissenschaftler

Dipl.-Ing. H. Belzner
Dr. H. Schmidt-Falkenberg
Dr. H. Schulz
Dr. J. Sievers
Dr. K. Niess

Verfügbare Ausrüstung

a) Bildinterpretation

Verschiedene Spiegelstereoskope und andere Betrachtungseinrichtungen

b) Bildverarbeitung Zeiss-Orthoprojektor GZ 1 mit Meßeinrichtung zur vollautomatischen Abtastung des Stereomodells und Einrichtungen zum Speichern der Meßdaten in analoger und numerischer Form.
Zeiss-Entzerrungsgerät SEG V.
Bildverarbeitungssystem Optronics P 1700

c) Meßgeräte

Verschiedene photogrammetrische (Präzisions-)Auswertegeräte

d) Sonstiges

Contraves-Digitalisiergerät Codimat B,
Bildschirmgerät Tektronix 4014 mit DEC-Rechner PDP-11/45,
Contraves-Zeichner 1700 mit Steuerrechner PDP-11/05

Zusammenarbeit mit anderen Institutionen

NASA, ESA, DFVLR
UN-Wirtschafts- und Sozialrat/Kartographisches Büro
OEEPE (Europäische Organisation für experimentelle photogrammetrische Untersuchungen)
DGK (Deutsche Geodätische Kommission)
AdV (Arbeitsgemeinschaft der Vermessungsverwaltungen der Länder der Bundesrepublik Deutschland)
verschiedene Hochschulinstitute

Karteibogen - Fernerkundung

Institut/Firma Art	Adresse	Austauschpartner
D F V L R Institut für Flugfunk und Mikrowellen	8031 Oberpfaffenhofen	

Einzelvorhaben, die ganz oder teilweise mit den Mitteln der Fernerkundung durchgeführt werden	Status *)
Stichwortartige Darstellung: (evt. Publikationen)	
1. Messung der thermischen Eigenstrahlung des Erdbodens im Mikrowellengebiet	4
2. Signaturforschung an Radiometer- und Radarbildern verschiedener Erdoberflächen	1, 4
3. Seegangsspektrumsmessung von Flugzeug und Satelliten aus	2, 3, 4
4. Systemanalysen zukünftiger Mikrowellen-Erderkundungssensoren für Flugzeug- und Satelliteneinsatz	4
5. Messung der Rückstrahlstatistik von Landzielen im mm-Wellen-Bereich	3

*)
1 = Experimentell
2 = direkte Anwendung
3 = geplant
4 = laufende Untersuchung
5 = abgeschlossene Untersuchung
6 = Ort der Untersuchung

Namen der beteiligten Wissenschaftler

Dipl.-Ing. Arko, Dipl.-Ing. Bartsch, Dipl.-Ing. Dittel, Dipl.-Ing. Fischer, Dipl.-phil. Fogy, Dr.-Ing. Grüner, Dipl.-Ing. Kleintz, Dipl.-Ing. Klement, Dipl.-Phys. Müller, Dipl.-Ing. Neugebauer, Dipl.-Ing. Preissner, Dipl.-Ing. Salzer, Dr.Ing. Seppl, Dr. Schlude, Dipl.Ing. Starker, Dr.Ing. Vogel, Dipl.Ing. Werner

Verfügbare Ausrüstung

a) Bildinterpretation

b) Bildverarbeitung
Bildverarbeitungsanlagen des German Space Operations Center (GSOC) und des Instituts für Nachrichtentechnik (554); Echtzeitprozessor für Mikrowellenbilder

c) Meßgeräte
E-SLAR flugfähig (X-Band), Scatterometer flugfähig (L-Band), Radiometer flugfähig (X-Band, 32 GHz, 90 GHz), Rückstrahlmeßapp. (X-Band, 34 GHz)

d) Sonstiges
Flugzeugpark der DFVLR-OP
Großrechenanlage Amdahl der DFVLR-OP
Flugfähiger 14 Kanal-Analog-Datenspeicher
Stabilisierung für Radarantennen im Flugzeug

Zusammenarbeit mit anderen Institutionen
Max-Planck-Institut für Meteorologie (Dr. Alpers) Hamburg

Fachrichtung: Erdeerkundung

Stand: ....

Karteibogen - Fernerkundung

Institut/Firma Art	Adresse	Austauschpartner
D F V L R Institut für Opto-elektronik	8031 Oberpfaffenhofen	

Einzelvorhaben, die ganz oder teilweise mit den Mitteln der Fernerkundung durchgeführt werden	Status *)
Stichwortartige Darstellung: (evt. Publikationen)	
1. Infrarot-Radiometrie der Erdoberfläche und Wasseroberfläche	4
2. Spektrale Emission und Reflexion von natürlichen und künstlichen Oberflächen	4
3. Radiometrie von natürlichen und künstlichen Oberflächen im sichtbaren Spektralbereich	1, 4
4. Metrisches Kamera-Experiment in Spacelab	1, 3

*)

1 = Experimentell

2 = direkte Anwendung

3 = geplant

4 = laufende Untersuchung

5 = abgeschlossene Untersuchung

6 = Ort der Untersuchung

Namen der beteiligten Wissenschaftler

Dipl.-Ing. G. Miosga; Dipl.-Ing. V. Tank; Dipl.-Ing. J.Fries; Dr. A. Rossbach; Dipl.-Phys. M. Schroeder; Dipl.-Phys.R. Stätter; Dr. K. O. Utech

Verfügbare Ausrüstung

a) Bildinterpretation

b) Bildverarbeitung

c) Meßgeräte

mehrere Radiometer (1,8 - 2,o um); Wärmebildkamera (3 - 5 um); Linescanner (3 - 5 um und 8 - 14 um) ; Luftbildkameras (Hasselblad); Michelson-Interferometer (Fourier Spektrometer) Radiometer von o,35 - 2,5 um; Spektral-Radiometer o,35 - 2,5 um; M²S Linescanner, 11 Kanäle

d) Sonstiges

Zusammenarbeit mit anderen Institutionen

Institut f. Meereskunde, Kiel

C T I , Bonn

Institut für Photogrammetrie und Ing.-Vermessung der TU Hannover

D H I , Hamburg

Fachrichtung: Geologie

Stand:

Karteibogen – Fernerkundung

Institut/Firma Amt	Adresse	Austauschpartner
Bundesanstalt für Geowissenschaften und Rohstoffe	Postfach 51 01 53 3000 Hannover 51	

Einzelvorhaben, die ganz oder teilweise mit den Mitteln der Fernerkundung durchgeführt werden	Status *)

Stichwortartige Darstellung:
(evt. Publikationen)

1. Digitale Bildauswertung multispektraler Satellitendaten zur Lagerstättenprospektion. — 1, 4
2. Lagerstättenkundliche Untersuchungen in Zentral-Marokko. Integrierte Auswertung von aeromagnetischen Messungen, multispektralen Landsat-Aufnahmen und großmaßstäbigen lagerstättenkundl.-tektonischen Kartierungen zur Vertiefung der Aussagen über erzhöffige Gangzonen. Erprobung digitaler Bildverarbeitung zur Steigerung des Informationswertes der Landsat-Bilder. (interne Berichte BGR und DFVLR) — 1, 4
3. Strukturgeologische Auswertung von Landsat-Bildern des Kanadischen Schildes in Quebec und Ontario im Hinblick auf Lagerstättenprospektion. — 1, 4
4. Untersuchung von Teilen der Sahel-Zone in der Republik Niger mit Satellitenbildern zur Ermittlung des natürlichen Potentials (Geologie, Hydrogeologie, Bodenkunde, Landnutzung) und der dynamischen Veränderungen durch Wetter und Klima. — 1, 4

*)
1 = Experimentell
2 = direkte Anwendung
3 = geplant
4 = laufende Untersuchung
5 = abgeschlossene Untersuchung
6 = Ort der Untersuchung

4.1-6a2

Namen der beteiligten Wissenschaftler

Dr. Mühlfeld, Dr. Leube, Dr. Scholz, Dr. Hoppe, Dr. Bosum, Dr. Andritzky, Dr. Ulbricht (DFVLR), Dr. Mollat, Dr. Kantor, Dr. Stranz (Seewetteramt Hamburg), Prof. Mensching (Geograph. Institut, Univ. Hamburg)

Verfügbare Ausrüstung

a) Bildinterpretation
Zoom Stereoskop – Bausch & Lomb; Zoom Transferscope (B.&L.),

b) Bildverarbeitung
Digitale Rechneranlage, Schnelldrucker-Ausgabe.

c) Meßgeräte
Exotech-Radiometer

d) Sonstiges

Zusammenarbeit mit anderen Institutionen

US Geological Survey, Reston USA;
DFVLR, Oberpfaffenhofen;
ZGF, München;
Photogrammetr. Institut TU Hannover;
Geological Survey of Canada;
Geograph. Institut der Univ. Hamburg;
Seewetteramt Hamburg

Fachrichtung: Informatik 4.1-70a.

Stand: ....

Karteibogen - Fernerkundung

Institut/Firma Amt	Adresse	Austauschpartner
Forschungsinstitut f. Informationsverarbeitung und Mustererkennung, FIM/FGAN	Breslauerstr. 48 7500 Karlsruhe 1	

Einzelvorhaben, die ganz oder teilweise mit den Mitteln der Fernerkundung durchgeführt werden	Status a)
	1 + 4

Stichwortartige Darstellung;
(evt. Publikationen)

1. Texturanalyse für ausgewählte Bilddaten und Objektklassen aus dem Bereich der Forstwirtschaft
2. Texturermittlung und Bereichsklassifizierung bei der Siedlungsanalyse
3. Untersuchungen der Maßstabsabhängigkeiten bei Texturparameter
4. Automatisierung der Objektdatenextraktion aus Luftbildern für die Regionalplanung
5. Implementierung eines Informationssystems für Objektdaten aus Luftbildern.

a)
1 = Experimentell
2 = direkte Anwendung
3 = geplant
4 = laufende Untersuchung
5 = abgeschlossene Untersuchung
6 = Ort der Untersuchung

Namen der beteiligten Wissenschaftler

Dipl.-Ing. B. Bargel
Dipl.-Ing. R. Hutter
Dipl.-Ing. K. Lütjen
Dipl.-Forstw. S. Masumy
Dipl.-Ing. U. Schlifkowitz
Dipl.-Math. W.D.Groch
Dr.-Ing. W. Kestner
Dipl.-Ing. B. Sanyal
Dr.-Ing. M. Sties

Verfügbare Ausrüstung

a) Bildinterpretation

2 Interaktive Displaysysteme (Tektonix 611, Keybord, TTY, Cursor, CDC-Anschluß)
Farbdisplay (COMTAL, Bildplatte, Keyboard, Cursor, PDP-Anschluß) / Interaktives Großflächendisplay (Philips-Lichtablenker, TTY, Cursor, CDC-Anschluß)

b) Bildverarbeitung

CDC-System - mit Standard- und Spezialperipherie gekoppelt mit:
PDP 11/45 - mit Standard- und Spezialperipherie
PDP 11/70 - mit Standard- und Spezialperipherie
Laser-Scanner - off line / DICOMED-Scanner on line, PDP 11/40

c) Meßgeräte

d) Sonstiges

Zusammenarbeit mit anderen Institutionen

Institut für Forsteinrichtung und forstl.Betriebswirtschaft, Univ.Freiburg (Prof. Hildebrandt)
Regionale Planungsgemeinschaft Untermain, Frankfurt (Dr.v.Hesler)
Bundesforschungsanstalt für Landeskunde und Raumordnung, Bonn (Prof. Dr. Schneider)
Institut für Graphische Datenverarbeitung und Strukturerkennung (IGS) der GMD (Dr. P. Wißkirchen)

Fachrichtung: Fernerkundung

Stand: ....

Karteibogen - Fernerkundung

Institut/Firma Amt	Adresse	Austauschpartner
Hilfseinrichtung Zentralstelle für Geo-Photogrammetrie und Fernerkundung der DFG	Luisenstraße 37 8000 München 2	

Einzelvorhaben, die ganz oder teilweise mit den Mitteln der Fernerkundung durchgeführt werden	Status *)
Stichwortartige Darstellung: (evt. Publikationen)	
1. Methodische und anwendungsorientierte Untersuchungen zur Fernerkundung	
a) Beteiligung am nationalen FMP	1,2,4
- Erfassung der Bodenfeuchte über die multispektrale und thermalinfrarote Aufnahmetechnik - Anwendung multispektraler Scanneraufnahmen für geologische Fragestellungen in einem subalpinen Bereich - methodische Untersuchungen zur anwendungsorientierten Reduktion multispektraler Daten - Entwicklung von digitalen Auswerteverfahren	
b) Erfassung von Braunkohlevorkommen über sekundäre Indikatoren mit Hilfe der Fernerkundung	
c) Beteiligung am NASA Landsat-2 Programm - Anwendung von Satellitendaten für Landnutzungskartierung in Italien konventionelle und digitale Auswertung - Einsatzmöglichkeiten von Landsat für geologische Fragestellungen	

*)
1 = Experimentell
2 = direkte Anwendung
3 = geplant
4 = laufende Untersuchung
5 = abgeschlossene Untersuchung
6 Art der Untersuchung

Stichwortartige Darstellung der Einzelvorhaben - Fortsetzung

4.4 - 80 b

d) photogeologische und tektonische Aufnahme der Insel Sardinien

e) Beteiligung am NASA - HCMM Projekt multidisziplinäre Anwendung von thermischen Satelliten-Infrarotaufnahmen

2. Entwicklung und Bereithaltung von Methoden im Bereich der geologisch orientierten Photogrammetrie.
Laufender Einsatz terrestrisch-photogrammetrischer Methoden für tektonische Fragestellungen.

3. Service-Leistungen der ZGF

Bereitstellung von Auswertemethoden und Auswertegeräten im Bereich der Fernerkundung (Bodenmeßgeräte, Bildauswertung) sowie für die photogrammetrisch-geologische Geländeaufnahme (Aufnahme- und Auswertesysteme).

Serviceleistungen im Bereich der Bilddatenverarbeitung.

Bereitstellung einer Bildverarbeitungs-Software (IMAGIN).

4.4-90 c

Fachrichtung: Forstwissenschaft

Stand: 4.4-90a

Namen der beteiligten Wissenschaftler

Prof. Dr. J. Bodechtel; Dr. R. Haydn; Dr. J. Nithack; Dipl.-Phys. M. Seiderer; Dipl.-Phys. S. Fernandez; Dipl.-Geol. Jaskolla; Dipl.-Geol. U. Münzer; Dipl.-Geol. DiBernardo; Dipl.-Geol. G. Gerstner,

Verfügbare Ausrüstung

a) Bildinterpretation

I^2S optisches Bildmischgerät
Planimat D 2 (Zeiss) mit Ecomat-11

b) Bildverarbeitung

Analog/digitales Bilddatenverarbeitungssystem ISI 47o mit PDP 11/4o Rechner (64 k byte) mit Massenspeicher und Peripherie; Optronics Photowrite System;

c) Meßgeräte

Landsat Radiometer Exotech; IR Radiometer Heimann KT-4 und Barnes PRT-1o; terrestr. Stereomeßkammern SMK 12o, SMK 4o und TMK ; diverse Bodenmeßgeräte

d) Sonstiges

Hasselblad EL 5oo

Zusammenarbeit mit anderen Institutionen

DFVLR; Landesämter; Hochschulen; sowie mit europäischen und außereuropäischen Institutionen.

Karteibogen - Fernerkundung

Institut/Firma Amt	Adresse	Austauschpartner
Abt. Luftbildmessung und -interpretation der Universität	Erbprinzenstraße 17 a 7800 Freiburg/Br.	

Einzelvorhaben, die ganz oder teilweise mit den Mitteln der Fernerkundung durchgeführt werden	Status *)
Stichwortartige Darstellung: (evt. Publikationen)	
1. Erkennung und Klassifizierung von Pflanzenart, Pflanzenzustand und Vegetationsschäden und Schadursachen aus Luftbildern und Scanneraufzeichnungen	4, 5
2. Anwendung der Fernerkundung für Wald- und Landnutzungsinventuren (qualitative und quantitative Flächenbestimmung, Waldkartierung, Holzvorratsermittlung, Erntevorhersage).	4, 5
3. Vergleichende Untersuchung verschiedener Klassifizierungssysteme	4
4. Erforschung spektraler Signaturen von Kulturpflanzen am Boden und mit Mitteln der Fernerkundung	3, 4
5. Abhängigkeit von Farb- und Texturmerkmalen von Maßstab, Bildortlage und Geländerelief	4, 5
6. Untersuchung der dynamischen Veränderungen verschiedener Pflanzengesellschaften im Jahresablauf.	4
7. Aufbau eines Software-Systems für digitale Bildverarbeitung	3, 4

*)
1 - Experimentell
2 - direkte Anwendung
3 - geplant
4 - laufende Untersuchung
5 - abgeschlossene Untersuchung
6 - Ort der Untersuchung

Namen der beteiligten Wissenschaftler

Prof. Hildebrandt; Dipl.-Forstwirt P. Reichert; Dipl.-Forstwirt H.J. Dörfel; Dipl.-Landwirt E. Sannwald; Rev.-Förster H. Dietz; Stipendiaten: Dipl.-Forstwirte K. Djawadi, M. Masumy, N. Al Homaid, Dipl.-Forsting. M. Cagirici, C.M. Ribeiro Carneiro

Verfügbare Ausrüstung

a) Bildinterpretation

Bausch & Lomb Zoomstereoskop + Spiegelstereoskope; Joyce-Loebl-Mikrodensitometer, Autodensidater incl. Nova 2/10; Mac beth Farb-Transmissionsdensitometer

b) Bildverarbeitung

Software-Paket für digitale Bildverarbeitung; 5-kanaliger Image-Analyzer (ISI System 150); I^2S-Color Additive Viewer 600

c) Meßgeräte

Zeiss-Doppelprojektor DP 1; Zeiss Stereotop; Radialschlitztriangulator; mehrere Luftbildumzeichner

d) Sonstiges

2 Hasselblad-Kameras (500 EL) für den Einsatz im Flugzeug

Zusammenarbeit mit anderen Institutionen

DFVLR, Oberpfaffenhofen; ZGF, München; FIM, Karlsruhe; Inst. f. Phys.Weltraumforschung/Fraunhofer Ges., Freiburg; Institut f. Phytomedizin, Univ. Hohenheim; BASF Limbergerhof; Bundesforschungsanstalt f. Forst-und Holzwirtsch./Waldinventur, Reinbek; Institut f. Forsteinrichtung, Univ. Göttingen; Institute der Univ. Freiburg
Forstdienststellen der intern. Organisationen (FAO/ESA/EURATOM)

ISSUE NO. 1 — LANDSAT DATA USERS NOTES — NOVEMBER 1978

IMAGE PROCESSING SOFTWARE SYSTEMS

COSMIC
112 Barrow Hall
Athens, Georgia 30601
Contact: W. Zipperer
(404)542-3265
(VICAR, SMIPS, LARSYS, LACIE)

International Business Machines
1322 Space Park Drive
Houston, Texas 77058
Contact: Charles Gilmore
(713)333-5300
(ERMAN II)

University of Kansas
Lawrence, Kansas 66045
(KANDIDATS)

ADDITIONAL INFORMATION ON TRAINING

The bulk of the training conducted at EDC consists of courses designed to meet the requirements of agencies of the U.S. Department of the Interior and other branches of the Federal government. Each course is planned individually, based on the requirement and schedule of the agency involved and the availability of instructors at EDC. Cost of instructional time and materials is borne by the sponsoring agency. Information on the planning of such a course can be obtained through the Chief, Training and Assistance Section, Applications Branch, U.S. Geological Survey, EROS Data Center, Sioux Falls, South Dakota 57198.

Two remote sensing workshops are presented at the Data Center annually, in May and September, for non-U.S. scientists. Application materials for the International Workshops can be obtained from:

Chief, Office of International Geology
U.S. Geological Survey
National Center (917)
Reston, Virginia 22092

These workshops are introductory in nature and emphasize manual interpretation of Landsat imagery.

Advanced remote sensing courses for foreign scientists are offered by the U.S. Geological Survey's field center in Flagstaff, Arizona. Information on the advanced series can also be obtained from the Office of International Geology, address given above.

Responsibility for training of State and local government personnel is assumed by NASA through its Regional Remote Sensing Applications Program. Those interested in the NASA training program should contact one of the following:

Dr. Phil Cressy
Code 902.1
NASA/Goddard Space Flight Center
Greenbelt, Maryland 20771

Mr. D. W. Mooneyhan
Code GA
Earth Resources Laboratory
Bay St. Louis, Mississippi 39520

Dr. Dale R. Lumb
Chief, Technology Applications Branch
MS 242-4
NASA/Ames Research Center
Moffett Field, California 94035

Also, several universities in the United States periodically offer short courses or workshops in various aspects of remote sensing, some of which are presented cooperatively with EDC. Information on these can be obtained from:

Charles E. Olson
Remote Sensing Program
School of Natural Resources
University of Michigan
Ann Arbor, Michigan 48109
(Vegetation Remote Sensing Workshops)

Charles Theisen
Director of Continuing Education
South Dakota School of Mines and Technology
Rapid City, South Dakota 57701
(Applications of Remote Sensing to Mineral Exploration)

Stephen D. DeGloria
Remote Sensing Research Program
Space Sciences Laboratory
University of California
Berkeley, California 94720
(Resources Inventory and Analysis: Water Resources)

Jules Bernard
Manager, Short Course Program
University of Tennessee Space Institute
Tullahoma, Tennessee 37388
(Transportation Engineering)

Office of Continuing Engineering Education
George Washington University
Washington, D.C. 20052
(Misc. short courses)

Paul Fishman
Director of Special Programs
Graduate School of Design
Gund Hall, Harvard University
Cambridge,
Massachusetts 02138
(Terrain Analysis Workshops)

Douglas B. Morrison
Laboratory for Applications of Remote Sensing
Purdue University
1220 Potter Drive
West Lafayette, Indiana 47906
(Computer Processing)

Indiana State University Remote Sensing Laboratory
Department of Geography and Geology
Indiana State University
Terre Haute, Indiana 47809
(Introductory Courses)

Donald G. Moore
Remote Sensing Institute
South Dakota State University
Brookings, South Dakota 57006
(Visiting Scientist Programs)

Robert D. Heller
College of Forest, Wildlife and Range Sciences
University of Idaho
Moscow, Idaho 83843
(Aerial Photo Interpretation)

IMAGE PROCESSING HARDWARE SYSTEMS

Aydin Controls
414 Commerce Drive
Fort Washington, Pennsylvania 19034
(215)542-7800

Broomall Industries, Inc.
982 Parkway
Broomall, Pennsylvania 19008
(215)353-4818
(GP-100 Graphics Processing System)
(VISICOM)

Comtal Corporation
169 Halstead
Pasadena, California 91107
Contact John Tant
(213)793-2134
(Comtal Series 8)

Control Data Corporation
P.O. Box 1249
Minneapolis, Minnesota 55440
Contact Chuck Spreitzer
(612)853-6300

DICOMED Corporation
9700 Newton Avenue South
Minneapolis, Minnesota 55431
(Image Data Processing Peripherals)

DIGICOM, Inc.
Parameter Bldg.
Chelmsford, Massachusetts 01863
(DIGICOLOR)

DeAnza Systems, Inc.
3444 De LaCruz Boulevard
Santa Clara, California 95050
(408)988-2666

ESL, Incorporated
495 Java Drive
Sunnyvale, California 94086
Contact John Baumgartner
(408)734-2244
(IDIMS)

Grinnell Systems
2986 Scott Boulevard
Santa Clara, California 95050
(408)988-2100

Institute for Advanced Computation
1214 S. Royal Street
Alexandria, Virginia 22314
(703)836-6878
(ILLIAC IV)

I2S (International Imaging Systems)
1050 Stewart Drive
Sunnyvale, California 94086
(408)737-4310
(LASCO System)

Interpretation Systems, Incorporated
P.O. Box 1007
Lawrence, Kansas 66044
Contact Jerry D. Lent
(913)842-5678
(ISI System 470 and BAND)

General Electric Company
5030 Herzel Place
Beltsville, Maryland 20705
Contact Dave Swan
(301)937-3500
(Image 100)

LEXIDATA Corporation
215 Middlesex Tpk.
Burlington, Massachusetts 10803
(617)273-2700
(System 6400)
(Models 200-D & 400-D)

Lockheed Electronics Company
Remote Sensing Applications Lab
1830 Space Park Drive
Houston, Texas 77058
Contact E. Tokunaf
(713)488-0080

Bendix Aerospace Systems Division
Ann Arbor, Michigan 48107
Contact Gene Zeroll
(313)665-7766
(M-DAS)

Ford Aerospace & Communications
Corporation
P.O. Box 58487
Houston, Texas 77058
Contact H. E. Dargent
(713)488-1270
(M-DAS)

MacDonald Dettwiler & Associates
Ste. 100, 2182 W. 12th Avenue
Vancouver, B. C., Canada V6K 2N4
(604)732-6823

Optronics International, Inc.
7 Stuart Road
Chelmsford, Massachusetts 01824
Contact James C. Geegan
(617)256-4511

Ramtek
585 North Mary Avenue
Sunnyvale, California 94086
(408)735-8400

STARAN
Goodyear Aerospace Corporation
Akron, Ohio 44315
(216)794-3631

Sci-Tex North American
1450 Broadway
New York, New York 10018
Contact Neil Yingling
4430 Willow Run Drive
Dayton, OH 45430
(513)426-0844

Spatial Data Systems, Inc.
Box 494
508 S. Fairview Avenue
Goleta, California 93017
(805)967-2383
(Data Image Recorder)
(Data Eye Camera)
(Data Color)
(Computer Eye)

International Imaging Systems
650 North Mary Avenue
Sunnyvale, California
Contact John Adams
(408)737-0200
(System 101)

Andrew Sterloff, Consultant
P.O. Box 416
Frederick, Maryland 21701
(301)874-2828

Battelle Corporation
Pacific Northwest Laboratories
Battelle Blvd.
Richland, Washington 99352
Contact Jay Eliason
(509)746-2277

Aeronutronic Science Technology Corp.
17137 East Gale Avenue
City of Industry, California 91745
(213)965-7252

COMARC Design Systems
The Agriculture Bldg.
Embarcadero at Mission
San Francisco, California 94105
Contact Don Johnson
(415)982-5200

Calspan Corporation
P.O. Box 235
Buffalo, New York 14221
Contact John E. Walker
(716)632-7500

Computer Sciences Corporation
8728 Colesville Road
Silver Spring, Maryland 20910
Contact Robert Caret
(301)589-1545

Comtal Corporation
169 North Halstead
Pasadena, California 91107
Contact John Tant
(213)793-2134

Control Data Corporation
P.O. Box 1249
Minneapolis, Minnesota 55440
Contact Leo Eichten
(612)853-3790

Earth Satellite Corporation
7222 47th Street
Washington, D.C. 20015
Contact Robert Gribben
(301)652-7130

Earth Sciences of America
1433 Mitchell Trail
Elk Grove Village, Illinois 60007
Contact James Wm. Smith
(312) 529-1140

Ecographics
International Environmental Analysts
P.O. Box 706
La Jolla, California 92038
Contact Timothy W. Foresman
(714)224-9841

Environmental Research Institute
of Michigan
P.O. Box 618
Ann Arbor, Michigan 48107
Contact Marvin Holter
(313)994-1200

ESL, Incorporated
495 Java Drive
Sunnyvale, California 94086
Contact John Baumgartner
(408)734-2244

Ford Aerospace & Communications
Corporation
P.O. Box 58487
Houston, Texas 77058
Contact H. E. Dargent
(713)488-1270

General Electric Company
5030 Herzel Place
Beltsville, Maryland 20705
Contact John Malone
(301)982-6095

Geospectra Corporation
202 East Washington, Suite 504
Ann Arbor, Michigan 48108
Contact R. K. Vincent
(313)994-3450

Goodyear Aerospace Corporation
Sensor Evaluation & Training
Facility
Akron, Ohio 44315

HRB - Singer, Inc.
Environmental Analysis Group
Science Park - Box 60
State College, Pennsylvania 16801

Institute for Advanced Computation
1214 S. Royal Street
Alexandria, Virginia 22314
(703)836-6878

International Business Machines
1800 Frederick Pike
Gaithersburg, Maryland 20760
Contact Ralph Bernstein
(301)840-7043

International Imaging Systems
650 North Mary Avenue
Sunnyvale, California 94086
Contact John Adams
(408)737-0200

Jet Propulsion Laboratory
4800 Oak Grove
Pasadena, California 91103
(213)354-4321

Lafayette Data Control
P.O. Box 2023
West Lafayette, Indiana 47906
Contact Stephen G. Luther
(317)743-9983

Lockheed Electronics Company
Remote Sensing Applications Lab
1830 Space Park Drive
Houston, Texas 77058
Contact E. Tokunaf
(713)488-0080

MacDonald - Dettwiler, & Associates
10280 Shellbridge Way
Richmond, B.C.
Canada
Contact Cil Bost
(604)278-3411

Mead Technology Laboratory
3481 Dayton-Xenia Road
Dayton, Ohio 45432
Contact Earl Schiller
(513)426-3111

OmegaDimensions, Inc.
800 East Girard, Suite 519
Denver, Colorado 80231
Contact Dana H.W. Bergman
(303)750-6731

Oregon State University
Environmental Remote Sensing
Applications Lab
Corvallis, Oregon 97331
Contact Barry Schrumpf
(503)754-3056

Pattern Recognition - Technology
and Application
S. S. Viglione and Associates
351 Peralta Hills Drive
Anaheim, California 92807
Contact Sam S. Viglione
(714)998-3620

Pennsylvania State University
Office of Remote Sensing of
Earth Resources
219 Electrical Eng. West Bldg.
University Park, Pennsylvania 16802
Contact George McMurtry
(814)865-0750

Public Technology, Inc.
1140 Connecticut Avenue, NW
Washington, D.C. 20036
Contact Peter Bushman
(202)452-7700

Purdue University
Laboratory for the Applications of
Remote Sensing
West Lafayette, Indiana 47906
Contact Terry Phillips
(317)749-2052

Radian Corporation
8500 Shoal Creek Boulevard
Austin, Texas 78758
Contact Dennis D. Hefter
(512)454-4797

Remote Sensing Lab
Dept. of Applied Earth Sciences
Stanford University
Stanford, California 94305
Contact Ronald J. Lyon
(415)497-3741

Remote Sensing Program
School of Civil and Environmental
Engineering
Cornell University
Hollister Hall
Ithaca, New York 14853
Contact T. Liang
(607)256-4330

Resources Development Associates
1101 W. San Antonio Rd.
Mountain View, California 94043
Contact Ken Crab
(415)961-7477

Scientific Data, Inc.
P.O. Box 36799
Houston, Texas 77036
Contact Russell H. Lyons
Leonard J. Nash
(713)785-4020

South Dakota State University
Remote Sensing Institute
Brookings, South Dakota 57006
Contact Victor I. Myers
(605)688-4184

TRW Systems Group
One Space Park
Redondo Beach, California 90278
Contact Sam Pelman
(213)536-2012

Texas A & M University
Remote Sensing Center
College Station, Texas 77843
Contact John Rouse, Jr.
(713)845-5422

University of California
Space Sciences Laboratory
Berkeley, California 94720
Contact Robert N. Colwell
(415)642-1363

University of Southern California
Image Processing Institute
Los Angeles, California 90007
Contact William Pratt
(213)746-8814

University of Kansas
Space Technology Center
Lawrence, Kansas 66045
Contact Robert Haralick
(913)864-3542

Western Geophysical Aero Services Division
8100 West Park Dr.
Houston, Texas 77036
Contact Stanley Wearing
(713) 784-5800

PERCEPCION REMOTA

ARTICULOS Y BIBLIOGRAFIA

DR. HANS PETERS BAHR.

FEBRERO DE 1980.

DESIGN [illegible]ARGE LAMBERT-TYPE REFLECTION STANDARD AND FULL-FRAME CALIBRATION OF A CAMERA LENS

H.-P. BÄHR

Institut für Photogrammetrie und Ingenieurvermessungen, Technische Universität Hannover

Presented at the International Society of Photogrammetry, Symposium Comm. VII

Freiburg / Brsg. 1978

ABSTRACT

A 1.20 m by 1.20 m large $BaSO_4$ - reflector has been developed in order to provide a full-frame standard of perfect diffuse surface for light fall-off calibration of a 60 mm-HASSELBLAD BIOGON. The calibration was executed analytically by least-squares adjustment, using cosine functions with additional linear parameters, which lead to ± 0.02 D rms error of the residuals.

ZUSAMMENFASSUNG

Zur flächenhaften Bestimmung des Lichtabfalls in einem 60 mm-HASSELBLAD BIOGON wurde ein 1,20 m x 1,20 m großer $BaSO_4$ - Eichstrahler mit vollkommen diffus streuender Oberfläche entwickelt. Die Eichung des Objektivs erfolgte durch eine Ausgleichung über Kosinus-Funktionen mit zusätzlichen linearen Anteilen, was auf mittlere Fehler von ± 0,02 D führte.

RESUME

Un réflecteur - $BaSO_4$ (1,20 m par 1,20 m) à surface parfaitement diffuse a été développé pour calibrer la répartition de la lumière à travers un objectif HASSELBLAD BIOGON (60 mm). La calibration fait intervenir l'ajustement de fonctions-cosinus par les moindres carrés, avec des paramètres linéaires supplémentaires. L'erreur moyenne sur les écarts résiduels atteint ± 0,02 D.

1. Basic Considerations

The photographic image is still the most important tool for Remote Sensing and there is no reason today to expect a quick change. The 6 x 6 cm format photography can be considered as a standard for many applications. It directly provides high density information (especially when colour film is used) for low cost. Scanner imagery needs specially equipped planes and sophisticated digital processing to receive an image suitable for further investigation. Consequently digital scanner imagery is about ten times more expensive than analog conventional photography.

Conventional photography is ideally appropriated for visual interpretation. Quantitative investigations can routinely be applied as far as geometry is concerned; semantic information however can be extracted visually rather than by "measurement". One reason for this situation is the difficulty to describe the image grey values as a function of the object characteristics properly. There exist too many factors which influence the original information, for example illumination, air light, instrument and film characteristics, as well as film development (see J. SIEVERS /6/). Principally two different approaches are possible in order to obtain nevertheless quantitative results from semantic image analysis:

1. The physical properties of the mentioned disturbing factors, which superimpose the original reflection from the object surface, are analysed one by one, and their particular contribution to the registered grey values is taken for digital or analog data correction.

2. The physical composition of the data is more or less neglected, and a statistical analysis of known surfaces ("training-sets") provide parameters for unknown objects in the image.

Approach No 2 is today widely applied and known as "Maximum - Likelihood - Classification". The disadvantage of that method is the need of training - sets, which often can not be defined in an appropriate manner (see DENNERT-MÖLLER /2/). Approach No 1 up to now does not lead directly to operational results for object classification. At the other hand, Maximum - Likelihood - Classification will yield optimal results only if the data is rigorously preprocessed for compensation of physical disturbing factors. Therefore the behavior of these factors is important, and from that point of view many theoretical investigations within that field get a practical objective.

This contribution concentrates on a single physical phenomenon, the light fall - off by a camera lens as well as its compensation using a reflection standard, which fills the field of view of the camera totally ("full - frame - reflector").

2. Analysis of the Problem

In August, 1974 pre - flights for the National German Aircraft - Program took place at the Jade test site (North Sea Coast near Wilhelmshaven). Coordinated by the Institut für Photogrammetrie und Ingenieurvermessungen (IPI) of the Technical University of Hannover, HASSELBLAD MK 70 Colour Photography was obtained from a prepared private CESSNA airplane, as well as radiometer profiles from ship. At that time the objective of the investigations was to find appropriate test fields for monitoring tidal flow, sediment transport etc. as well as best suited spectral channels.

Fig. 1 shows microdensitometer profiles of the Jade seaway perpendicular to the dredged navigable water of 20 m depth. For the profiles the original HASSELBLAD MK 70 Kodak Ektachrome film was used. The microdensitometer was a JOYCE - LOEBL MK III CS with analog recording. The phenomena shown on the photography are water bodies of different sediment concentration. In the middle of the image and the profiles, relatively deep and clear water of greenish colour can be interpreted. At both sides brown/yellow water bodies indicate sedimental plumes, which flow from the tidal land into the navigable water.

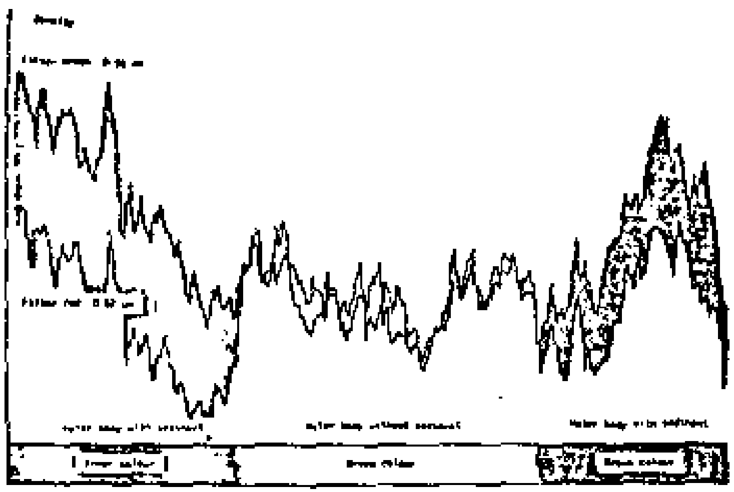

Fig.1: Microdensitometer profiles of the Jade seaway in HASSELBLAD MK 70 KODAK EKTACHROME photography

The microdensitometer records this situation best using green filter (0,55 µm) and red filter (0,62 µm). This matter of fact has been confirmed by multispectral scanner imagery some years later.

The correlation of microdensitometer profiles with in-situ radiometer profiles from ship leads to many particular problems. Apart from geometric registration, atmospheric disturbing factors and film properties, the influence from light fall - off by the camera lens has obviously to be corrected. In Fig. 1 the light fall - off affects the micro - densitometer - profiles by superimposing a "catenoid" - shaped curve, most clearly observed at both ends. Correction of this influence can be provided only if appropriate compensation procedures for light fall - off are applied.

3. Design of a LAMBERT-Type Reflector

To determine the transmission properties of the incident light by the camera lens, a configuration has to be found, where all the other parameters which influence on the grey values could be neglected. These are primarily the differnces in reflection by the object per sq. and the directions of both incident radiation and lens axis. Therefore a perfect

diffuse surface would allow to get imagery which are only affected by lens and film properties.
Different approaches were made in order to find a perfect diffuse surface, which covers the field of view of the camera totally *. First an opaque plate was put in front of a projection screen, which was illuminated indirectly. However the distribution of densities on the photographed opaque plate was not uniform, as proved by microdensitometer profiles. Then the cloud - covered, hazy sky was taken for a diffuse target. The result of this approach is shown in Fig. 2: the negative photography obtained from the sky was used as a mask for compensation of the original light fall - off effect, but without success. Obviously the mask compensates only the left branch of the profile; at the right one the presence of the sun - though not visible - disturbes the mask effect.

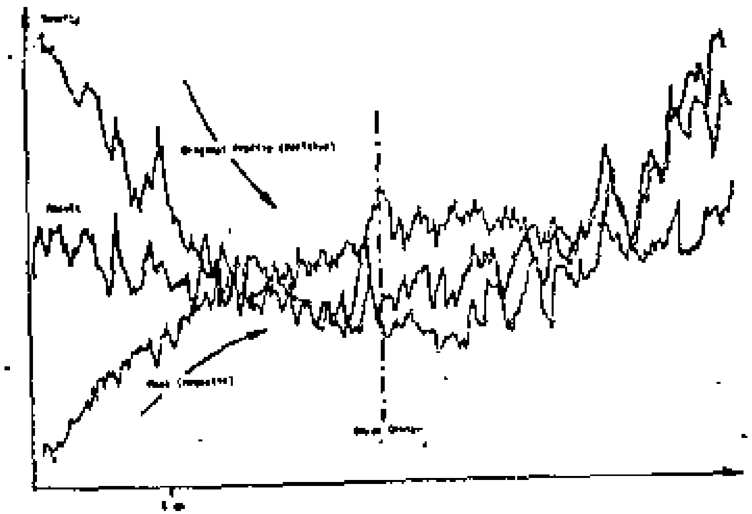

Fig. 2: Original light-fall-off effect superimposed by a negative mask obtai from hazy sky photography (Microdensitometer profiles through image

Finally Bariumsulfat ($BaSO_4$), the "classical" substance for the design of reflection standards was tried in order to obtain a perfect reflecting, plate - shaped diffuser. A so - called "LAMBERT - Reflector" provides theoretically uniform diffuse reflection, so that

$$\text{Reflectance } \rho = \frac{\text{Reflected Radiance Flux } \Phi_r}{\text{Incident Radiance Flux } \Phi_i} = 1$$

In practise, LAMBERT - Reflectors have to be used basically for determining the reflectance factor R, which characterises the reflectance of

---

* "ULBRICHT'S Sphere Photometers" used at the "Physikalisch - Technische Bundesanstalt" in Braunschweig, which provide diffuse illumination, were too small for the HASSELBLAD camera, though up to 130 cm in diameter.

an objec... ..d therefore the object itself:

$$R = \frac{\int_{\Omega_r} L_r(\vartheta_r, \varphi_r) \cos \vartheta_r \, d\Omega_r}{L_w \int_{\Omega_r} \cos \vartheta_r \, d\Omega_r}$$

(see KASTEN, RASCHKE /3/; KRIEBEL /5/)

Herein L_r is the reflected radiance of an object as a function of zenith angle ϑ and azimuth φ, integrated over a solid angle Ω. L_w denotes the (100 %) reflected radiance of a LAMBERT - Reflector. Therefore a reflection standard of this type has an importance, which exceeds the specific application of light fall - off compensation discussed here.

Generally reflection standards do cover only a small portion of the camera's field of view; nevertheless it is possible to determine light fall - off corrections (see SIEVERS /6/). A more rigorous procedure requires standards which fill the camera's field of view totally. For the used camera / lens - configuration + a 120 cm diameter standard was requested. This is a size where the Bariumsulfat - substance may not layed on by a spattle and polished accurately, as done for small - size plates.

Many approaches were made in order to find suitable material for the plate and appropriate methods for application of the substance. Because of the large size, a metal plate can not be used. Glass plates have to be roughened by sand blast and stabilized before putting Bariumsulfat on it. Application of the substance was tried first by a machine, which rotates the plane horizontally, generally used for putting emulsion on photographic film ("KLIMSCH - ROTOR"). Caused by the rotation, bubbles of ca. 0,05 mm diameter appeared, and the dry layer was entirely covered by tiny "craters". Also pouring the substance onto the plate without rotation did not lead to suitable results, because the layer cracked.

Finally, excellent results were obtained by using a roughened, 120 x 120 x 1,2 cm PVC - covered wooden plate and application of liquid $Ba\,SO_4$ - substance by a spray gun, observing the general instructions for varnishing. The spray effect leads to the desired degree of roughness, which excludes specular reflection. The surface has a uniform thickness, a uniform texture and a spectral reflectance of about 0,98 (see KORTE /4/).

The composition of the layer differs from the standard type, roughly described in /9/, which uses MgO:

1. mix 20 parts Polyvinylalcohol and 100 parts aqua destillata; heat and sift the solution
2. sift $Ba\,SO_4$ powder and add aqua destillata to get a pulpy mass
3. take 125 ml of that mass and add 2 ml of the solution
4. now add aqua destillata until the consistency is ready for the spray gun

+ HASSELBLAD MK 70, Reseau 1138, ZEISS BIOGON, f = 60 mm Nr. 5198261

4. Calibration of the Camera Lens by Least Squares Adjustment Using the LAMBERT Reflector

Photography of the LAMBERT reflector was taken during hazy sky, paying attention to the configuration described by Fig. 3. For the practical approach, KODAK - EXTACHROME COLOUR film was used, taking pictures with apertures of 1 : 5,6 and 1 : 8. As tests had shown, film development by fully automatic procedures provided best results; i. e. no disturbing influence was added by the film development. Manual tank development however means a real risk for the photography (see ALVES /1/). The camera at 1 m distance from the reflector, did not affect the plate by shadows.

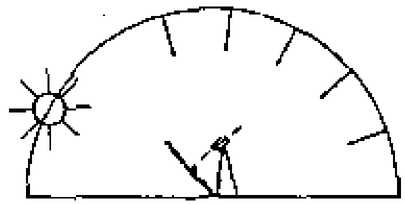

Fig.3: Configuration for taking photos from the LAMBERT reflector (hazy sky)

This is in accordance with Fig. 4 which shows microdensitometer profiles at 4 different sections of the original image. The profiles run in a very smooth way (compared for instance with Fig. 2), which proves the excellent quality of the LAMBERT reflector.

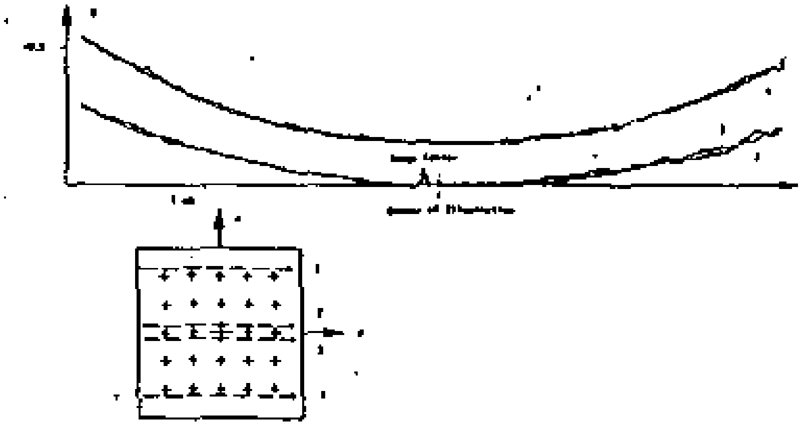

Fig. 4: Microdensitometer profiles along 4 different sections of full-frame reflector photography (scan direction from top to bottom)

The peak is caused by the reseau mark and indicates the image center

However, a slight difference of the "top" and the "bottom" branches is obvious, caused by a shadow from the ground. This effect could be avoided by illuminating the reflector according to the principle of ULBRICHT's Sphere Photometer. Apart from the ground effect the profiles characterize nothing but the light fall - off by the camera lens. As there is a slight density displacement from the image center (indicated by the reseau mark's peak), the image itself can not correctly be taken for a mask in order to compensate for light fall - off in a pure analog mode. It is anyway more rigorous to execute the following steps analytically.

For the analytical determination of light fall - off, exact coordinates for particular grey values have to be known, related to the image center as origin. Consequently the reseau marks were used to guarantee uniform distribution of measurements.

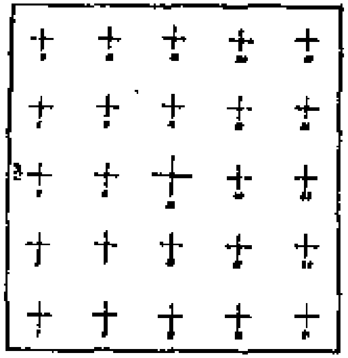

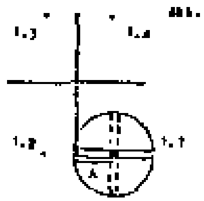

Fig.5: Configuration during pointwise measurement of grey values

Distance A was controlled by the iris edge of the microdensitometer

Fig. 5 illustrates the point configuration: per image 100 measurements had to be made (executed by ALVES /1/). For each f = 1 : 5,6 and f = 1 : 8 14 images were evaluated: this finally makes 2800 values.

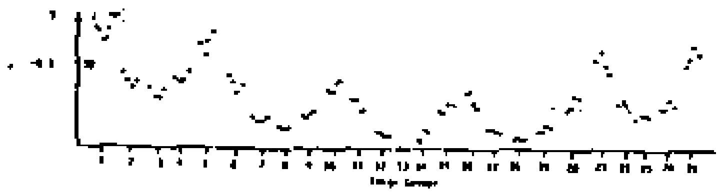

Fig. 6: Distribution of densities at reseau marks within the LAMBERT-reflector full frame photography

Fig. 6 shows a result for one image (f = 1 : 5,6). Every point corresponds to one measurement. The "nests" of 4 points around the reseau marks and the characteristic behavior of the grey level along the scan lines (1 ... 4, 5 ... 8 etc., see Fig. 4) can be detected clearly. For all measurements, grey wedge D 1247 was used, where 1 cm (z) corresponds to 0,1 D. All values were related to the brightest point in the image center.

It is common to describe the light fall - off by a cosine function, admitting a radial and symetric behavior of the phenomenon (see SIEVERS /7/). This actually can be done here, yet with respect to a superimposed linear light fall - off caused by the shadow from the ground. Approximative computation showed that

$$D_\alpha = f\,(1 - \cos^3 \alpha)\ ;\ D_\alpha = f\left(\frac{1}{\cos^3\alpha} - 1\right)$$

$$D_\alpha = f\,(1 - \cos^4 \alpha)\ ;\ D_\alpha = f\left(\frac{1}{\cos^4\alpha} - 1\right)$$

$$\text{and} \qquad D_\alpha = f\,(1 - \cos^5\alpha)$$

could successfully be applied for description of the radial part of the function.

For a least - squares adjustment, error equations are written as follows

$$L_i + v_i = f\,(\cos\alpha)_i\; c_1 + y_i\, c_2$$

$$\text{or} \qquad v_i = a_i\, c_1 + b_i\, c_2 - L_i$$

The unknown parameter c_1 signifies a factor, which adapts the cosine function to the microdensitometer profile, whereas c_2 describes the linear part of the light fall - off as a function of the y - coordinate. For each image 100 error equations exist to determine the two unknowns c_1 and c_2.

Function		$1-\cos^3$	$1/\cos^3-1$	$1-\cos^4$	$1/\cos^4-1$	$1-\cos^5$
	c_1	1,0892	0,8665	0,8458	0,6229	0.7000
	c_2	0,0019	0,0019	0,0019	0,0019	0,0019
f = 1:5,6	m_0 (0)	± 0,0282	± 0,0197	± 0,0297	± 0,0185	± 0,0312
	c_1	0,8822	0,6963	0,6858	0,5090	0,5683
	c_2	0,0014	0,0014	0,0014	0,0014	0,0014
f = 1 : 8	m_0 (0)	± 0,0193	± 0,0207	± 0,0195	± 0,0210	± 0,0198

Table 1: Results from least - squares adjustments

The results of the adjustment are summarized in Table 1. m_0 is the weighted root mean square error, computed from the residuals which consequently signifies the accuracy of the procedure. Hence for f : 5,6 we get

$$D_\alpha = \left(\frac{1}{\cos^4\alpha^0} - 1\right)\, 0{,}6229 + y_{[mm]}\ 0{,}0019$$

and for f = 1 : 8 we get

$$D_\alpha = (1 - \cos^3\alpha^0)\ 0{,}8822 + y_{[mm]}\ 0{,}0014$$

as the best fit. The root mean square errors of c_1 are all below ± 0,0035, those of c_2 are all below ± 0,00006. There exist no correlation between the unknowns.

Obviously there is a steeper light fall - off for f = 1 : 5.6 than for f = 1 : 8, but the difference is only about D = 0,05 at the maximum (α = 25 °). Even less is the difference between the particular functions: ΔD = 0,02 for f = 1 : 5,6 and ΔD = 0,015 for f = 1 : 8, both at α = 17 °. For many practical applications an appropriate mean function will be sufficient.

Once the pa   rs of light fall - off are known, compensation of this particu... effect can generally be executed analytically. This affords, however, images in digital form. The formulas have to be applied in the negative sense defining the image center as the origin of a with D = 0, neglecting the linear part.

5. Digital Reproduction of the Light Fall - Off Phenomenon

General advantage of a rigorous analytical approach is the possibility to analyse the behavior of a phenomenon theoretically. For the problem discussed here this means, that we can reproduce the measured conditions digitally. Moreover the particular effect caused by an additional linear disturbing function can be demonstrated. Two examples are displayed in Fig. 7.

The study of light fall - off in camera lenses is a limited, but necessary step with regard to describe the image grey values as a function of the object characteristics properly. The LAMBERT reflector used for full frame calibration here, can be applied beyond that in order to determine the reflectance factor of particular objects and thus provide another contribution to the entire complex.

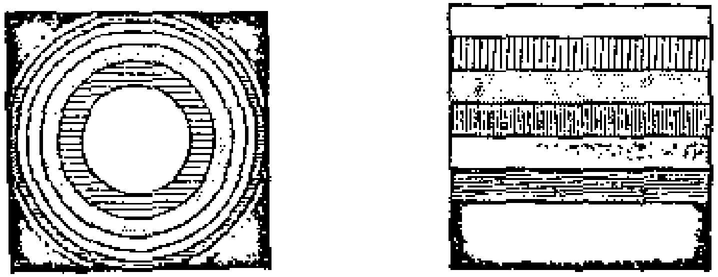

a b

Fig. 7: Simulation of light fall-off components for the evaluated configuration (f = 5.6)
a) Radial component (c_1 = 0.6229 ; c_2 = 0)
b) Linear component (c_1 = 0 ; c_2 = 0.00194)

The steps correspond to the following densities [D] :

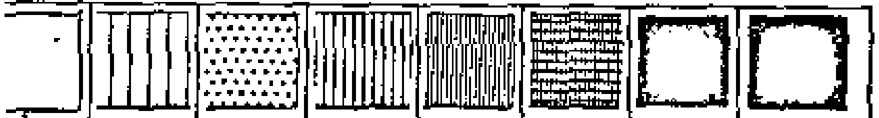

0	0.42	0.84	1.25	1.67	2.09	2.50	2.92
0	0.12	0.24	0.36	0.48	0.61	0.73	0.85

Literature

/1/ ALVES, K. : Radiometrische Untersuchung von Farb-Umkehr-Diapositiven. Diplomarbeit TU Hannover, 1976

/2/ DENNERT-MÖLLER, E.: Multispectral Classification of Tidal Lands. Mitteilungen der Geodätischen Institute der TU Graz, Folge 29, 1977

/3/ KASTEN, F. RASCHKE, E. : Nomenklatur zur Beschreibung von Strahlungsmessungen und -rechnungen. Bundesministerium für Bildung und Wissenschaft, Forschungsbericht W 72 - 30, 1972

/4/ KORTE, H. : Über Messung des Leuchtdichtefaktors an beliebig reflektierenden Proben. Mitteilungen der Physikalisch - Technischen Bundesanstalt Braunschweig in LICHTTECHNIK 11/1967

/5/ KRIEBEL, K. Th. : Reflection Terminology for Remote Sensing Applications. ISP, Comm. VII, WG 9 Correspondence, 1977

/6/ SIEVERS, J. : Zusammenhänge zwischen Objektreflexion und Bildschwärzung in Luftbildern. Deutsche Geodätische Kommission, Reihe C, Heft 221, München 1976

/7/ SIEVERS, J. : Density Corrections and Directional Reflectances of Terrain Objects from Black- and White Aerial Photos. Photogrammetria 33/1977, S. 95 - 111

/8/ STEINER, D : Die Jahreszeit als Faktor bei der Landnutzungsinterpretation. Schriftenfolge des Instituts für Landeskunde, Bad Godesberg 1961

/9/ : DIN 5032 "Lichtmessung", Bl. 1 S. 5, 1966

Sonderdruck aus der
Zeitschrift

Bildmessung und Luftbildwesen

Zeitschrift für
Photogrammetrie
und
Fernerkundung

Schriftleiter
Prof. Dr. Dr.-Ing. E. h.
Kurt Schwidefsky
Universität Fridericiana
Karlsruhe (TH)

Herbert Wichmann
Verlag
Karlsruhe

Gegründet 1926

Acknowledgement

The authors are grateful for the support of the Laboratory for Application of Remote Sensing (LARS) at Purdue University in this research effort. Also they wish to thank D. W. Rusco and J. E. Unruh of the School of Civil Engineering for their assistance in work related to linear least squares filtering.

Summary

Treatment of single (non-overlapping) digital MSS data is performed using both parametric and non-parametric techniques. Parametric methods are based on the collinearity equations and applying polynomials to express the behavior of the sensor exterior orientation elements. The resulting expressions may include the object point elevations if they are externally available.

Non-parametric procedures considered include: the arithmetic mean, the moving average, the meshwise linear transformation and linear least squares filtering.

Test results are given for the purpose of comparison. The paper is concluded with a discussion of the specific characteristics involved in the reduction of digital data.

Zusammenfassung

Einzelne (einander nicht überlappende) digitale Sätze von Multispektral-Abtaster-Daten werden mit parametrischen und nicht-parametrischen Techniken behandelt. Die parametrischen Methoden basieren auf den Kollinearitäts-Gleichungen und verwenden Polynomansätze, welche das Verhalten der Elemente der äußeren Orientierung ausdrücken. Die resultierenden Ausdrücke können die Objektpunkthöhen einschließen, wenn diese zusätzlich erhältlich sind.

Die betrachteten nicht-parametrischen Prozeduren enthalten: das arithmetische Mittel, das gleitende Mittel, die maschenweise lineare Transformation und eine Filterung nach kleinsten Quadraten.

Für Vergleichszwecke werden Testergebnisse genannt. Der Bericht schließt mit einer Diskussion der Charakteristika bei der Reduktion digitaler Daten.

References

[1] Mikhail, E. M., and J. R. Baker, Geometric Aspects in Digital Analysis of Multi-Spectral Scanner (MSS) Data. Presented at the Annual Convention, ASP, March 1973.

[2] Leberl, F., Untersuchung über die Geometrie und Einzelbildauswertung von Radarschrägaufnahmen, Diss. Techn. University, Vienna, 1971. (The Geometry of, and Plotting from, Single Strips of Side Looking Airborne Radar Imagery, English translation, ITC, October 1973).

[3] Kraus, K. and E. M. Mikhail: Linear Least-Squares Interpolation, Phm. Eng. 38, 1972.

Carl-Pulfrich-Preis 1975

Der im Jahre 1968 von der Firma Carl Zeiss, Oberkochen, gestiftete Carl-Pulfrich-Preis soll im Rahmen der Geodätischen Woche in Köln im Mai 1975 zum vierten Male verliehen werden. Die bisherigen Preisträger sind die Herren Prof. Dr.-Ing. M. Bonatz, Bonn (1969), Prof. Dr.-Ing. Karl Kraus, jetzt Wien (1971) und Dr.-Ing. Jürgen Müller, Hannover (1973).

Der volle Text des Stiftungsstatutes ist in BuL 37, 67 f., 1969 abgedruckt.

Bewerber, die auf Grund ihrer wissenschaftlichen, anwendungstechnischen oder konstruktiven Arbeiten auf dem Gebiet des Vermessungswesens in Verbindung mit geodätischen oder photogrammetrischen Instrumenten für die Verleihung des Preises in Betracht kommen, sollten zusammen mit den zur Beurteilung erforderlichen Unterlagen dem Verleihungsrat bis spätestens zum 1. Februar 1975 genannt werden. (Anschrift: Carl Zeiss, 7082 Oberkochen, Postfach).

Interpolation and Filtering of ERTS-Imagery

by H. P. Bähr, Hannover

1. Investigated Imagery

Least-squares interpolation methods have recently been applied in photogrammetry (see [2], [3], [4]). Since results from ordinary interpolation using polynomials for ERTS-Imagery are already available ([1]), it should be of interest to test other methods and to compare the results.

Independent measurements have been carried out in the same frame used for [1] both in channel 7 and channel 5 (bulk photo from September 21st, 1972, showing parts of northern Germany, 40 % cloud cover). All points used in channel 7 (41) were again related to water bodies, while most points used in channel 5 (20) were related to forest features. A simple 4-parameter linear transformation („Helmert-Transformation" using all observations as reference points was applied as a first step in oder to have a suitable reference surface for further statistical analysis.

2. Covariance Function and Filtering Coefficient

The residual errors after the 4-parameter-fit contain both correlated („systematic") and uncorrelated („observational") components. By leastsquares filtering, both parts can be separated; by least-squares interpolation, both parts can be predicted at any point, if suitable reference points are available.

First, the covariance function was determined empirically from the residual errors at all reference points. The calculated values were smoothened by a continuous Gaussian error function:

$$C\,(\overline{P_i\,P_k}) = C\,(0)\,e^{-k^2 s^2}$$

C (0), the vertex of the curve, represents the variance of the correlated error components V_s. It is smaller than the variance of the total error component V by the amount of V_r, variance of the uncorrelated components. V is known a priori from the residual errors after the 4-parameter fit.

The covariance function includes the whole information of the error distribution. It allows to estimate the magnitude of the correlated components l_s by the following equation (see [3]):

$$l_{si} = c_i^t\,C^{-1}\,l.$$

The elements of c and C represent values of the covariance function; the diagonal elements of C contain V. Thus the ratio

$$\frac{V_s}{V} = \frac{C\,(0)}{V} = F$$

– which is known if the covariance function has been determined –, becomes the fundamental parameter for the interpolation procedure. F is called „filtering coefficient". For the evaluated ERTS-frame one obtains $F_5 \sim 0.5$ and $F_7 \sim 0.7$. For a larger F the l_s values become larger and the filtering is stronger than it should be. For a smaller F the filter is too small.

3. Results

Column 4 and 6 list the mean square errors of the residuals after the 4-parameter fits, column 5 and 7 the mean square errors of uncorrelated components after filtering or least-squares interpolation. The more reference points are introduced the better the result becomes. It has about the magnitude of theoretical resolution. For $k^2 = 0.01$, i.e. a larger bandwidth of the Gauss curve the M values decrease somewhat as to the values from $k^2 = 0.1$. This is due to 2 isolated points, which are not influenced by the covariance function for $k^2 = 0.1$, which becomes zero for 5 = 6 cm but not for $k^2 = 0.01$.

The last two lines of the table give the results for interpolation by second order polynomials (6 unknowns for each coordinate). The values tend to be slightly better than after application of least-squares interpolation, but this is because of extrapolation at the 2 isolated points. This extrapolation accidently leads to error reduction at these points. Here least-squares interpolation does not transfer any information, if $k^2 = 0.1$, which seems more correct. The vector diagrams show very good accordance of both methods at all other points. Because of the small number of reference points and their poor distribution the results are not conclusive. A more sophisticated error analysis as KRAUS suggests in [4] has to be carried out with other frames. It seems obvious, however, that polynomials are easier to process than least-squares interpolation. But the latter is more flexible (k^2, F) and can be successfully applied as shown.

Channel	Reference points	Interpolated points	M_x [m]	M_{xr} [m]	M_y [m]	M_{yr} [m]	F	k^2
1	2	3	4	5	6	7	8	9
7	41	—	131	50	136	45	0.75	0.05
	31	10	134	57	134	58	0.70	0.10
	10	31	138	79	145	88	0.75	0.10
				71		77		0.01
	5	36	134	91	141	101	0.70	0.10
5	20	—	109	41	127	60	0.75	0.02
	9	11	134	80	122	88	0.70	0.02
	4	17	152	103	126	96	0.70	0.02
7 (Polyn.)	10	31	138	59	145	87	—	—
5 (Polyn.)	9	11	134	59	122	77	—	—

References

[1] BÄHR, H. P. und W. SCHUHR: Versuche zur Ermittlung der geometrischen Genauigkeit von ERTS-Multispektral-Bildern. BuL 42, 22–24, 1974.

[2] KRAUS, K.: Interpolation nach kleinsten Quadraten in der Photogrammetrie. BuL 40, 4–12, 1972.

[3] KRAUS, K. and E. M. MIKHAIL: Linear Least-Squares Interpolation. Phm. Eng. 38, 1016–1029, 1972.

[4] KRAUS, K.: Untersuchung zur Genauigkeit der Interpolation nach kleinsten Quadraten. ZfVermess. 99, 198–205, 1974.

Geometric calibration of Canadian ERTS photoreproduction system

by Dr. VLADIMIR KRATKY, Ottawa, Ontario, Canada

Introduction

The Earth Resources Technology Satellite (ERTS) imagery is acquired by a four-channel Multispectral Scanner (MSS) which continuously covers a 185 km wide ground swath in a single orbit. The raw data, radio-received at a ground station, is recorded on video tape and transmitted to a data processing station where it is converted into photographs and computer compatible tapes.

In the Canadian ERTS image processing system [4] which is in many respects different from that adopted by NASA [3], the photographs are produced with the aid of two special reproduction instruments. An Electron Beam Image Reproducer (EBIR) converts the pictorial information from its digital record on video tape into a latent photographic negative on a 70 mm film. This is accomplished in the data processing facility of the Canada Centre for Remote Sensing (CCRS) in Ottawa. The exposed film is delivered to the National Air Photo Library (NAPL) reproduction centre where it is processed and enlarged to the final 1 : 1000000 photographs on a 230 mm film in a special Enlarger-Printer (E-P).

The MSS image is distorted due to several physical, instrumental and geometric factors which may affect the imaging, recording and reproducing process, as analyzed, e. g. in [2]. Most of the systematic distortions can be determined with the use of auxiliary information provided from satellite sensors, predicted from orbital parameters, obtained from geometric calibrations of instruments and also derived from suitable photogrammetric transformations based on available ground control points. As a result, an analytical model of the distortions is derived, the parameters of which are used to control the reproduction process in the EBIR. Further details about the correction process developed for the Canadian ERTS program can be found in [1], [2].

It is obvious that the performance of both reproducing units affects the geometric quality of ERTS photographs. It is, therefore, imperative to have these devices regularly calibrated, and to use parameters of the calibration, together with other correction parameters, for the control of the process. The present paper describes the way in which this is accomplished in the Canadian ERTS program in the CCRS.

Description of reproducing system

The EBIR is a precision film recording device designed and built for CCRS by the Minnesota Mining (3M) Company. Basically, it is a modified cathode ray tube in which the face-plate is substituted by an ultra-fine grain film placed in a vacuum. Thus, the film is directly bombarded by electrons in a line-by line mode reproducing the original line-scanning pattern of the MSS, retained in the video signal. A special unit, the EBIR controller, acts as an interface between a computer and the EBIR, adding annotation, correction and calibration information which is provided by the computer, to the video signal. Data are directed from the video tape to the controller which controls the timing of the readout and the deflection of the electron beam in a way corresponding to the analytical model of those geometric corrections to be applied.

The Enlarger-Printer developed by the International Imaging Systems (I²S Company) provides an accurate optical scaling of images into the final format. The system is fixed to yield a 3.7 × enlargement ratio and can be used in a semi-automatic mode to produce colour composite prints in different combinations of the four available spectral images. For this purpose, a precision pin-registered framing mechanism is used to ensure an accurate image registration, identical to that in the EBIR, with respect to sprocket holes of the perforated film.

Geometry of photoreproduction

Information flow

The analog video outputs from the MSS sensors are converted into a digital signal which is radio-transmitted and received at the ground station. The received data are digitally recorded on a video tape in separate channels for each spectral band. The MSS system preserves an inherent registration of data in all spectral bands, which means that their geometric distortions are identical. The physical flow and transformation of information in the reproduction phase is presented in Fig. 1 and described in the following steps:

- Digital video signal (VID) is input information; any geometric distortions caused by deficiencies in preceding operations are irrelevant to the calibration of the reproduction system and thus disregarded. The x,y-coordinates of any image detail are implied in the position of the corresponding pixel within the video image stream.
- Modified image stream (MIS) is derived by a transformation of the video signal VID in the EBIR controller. The effect of this control can be analytically described by a transformation T_C.

Sonderdruck aus „Bildmessung und Luftbildwesen" Heft 3/1979, Seite 81-87

Analytische Bestimmung und digitale Korrektur des Lichtabfalls in Bildern eines Hochleistungsobjektivs

Von H.-P. BÄHR, Hannover

Herbert Wichmann Verlag GmbH, Rheinstraße 122, 7500 Karlsruhe 21

Analytische Bestimmung und digitale Korrektur des Lichtabfalls in Bildern eines Hochleistungsobjektivs

Von H.-P. BÄHR, Hannover

Zusammenfassung

Zur flächenhaften Bestimmung des Lichtabfalls in einem 60 mm-ZEISS-BIOGON wurde ein 1,20 × 1,20 m² großer Eichstrahler mit vollkommen diffus streuender Oberfläche entwickelt. Die analytische Bestimmung der Lichtabfallsfunktion erfolgte durch Ausgleichungen über Kosinus-Funktionen mit zusätzlichen linearen Anteilen. Nach der digitalen Korrektur der HASSELBLAD-Aufnahmen bleiben Restfehler in der Größenordnung von ± 0,02 D

Analytical Determination and Digital Correction of Light Fall-Off in Photogrammetric Imagery

A 1.20 by 1.20 m² large $BaSO_4$-reflector has been developed in order to provide a full frame standard of perfect diffuse surface for light fall-off correction of a 60 mm ZEISS-BIOGON. The analytical determination of the light fall-off function was executed by least-squares adjustment, using cosine functions with additional linear parameters. After digital correction of the HASSELBLAD imagery, residual errors are in the order of magnitude of ± 0.02 D.

Détermination analytique et correction digitale de la répartition de la lumière dans des clichés photogrammétriques

Un réflecteur-$BaSO_4$ (1.20 m par 1.20 m) à surface parfaitement diffuse a été développé pour corriger la répartition de la lumière à travers un objectif ZEISS-BIOGON (60 mm). La détermination analytique des fonctions convenables fait intervenir l'ajustement de fonctions-cosinus par les moindres carrés, avec des paramètres linéaires supplémentaires. Après la correction digitale des clichés HASSELBLAD, l'erreur moyenne sur les écarts résiduels atteint ± 0,02 D

1. Einordnung der Untersuchungen

Bildverarbeitung, gleichviel ob digital oder analog, muß unter kritischer Würdigung des Ausgangsmaterials erfolgen. Weltweit und mit großer Energie betriebenen Versuchen, mit Methoden rechnergestützter digitaler multispektraler Klassifizierung die konventionellen, subjektiv ausgerichteten Verfahren der „Bildinterpretation" abzulösen, ist bisher, trotz beachtlicher Teilerfolge, der große Durchbruch versagt geblieben. Multispektrale Klassifizierung ist heute noch nicht immer *allgemein* und *wirtschaftlich* anwendbar. Der Grund dafür liegt u. a. darin, daß vielfach „drauflos"-klassifiziert wird, ohne die notwendige Korrektur des Ausgangsmaterials nach physikalischer Analyse der Originalinformation.

Photogrammeter haben dafür gesorgt, daß die *geometrischen* Gesetze des Zustandekommens der Bildinformation gut bekannt sind (vgl. z. B. H. K. MEIER [6, 7], H. ZIEMANN [14]). Was die *radiometrischen* Gesetze anbetrifft, so besteht die *Schwierigkeit, die Bild-Dichtewerte exakt als eine mathematische Funktion spektraler Signaturen*[1] *und somit von Objekteigenschaften zu beschreiben.* Zu viele, schwer erfaßbare und einander überlagernde Störfaktoren tragen zur Beeinflussung der Originalinformation bei, z. B. die Beleuchtung, das Luftlicht, Kamera und Filmeigenschaften wie auch die Filmentwicklung (vgl. J. SIEVERS [11, 12]).

Der vorliegende Aufsatz soll ein Beitrag im Hinblick auf die Notwendigkeit sein, Original-Bilddaten radiometrisch zu korrigieren. *Er befaßt sich mit einem einzigen physikalischen Phänomen, dem Lichtabfall in einem Kameraobjektiv, seiner Ermittlung sowie seiner digitalen Darstellung und Korrektur.*

Theoretisch ergibt sich für den Lichtabfall eine $\cos^4\alpha$-Funktion, aber nur unter der Voraussetzung, daß das Objektiv durch eine dünne Linse mit kleiner Öffnung ersetzt wird, welches ein verzeichnungsfreies Bild liefert („LAMBERT'sches Gesetz des Lichtabfalls" (vgl. K. SCHWIDEFSKY [10] S. 38, 43). α ist dabei der von Objektivachse und Hauptstrahl eingeschlossene Winkel. Praktisch liegen die Verhältnisse weitaus komplizierter. Bedingt durch die Objektivlänge werden schräg einfallende Strahlen teilweise herausgeblendet („Vignettierung"). Dies führt zu stärkeren Lichtverlusten an den Bildrändern als durch

[1] „Spektrale Signaturen" sei unter Schärferfassung der im „Manual of Remote Sensing" [15] S. 2174 gegebenen Erläuterung definiert als die „Verteilung spektraler Eigenschaften, gemessen in einem (oder mehreren) Wellenlängenintervall(en)".

das LAMBERT'sche Gesetz ausgedrückt wird. Dieser Nachteil wird bei manchen Objektivtypen dadurch vermieden, daß ein Lichtstrahl unter einem flacheren Winkel als dem Einfallswinkel durch das Objektiv geführt wird. Zu einem solchen Objektivtyp zählt auch das ZEISS-BIOGON, welches für die vorliegenden Untersuchungen verwendet wurde[1]. Nach JORDAN/EGGERT/KNEISSL [5] S. 112, gelingt es sogar, den Lichtabfall bis auf $\cos^{2.?}\alpha$ zu reduzieren.

Grund für die allgemein geringe Beschäftigung mit dem Phänomen des Lichtabfalls mag die Tatsache sein, daß es das menschliche Auge häufig gar nicht wahrnimmt. Dies liegt daran, daß dem Lichtabfall überlagerte Kontraste „ins Auge springen" und die Information des Lichtabfalls verdrängt wird; es kann aber auch sein, daß die durch den Lichtabfall verursachten Kontraste zu gering sind, als daß sie das Auge überhaupt erkennen könnte, wie im vorliegenden Fall beim BIOGON. Für digitale Bildverarbeitung jedoch wird der Lichtabfall, auch wenn für das Auge unsichtbar, zu einem Störfaktor, der eliminiert werden muß.

2. Herstellung eines „LAMBERT"-Reflektors

Um die Transmissionseigenschaften eines Kameraobjektivs für einfallendes Licht zu bestimmen, muß eine Möglichkeit gefunden werden, den Lichtabfall separat darzustellen. Dies bedeutet, daß alle anderen Parameter, welche die Filmschwärzung beeinflussen, ausgeschaltet werden müssen. Dieses sind primär die Differenzen der Objekt-Helligkeitsunterschiede per se sowie die Abweichungen der Aufnahme- und Beleuchtungsrichtungen von der Flächennormalen. *Eine perfekt diffuse Objektoberfläche ist Voraussetzung für die Herstellung von Bildern, welche allein durch Objektiv- und Filmeigenschaften beeinflußt sind.* Am Institut für Photogrammetrie und Ingenieurvermessungen (IPI) der Universität Hannover wurden verschiedene Versuche unternommen, um eine perfekt diffuse Oberfläche herzustellen (vgl. K. ALVES [1]). Schließlich wurde Bariumsulfat ($BaSO_4$, in Pulverform) zur Herstellung einer perfekt diffus reflektierenden Oberfläche herangezogen, eine Substanz, welche auch zur Innenbeschichtung von ULBRICHT'schen Kugeln benutzt wird. Die theoretisch homogen diffuse Reflexion eines sogenannten „weißen LAMBERT-Reflektors" (wL: vgl. F. KASTEN, E. RASCHKE [8]) liefert

$$\text{Reflexion } \rho = \frac{\text{Reflektierter Strahlungsfluß } \Phi_{r,wL}}{\text{Einfallender Strahlungsfluß } \Phi_i} = 1 \tag{1}$$

In der Praxis können LAMBERT-Reflektoren in erster Linie dazu dienen, den Reflexionsfaktor R zu ermitteln, welcher die Reflexion eines Objekts charakterisiert und damit das Objekt selbst (vgl. [8, 9]):

$$R = \int_{\Omega_r} \frac{L_r(\vartheta_r, \varphi_r)\cos\vartheta_r \, d\Omega_r}{L_w \int_{\Omega_r} \cos\vartheta_r \, d\Omega_r} \tag{2}$$

Hierin ist L_r die Strahldichte eines Objekts als Funktion der Zenitdistanz ϑ und des Azimuts φ, integriert über einen festen Winkel Ω. L_w bedeutet die (zu 100%) reflektierte Strahldichte des LAMBERT-Reflektors („Referenzstrahler"). Als Reflexionsstandard hat dieser Strahlertyp daher eine Bedeutung, welche über die hier diskutierte Verwendung im Zusammenhang mit der Lichtabfalls-Kompensation weit hinausgeht.

Reflexionsstandards bedeckten bei bisherigen Untersuchungen nur einen kleinen Teil des gesamten Gesichtsfeldes der Kamera; trotzdem waren Bestimmungen des Lichtabfalls möglich (vgl. J. SILVERS [11, 12]). Eine strengere Behandlung dieser Aufgabe erfordert einen Reflexionsstandard, welcher das Gesichtsfeld der Kamera voll ausfüllt. Die hier vorliegende Konfiguration von Kamera und Objektiv benötigt einen Standard mit ebener Oberfläche von 120 cm Kantenlänge eine Größe, welche bisher nicht existierte. Für Flächen dieses Ausmaßes muß die Bariumsulfat-Substanz mit einer Sprühpistole auf eine PVC-beschichtete Spanplatte aufgebracht werden. Details zur Ansetzung der Substanz beschreibt der Autor in einem anderen Beitrag (H.-P. BAHR [3]).

---
[1] HASSELBLAD MK 70, Reseau 1039, Zeiss-Biogon f = 60 mm, Nr. 5195241

3. Analytische Bestimmung der Lichtabfallsfunktion

Die photographischen Aufnahmen des Lambert-Strahlers wurden bei dunstigem Himmel auf dem Meßdach des Geodätischen Instituts der Universität Hannover vorgenommen, wobei die Platte auf dem Boden stand und unter 135° geneigt war. Die Aufnahmen erfolgten unter Benutzung von Kodak-Ektachrome Farbumkehrfilm mit Öffnungsverhältnissen von 1:5,6 und 1:8. Die in 1 m Entfernung von der Platte aufgestellte Kamera führte nicht zu Schatten auf dem Bild.

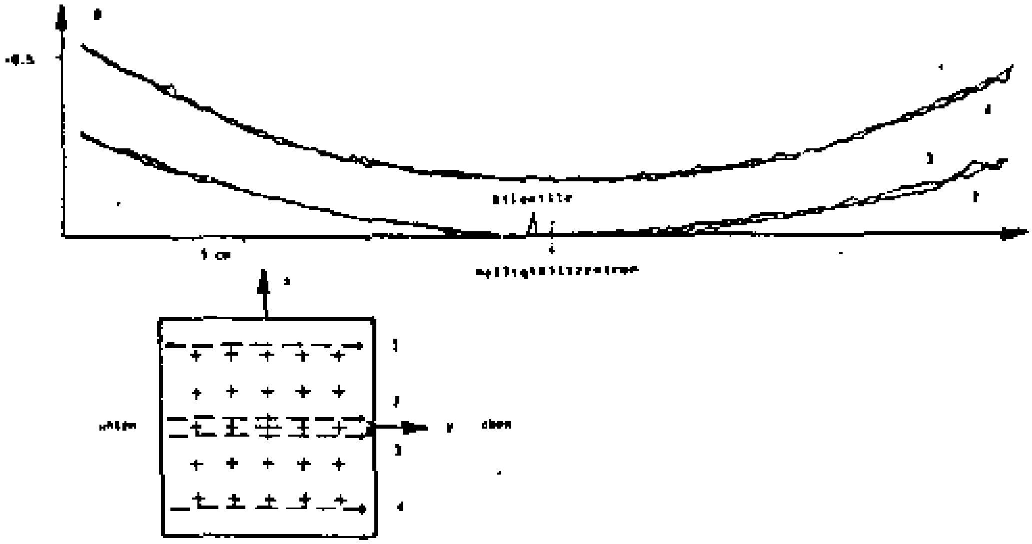

Abb. 1 Mikrodensitometerprofile über 4 verschiedene Bildbereiche der Aufnahme des Lambert-Reflektors (Mikrodensitometer Joyce-Loebl).

Dies ist in Übereinstimmung mit Abb. 1, welche Mikrodensitometerprofile in vier verschiedenen Bildbereichen zeigt. Die Profile verlaufen, verglichen mit anderen Ergebnissen (H.-P. Bahr [3]), sehr glatt, was die gute Qualität des Lambert-Reflektors demonstriert. Allerdings ist in Abb. 1 eine leichte Abweichung der Profile zwischen dem oberen und unteren Teil auf der Platte erkennbar, indem der geometrische Bildmittelpunkt nicht mit dem Punkt größter Helligkeit zusammenfällt. Dieser Effekt kann durch einen Schatten vom Boden oder durch nicht strenge Parallelstellung von Reflektor- und Aufnahmeebene verursacht sein. Vor Auswirkungen des zuletzt genannten Fehlers, welche nach (2) nicht linear verlaufen, warnt auch H. J. Bernath [4]. Diese Verhältnisse müssen bei der Bestimmung der Lichtabfallsfunktion berücksichtigt werden. Abgesehen von Schatteneffekt und „Rauschen" stellen die Profile in Abb. 1 ausschließlich den Einfluß des Lichtabfalls im Kameraobjektiv dar. Wegen der leichten Verschiebung zwischen Bild- und Helligkeitszentrum kann dies Bild auch nicht als Maske für eine *rein analoge* Form der Lichtabfallskompensation dienen. Da, wie eingangs erläutert, eine Lichtabfallskompensation auch nur bei den Verfahren der *digitalen* Bildverarbeitung (z. B. Klassifizierung) angewandt zu werden braucht, erscheint es ohnehin näherliegend, für die folgenden Schritte die *strengere analytische* Methode zu wählen.

Zur analytischen Bestimmung des Lichtabfalls müssen exakte Koordinaten für bestimmte Grauwerte im Bild bekannt sein, bezogen auf den Bildmittelpunkt als Ursprung. Aus diesem Grunde wurden die Gitterkreuze dazu verwendet, eine gleichmäßige Verteilung der nötigen Messungen zu garantieren. Pro Bild waren 100 Messungen (4 × 25) am Mikrodensitometer zu machen (ausgeführt durch K. Alves). Sowohl für Blende 1:5,6 als auch für Blende 1:8 wurden 14 Bilder untersucht, was schließlich auf 2800 Meßwerte führte.

Wie anfangs erläutert, läßt sich der Lichtabfall gut durch eine Kosinus-Funktion beschreiben, wobei man Radialsymmetrie des Phänomens annimmt. Dies kann auch hier geschehen, allerdings unter Berücksichtigung der Überlagerung der Funktion durch den genannten Störanteil. Näherungsrechnungen zeigten, daß

$$D_\alpha = f(1 - \cos^2 \alpha); \quad D_\alpha = f\left(\frac{1}{\cos^2 \alpha} - 1\right)$$

$$D_\alpha = f(1 - \cos^4 \alpha); \quad D_\alpha = f\left(\frac{1}{\cos^4 \alpha} - 1\right) \tag{3}$$

grundsätzlich zur Beschreibung des radialen Funktionsanteils geeignet erscheinen.

Für eine Ausgleichung nach kleinsten Quadraten werden die Verbesserungsgleichungen folgendermaßen geschrieben:

$$L_i + v_i = f(\cos \alpha)_i c_1 + y_i c_2 \tag{4}$$

oder

$$v_i = a_i c_1 + b_i c_2 - L_i \tag{5}$$

Die Unbekannte c_1 charakterisiert einen Faktor, welcher die Kosinusfunktion dem Mikrodensitometerprofil anpaßt, während c_2 den Störfaktor als eine lineare Funktion der y-Bildkoordinate erfassen soll.

Tabelle 1 Ergebnisse der Ausgleichung.

	Funktion	$1 - \cos^2$	$1/\cos^2 - 1$	$1 - \cos^4$	$1/\cos^4 - 1$
	c_1	1,0892	0,8665	0,8458	0,6229
	c_2	0,0019	0,0019	0,0019	0,0019
f = 1:5,6	m_0 (D)	± 0,0282	± 0,0197	± 0,0297	± 0,0185
	c_1	0,8822	0,6963	0,6858	0,5000
	c_2	0,0014	0,0014	0,0014	0,0014
f = 1:8	m_0 (D)	± 0,0193	± 0,0203	± 0,0195	± 0,0210

Die Ausgleichungsergebnisse sind in Tabelle 1 zusammengefaßt. m_0 ist der Gewichtseinheitsfehler, errechnet aus den Restfehlern, welcher die Genauigkeit des Verfahrens angibt. Die mittleren Fehler für c_1 sind in jedem Fall $< \pm 0{,}0035$, die von $c_2 < \pm 0{,}0006$. Zwischen den Unbekannten existiert keine Korrelation.

4. Digitale Korrektur des Lichtabfalls

Die Korrektur des Lichtabfalls kann *exakt* nur *digital* erfolgen; sie wird strenggenommen für Hochleistungsobjektive auch erst bei Anwendung digitaler Bildverarbeitung (z. B. Klassifizierung) notwendig: *ein Beispiel dafür, wie neue Techniken neben neuen Problemen gleichzeitig auch deren Lösungsmöglichkeiten liefern.*

Da das hier behandelte Bild nicht original digital vorlag, mußte es in einem ersten Schritt am OPTRONICS-Lesegerät digitalisiert werden, wobei Bildelementgrößen von $0{,}1 \times 0{,}1$ mm² ausreichten (518×522 mm² ergeben $0{,}270 \times 10^8$ Pixel). Ausgehend vom digitalen Bild können nun die Helligkeitsverhältnisse leicht dargestellt werden.

Abb. 2 zeigt eine Abspielung des digitalisierten Originalbildes nebst zugehörigem Histogramm. Man erkennt, daß die Dichtewerte sich auf den Grauskala-Bereich zwischen etwa 75 und 100 konzentrieren. Die Werte liegen zu dicht zusammen, als daß sie das Auge im Bild unterscheiden könnte. Zwar ist es grundsätzlich möglich, eine Differenz von 25 Graustufen in diesem Bereich noch wahrzunehmen ($\Delta D \sim 0.12$), allerdings nur unter der Voraussetzung, daß diese sprunghaft und nicht kontinuierlich auftritt wie hier.

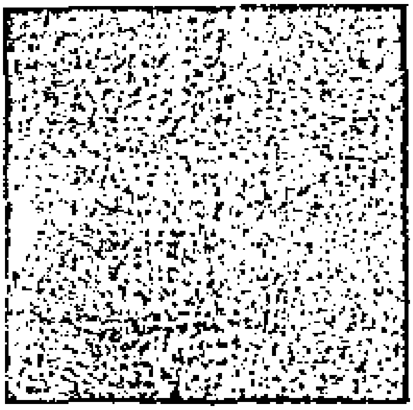

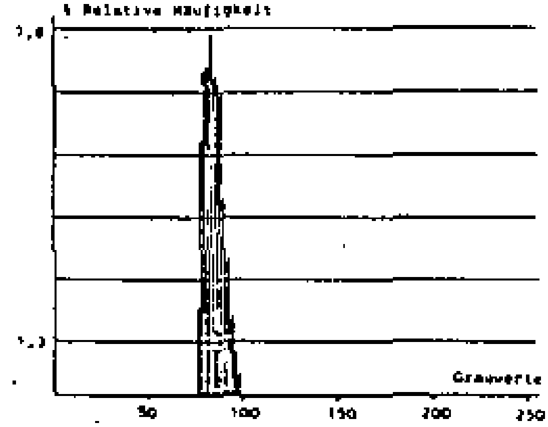

Abb. 2 Abspielung des digitalisierten Originalbildes mit zugehörigem Histogramm.

Eine anschauliche Darstellung der Helligkeitsverhältnisse ergibt sich nach einer angepaßten linearen Transformation der Original-Grauwerte (Abb. 3). Beginnend beim Betrag von 73 sind jeweils 4 Grauwerte äquidistanten Stufen vom Betrag 40 zugeordnet worden, was auf insgesamt 8 gut unterscheidbare, abzählbare Stufen führt. Wegen der dadurch erfolgten etwa 20-fachen Verstärkung des Kontrastumfangs zeigt Abb. 3 den Lichtabfall-Effekt extrem deutlich. Diese *flächenhafte* Darstellung eignet sich viel besser zur Beschreibung des Lichtabfalls als die Mikrodensitometerprofile (Abb. 1). Man erkennt sofort den Effekt der radialen Komponente sowie des von unten einfallenden „Schattens". Darüber hinaus existieren aber auch noch geringe andere Einflüsse, welche durch den analytischen Ansatz (4) nicht erfaßt werden, wie z. B. Streifigkeit im rechten Bildteil, hervorgerufen wahrscheinlich durch ungleichmäßig angesetzte Entwicklung beim Farboriginal.

Die digitale Korrektur des Lichtabfalls erfolgte mit Modul „KOLA" (für ein Bild der Blende 1:8) des digitalen Bildverarbeitungspakets MOBI des IPI (siehe hierzu H.-P. BAHR [2]). Das Ergebnis ist in Abb.

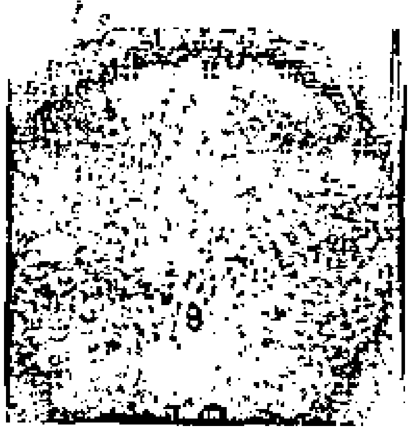

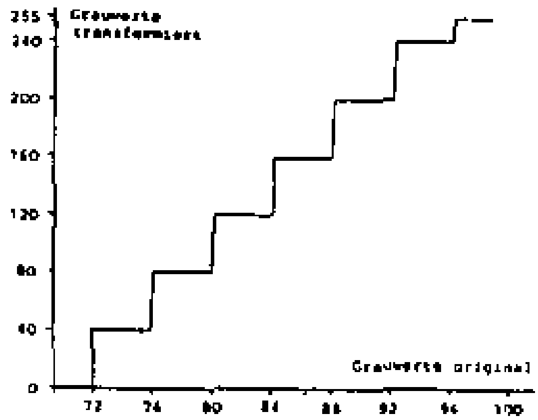

Abb. 3 Anwendung einer 8-stufigen linearen Transformation der Grauwerte des digitalisierten Originalbildes zur quantifizierten Darstellung der Kontrastverhältnisse.

4 dargestellt. Schon das Histogramm des verbesserten Bildes veranschaulicht, daß nun fast alle Grauwerte zwischen 75 und 79 liegen (ΔD ~ 0,02), während im Originalbild (Abb. 2) die gleiche Menge zwischen 73 und 103 liegt (ΔD ~ 0,15). Dies entspricht einer Verminderung des durch den Lichtabfall bewirkten Kontrastumfangs etwa um den Faktor 7. Nach der Anwendung der in Abb. 3 erläuterten Transformation auf das korrigierte Bild fallen zunächst die konzentrischen Ringe auf. Diese werden hervorgerufen durch den Umstand, daß die Korrektur nicht kontinuierlich, sondern nur in Sprüngen von Grauwerteinheiten erfolgen kann. Daher ist in jedem einzelnen Ring noch die Tendenz des Lichtabfalls von innen nach außen erkennbar, was die Ringstruktur hervorruft. Auf das gesamte Bild bezogen, ist der Effekt des Lichtabfalls aber fast vollständig eliminiert. Spuren von Kontrastdifferenzen sind die Folge von

1. ungleichmäßiger Filmentwicklung des Farboriginals (z. B. vertikale Schlieren im Bild rechts)
2. Fehlern bei der Digitalisierung (z. B. horizontale Streifenstrukturen) und
3. Restfehlern aus dem analytischen Modell.

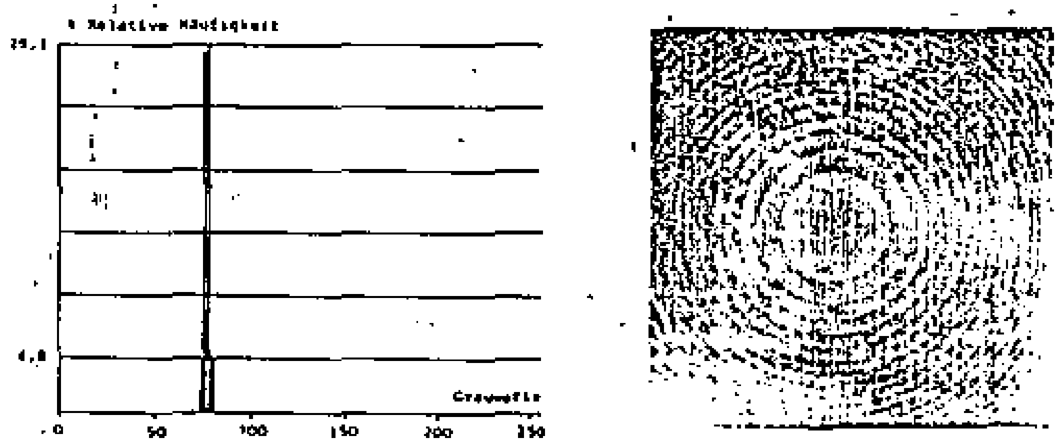

Abb. 4 Histogramm des korrigierten Bildes sowie Anwendung der Transformation von Abb. 3 auf das korrigierte Bild zur Veranschaulichung des Korrektureffekts.

Bei der Einschätzung der durch die noch vorhandenen Kontraste ausgedrückten Restfehler muß bedacht werden, daß Abb. 4 durch extremste Kontrastanreicherung entstanden ist (Verteilung der Werte zwischen etwa 75 und 79 auf den Bereich zwischen 1 und 256). Die Streuung der Grauwerte zwischen 75 und 79, welche auf ΔD ~ 0,02 führt, ist daher in Übereinstimmung mit dem mittleren Fehler von $m_{ls} = \pm 0{,}02$ D, der aus dem analytischen Ansatz folgte. Das Korrekturergebnis entspricht damit den Erwartungen, die nach der analytischen Ermittlung der Lichtabfallsfunktion gehegt werden konnten.

Der Lichtabfall-Effekt wird in der Praxis von vielen anderen Störeinflüssen überlagert, insbsondere auch durch Helligkeitsunterschiede, die durch Abweichung der Aufnahme- und Beleuchtungsrichtungen von der Nadirrichtung entstehen (vgl. (2) sowie Beispiele bei D. STEINER [13]). Diese Einflüsse müssen ebenfalls analytisch bestimmt und digital korrigiert werden, eine im Hinblick auf die Leistungssteigerung automatischer Klassifizierung aktuelle, bislang unbewältigte Aufgabe.

Literatur

IGP: Internationale Gesellschaft für Photogrammetrie
[1] ALVES, K.: Radiometrische Untersuchung von Farb-Umkehr-Diapositiven. Diplomarbeit TU Hannover, 1976.
[2] BAEHR, H.-P.: Digital Image Processing Experience at Hannover Institute for Photogrammetry. Mitteilungen der Geodätischen Institute der Universität Graz, Folge 29, 1977, S. 19–25.

[3] BAEHR, H.-P.: Design of a Large LAMBERT-Type Reflection Standard and Full Frame Calibration of a Camera Lens. IGP Komm. VII. Freiburg 1978.
[4] BERNATH, H.J.: Radiometric Calibration of a Multi-Spectral Aerial Camera. Photogrammetric Engineering 39 (1973) S. 939-947.
[5] JORDAN/EGGERT/KNEISSL: Handbuch der Vermessungskunde. Band IIIa. Photogrammetrie. 3 Bände. Stuttgart 1972. 2321 S.
[6] MEIER, H. K.: Diskussion der Bewegungsunschärfe bei Luftbildern mit Hilfe einer Kontrastübertragungsfunktion. BuL (1960) S. 65–77.
[7] MEIER, H. K.: Verzeichnung, Kammerkonstante und Fokussierung von Luftbildkammern unter dem Einfluß bildflugspezifischer Umweltbedingungen. BuL 46 (1978) S. 193-198.
[8] KASTEN, F. und RASCHKE, E.: Nomenklatur zur Beschreibung von Strahlungsmessungen und -rechnungen. Bundesministerium für Bildung und Wissenschaft, Forschungsbericht W72 – 30. 1972.
[9] KRIEBEL, K. T.: Reflection Terminology for Remote Sensing Applications. IGP Komm. VII Symposium, Freiburg 1978.
[10] SCHWIDEFSKY, K.: Grundriß der Photogrammetrie. 5. Aufl. Stuttgart 1954. 282 S.
[11] SIEVERS, J.: Zusammenhänge zwischen Objektreflexion und Bildschwärzung in Luftbildern. Deutsche Geodätische Kommission, Reihe C. Heft 221. München 1976. 128 S.
[12] SIEVERS, J.: Density Corrections and Directional Reflections of Terrain Objects from Black- and White Aerial Photos. Photogrammetria 33 (1977) S. 95-112.
[13] STEINER, D.: Die Jahreszeit als Faktor bei der Landnutzungsinterpretation. Landeskundliche Luftbildauswertung im mitteleuropäischen Raum. Heft 5. Bad Godesberg 1961. 81 S.
[14] ZIEMANN, H.: Image Geometry-Factors Contributing to its Change. IGP Komm. I. Ottawa 1972.
[15] AMERICAN SOCIETY OF PHOTOGRAMMETRY: Manual of Remote Sensing. 2 Bände. Falls Church (Virginia) 1975. 2144 S.

Printed and published by
Institut für Angewandte Geodäsie, Frankfurt a. M.

1978

Separate print taken from:
Nachrichten aus dem Karten- und Vermessungswesen, Reihe II: Übersetzungen — Heft Nr. 36
Paper presented to the Symposium of Commission III
International Society for Photogrammetry, Moscow, USSR, 1978
Printed and published by Institut für Angewandte Geodäsie, Frankfurt a. M. 1978
DK 528.727:778.151.2
528.711.18(202)—187

Geometrical Analysis and Rectification of LANDSAT MSS Imagery: Comparison of Different Methods

(with 8 Figures and 4 Tables)

By H.-P. Bähr, Hannover

SUMMARY: Quality of 4 different mathematical models (Helmert-transformations, 2nd-order polynomials, collinearity equations, prediction) is discussed with respect to geometrical analysis of LANDSAT imagery. This leads to operational digital rectification procedures, providing two levels of accuracy (bulk/precision).

RÉSUMÉ: L'auteur examine et compare 4 méthodes mathématiques (transformations de Helmert, polynomes du 2e degré, équations collinéaires, prédiction) pour l'analyse géométrique des images LANDSAT. Il en déduit deux méthodes pratiques pour la correction digitale des images, fonctionnant à deux niveaux de précision (approximative/élevée).

ZUSAMMENFASSUNG: Vor- und Nachteile 4 verschiedener mathematischer Modelle (Helmert-Transformationen, Polynome 2. Grades, Kollinearitätsgleichungen, Prädiktion) werden im Hinblick auf geometrische Analyse von LANDSAT-Bildern diskutiert. Daraus folgen dann praxisgerechte digitale Entzerrungsverfahren in zwei Genauigkeitsstufen (grob/fein).

1 General objectives

The launch of LANDSAT had caused enormous world-wide activities in the domain of applied earth sciences: only 7 months after LANDSAT imagery was available, 180 publications of "significant results" were presented at a NASA Symposium at New Carrollton [22]. In the meantime, application of LANDSAT imagery covers an immense field, leading to numerous direct or indirect economical advantages.

In practise, LANDSAT data usually is not applied exclusively; it is used in addition to existing maps and airborne imagery. This raises the problem of geometrical registration for data from different origin. Moreover a very important related task is the observation of time varying phenomena ("change detection"), which are most frequent on earth. Here again geometrical rectification of the imagery has to be provided.

In the past, many LANDSAT users did not care much about geometry. The "bulk" hard copies disseminated by NASA presented good geometrical fidelity and were sufficient for many practical applications. Simultaneously, digital processing of LANDSAT CCT's became more and more common, and the results prove that these methods will become the standard ones. In the course of digital image processing geometrical rectification presents the first step; therefore many users, who originally concentrate on classification, try to deal with the complex problems of digital geometrical rectification procedures for LANDSAT imagery.

Control points have to be selected very carefully, and image coordinates should be measured in a comparator of high precision (e. g. ZEISS PSK used here). The pointing accuracy can be determined by repeating measurements individually:

$$m_d = \pm \sqrt{\frac{\sum_{i=1}^{n} d_i d_i}{2n-1}} \tag{1}$$

m_d is the mean root square error computed from n individually repeated measurements with the difference d_i. For the evaluated images we get

Image (n)	Bavaria (234)			North Germany (82)	
Operator	A	B	G	B	J
$m_d(x/y)$ ±	2.8/2.7	8.4/9.1	4.9/5.4	7.5/7.5	7.4/5.3

The values are in [µm] or [m] respectively, when related to the terrain. Obviously definition of d i s c r e t e points is possible down to ± 1/10 pixel approximately.

The quality of coordinate determination is more significantly tested by transforming the entire individual vectors, using conformal equations (Helmert-transformation):

$$\begin{aligned} x' &= a_0 + a_1 x - a_2 y \\ y' &= b_0 + a_2 x + a_1 y \end{aligned} \tag{2}$$

where the vectors x, y and x', y' signify results obtained from different operators A, B, G and J. The transformations led to

Combination	A/B	A/G	B/G	B/J
M (x/y) ±	17.2/18.6	21.1/20.5	20.8/20.7	12.3/11.2

where M is computed from the residuals (dimensions as described above). M is larger than m_d (which is necessarily so) and represents an i n t e g r a l value for the relative individual pointing error. The value may obtain ± 1/4 pixel.

The types of control points will vary depending on the local scene as well as on the maps or airborne imagery used for ground check. In Germany, road intersections can hardly be determined; most points are related to water bodies or edges from forest areas. Many attempts were made in order to figure out which shape of control point was best suited for geometrical control. The Bavarian scene provides 234 homogeneous points, which were submitted to statistical tests. For this attempt, 5 classes of points were formed: "spot", "edge", "angle", "tip" and "others". Residuals of every class showed normal distribution, proved by χ^2-tests. The values of the corresponding rms errors did not differ significantly, tested by *Fisher*-distributions, with one exception: type "angle" was significantly better than type "tip". The latter type consequently has to be avoided. Classification according to "water" points and "others" did not lead to significant difference, a fact, which was already expected in [5].

Control medium can be small-scale aerial imagery, where ground coordinates are determined by aerial triangulation. If good maps are available, they can be used without disadvantage if in scale 1 : 50 000 and larger. The German TK 50, topographic map in 1 : 50 000 scale, was taken for all German scenes with good success. Interpretation of a ground control point for measurement, has to be executed very thoroughly, and therefore takes up to 1/2 hour.

The map projection of the TK 50 is a "Gauß-Krüger", a Transversal Mercator type like UTM, but with reference meridians every 3° longitude. Here the ordinates y of the earthbound system are stretched by the supplement $\Delta Y = Y^3 / 6R^2$ (in order to get conformity, see *Grossmann* [11]). If this supplement exceeds a certain value, the LANDSAT scene cannot easily be made fit to the map. In Fig. 1 the values for ΔY are written as a function of Y, where we have to distinguish between two cases: if the scene contains the reference meridian, the supplement may be at most 24 m. If the scene is situated between two reference meridians, ΔY may achieve at the equator a maximum of 67 m (for Gauß-Krüger; $Y = 76$ km) or 239 m (for UTM; $Y = 234$ km), when related to the distance of 180 km. For Germany, ΔY may become 33 m (Gauß-Krüger $\phi = 48°$). Ordinate stretch correction, which is nonlinear, can therefore practically be neglected if the ground control coordinates are available in Gauß-Krüger.

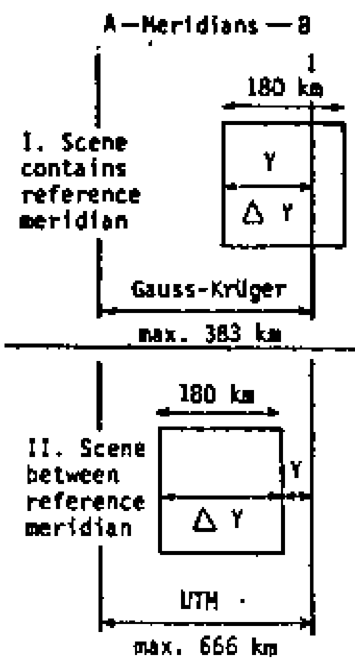

Y [km]	0	10	50	76	100	150	180	200	234
ΔY [m]	0	0	0.5	2	4	14	24	-	-
ΔY [m]	24	28	49	67	86	133	168	192	239

Fig. 1 – Supplements ΔY of ordinates Y for UTM and Gauß-Krüger projections

For UTM it may frequently happen, that the supplement ΔY has to be applied if a good fit to the map is desired.

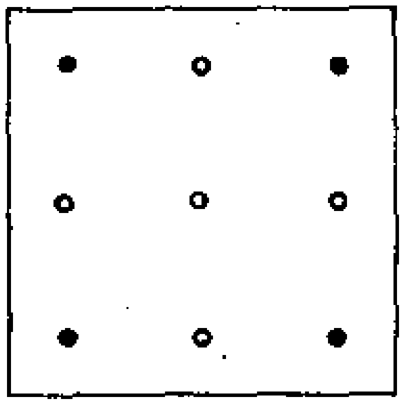

Fig. 2

Fig. 2 shows the recommended configuration of ground control points. 4 points in the corners of the image represent the minimum necessary for application of (1) together with accuracy control. 9 well-distributed points will be sufficient for application of second-degree polynomials (see paragraph 3.2). In order to hold cost down, principally no more points should be entered for practical purpose, as accuracy will not significantly grow by using more points (see *Bähr* [5]).

3 Different methods for geometrical analysis of LANDSAT MSS imagery

3.1 Helmert-transformations and affine correction terms

As mentioned above (1), Helmert-transformations are similarity projections, providing two translations (a_0, b_0) a rotation ($\tan \phi = a_2/a_1$) and a scale factor ($M = \sqrt{a_1^2 + a_2^2}$).

For the problems discussed here, two properties are of fundamental importance:

1) A Helmert-transformation conserves the internal geometry of an image. Therefore it is ideally suited for defining the geometric difference between two images simply by the root mean square errors computed from the residuals after transformation.

2) 2 translations, rotation and scale are available for an operator, projecting a LANDSAT scene by an ordinary photographic enlarger onto a map. His analog best fit will contain the same residuals like the analytical Helmert least-squares adjustment.

From this point of view Helmert-transformations are used here for two different reasons: firstly in order to obtain an appropriate measure for geometric accuracy and secondly in order to compute an exact scale factor for digital rectification (see paragraph 4.2).

For the two images described above the transformations are computed using all control points as well as 9 or 4. Moreover the full scenes were divided into quadrants in which the control point configuration was selected in the same manner as described by Fig. 2. The Helmert-transformation here simply serves as a comprehensive geometric check of the imagery. Table 1 summarizes the results in rms errors ([meter]) computed from the residuals. We realize that

(1) the quantity of used control points for determining the transformation parameters is not essentiel, for practical reasons 4 may be sufficient

(2) dividing the scene into quadrants leads to a significant improvement of accuracy.

Division of images into quadrants was already successfully tried by *Trinder* and *Nasca* [20]. We find, that the number of 12 . . . 20 ground control points for every quadrant suggested there seems not to be realistic for practical purposes (e. g. for mapping developing countries). The results here prove that 4 control points for every quadrant, this means 9 for every scene, may be sufficient. The increase of accuracy is about 70 % for "original" imagery (not specially corrected for affinity). Many practical applications in respect to remote sensing programs frequently use even smaller portions than an image quadrant (see *Bähr* [6]). The smaller the processed area, the easier a good fit even with geometrically bad imagery (see values for area 6, which covers only 1/20 of a full scene).

The bad geometric quality of the original imagery is illustrated by Fig. 3 displaying the plots of residual vectors. The residuals from both original Bavaria and original Northern Germany show characteristical systematic behavior, caused by affinity. This seems to be the typical trend for "bulk" processed imagery, which we find displayed in a similar manner in *Wong* [21] and *Bernhardson* [7] after "conformal" transformation. The "center of gravity" of the control points is free from systematics, whereas the errors grow continuously towards the edges. Apart from the large values this is of particular disadvantage if LANDSAT scenes are used for mosaicking.

If no device for affine geometric correction is available, best solution is to process every quadrant separately, e. g. to project only parts of a scene onto a map. This would yield for "Bavaria" residuals of about ± 150 m, where the components behave in a less systematic way at the edges than in the scene processed in a whole (see Fig. 3b). This primitive method should only be applied if no CCT's are available and the obtained geometrical accuracy of about ± 150 . . . 200 m is sufficient for the specific task.

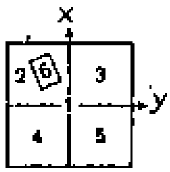

Dividing the full scene 1 into the 4 quadrants 2, 3, 4, 5 and one separate area 6 (Aircraft Program Test Site North Sea Coast)

Table 1 – RMS errors in [meter] at ground computed from residuals after Helmert-transformation

Area	Bavaria (Original)				North Germany					
							Original Image		Corrected Affinity	
	Ground Control Points	Used Points	$m_x \pm$	$m_y \pm$	Ground Control Points	Used Points	$m_x \pm$	$m_y \pm$	$m_x \pm$	$m_y \pm$
1	2	3	4	5	6	7	8	9	10	11
1	234	234	215.0	245.3	82	82	322.8	356.3	112.4	109.4
		9	239.5	260.7		9	340.9	359.8	77.7	125.9
		4	223.2	309.7		4	293.2	479.1	130.8	168.7
2	43	43	133.3	118.2	26	26	92.4	112.1	81.3	85.6
		9	130.4	133.9		9	97.6	118.0	78.6	90.4
		4	114.9	178.6		4	95.2	120.1	88.2	97.2
3	62	62	112.9	136.6	18	18	193.2	201.1	66.3	55.2
		9	162.6	108.9		9	159.4	246.1	67.7	54.6
		4	141.8	138.2		4	187.6	258.3	92.4	74.0
4	49	49	75.3	98.9	17	17	160.1	103.6	57.0	50.7
		9	76.8	97.6		9	147.2	127.0	55.3	58.7
		4	77.1	98.4		4	166.7	99.1	65.9	56.9
5	80	80	180.2	171.1	21	21	241.6	296.2	94.2	153.1
		9	176.8	175.6		9	306.0	268.1	133.3	133.7
		4	189.1	171.6		4	285.0	325.4	117.6	160.2
6					14	14	47.6	45.4	64.9	58.9
						9	49.4	45.8	70.2	57.1
						4	48.5	55.0	79.1	59.8
2,3, 4,5	234	4 for every quadr.	145.7	148.9	82	4 for every quadr.	208.2	218.6	93.1	106.2

$$(m_{x,y} = \pm \sqrt{\frac{\sum_{i=1}^{n} \epsilon_i \epsilon_i}{n}}, \text{ where } \epsilon_i = x, y_{(map)i} - x, y_{(image)i})$$

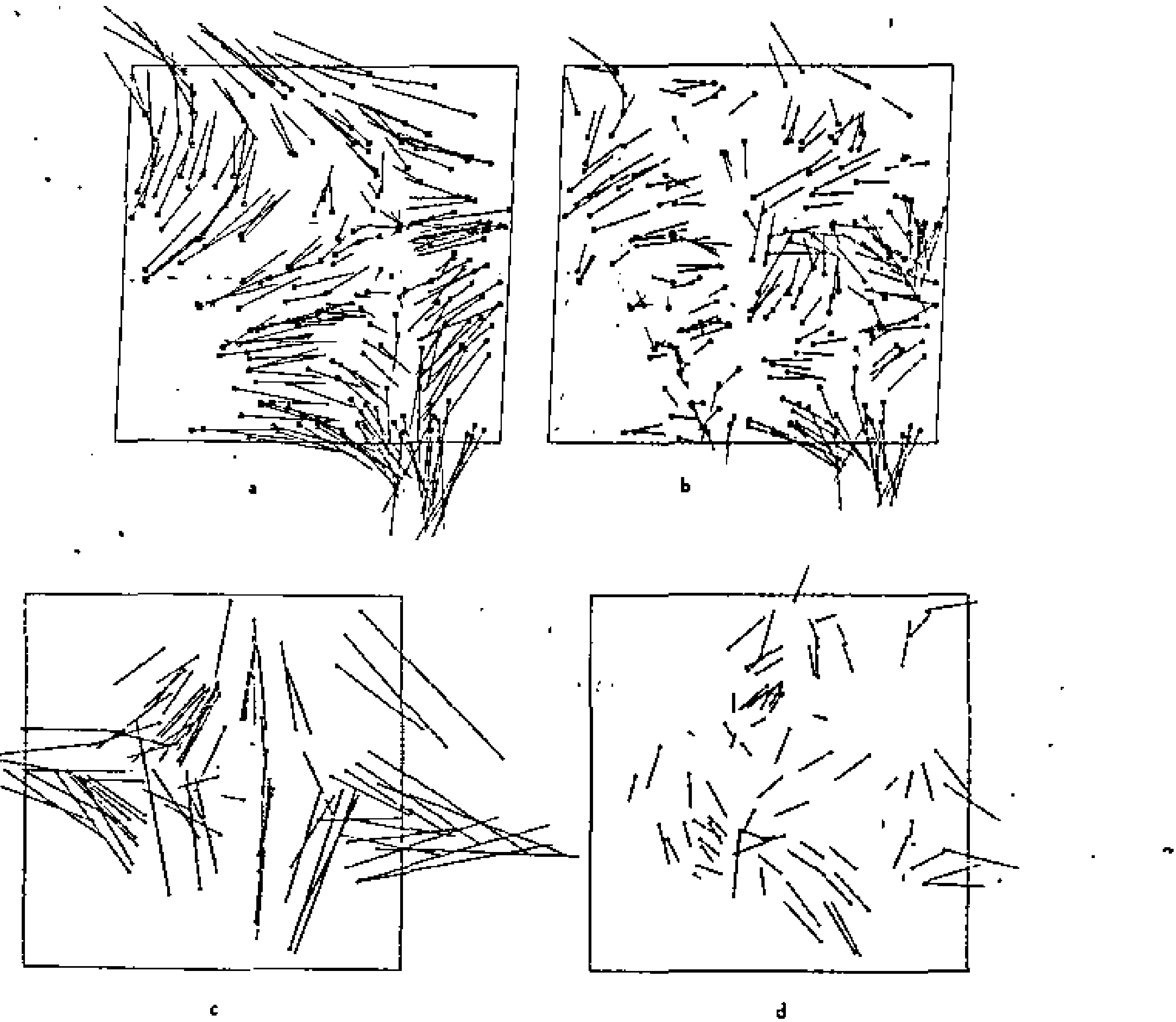

Fig. 3 – Residual vectors after Helmert-transformation

├––┤ corresponds to 25 km on ground
250 m as vector

a: Bavaria	234 control points	original
b: Bavaria	4 quadrants à 4 control points	
c: North Germany	82 control points	original
d: North Germany	82 control points	affine correction

The affinity, caused by different scales in x and y direction, can be determined after Helmert-transformation without least squares adjustment, as well as in a single step applying

$$\begin{aligned} x' &= a_0 + a_1 x + a_2 y \\ y' &= b_0 + b_1 x + b_2 y \end{aligned} \quad (3)$$

where

$$\text{Factor of affinity} = \text{FA} = \frac{a_1^2 + a_2^2}{b_1^2 + b_2^2} \quad (4)$$

Affine geometric correction is recommended to be executed digitally (see paragraph 4.2), though there are examples for analog treatment (see *Trinder* and *Nasca* [20]). Therefore the effect from affine correction is demonstrated for the North German scene, where CCT's are available. For the original image, FA was determined after Helmert-transformation as 1.015; i. e. the x-coordinates had to be stretched by that factor in order to obtain conformity. The results from Helmert-transformations after affine correction of the data are written in the last two columns of Table 1. For the processing of the whole scene the values are improved by the factor of 3; for the quadrants the improvement is less spectacular, but still important. Fig. 3d displays the vectors, which do not show large systematics if compared with Fig. 3c, though the covariance functions demonstrate local correlations down to 45 km for both directions.

The exact determination of scales in x and y contributes the most important step from "bulk" to "precision" processing. We have to take into consideration, whether more sophisticated, i. e. more expensive procedures are finally effective.

3.2 Second-order polynomials

Polynomials similar to

$$\begin{aligned} x' &= a_0 + a_1 x + a_2 y + a_3 x^2 + a_4 y^2 + a_5 xy \\ y' &= b_0 + b_1 x + b_2 y + b_3 x^2 + b_4 y^2 + b_5 xy \end{aligned} \quad (5)$$

have been applied by most authors in order to describe LANDSAT MSS geometry (*Bähr/Schuhr* [1], *Bernhardson* [7], *Forrest* [10], *Trinder/Nasca* [20], *Wong* [21]). The results were excellent in general, and one could propagate this approach for operational application. For digital correction of the imagery, however, the processing algorithm may be costy (see paragraph 4.3), apart from the fact, that more ground control than for simpler methods has to be provided. Therefore we have to check whether the results will justify the costs.

Table 2 summarizes the results after application of (5) to the two scenes "Bavaria" and "North Germany". Rms errors, quadrants and dimensions are composed in the same manner as for Table 1. As (5) contains affine parameters (first three terms), affine pre-correction of the data was not necessary. We realize, that

(1) the polynomials describe the geometry of the Bavarian scene better than the North German one, where the residuals are still in the order of magnitude of about 1 pixel;

(2) dividing the scene into quadrants does not improve the accuracy for "Bavaria", yet for "North Germany", where the residuals achieve the same magnitude as for "Bavaria".

For application of (5) 9 control points are practically the minimum necessary for determining accurate polynomials. However, 9 control points for every quadrant mean at least 25 for a whole scene, a number, which seems not to be realistic for operational application. On the other hand we have to admit, that this approach yields the best results from all methods applied to the North German scene (see following paragraphs).

Fig. 4 shows the residual vectors for 3 examples which illustrate the more homogeneous internal geometric conditions in the Bavarian scene.

Table 2 – RMS errors in [meter] at ground computed from residuals after application of polynomials (5)

	Bavaria				North Germany			
Area	Ground Control Points	Used Points	m_x ±	m_y ±	Ground Control Points	Used Points	m_x ±	m_y ±
1	234	234 9	43 53	49 54	82	82 9	65.7 77.7	80.5 104.3
2	43	43 9	41 54	32 42	26	26 9	58.5 64.4	43.6 45.9
3	62	62 9	37 39	45 55	18	18 9	27.8 33.0	24.9 34.2
4	49	49 9	39 42	47 52	17	17 9	42.0 60.4	33.1 59.4
5	80	80 9	45 56	44 48	21	21 9	37.3 45.0	47.1 57.0
6					14	14 9	41.2 47.7	42.0 42.5
2,3, 4,5	234	9 for every quad.	48.8	49.8	82	9 for every quad.	53.2	49.9

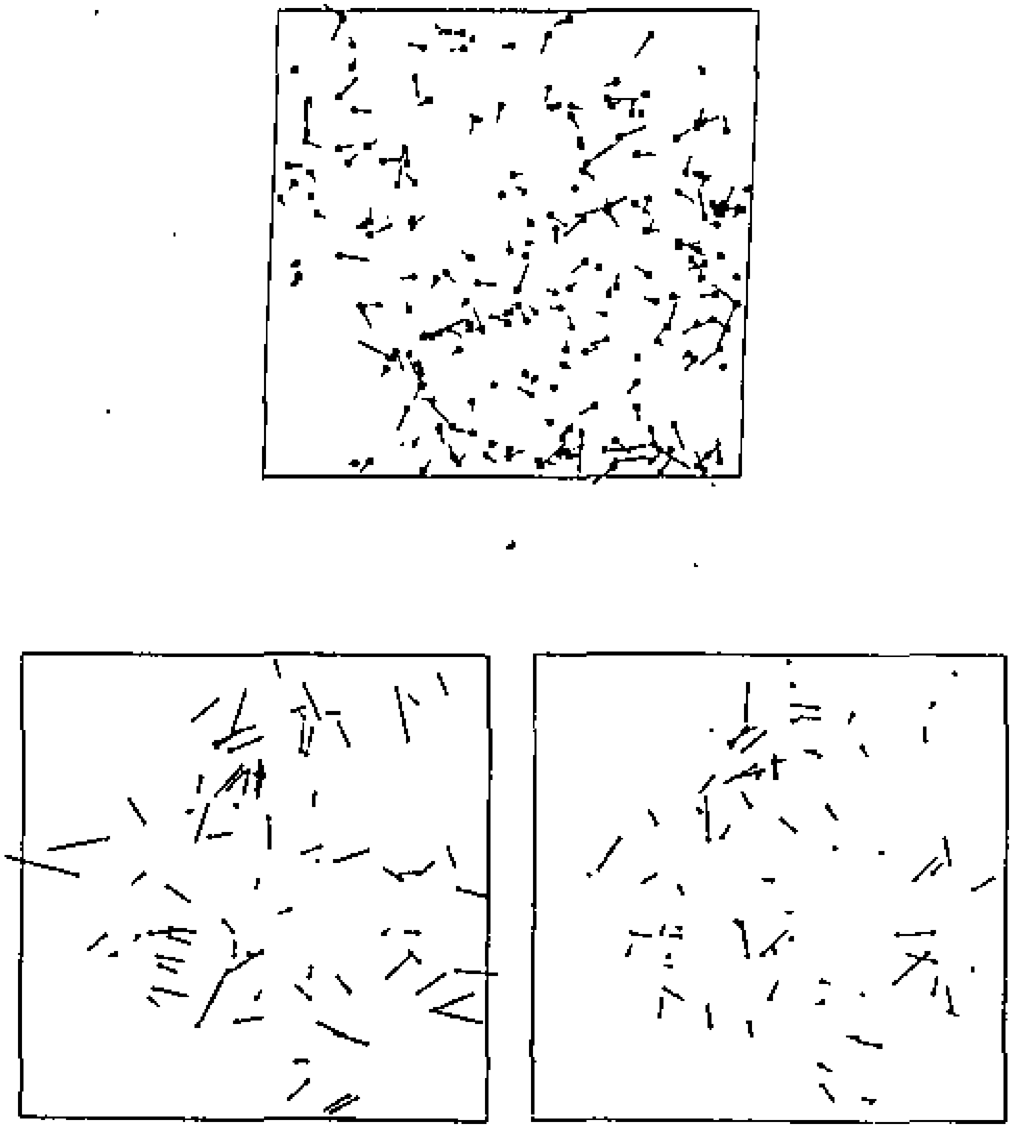

b c

Fig. 4 – Residual vectors after second-order polynomials

⊢–––⊣ corresponds to 25 km on ground
250 m as vector

a: Bavaria 234 control points
b: North Germany 82 control points
c: North Germany 4 quadrants à 9 control points

3.3 Collinearity equations

With respect to other mathematical formulations, photogrammetrists generally prefer collinearity equations when describing the relations between image and object coordinates (*Konecny* [15]). This offers a lot of advantages, e. g.

(1) complex geometric conditions can be rigorously derived in an evident, general form and easily be simplified if necessary;

(2) the accuracy of geometrical models applying collinearity equations may be checked theoretically;

(3) analytical bloc formation is possible using even imagery of non-conventional geometry (see *Dowideit* [9]) as well as combination of different types;

(4) collinearity equations mostly provide non-correlated relations together with the possibility for introduction of specific additional parameters (e. g. DTM).

As far as satellite imagery is concerned, collinearity equations were used by *Kratky* [12] for theoretical considerations on LANDSAT, whereas *Bähr* [3], [5] applied different collinear models for geometrical analysis of NIMBUS imagery. Therefore it seems consequent, to try here the formulas in [3] and [5] for evaluation of LANDSAT: with reference to [3] we get from Fig. 5:

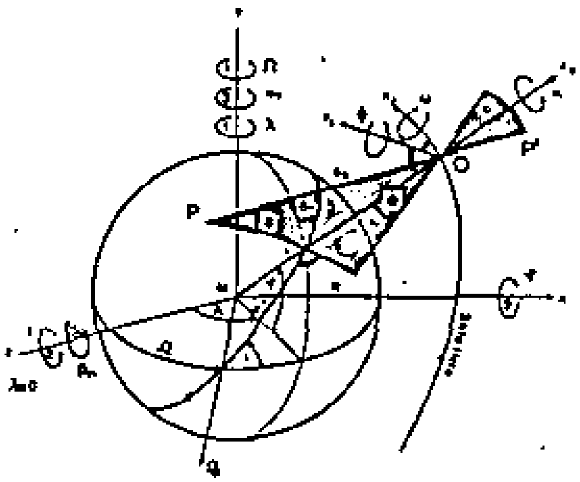

Fig. 5 – Geometric relations between image points P' and ground points P for satellite scanner imagery

$$\begin{pmatrix} x \\ y \\ z \end{pmatrix}_{ground} = D^T_{u,\,i,\,\Omega} \left(D^T_{\phi,\,\omega,\,\kappa}\, D^T_{\theta} \begin{pmatrix} 0 \\ 0 \\ -\bar{d}_{\theta} \end{pmatrix} + \begin{pmatrix} 0 \\ 0 \\ r \end{pmatrix} \right) \qquad (6)$$

where

$$\bar{d}_{\theta} = d_{\theta} - \frac{d_{\theta}\, r \sin\theta}{r \cos\theta - d_{\theta}} \qquad (7)$$

This approach needs the orbital parameters u, i, Ω and r, which are provided by NASA for every two days. As correction parameters serve the unknown orientations ϕ, ω, κ as well as r, which are defined as polynomials of second (ϕ, κ, r) and third (ω) degree, regarding time dependency. The mathematical model, which finally leads to a least-squares adjustment procedure is a general one and can easily be arranged for all types of satellite scanner imagery.

Collinearity equations afford data, for which the internal geometric properties are defined. This is not the case if the imagery has already been geometrically preprocessed in an unspecified manner, like NASA bulk copies. Therefore only the "North German" scene was used for application of collinearity equations.

Table 3 and Fig. 6 show the results. If all 82 points are used and 13 unknowns are introduced (as polynomial coefficients in order to determine ϕ, ω, κ and r as a function of the "time-coordinate" x_t), we receive $m_x = \pm 71$ m rms error and $m_y = \pm 81$ m rms error. This is nearly exact the same result as from polynomials for 82 used points, a fact, which is illustrated too by comparing the corresponding vector plots displayed in Fig. 4a and Fig. 6. If ϕ, ω, κ and r are not expressed by polynomials, only 4 unknowns are necessary, which yields poorer results. Like for Helmert-transformations and for polynomials, we find a significant improvement of accuracy when processing the image in sections (example executed for quadrant 2).

We can finally say, that for processing LANDSAT MSS imagery p o l y n o m i a l s a n d c o l l i n e a r i t y e q u a t i o n s l e a d t o t h e s a m e r e s u l t s. This is an interesting and important fact, from which follows, that for operational purpose polynomials should be preferred generally because of their simpler structure. This, however, does not touch the advantages of collinearity equations mentioned above.

Table 3 — RMS errors in [m] at ground computed from residuals after application of collinearity equations

	North Germany				
Area	Ground Control Points	Used Points	Unknowns	m_x ±	m_y ±
1	82	82	13	71	81
			4	125	96
2		29	13	50	34
			4	81	59

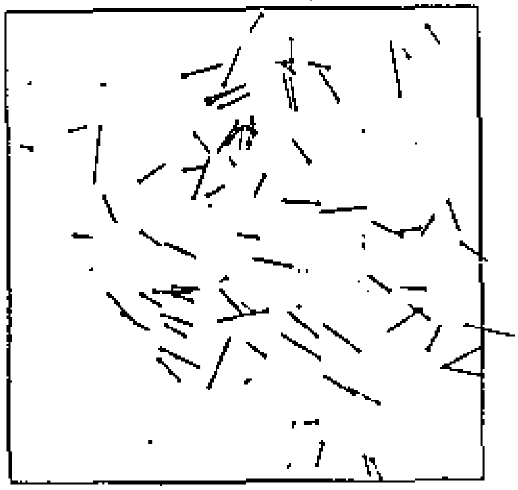

Fig. 6 — Residual vectors after collinearity equations

⊢——⊣ corresponds to 25 km on ground
· 250 m as vector

North Germany 82 control points

3.4 *Prediction methods*

In geodesy (*Moritz* [18]) as well as in photogrammetry (*Kraus/Mikhail* [13], [14]) least-squares interpolation ("prediction") has become a useful tool for numerous applications. This statistical method never stands alone but is in communication with the task to separate a trend function from correlated residuals, which have to be provided for the prediction procedure.

The evaluated methods, like Helmert-transformations, polynomials and collinearity equations can be considered to be such "trend functions". Therefore, prediction is applied to r e s i d u a l s , particularly to residuals created by polynomials and collinearity equations: empirical covariance functions proved, that the values still showed significant correlation in *y*-direction. With reference to *Bähr* [2] we take

$$C\,(P_i P_K) = C\,(0)\,e^{-K^2 s^2} = F V\,e^{-K^2 s^2} \tag{8}$$

for describing the covariance function analytically and may write

$$l_{si} = c_i^T\,C^{-1}\,l \tag{9}$$

where l_{si} are the estimated correlated components of the residuals l · c and C contain elements of the covariance function (8) including the variance V and the "filter factor" F.

The prediction procedure improves the result slightly: using $K^2 = 0.45$, $V = 0.005$, $F = 0.8$, and 9 control points, we receive $m_y = \pm 70.6$ m, which is an improvement of about 10 m. The residuals in x- and y-direction are now of the same magnitude and show the best result for all approaches which take the scene as a whole. Nevertheless the values are not fully satisfactory, because of relatively high-level rms error and remaining correlation in some areas. For the Bavarian scene, prediction procedures improved the results from $m_x = \pm 43$ m / $m_y = \pm 49$ m after polynomials up to $m_x = m_y = \pm 42$ m (40 control points, see [5]). Other results for LANDSAT MSS least-squares interpolation including filtering is reported by *Bähr* in [2]: For another North German scene $m_x = \pm 71$ m / $m_y = \pm 77$ m were obtained (using 10 control points) from $m_x = \pm 138$ m / $m_y = \pm 145$ m residuals after Helmert-transformation. In this frame, the uncorrelated components of the residuals were about ± 45 m in both x and y, which corresponds to the result obtained from the Bavarian scene.

We may state, that linear least-squares interpolation can generally be applied to LANDSAT imagery, though not always with spectacular success. As it is a typical "post-processing" method and a little bit delicate, it adds costs to the main part of the procedure. In most practical cases these costs seem not be justified by the obtained results.

4 Digital rectification

4.1 The Hannover modular digital image processing package

Digital rectification procedures afford techniques, which differ entirely from the analytical approaches discussed above. Geometrical analysis is a common tool for photogrammetrists, well-known from analytical triangulation for instance, but rectification is more computer-oriented: appropriated programs can very well be developed by computer scientists including hardware specialists. However, results from rectification can necessarily not exceed the accuracy of the analytical models on which the rectification is based. Consequently, the quality of the result is established by the analytical model, whereas the costs originate mainly from the rectification procedure.

At the Institut für Photogrammetrie und Ingenieurvermessungen (IPI), a modular digital image processing package has been developed by the institute members sequentially: individual computer programs were written in modular form upon need and added to the library, where they are freely available for the user. At the moment about 60 modules exist. The application of the package is very simple, because only one punch card is necessary for calling a module. 2 to 9 parameters can be punched and allow the introduction of the desired specifications (see *Bähr* [6]).

For the subject discussed in this paper, apart from read/write calls, 5 modules are of main interest:

1. "HILIN" = Histogram linearisation
2. "REDUK" = Definition of image portion

3. "DEHN" = Application of any scale factors, independent for both directions (affine stretch)

4. "EDREH" = Application of earth rotation effect for LANDSAT*)

5. "POLY" = Application of 2^{nd}-order polynomials (formula (5)) and overlay of a Gauß-Krüger grid.

All computations were executed by the CONTROL DATA CYBER 73/76 machine of the Computer Center at Hannover University; the imagery was displayed at the OPTRONICS MARK 17 at the IPI.

4.2 Rectification by bulk procedures

Distribution of rectified data in two different levels of accuracy ("bulk" and "precision") as NASA did, can generally be propagated. "Bulk" approaches here are defined as procedures which principally work without or with little ground control (up to 4 points). Therefore only linear transformations, like (2) and (3) which lead to the results displayed in Table 1 will be considered in this paragraph.

Original CCT data is distributed in a form, where the pixel dimensions (referred to the ground) are approximately 56 m in scan direction and 79 m in flight direction. This is caused by the scanning procedure in order to obtain equal MTF characteristics in both directions (see *Bähr* [5]). The corresponding hard copies are distorted in a manner, which make determination of ground control points practically impossible. Therefore the first step in the rectification procedure is an approximate implementation of the affine factor (appr. 79/56 = 1.4107) by module "DEHN". As a second step, the non-linear earth rotation effect has to be introduced simply by calling "EDREH". Afterwards the corresponding imagery is prepared for measurement of ground control coordinates.

The image coordinates together with the ground coordinates allow application of (2) or (3). Helmert-transformations (2) provide translations, rotation and scale factor, as discussed in paragraph 3.1. For bulk rectification, practically only the scale factor has to be considered, if translations and rotation are applied during map overlay. Remaining affinity can be determined from the residuals after Helmert-transformation (or directly from (3) and (4)) and applied together with the scale factor by "DEHN" in a third step.

Disadvantage of this procedure is the double call of "DEHN", as this module is the most expensive one for the whole bulk rectification. Table 4 summarizes costs for applications of the "DEHN" module. Example No. 1 refers to the general case, that unprocessed data

---

*) Earth rotation changes the angle γ between satellite heading and meridian as a function of geographical longitude ϕ, orbital inclination i, and anomalistic period U_T (see *Bähr* [5]):

$$\tan \gamma = \frac{\sqrt{\sin^2 i - \sin^2 \phi}}{1400/U_T - \cos i} \qquad (10)$$

U_T in [min]

Table 4 – Computing time for different applications of the "DEHN" module (affine stretch) for CCT "North Germany"

Original Data		Image* Scale Desired	Scale Factors for		Affinity Factor Applied	Data after "DEHN"		Pixel Number $[10^6]$	Execution Time in CDC 73/76 Computer [sec]	Example No.	Remarks
Rows	Columns		Rows	Columns		Rows	Columns				
2340	3264	1 : 1 Mill.	1.596	1.146	1.392	3734	3740	13.9	82.8	1	Full scene, enlarged; approximate affinity
3734	3740	1 : 1 Mill.	1.000	0.985	1.015	3734	3683	13.7	88.3	2	Application of small affinity factor to full scene
2340	3264	1 : 2 Mill.	0.798	0.564	1.415	1867	1841	3.4	26.3	3	Full scene, reduced; correct affinity
1632	2091	1 : 1 Mill.	1.592	1.144	1.392	2597	2391	6.2	80.5	4	~ 1/4 scene, enlarged
1632	2091	1 : 0.5 Mill.	3.185	2.288	1.392	5195	4782	24.8	279.1	5	~ 1/4 scene, enlarged

*: scale valid for 50 μm pixel size at OPTRONICS display

is stretched and enlarged up to approximately 1 : 1 Mill. image scale (1 Pixel corresponds to 50 µm in the OPTRONICS). If the applied affinity was not fully correct, a second call of "DEHN" doubles the costs (example 2), though only 0.15 % reduction in y-direction is introduced. Therefore a precise a priori knowledge of both scales is welcome, which is generally available from previous procedures. Theoretically, ground coordinates are not necessary for this approach, though highly recommended for a following control of accuracy.

The whole execution runs even considerably cheaper, if only 1 : 2 Mill. image scale is desired (Table 4, example 3). This however, incorporates the disadvantage of image information reduction of about 50 %. As visually only little deterioration of quality is observed, one has to decide for the specific task what to do. From the operational point of view, this way of information reduction might be propagated, the more so as the number of $13.9 \cdot 10^6$ pixel corresponding to a 1 : 1 Mill. full-frame scene will be too large for many computers.

Processing of smaller portions of the imagery (Table 4, examples 4 and 5) does not reduce the computing time as expected. Therefore, dividing the scene into 4 quadrants as proposed in paragraph 3.1, will lead to relatively costy geometrical processing. Obviously, cost/pixel number-dependency cannot rigorously be defined because of "DEHN" module structure.

This however is possible for "EDREH", a module, which follows "DEHN" in order to apply the earth rotation effect (1.5 sec per 10^6 pixel), as well as for "HILIN" (Histogram linearisation: 3.4 sec per 10^6 pixel). Together with input and output finally 140 sec are needed for example 1, 75 sec for example 3. The computing time for the analytical procedures necessary for determining the geometrical parameters for rectification is between 3 and 8 sec and can therefore practically be neglected with respect to the relatively long execution time needed for geometrical rectification. This is also valid for precision procedures.

4.3 *Rectification by precision procedures*

"Precision" approaches here are defined as procedures which use more than 4 ground control points in order to compute parameters for non-linear rectification. Principally the 3 methods discussed in the paragraphs 3.2 to 3.4 are for disposition. Here only polynomials will be applied because of the advantages mentioned in 3.3.

For digital rectification, the "indirect method" is chosen because of the advantages discussed in *Konecny/Schuhr* [16] and *Konecny* [17]. This means, according to Fig. 7, that starting from the rectified "pixel"-system x (PIX), y (PIX) the geometrical positions for the pixels 1, 2, 3 ... are computed within the distorted "pixel"-system x' (PIX), y' (PIX) using (5). The grey values for 1, 2, 3 ... then are interpolated from the adjacent pixels.

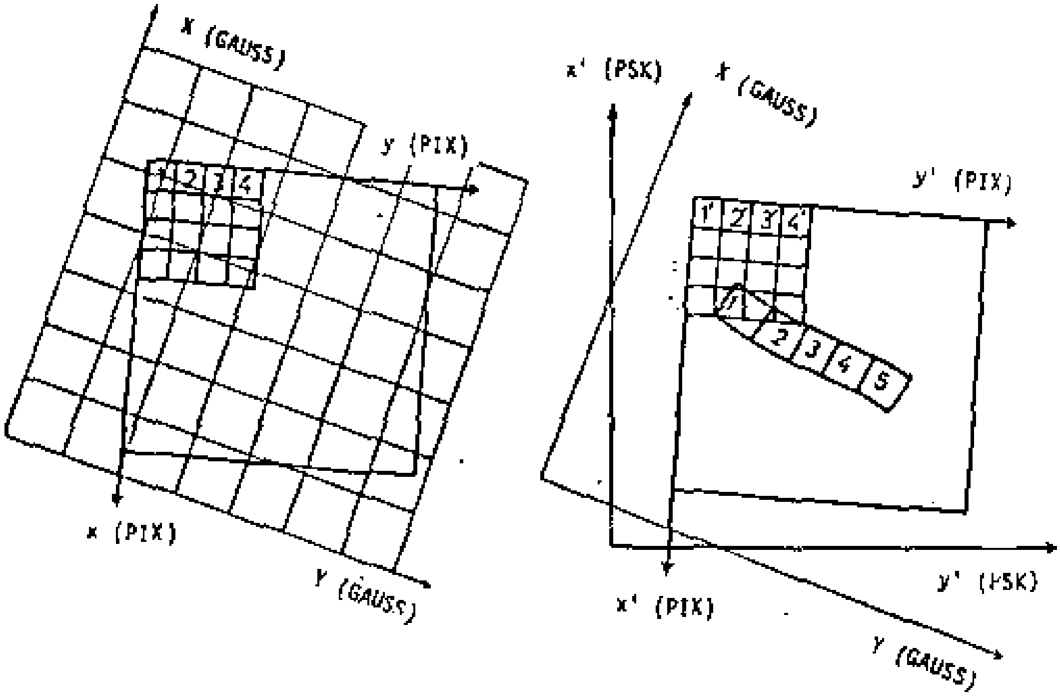

Fig. 7 – Coordinate systems for precision rectification using the "indirect method" (principle)

Left: rectified image; right: distorted image

For the application of (5) image coordinates, which are originally provided in x' (PSK), y' (PSK) stereocomparator-system, have to be transformed into the x' (PIX), y' (PIX) "pixel"-system, simply by (2), taking the edges as identical points. Moreover, ground control coordinates, originally provided in X (GAUSS), Y (GAUSS) Gauß-Krüger-system, have also to be transformed into x' (PIX), y' (PIX), which can be done taking ground control points as identical points.

Module "POLY" executing the rectification procedure, also designs a Gauß-Krüger grid as a precise overlay to the result. In order to avoid relatively costy massive digital rotation, the grid is rotated in respect to the "pixel"-system and not the other way round.

Example No. 3 (see table 4) is taken for rectification by precision procedures, because the reduced pixel quantity seems to be the most economical version for operational application. Computing time for "POLY"*) is 40 sec, i. e. about 1.5 times more than for the bulk "DEHN" procedure, which has to preceed. Therefore one has to check thoroughly, whether 50 % increase of accuracy (compare table 1 and 2) will justify 150 % increase of costs. The decision will depend on the specific problem evaluated.

Fig. 8 shows the result obtained from "POLY".

---

*) Program written by cand. rer. nat. *H. Schäfer*

Fig. 8 – LANDSAT scene "North Germany" from Aug. 11th, 1975 rectified by polynomials

Scale 1 : 2 Mill.

Grid meshes correspond to 25 x 25 km

5 Conclusions

Geometrical image processing never is "l'art pour l'art": the results provide imagery ready for multisensor/multitime correlation, necessary for many important applications. Since image processing systems become more and more popular, the user possesses the tool for both semantic and geometrical processing. As far as LANDSAT is concerned, geometrical treatment of the data is recommended to be executed operationally in two steps: a "bulk" approach, applying scale factors and earth rotation, needs no or little ground control and yields an accuracy of about ± 1.5 . . . 2 pixel units. A "precision" approach, taking second-order polynomials and 9 ground control points, yields about ± 1 pixel or better. The geometric quality obtained has to be discussed with respect to the theoretical threshold, which is about ± 0.3 pixel units (see *Bähr* [5]).

Finally, the costs for digital geometrical processing will play a most important role for practical applications. Costs for computing time, however, do not represent a fixed factor but may differ by the factor of 10 even for the same computer because of variable modals, corresponding to the type of user and the executed task. Therefore, only relative costs have been reported here by the computing time values. The precision processing module "POLY" is 1.5 times more than the bulk processing module "DEHN", and one has to take into account, that always a "DEHN" procedure has to preceed a precision rectification, in order to produce imagery suitable for determination of ground control coordinates.

Since computing costs are still going down, they may not necessarily represent the main cost factor in future. One therefore has to focus the expense introduced by the ground control, necessary for precision processing. Only a tiny part of the earth's surface is covered by maps of 1 : 50,000 scale, which would provide cheap and sufficient geometrical reference. In developing countries, where the application of LANDSAT data is of particular interest, "bulk" rectified imagery will often be a first useful tool. For further geometrical processing of LANDSAT, ground control can be provided for discrete points by aerotriangulation, and the imagery can be used for large scale mapping later. This example proves the necessary and fruitful interaction between conventional photogrammetric procedures and advanced digital techniques.

Literature

[1] *Bähr, H. P.; Schuhr, W.:* Versuche zur Ermittlung der geometrischen Genauigkeit von ERTS-MSS Bildern. – Bildmessung und Luftbildwesen, 1974, p. 22–24.

[2] *Bähr, H. P.:* Interpolation and Filtering of ERTS Imagery. – ISP Comm. III Symposium, Stuttgart 1974.

[3] *Bähr, H. P.:* Geometrical Models for Satellite Scanner Imagery. – ISP Comm. III, Helsinki 1976.

[4] *Bähr, H. P.:* Geometrische Modelle für Abtasteraufzeichnungen von Erderkundungssatelliten. – Bildmessung und Luftbildwesen, 1976, p. 198–202.

[5] *Bähr, H. P.:* Analyse der Geometrie auf Photodetektoren abgetasteter Aufnahmen von Erderkundungssatelliten. – Schriftenreihe des Niedersächsischen Landesverwaltungsamtes – Landesvermessung –, Hannover 1976.

[6] *Bähr, H. P.:* Digital Image Processing Experience at Hannover Institute for Photogrammetry (IPI). – IGP, Comm. III, WG. 2, Symposium Graz, 1977.

[7] *Bernhardson, T.:* Undersøkelse av den geometriske nøyaktighet i ERTS-bilder. – Institutt for landmåling Norges landbrukshøgskole.

[8] *Colvocoresses, A. P.; Mc Ewen, R. B.:* Progress in Cartography, EROS Program. – USGS. Mc Lean, 1973.

[9] *Dowideit, G.:* Eine Blockausgleichung für Abbildungen des seitwärtsschauenden Radars (SLAR). – Wissenschaftliche Arbeiten der Lehrstühle für Geodäsie, Photogrammetrie und Kartographie an der Technischen Universität Hannover, 1977.

[10] *Forest, R. B.:* Geometric Correction of ERTS-1 MSS Images. – ISP Comm. III Symposium, Stuttgart 1974.

[11] *Grossmann, W.:* Geodätische Rechnungen und Abbildungen. – Stuttgart 1964.

[12] *Kratky, V.:* Cartographic Accuracy of ERTS. – Phot. Eng. 1974, p. 203–212.

[13] *Kraus, K.; Mikhail, E. M.:* Linear Least-Squares Interpolation. – Photogrammetric Engineering, 1972, p. 1016–1029.

[14] *Kraus, K.:* Rectification of Multispectral Scanner Imagery. – Photogrammetric Engineering, 1978, p. 453–457.

[15] *Konecny, G.:* Geometrical Aspects of Remote Sensing. – ISP Comm. III, Ottawa 1972.

[16] *Konecny, G.; Schuhr, W.:* Digitale Entzerrung der Daten von Zeilen-Abtastern. – Bildmessung und Luftbildwesen, 1975, p. 135–143.

[17] *Konecny, G.* et al.: Digitale Prozessoren für Differentialentzerrung und Bildkorrelation. – Bildmessung und Luftbildwesen, 1978, p. 99–109.

[18] *Moritz, H.:* Neuere Ausgleichungs- und Prädiktionsverfahren. – Zeitschrift für Vermessungswesen, 1973, p. 137–146.

[19] *Schoonmaker, J. W.:* Geometric Evaluation of MSS Images from ERTS-1. – ASP St. Louis, 1974.

[20] *Trinder, J. C.; Nasca, S. U.:* Test on the Mapping Application of LANDSAT Imagery. – ISP Comm. III, Helsinki 1976.

[21] *Wong, K. W.:* Geometric and Cartographic Accuracy of ERTS-1 Imagery. – Phot. Eng. 1975, p. 621–635.

[22] Proceedings of Symposium on Significant Results Obtained from the ERTS-1. – NASA Sponsorship, 1973; Library of Congress Catalog Card No. 73 – 600 115.

GEOMETRICAL MODELS FOR SATELLITE SCANNER IMAGERY

H.P. BÄHR

Presented Paper

Commission III

International Congress for Photogrammetry

Helsinki 1976

Institut für Photogrammetrie

und Ingenieurvermessungen

- Technische Universität Hannover -

XIIIth Congress of the International Society for Photogrammetry

Commission III, Presented Paper, Helsinki,

July 11th to 23rd, 1976

Geometrical Models for Satellite Scanner Imagery

by H. P. Bähr, Hannover, Fed. Rep. of Germany
Technische Universität, Institut für Photogrammetrie
und Ingenieurvermessungen

Zusammenfassung

Das beste Modell ("213") zur Erfassung der Geometrie abgetasteter Satellitenaufnahmen benutzt Kollinearitätsgleichungen und läßt die Ausgleichungsunbekannten in Form von Polynomen entlang des Flugweges variabel. Dies führt auf mittlere Restfehler von etwa ± 0,85 Auflösungselementen und liegt damit um 46 % besser als mit konstant bleibenden Ausgleichselementen. Für ein LANDSAT-1 Bild ("bulk", 254 Punkte) wird gezeigt, daß Polynome 2. Ordnung die geometrischen Verhältnisse mit ausreichender Genauigkeit beschreiben (± 0,54 / 0,83 Auflösungselemente). Prädiktionsfilterung verbessert das Ergebnis nur noch unwesentlich. Paßpunktkoordinaten sind wegen zufälliger Lage Punkt / Sensor nur auf 1/3 Bildelement sicher; hinzu kommt noch eine vom Beobachter abhängige Einstellunsicherheit von 1/4 Bildelement, so daß allgemein etwa 1/2 Bildelement als Grenze für die insgesamt erreichbare Genauigkeit anzusehen ist.

Abstract

The best approach for describing the geometry of satellite scanner imagery applies collinearity equations and leaves the adjustment parameters variable along the flight path. This results in residual errors of about ± 0,85 pixel which improves the values for constant adjustment parameters by 46 %. The geometric conditions in a LANDSAT - 1 image ("bulk", 254 points) are well described by simple 2nd order polynomials (± 0,54 / 0,83 pixel). Least-squares filtering does not improve the result significantly. Because of absolute random pointing accuracy and relative point determination accuracy of ground control points, 0,5 pixel finally represents the limit of possible accuracy for all geometric models.

Introduction

Since after the launch of LANDSAT - 1 large scale satellite imagery has become applicable for various means, geometrical rectification is an important step within the image processing loop (see KONECNY (7), KRATKY (8)). For the solution of these problems, 3 analytical models are theoretically derived and practically tested by NIMBUS and LANDSAT photography. Calculations have been performed in the object space and residuals between ground control coordinates and adjusted model coordinates are referred to ground resolution elements ("pixel"). It is suggested, that in general results from scanner imagery processing are given in units of resolution elements in order to become comparable.

2. Evaluated Imagery

For practical considerations, 5 satellite images have been evaluated, taking NIMBUS - 3 (High Resolution Infrared HRIR), NIMBUS - 4 (Temperature Humidity Infrared THIR) and LANDSAT - 1 photography, performed by NASA or Institute for Photogrammetry, Hannover (IPI). Table 1 specifies spacecraft orbits, sensors and photography.

	NIMBUS - 3	NIMBUS - 4	LANDSAT - 1
Start	1969	1970	1972
Flying height h (km) ~	1107	1100	914
Inclination i(°)	99.9	99.9	99.1
excentricity e	0,004	0,0007	0,0006
Equator crossing time ~	12 h	12 h	9h 42 min
max. Scan Angle θ (°)	58	58	6
Channels used (μm)	0,7...1,3	10.5...12.5 (therm al infrared)	0,8...1.1
Instantaneous field of view (m Rad)	8,7	7.0	0,086
Ground Resolution A (km²)	9,5*9,5	7.5*7.5	0,079*0,056
Images	(1) 9. 6. 1969 67 control points Europe, North Africa (2a) 8. 6. 1969 84control points Europe, North Africa, performed by IPI (2b) see above performed by NASA	(3) 20. 6. 1970 40 control points Europe, North Africa	(4) 28. 5. 1975 (bulk) 234 control points Bavaria

Table 1: Spacecraft, sensors and imagery evaluated

3. Limitations of Check Point Accuracy

Evaluation of the analytical models has to be referred to discrete ground control points. The image function is not continuous, but separated by picture elements ("pixel"). If "mathematical" high-contrast points are considered, these points will not necessarily be situated in the pixel centers, though pixel contrast influences on the w h o l e pixel area. The distance between pixel center coordinates (which theoretically are measured) and true point coordinates depend on random relative position "sensor to ground point". The mean a b s o l u t e random pointing accuracy for A*A picture element is $M_v \sim A/3$ (see BAHR(3)). This is a limit, which may not be undercut, nor by digital methods.

To evaluate r e l a t i v e point determination accuracy, 234 LANDSAT - 1 check points (image 4) have been measured twice by 3 operators A, B, C - Linear low-degree transformation (4-parameter-fit) yields relative pointing accuracy M_r :

	M_{Ax}	M_{Ay}	M_{Bx}	M_{By}
M_C	21, 1	20, 5	20, 8	20,7
M_B	17, 2	18,6		

Table 2 : Relative pointing accuracy obtained from 234 LANDSAT - 1 points, measured by 3 operators A, B, C ([m] RMS)

Regarding table 2, the mean relative random pointing accuracy M_r is about $\Delta/4$. M_v and M_r sum up to about $\Delta/2$. For practical work, this is the mean error introduced by ground control points. Obviously, geometrical models should take into account this limitation.

4. Approximated Model by Image Simulation

If the 6 parameters for the satellite orbital path are available (semi major axis a, excentricity e, inclination i, right ascension of ascending node Ω, mean anomaly M_T and argument of perigee ω_T), satellite position φ, λ, r (= h + R) and azimuth β_n ("nominal heading") can be calculated as a function of time T .

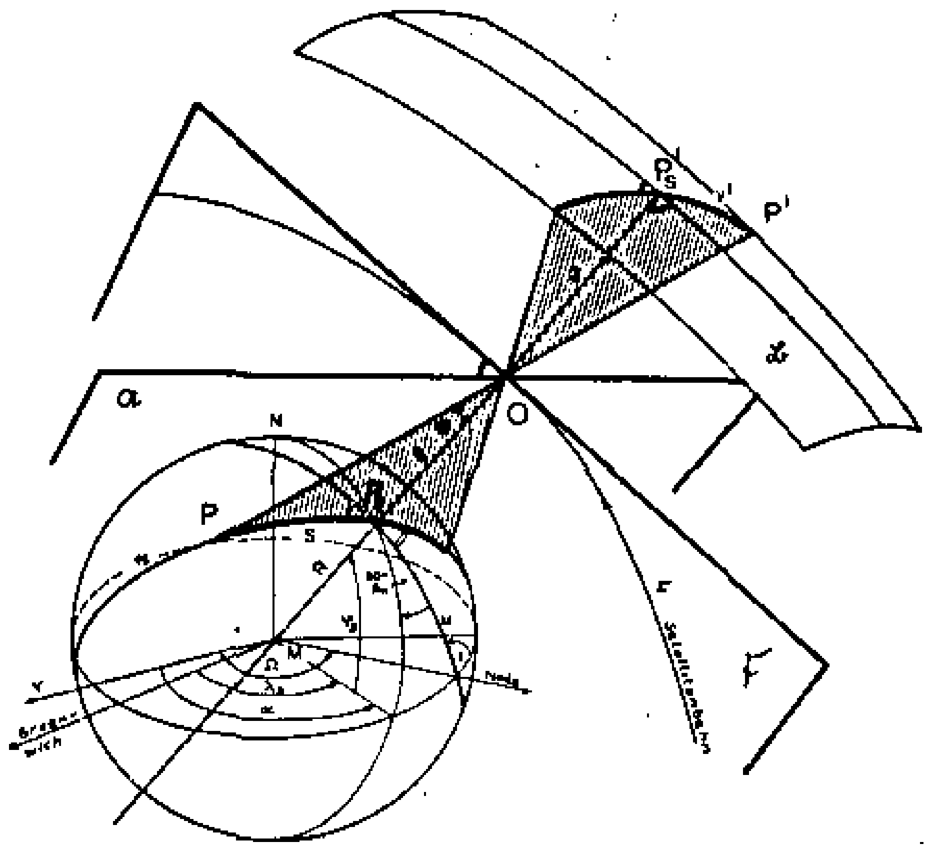

Fig. 1 : Scanning the Earth's surface from a Satellite

$$\sin \varphi_s = \sin u_T \sin i \quad (1)$$

$$\lambda_s = \lambda_{(NODE)} + (\alpha - \Omega)_T \quad (2)$$

$$r_s = a\left(1 - e \cos M_T - \frac{e^2}{2}(\cos 2M - 1)\right) + \ldots \quad (3)^*$$

$$\cot \beta_n = \cos u_T \tan i \quad (4)$$

where

$$u_T = \omega_T + M_T + 2e \sin M_T + \frac{5}{4} e^2 \sin 2 M_T + \ldots \quad (5)^*$$

$$\tan(\alpha - \Omega)_T = \tan u_T \cos i \quad (6)$$

---

* see BROUWER, CLEMENCE (5)

Image generation now may be simulated assuming satellite coordinates as perspective centers, neglecting

a) orbital perturbations of higher degree
b) deviation from satellite orientation towards the earth center
c) true earth shape (best-fitting local spheres will be accurate enough even for the rigorous model (see 5.))

Regarding Fig. 1, ground coordinates of a discrete image point then may be written as follows:

$$\varphi_i = \arcsin (\cos s_i \sin \varphi_s - \sin s_i \cos \varphi_s \sin An) \qquad (7)$$

$$\lambda_i = \lambda_s - \arcsin \left(\frac{\cos An \sin s_i}{\cos \varphi_s} \right) \qquad (8)$$

where

$$s_i = R \left(\arcsin \left(\frac{r}{R} \sin \theta_i \right) - \theta_i \right) \qquad (9)$$

$$\theta_i = \frac{y'_i}{\sigma} \qquad (\theta : \text{scan angle};\ y'_i : \text{image ordinate};\ \sigma : \text{scale factor}) \qquad (10)$$

Image abscissae, proportional to time T and mean anomaly M, serve for determining u_T (5).

Least-squares adjustment now corrects for translation, rotation and scale, independent for flight direction and scan direction (corresponding to "affine transformation"). Absolute terms are found comparing ground control coordinates with best fitting simulated values. If the difference exceeds a certain amount G, the point may be rejected.

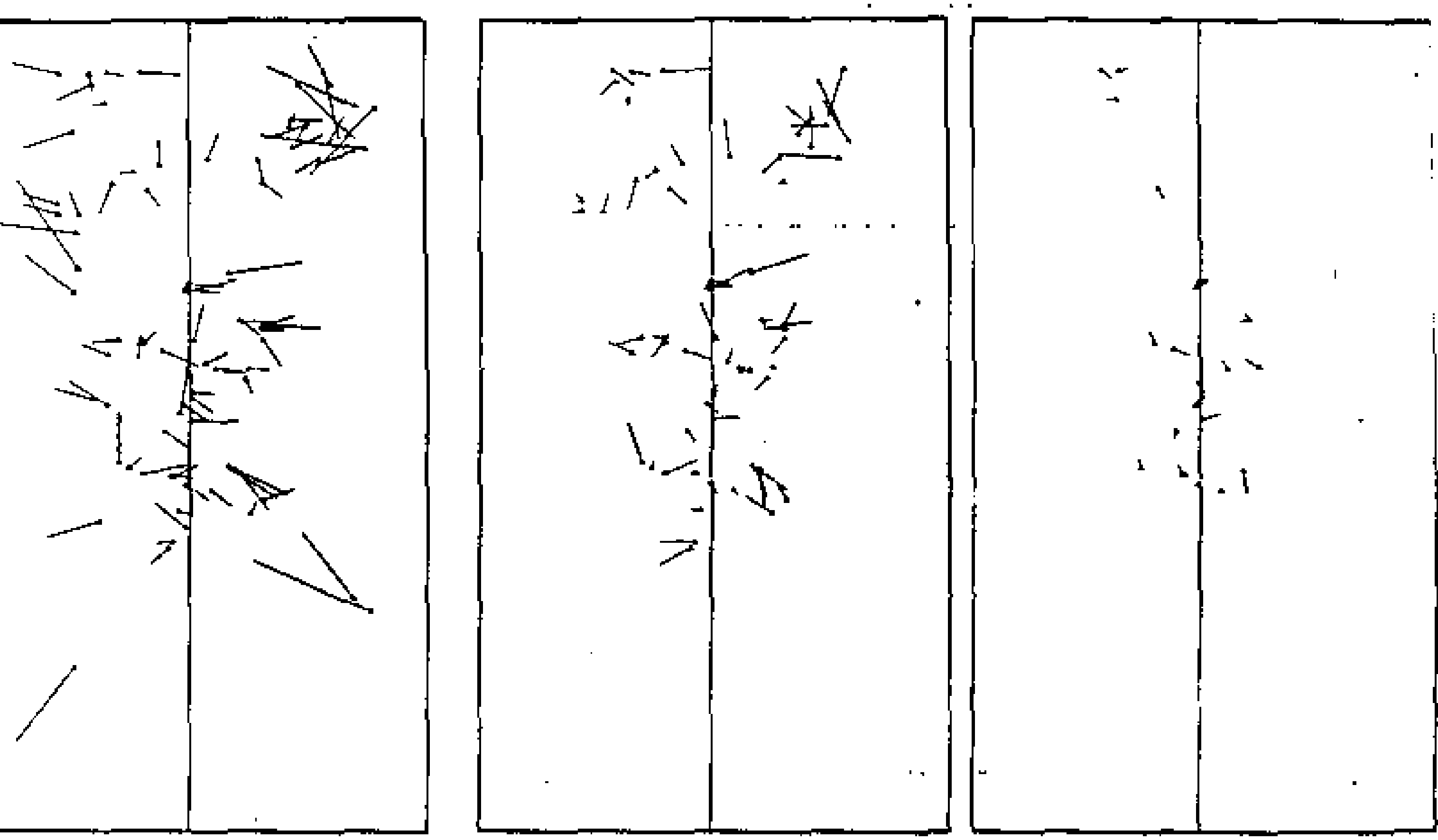

G = 0,0500 ; 84 points found (all)
$m_x = \pm 1{,}24$; $m_y = \pm 1{,}64$ (pixel)

G=0,0125; 56 points found
$m_x = \pm 0{,}74$; $m_y = \pm 0{,}87$ (pixel)

G=0,0031; 23 points found
$m_x = \pm 0{,}37$; $m_y = \pm 0{,}38$ (pixel)

Fig. 2 shows the behavior of residuals in image 2b as a function of G . For G = 0,05 all points are "found" ; for smaller G values "bad" points are not introduced into the adjustment, which leads to smaller residual errors. Table 3 reports the results for all images evaluated by this method (1, 2a, 2b, 3). Obviously, this method is flexible enough to describe the geometry up to ± 1,2 pixel approximately.

	Approximated Model (simulation)				Rigorous Model (Collinearity Equations)							
	All points G=0,05		Selected Points G=0,0125		104		204		113		213	
	mx ±	my ±	mx ±	my ±	mx ±	my ±	mx ±	my ±	mx ±	my ±	mx ±	my ±
Image 1 (67 points)	1,12	0,85	0,89 (59 points)	0,75	1,26	0,72	1,13	0,80	0,90	0,75	0,68	0,80
Image 2a (84 points)	1,22	1,03	0,92 (73 points)	0,97	3,70	1,66	3,68	1,66	0,82	0,83	0,83	0,83
Image 2b (81 points)	1,24	1,64	0,74 (66 points)	0,87	1,06	0,90	0,96	0,99	0,86	0,80	0,79	0,86
Image 3 (40 points)	1,17	1,25	1,08 (39 points)	1,25	1,31	1,08	1,16	1,30	0,91	0,81	0,81	0,89
Mean	1,19	1,19	0,91	0,96	1,83	1,09	1,75	1,19	0,87	0,80	0,78	0,85

Table 3 : Results from geometrical models (in pixel units)

5. Rigorous Models using Collinearity Equations

If ground coordinates are explicitely expressed by a function of image coordinates (collinearity equations), let us call this approach "rigorous". Fig. 3 illustrates that 3 orthogonal rotations of the geocentric coordinate system will transform discrete ground points into the position of the subsatellite points P_s .

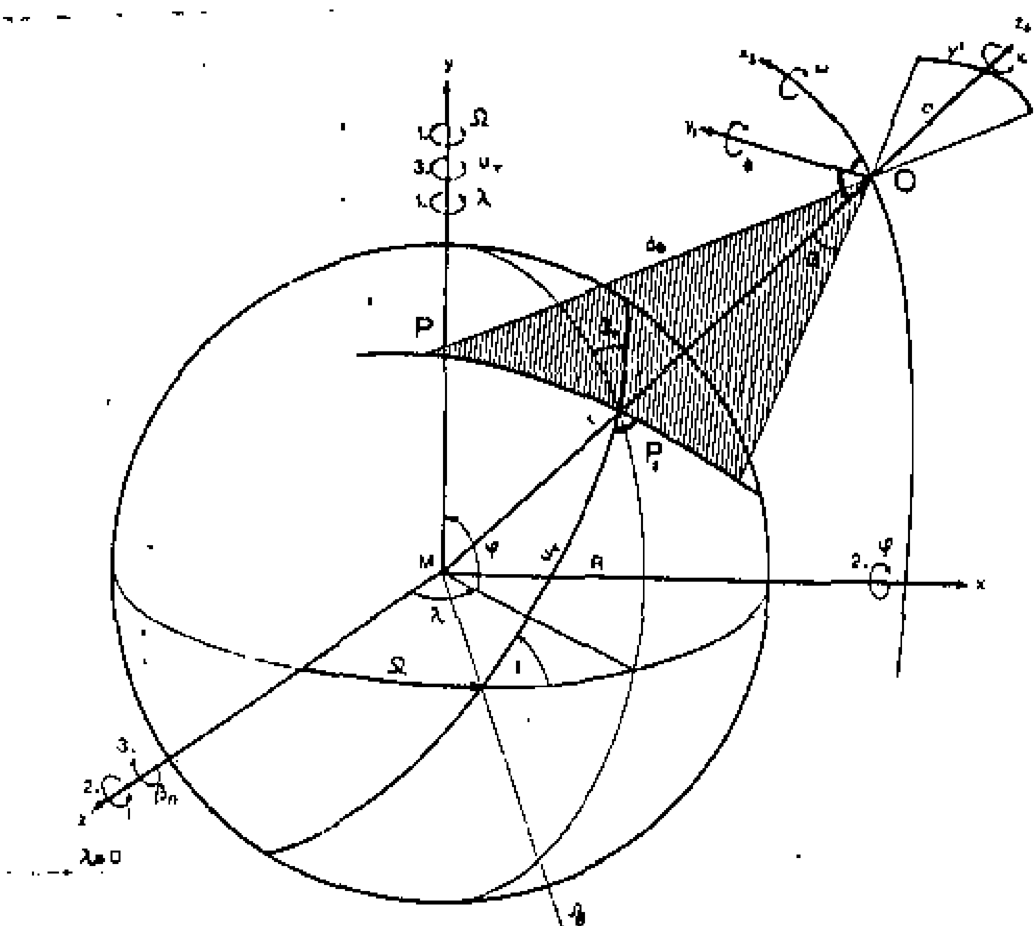

Fig. 3 : Transformation from image system to geocentric system

$$\mathcal{J}_{u,i,\Omega} = \mathcal{J}_{uT}\,\mathcal{J}_i\,\mathcal{J}_\Omega = \mathcal{J}_{\Theta\Omega}\,\mathcal{J}_\varphi\,\mathcal{J}_\lambda$$

Further transformation using d_θ (distance from ground point P to perspective center ω) and θ (see (10)) connect ground coordinates with image coordinates.

$$\begin{pmatrix} x \\ y \\ z \end{pmatrix}_{Ground} = \mathcal{J}^T_{u,i,\Omega}\left(\mathcal{J}^T_\theta \begin{pmatrix} 0 \\ 0 \\ -d_\theta \end{pmatrix} \cdot \begin{pmatrix} 0 \\ 0 \\ r \end{pmatrix}\right) \qquad (11)$$

where $$d_\theta = r \cos\theta - \sqrt{R^2 - r^2 \sin^2\theta} \qquad (12)$$

and $$\mathcal{J}_\theta = \begin{pmatrix} 1 & 0 & 0 \\ 0 & \cos\theta & \sin\theta \\ 0 & -\sin\theta & \cos\theta \end{pmatrix} \qquad (13)$$

or

$$\begin{aligned} x = & -d_\theta \sin\theta \sin i \cos\Omega + r \sin u_T \cos i \cos\Omega + \ldots \\ & + r \cos u_T \sin\Omega - d_\theta \cos\theta \sin u \cos i \cos\Omega - \ldots \\ & - d_\theta \cos\theta \cos u_T \sin\Omega \\ y = & \; d_\theta \sin\theta \cos i + r \sin u_T \sin i - d_\theta \cos\theta \sin u_T \sin i \\ z = & \; d_\theta \sin\theta \sin i \sin\Omega + r \cos\Omega \cos u_T + \ldots \\ & - r \sin\Omega \cos i \sin u_T - d_\theta \cos\theta \cos\Omega \cos u_T + \ldots \\ & + d_\theta \cos\theta \sin\Omega \cos i \sin u_T \end{aligned} \qquad (14)$$

The image ordinates y' determine θ (10), whereas the image abscissas x', proportional to mean anomaly M, are essentially used to calculate u_T (5).

If we permit roll (ω), pitch (ϕ), yaw (κ) rotation of the satellite, equation (11) has to be extended by (15) (assuming small values):

$$\mathcal{J}_{\phi,\omega,\kappa} = \begin{pmatrix} 1 & -d\kappa & d\phi \\ d\kappa & 1 & -d\omega \\ -d\phi & d\omega & 1 \end{pmatrix} \qquad (15)$$

$$\begin{pmatrix} x \\ y \\ z \end{pmatrix}_{Ground} = \mathcal{J}^T_{u,i,\Omega}\left(\mathcal{J}^T_{\phi,\omega,\kappa}\;\mathcal{J}^T_\theta \begin{pmatrix} 0 \\ 0 \\ -\bar{d}_\theta \end{pmatrix} \cdot \begin{pmatrix} 0 \\ 0 \\ r \end{pmatrix}\right) \qquad (16)$$

where $\bar{d}_\theta$ is

$$\bar{d}_\theta = d_\theta - \frac{d_\theta\, r \sin\theta}{r \cos\theta - d_\theta}\, d\omega \qquad (17)$$

Equation (16) allows to evaluate the influence of rotational and orbital parameters on ground coordinates. As these parameters do not remain constant along the satellite flight path, we assume variational effects described by polynomials, for example

$$r_i = r_o + dr_i = r_o + a_o + a_1 T_i + a_2 T_i^2 + \ldots \qquad (18)$$

Least squares adjustments have been performed for 4 cases

- "104" ; 4 unknowns r, u, i, θ ; no variation along flight path
- "113" ; see "104", but variation along flight path by polynomials of 2nd order (r, u, i) and 3rd order (θ); makes 13 unknowns.
- "204" ; 4 unknowns R, $d\phi$, $d\omega$, $d\kappa$; no variation along flight path.
- "213" ; see "204", but variation along flight path by polynomials of 2nd order (R, $d\phi$, $d\kappa$) and 3rd order ($d\omega$) ; makes 13 unknowns.

Results are listed in table 3. Variation of unknowns along the flight path improve the results considerably (46 %)*. For 104/204 and 113/213 the mean square errors of the residuals do not differ much. Nevertheless better results are obtained using ϕ, ω, κ as unknowns rather than u, i, θ, because the covariance functions** show neither trend nor correlation terms for model "213". For model "113" correlation between i and θ leads to slight correlation of the x-residuals in some images. This fact is illustrated by Fig. 4 and Fig. 5. ** see following paragraph * compared by $\sqrt{mx^2 + my^2}$

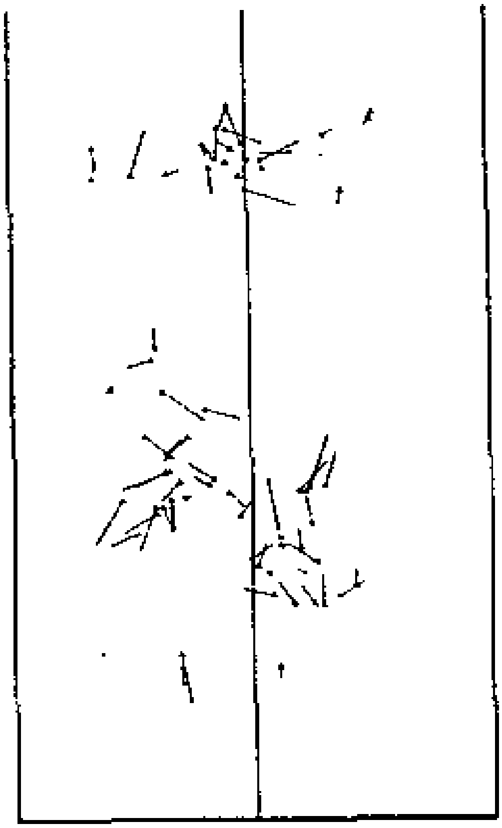

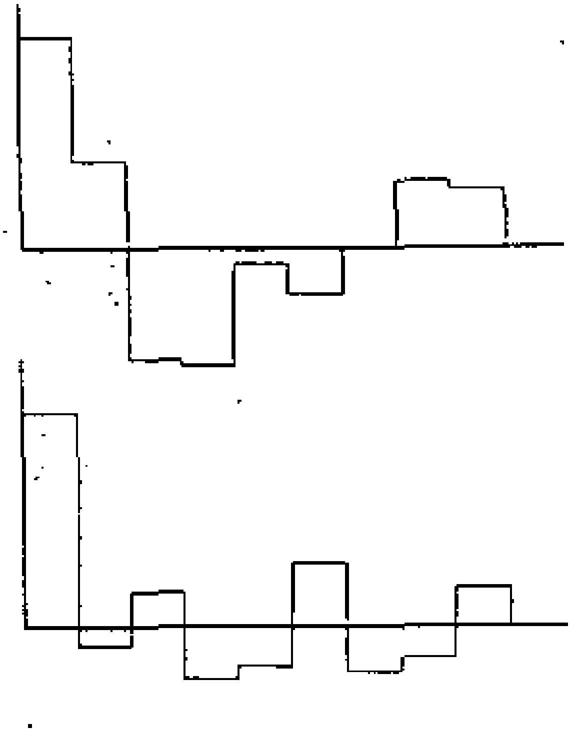

Fig. 4 : Image 1, model 113

⊢⊣ corresponds to 1 pixel error

Covariance functions for x (above) and y (below) at 5mm steps

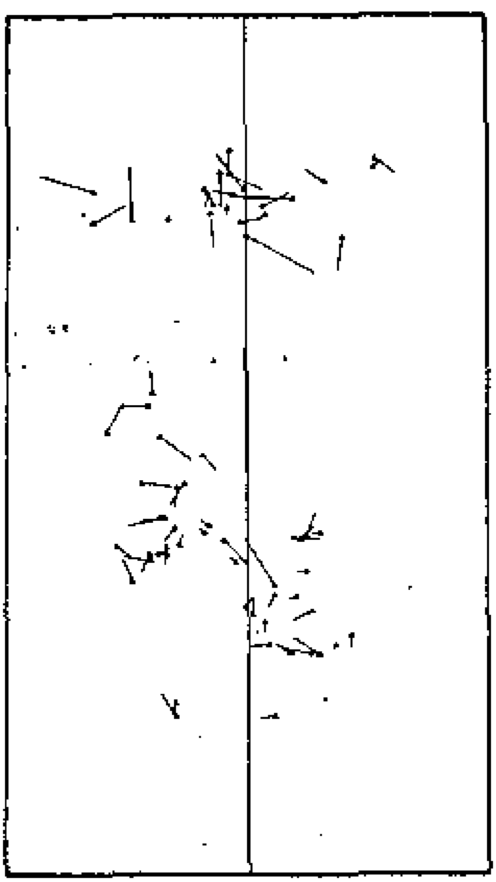

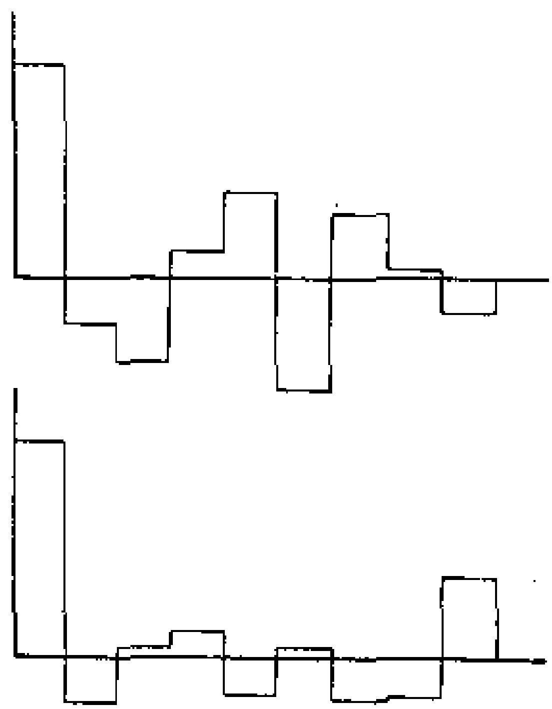

Fig. 5 : Image 1, model 213

⊢⊣ corresponds to 1 pixel error

Covariance functions for x (above) and y (below) at 5mm steps

In conclusion we may state, that model "213" (collinearity equations; unknowns R, φ, ω, κ; variation along flight path) is best suited as it is describing the geometrical conditions down to 0.85 pixel. No more unknowns should be introduced in order to limit the number of ground control points.

6. Interpolation Methods

If it is not possible to determine an analytical geometrical model a priori it is necessary to use interpolation methods. Interpolation parameters do not necessarily correspond to geometrical parameters like scale or rotational effects. They are mostly applied for post - processing geometrical approaches, if the geometrical model was imperfect, which led to correlated residual errors.

After application of model "213" no further post - processing is necessary (see paragraph 5). "Classical" case for interpolation however is LANDSAT bulk imagery (see BAHR, SCHUHR (1), (2), BERNHARDSEN (4), EROUCHIE, FORREST (6), SCHOONMAKER (9), WONG (10)).
For interpolation, both polynomials

$$x' = a_0 + a_1x + a_2y + a_3xy + a_4x^2 + a_5y^2 + \dots$$
$$y' = b_0 + b_1x + b_2y + b_3xy + b_4x^2 + b_5y^2 + \dots \qquad (19)$$

(see references(1), (2), (3), (4), (6), (9), (10))
and least - squares interpolation

$$\tilde{l}_i = c_i^T (C_{ss} + Q_{rr})^{-1} \qquad (20)$$

((2), (3))

have been suggested. To supply significant ground truth, 234 ground control points have been selected for evaluating a LANDSAT - 1 image ("Bavaria", see table 1). The processing goes towards least squares interpolation, where the trend function is eliminated by polynomials first. Thus, 3 approaches have been executed

I) 4 - parameter - fit ("Helmert - Transformation"), which does not affect the relative geometrical neighbourhood of image points. Residuals correspond to the "accuracy" of the bulk image.

II) 2nd order polynomial (equation (19))

III) Least squares interpolation by prediction plus filtering after I or II, using empirical covariance functions Mean $\{l_i\, l_k\}$, described by continuous Gaussian functions $C_{i,k} = F\, V\, e^{-K^2 s^2}$ (F = filtering factor, see (2))

Table 4 lists the results.

The residuals from the original bulk image show large trend influence on both x and y direction (Fig. 6 and 7) It is most important to realize, that simple 2nd order polynomials may describe this behavior very well. They eliminate the trend function completely (Fig. 8) and reduce the residuals down to ± 0.54/0.83 pixel. Least squares filtering afterwards does not improve the result significantly. Best result is shown in Fig. 9 .

In conclusion we suggest 2nd order polynomials with about 15 ground control points to process LANDSAT - 1 bulk imagery for operational purposes. However, since we suppose similar geometrical behavior of bulk imagery in general (see (2), (6)), correction terms of 2nd order polynomials could be applied without any difficulty a priori to all images. Thus we got residuals in the order of magnitude corresponding to results obtained by a rigorous approach like model "213".

Approach	Number of points used for adjustments	mx ± meters (pixel)	my ± meters (pixel)
4-parameter fit	234	214 (2.71)	244 (4.52)
2nd-order polynomial	7	91 (1.15)	60 (1.11)
– " –	9	54 (0.68)	62 (1.15)
– " –	13	47 (0.60)	55 (1.02)
– " –	40	48 (0.61)	48 (0.89)
– " –	234	43 (0.54)	45 (0.83)
Least squares filtering after 4-parameter fit; P = 0,8	13	52 (0.66)	62 (1.15)
Least squares filtering after 4-parameter fit; P = 0,9	40	44 (0.56)	47 (0.87)
Least squares filtering after 2nd order polynomial (234 points)	40	42 (0.53)	42 (0.78)

Table 4 : Interpolation procedures applied to a LANDSAT - 1 image (1 resolution element = 79*56 m^2)

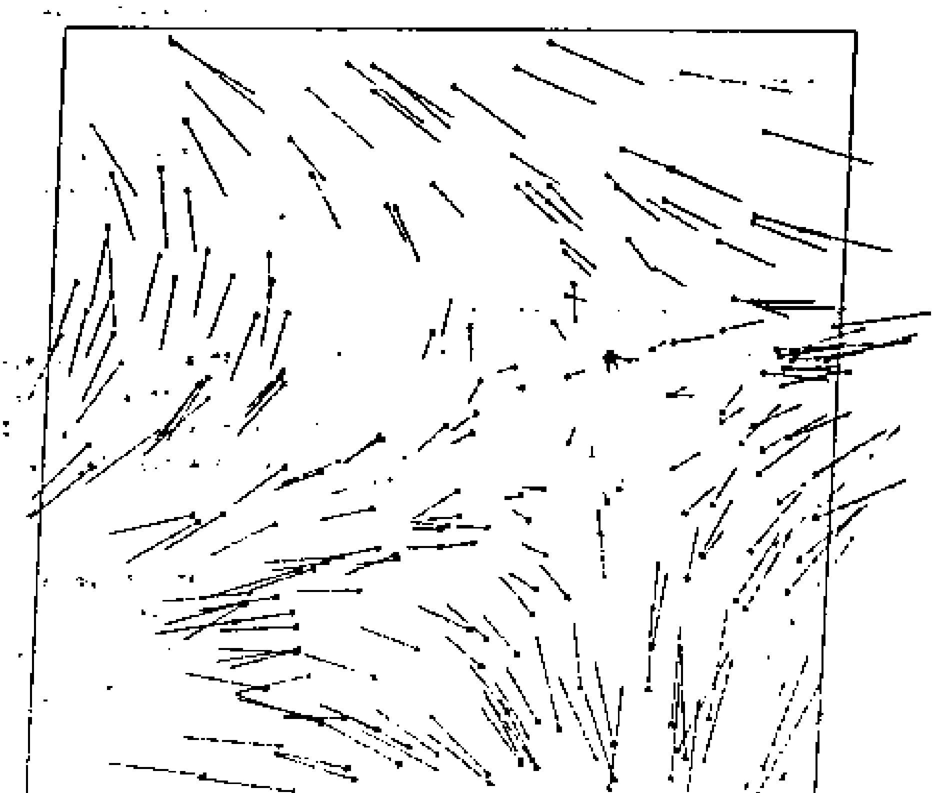

Fig. 6 : Residuals after 4-parameter fit

⟼ corresponds to 300m error

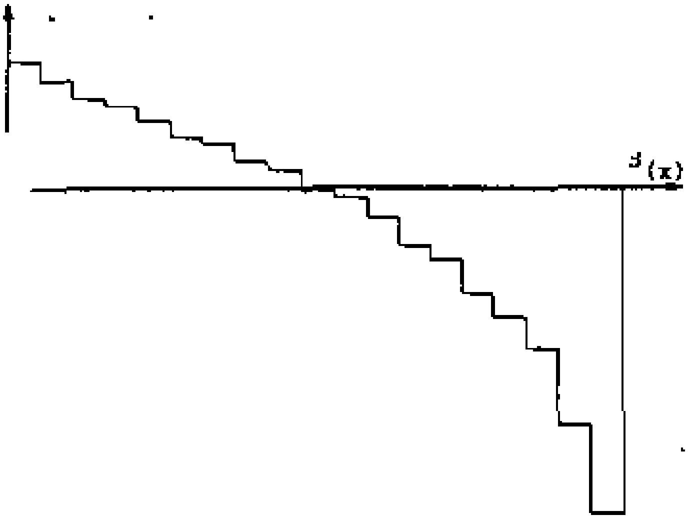

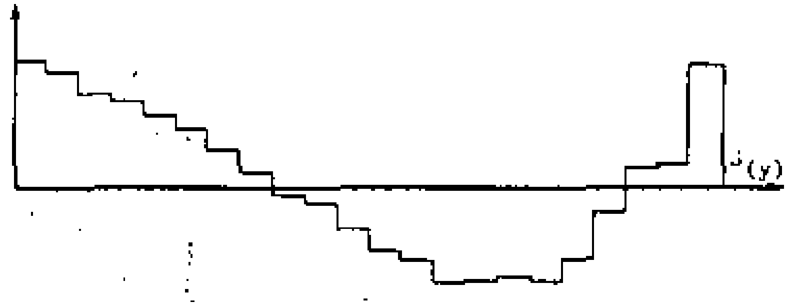

Fig. 7: Covariance functions after 4-parameter fit

(1 step corresponds to 1cm in 1/1Mill. image)

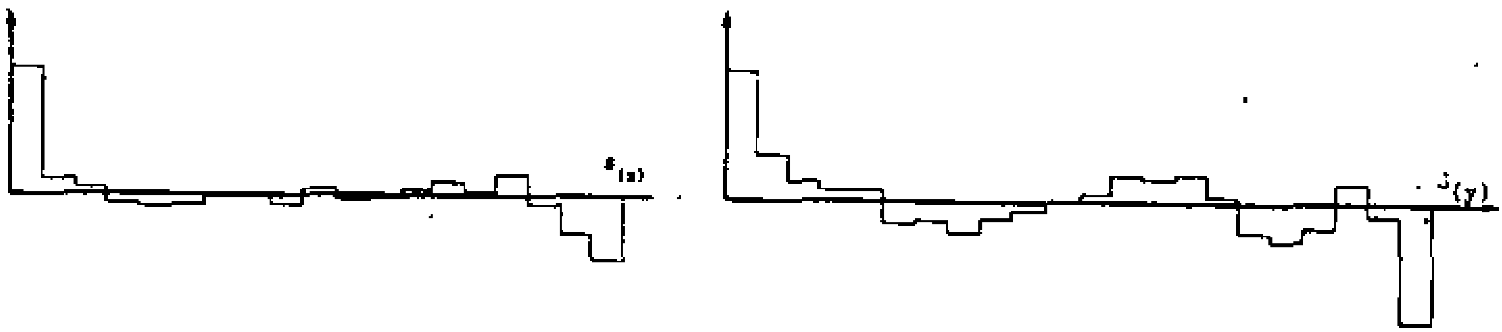

j. 8 : Covariance functions after interpolation by polynomial(234 points)

(1 step corresponds to 1cm in 1/1Mill. image)

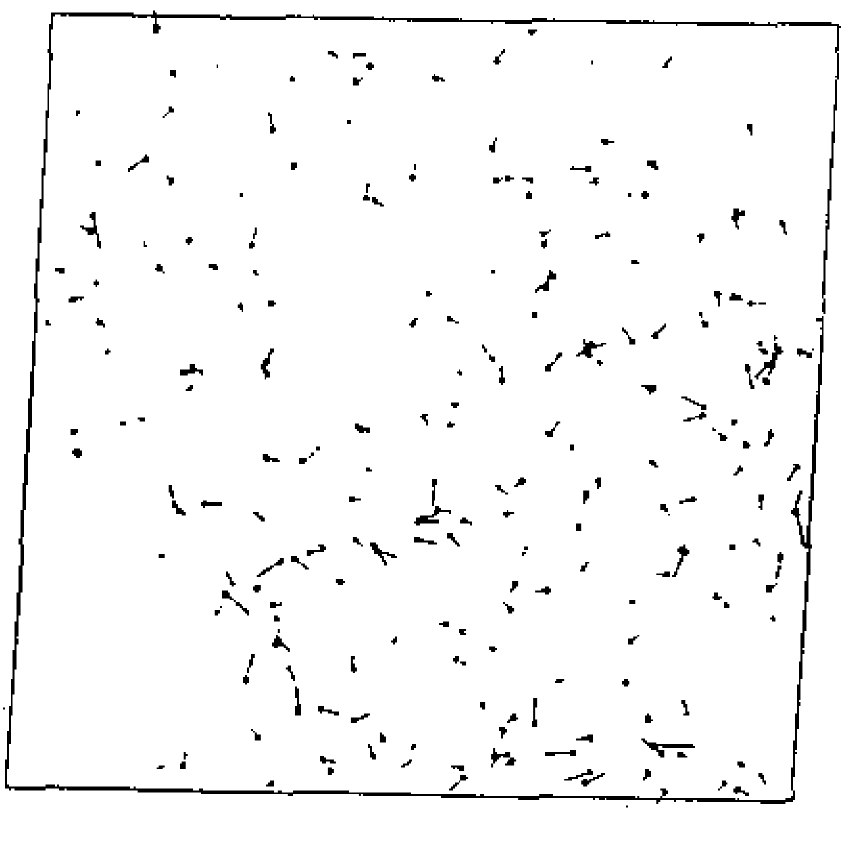

Fig. 9 : Residuals after least-squares filtering

⊢—⊣ corresponds to 300m error

References

(1) BÄHR, H. P. ; SCHUHR, W.: Versuche zur Ermittlung der geometrischen Genauigkeit von ERTS - Multispektral - Bildern
Bildmessung und Luftbildwesen
1/1974

(2) BÄHR, H. P. : Interpolation and Filtering of ERTS - Imagery
ISP, Comm. III Symposium,
Stuttgart 1974

(3) BÄHR, H. P. : Analyse der Geometrie auf Photodetektoren abgetasteter Aufnahmen von Erderkundungssatelliten.
Wiss. Arbeiten Lehrst. Geod., Phot. Kart.
TU Hannover, to be published 1976

(4) BERNHARDSEN, T. : Undersøkelse av den geometriske nøyaktighet i ERTS - bilder
Institutt for landmåling Norges landbrukshøgskole, 1975

(5) BROUWER, D. ; CLEMENCE, G. M. : Methods of Celestial Mechanics
Academic Press, New York and London

(6) DEROUCHIE, W. F. and FORREST, R. B. : Potential Positioning Accuracy of ERTS - 1 MSS Images
ASP Spring Convention 1974
St. Louis

(7) KONECNY, G. : Geometrical Aspects of Remote Sensing
ISP Comm. IV,
Ottawa 1972

(8) KRÁTKY, V. : Cartographic Accuracy of ERTS
Photogrammetric Engineering 1974

(9) SCHOONMAKER, J. W. jr. : Geometric Evaluation of MSS Images from ERTS - 1
ASP Spring Convention 1974
St. Louis

(10) WONG, K. W. : Geometric and Cartographic Accuracy of ERTS - 1 Imagery
Photogrammetric Engineering 1975

Proceedings of the International Symposium on Image Processing, Interactions with Photogrammetry and Remote Sensing, Graz, 3-5 October 1977, pp. 19-25

DIGITAL IMAGE PROCESSING EXPERIENCE AT HANNOVER INSTITUTE FOR PHOTOGRAMMETRY (IPI)

H. P. Bähr

Institut für Photogrammetrie und Ingenieurvermessung (IPI), Technical University, D-3 Hannover, F.R.G.

ABSTRACT

An image processing system configuration (CDC-Cyber 73/76, Optronics Mark 1700, Modular Software Package) is available at IPI-Hannover. The paper concentrates on the Software Package and applications to images from (a) a metric camera; (b) Hasselblad camera; (c) Bendix M²S Scanner; (d) LANDSAT. Emphasis is on geometric processing (Editor).

1. GENERAL BACKGROUND

Photogrammetrists have a long tradition in conventional image processing. *Digital* image processing however principally requires, in addition to conventional instrumentation like stereoplotters, digital imagery and digital computers. The Institut für Photogrammetrie und Ingenieurvermessung (IPI) at the Technische Universität Hannover started digital image processing, initiated by Professor Konecny, in the year of 1971. The first computer compatible tapes containing digital image information were data from the NIMBUS-3 satellite. At that time, basic software was developed mainly for suitable image display.

Digital image processing has to be preceded by image analysis. Consequently, practically oriented procedures have to be accompanied by scientific investigations for theoretical model formation. These aspects are covered by basic IPI publications (like Konecny, 1972, 1976, Bähr 1976a, 1976 b, Schuhr, 1976, Dowideit 1976, 1977, Clerici 1977).

This paper reports briefly on some investigations done in image enhancement and geometric image processing techniques at the IPI. Work executed in the field of digital classification is described separately (Donnert-Möller, 1977).

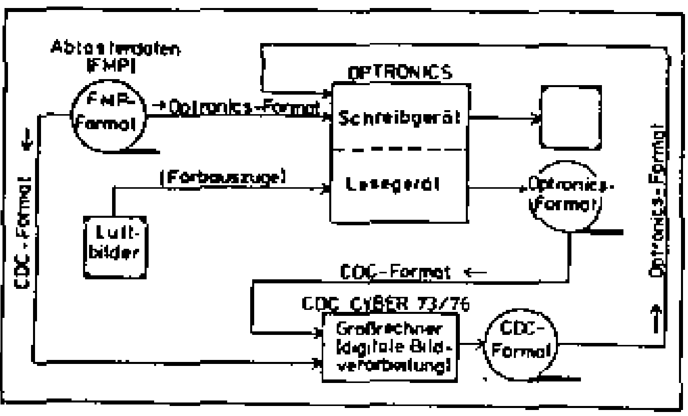

Figure 1. Principal data flow for digital image processing at the IPI .

The IPI hardware background, like it is mainly applied, can be described very simply (see Fig. 1). It consists of a large CDC CYBER 73/76 computer and an OPTRONICS-P 1700 digital read/write image plotter. As an input to the OPTRONICS, both tapes (as LANDSAT and M²S) and conventional imagery (i.e. frame camera photography, SONAR and RADAR digital) are possible. Digital image processing essentially is executed within the computer. The data flow generates specific problems caused by the variety of different data formats: LANDSAT format, M²S format, OPTRONICS format, CDC format. These problems had to be solved first.

2. SOFTWARE SYSTEM AND IMAGE ENHANCEMENT TECHNIQUES

The software philosophy is displayed exemplarly by Fig.2 The programs are modular and user-oriented: just one punch card allows the application of a module. Module "READ" (Number 42) for instance reads tape number 1, which is written in M²S -format, and converts it into CDC-format tape number 2. Number of scans and pixels have only to be mentioned on the first card. The second card calls module 3, which stretches the data into x-direction by the factor 1.392 . A linear histrogram is obtained simply by calling module number 5 without additional information. Even more complicated procedures, like application of earth rotation (module number 43), do need only a few additional parameters.

	Modul Number	Input Tape Number	Output Tape Number			Number Scan Lines	Number Pixel per line		
READ (FMP-format)	42	1	2	0	0	[illegible]	[illegible]	0	0
STRETCH X (Factor 1.392)	3	2	3	0	0	[illegible]	[illegible]	1.392	1.
LINEAR HISTOGRAM	5	3	4	0	0	[illegible]	[illegible]	0	0
REDUCTION	22	4	7	[illegible]	1	[illegible]	[illegible]	0	0
EARTH ROTATION	43	7	8	0	0	[illegible]	[illegible]	[illegible]	[illegible]
WRITE (OPTRONICS format)	7	8	(99)	0	0	[illegible]	[illegible]	0	0

Figure 2: The Hannover Modular software package. Example for LANDSAT data processing (see Fig.3 and 4)

ters. Finally, output generally is in OPTRONICS format, in order to make visible what has happened to the data.

Original data and result obtained by the procedures described above, is shown in Fig. 3 and 4. The modules have been applied to a LANDSAT scene from Northern Germany. In the final result the Jade estuary, an area which the IPI is very much interested in, can be investigated very clearly Cost of the whole procedure is about $ 150.

Simple digital enhancement techniques may be executed within the 8 K - OPTRONICS computer itself. More sophisticated procedures can be applied by the modular software package in the CDC computer. This approach is illustrated exemplarly by Fig. 5 and 6[+], showing the west end of Wangerooge, one of the East Frisian Isles near the Jade estuary. The original data does not offer much information to the human eye. Edge and line enhancement, after correction of panoramic distortion, however leads to an output, which resembles a line map. Anthropic features now dominate (see the dams and roads), a first step towards digital pattern recognition.

[+] Imagery recorded by Kolouch (1977).

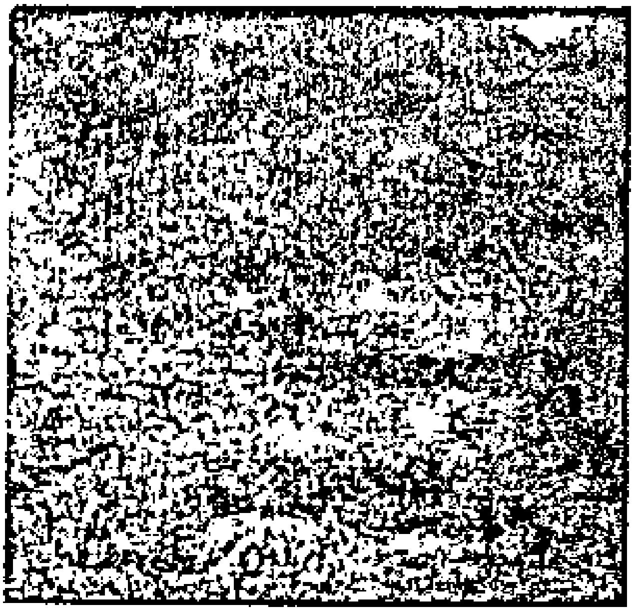

Figure 3. LANDSAT, 10.8.1975, channel 7.Original data

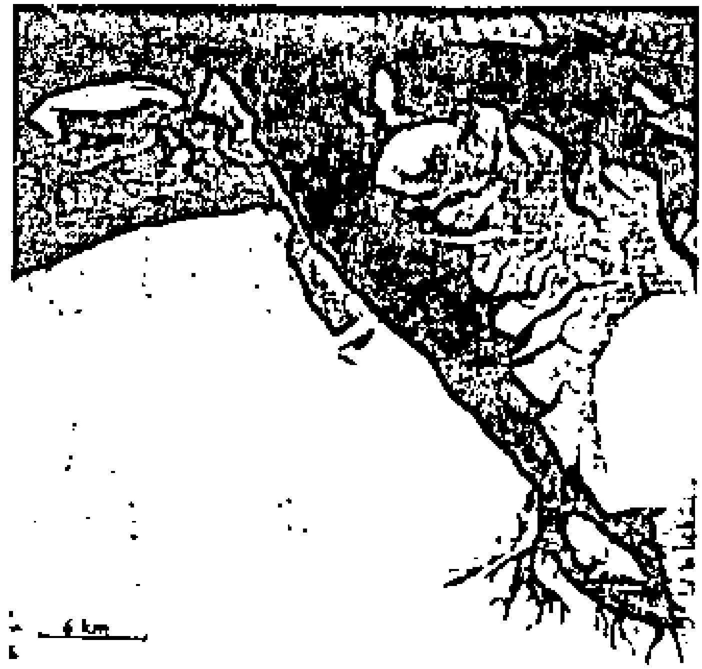

Figure 4. LANDSAT, 10.8.1975, channel 7 (section), Correction for earth rotation, Contrast enhancement for water/land

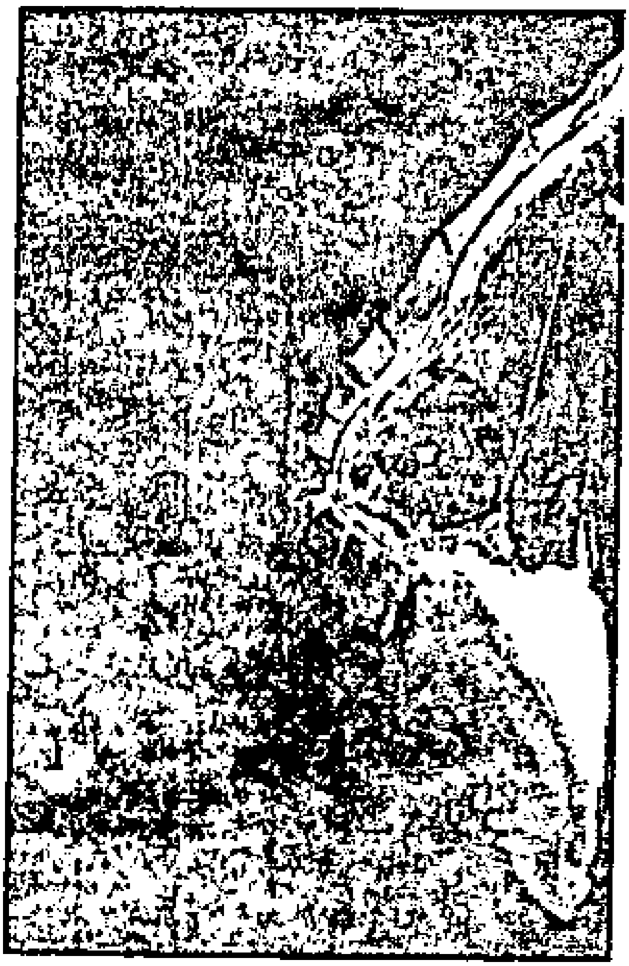

Figure 5. West-end Isle of Wangerooge Original scanner data (near IR)

Figure 6. Geometric correction for panoramic distortion. Edge and line enhancement.

Image enhancement techniques as the presented ones can be categorized as the simplest digital image processing methods. However, their results are most useful, particularly if one analyses the cost/benefit ratio.

3. GEOMETRICAL IMAGE PROCESSING

Geometrical image processing represents a much more complex field. Because of high costs, it is important to take into account the purpose of the geometrical processing thoroughly and to find an adequate procedure.

These methods also depend very much on the image data itself. Therefore different image types are going to be compared here geometrically: a conventional Photogrammetric Camera Image, a Hasselblad photo, a Bendix M^2S Airborne Scanner strip and a LANDSAT scene (see Table 1). They all cover again the Jade estuary area. The size of a resolution element on the ground is about 80 m for LANDSAT, 9 m for M^2S, 2,5 m for Hasselblad and 1/2 m for the Photogrammetric Camera image. The resolution element size is more important than image scale factor, because ±1/3 of an element defines the theoretical threshold of geometrical image processing accuracy.

The geometrical accuracy of the imagery will be tested by similarity transformations, so-called Helmert-transformations (see Fig. 7). This analytical procedure does not affect the internal geometric conditions. It simulates the important case, that the user puts the image into an enlarger and projects it into a map by rotation, translation and scale manipulation. The residual vectors provide useful illustration of the geometric conditions in the image. The mean square error, computed from the residuals, defines the geometrical image accuracy.

Analog imagery, as conventional photography, should be processed geometrically in an analog way if possible. Fig.8 shows an example for conventional restitution and mosaicking of the photogrammetric camera image. The geometric accuracy of the mosaic is about ± 5 m in x direction and ± 6m in y direction++), a good result.

Table 1: Parameters of compared imagery

Reihenmeßkammer	M^2 S -Abtaster
h = 3000 m M = 20.000 A = 0,5 m	h = 3500 m M = 300.000 A = 9 m
Hasselbladkamera	**Landsat**
h = 3000 m M = 150.000 A = 2,5 m	h = 935 km M = 1000.000 A = 80 m

h = Flying height;
M = Original scale factor
A = Resolution element on the ground.

The Hasselblad image is a 35 mm super wide angle photograph with typical radial distortions. Many applications in oceanography need small scale imagery which often can not be obtained by normal angle photography. However, geometrical distortions of fisheye objectives lead to severe problems. The geometrical accuracy of the image computed from residuals after Helmerttransformation is ± 329 m in x and ± 466 m in y direction. The distortions can not be corrected by analog methods. A digital approach is necessary, but it has to be asked critically, whether the results will justify the costs at all.

If the original data is digital, like for the M^2S image strip (see Fig. 9), application of digital image processing is obvious. Geometric processing can be done in two steps: first one should remove the largest systematic errors. These are panoramic distortion, caused by the scanning principle, and affinity, caused by overscan. These corrections can be applied very simply, because no ground control is necessary and the procedures work either in scan direction or in flight direction. The residuals on Fig.10 give an idea of the accuracy of both the original M^2S strip and the strip after panoramic and affine correction. We get an improvement from ± 447 m to ± 106 m root mean square error in x and from ± 940 m to ± 144 m in y. The improved values correspond to about 12 to 15 pixel elements. For some applications, especially in oceanography, this result perhaps might be good enough. Mostly one needs better geometric performance, so that more sophisticated methods have to be applied in a second step.

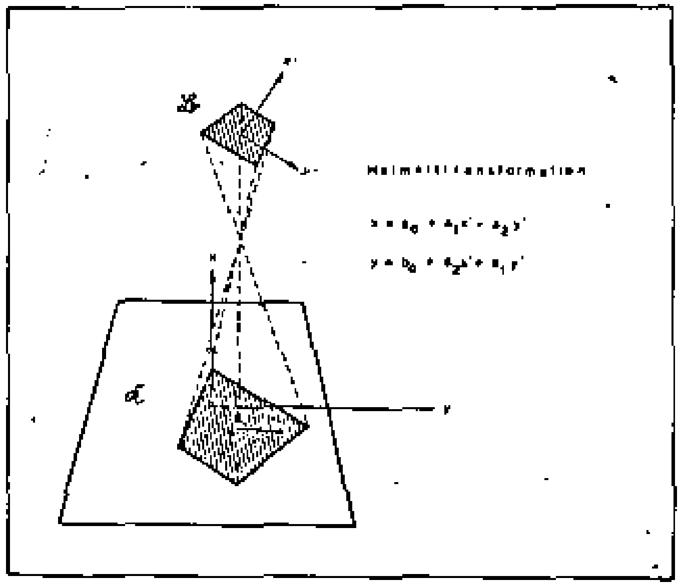

Figure 7. Principle of Helmerttransformation

The second step incorporates ground control points and collinearity functions. Hence it is the classical approach of analytical photogrammetry. The work executed by Schuhr (1977) shows that these procedures applied to airborne scanner data give ± 2 to ± 4 pixel accuracy, confirmed by latest results from Freiburg area. The high geometric quality has to be paid for: the computing costs are about $ 1800 for a 1 100 x 2 000 pixel scene. An adequate area with removal of panoramic and affine distortion would only cost $ 100.

The investigated LANDSAT image is the scene displayed in Figure 4, corrected for earth rotation by module number 43. We obtain excellent geometric accuracy, which is about ± 45 m root mean square error in both directions. This is nearly half pixel size which approaches the theoretical threshold of ± 1/3 pixel size. This result is explained by the fact, that the area covers only 1/20 of a full scene. For larger areas more rigorous photogrammetric solutions have to be applied after removal of earth rotation effects.

The adequate example in Fig. 11 shows again a recording computed by Schuhr (1977), investigation executed for the German government to figure out the suitability of LANDSAT data for land use mapping. It contains an area of the Rhine valley near Mannheim which covers about a quarter of a LANDSAT scene. Here, collinearity equations and ground control points are used for correction. The result with UTM grid overlay, has an accuracy of about ± 100 m root mean square error. Processing costs are $ 1 800. For this particular application, geometric quality has to be as high as possible, because of geodetic map references. In this respect c h a n g e d e t e c t i o n requires the same high standard, unless it is not approached by correlation methods.

++) x is the in-flight direction

Figure 8: Mosaic from photogrammetric camera imagery after geometric camera imagery ofter geometric restitution at ZEISS-SEG V. Original data true colour photography.

(a)

(b)

(c)

Figure 9: M^2S strip Jade channel (a) Original data; (b) Corrected for panoramic distortion; (c) Corrected for panoramic distortion and affinity; (a) Green/yellow band; (b + c) Near infrared band.

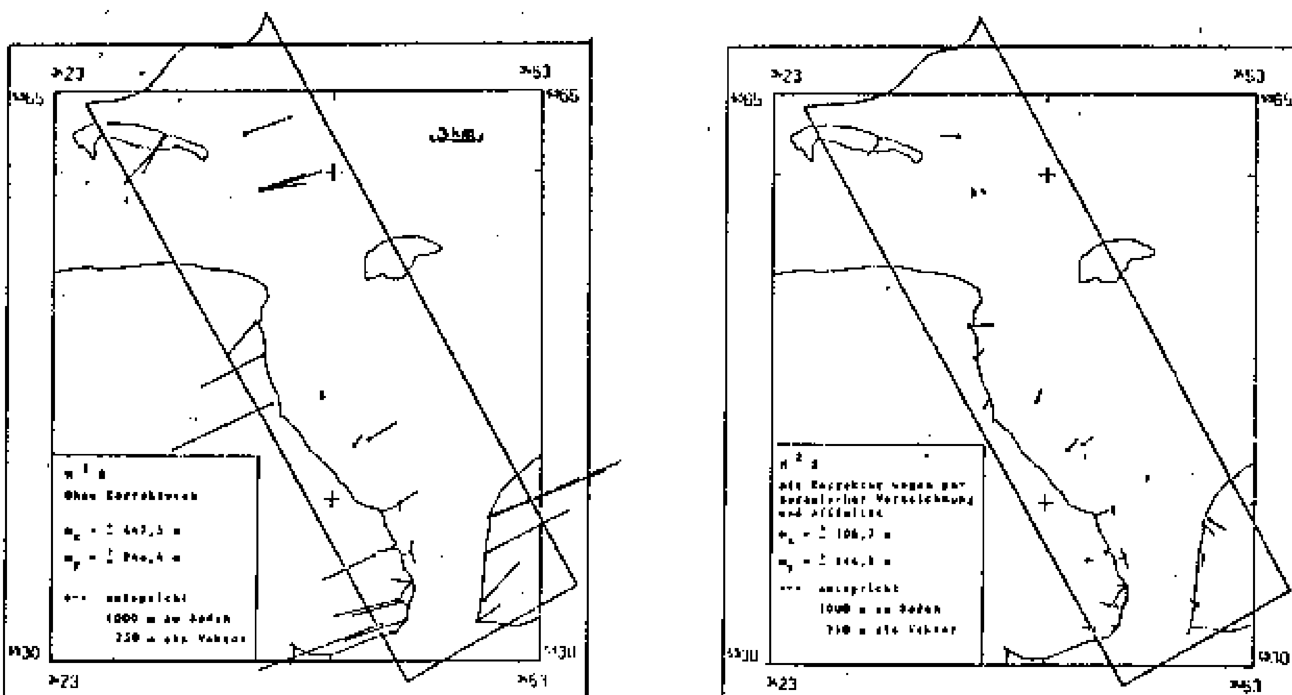

Figure 10: Residuals after Helmert-transformation in original M^2S strip (left, see Fig. 9 a) and corrected M^2S strip (right, see Fig. 9 c). Vectors 4 x exaggerated.

Figure 11: LANDSAT (Rhine/Neckar) 9.8.1976 (section). Geometric correction by rigorous methods. Scale of corrected image 1:1 060 000.

4. EXAMPLES FOR APPLICATION

Although IPI activities are very much methodically oriented, intensive links to practical use is permanently maintained. Consequently, IPI is involved in two big aircraft programs, sponsored by governmental agencies: the Sonderforschungsbereich 149 of the Deutsche Forschungsgemeinschaft and the Flugzeugmeßprogramm of the Bundesministerium für Forschung und Technologie. Many IPI publications report specifically on these programs (SFB 1976 a,b,c Bähr, 1977; Dennert-Möller, 1977, Kolouch,1977; Konecny, 1977; Lohmann,1977; Schuhr,1977). Here only a brief introduction to the main problems focused in the Jade estuary test area and three applications will be given for illustration.

For many reasons the Jade estuary offers for an ideal test area. Here we find intimate interaction between water and land. From here result problems of tidal current, sediment transportation and water exchange between the Jade bay and the Jade channel. These natural phenomena are superimposed by anthropogical activities, like dredgeing, construction of large bridges, oil harbour operation and industrialisation on artificial polders. This is accompanied by many, non-predictable consequences. The Jade area therefore represents one of our today's ecological problems.

One of the most promising techniques to detect water pollution is investigation of thermal band imagery. Lohmann is involved in finding mathematical models for transformation of thermal scanner data into surface temperatures. The principle of least square adjustment is applied, which leads to an accuracy of ± 0,2 ° Celsius root mean square error. Geometrically corrected image data is necessary to link groundand scanner information properly.

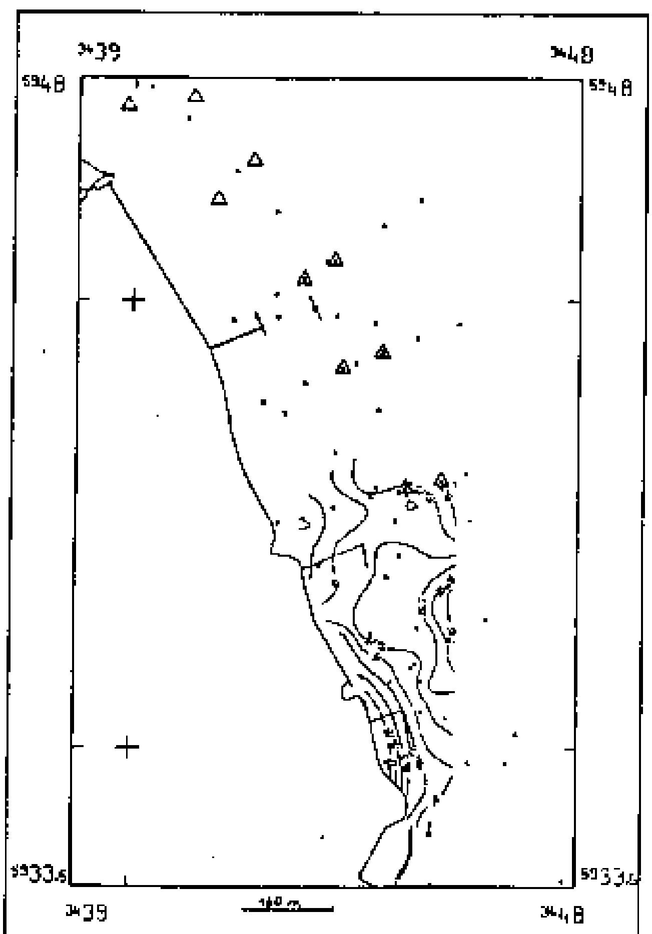

Figure 12: Surface water temperatures display by isothermal lines. In situ control at x.

Fig. 12 contains a map, where the water surface temperatures are displayed in the form of isothermal lines. Another very important practical application is monitoring sediment transport. The waterway administration spends millions of mark yearly to keep the Jade channel free of sand. The waterflow conditions are rather complex, and nobody knows exactly in which manner the sediment deposits move. Fig. 13 shows a 5 th-channel LANDSAT scene from that problematic area. Special non-linear contrast manipulation make the sands clearly come out. Most spectacular is the fact, that even underwater banks can be detected. This is proved by comparison with map information, which points out penetration down to about 15 m under water surface. The navigable water of the Jade channel can very well be distinguished. Even the well-known most problematic parts like the waterway band north of Minsener Oog island get an

Figure 13: LANDSAT, 18.8.1975, Channel 5 (section) Enhancement for underwater sediments.

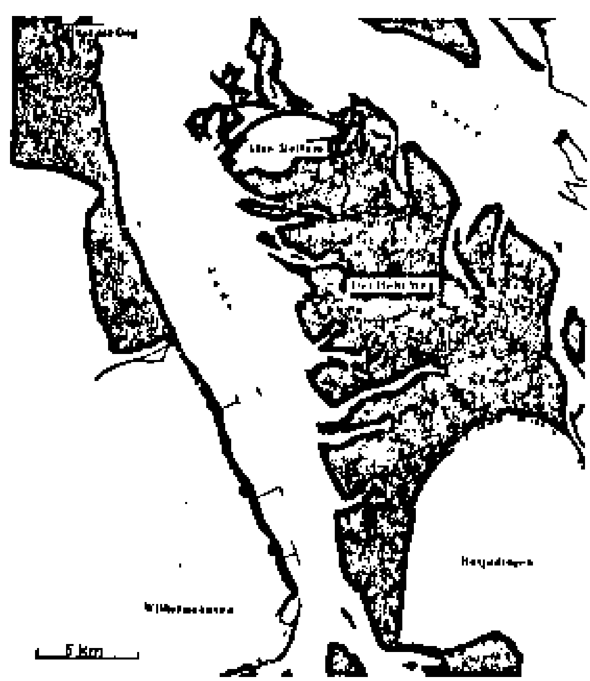

Figure 14: Water line differences (black) between German Nautical Chart No.7 and LANDSAT scene 18.8.1975,Channel 7.

explanation by this integral display. However, underwater Jade sands do not come out clearly on aircraft scanner imagery. This depends on the larger scale factor where local water body pattern modulate the regional underwater sand information signal. By the way, the 3 bridges, the Wilhelmshaven oil pier, can be detected on Fig.13, though they are much below the resolution power of the LANDSAT scanner. This phenomen occurs because of high contrast between water and buildings.

Another application is very much connected with the previous example: The map in Fig. 14 has been drawn after projection of the LANDSAT scene in Fig. 4 onto the German Nautic Chart No.7, scale 1:50 000. The exact scale is known from Helmerttransformation. The map displays the differences between the sea chart waterline and the waterline from the LANDSAT scene in Fig. 4. The real difference between the two water levels is 15 cm, pointed out by in situ water marks. In most areas both lines are identical. Differences between chart and satellite image have been displayed in black areas. The largest differences can be detected north of Alte Mellum island. Here, no actual topographic data is available. Although satellite image and nautical chart date from the same year of 1975, the satellite image is more up to date.

REFERENCES

Wiss.A.: Wissenschaftliche Arbeiten der Lehrstühle für Geodäsie, Photogrammetrie und Kartographie an der Technischen Universität, Hannover.

ISP 1972: Internationale Gesellschaft für Photogrammetrie: Commission III, Congress Ottawa 1972 and
ISP 1976: Helsinki 1976.

FMP: Symposium Flugzeugmeßprogramm Hannover, 28 - 30 August 1977.

Bähr H.P. (1976): Geometrical Models for Satellite Scanner Imagery. ISP 1976.

Bähr H.P. (1976): Analyse der Geometrie auf Photodetektoren abgetastater Aufnahmen von Erderkundungssatelliten. Wiss.A. Nr. 71.

Bähr H.P. (1977): Vom Satellitenbild zur Reihenmeßkamer-Aufnahme: Das Jadegebiet im Vergleich unterschiedlicher Sensoren. FMP.

Clerici E. (1977): Über die Anwendbarkeit von Side Scan Sonar zur Erstellung von topographischen Karten des Meeresbodens. Wiss.A. Nr. 74.

Dennert-Möller E. (1977 a): Multispektrale Klassifizierung von Wattgebieten. FMP.

Dennert-Möller E. (1977 b): Multispectrale Classification of Tidal Lands. Symposium "Image Processing", Graz. 3 -5 Oct.

Dowideit G. (1976): A Block-Adjustment for SLAR Imagery. ISP.

Dowideit G. (1977): Eine Blockausgleichung für Abbildung des seitwärtsschauenden Radars (SLAR). Wiss.A. Nr.75.

Lohmann P. (1977): Auswertungen von Thermalaufnahmen des Jadegebietes.

Kolouch D. (1977): Strömungsuntersuchungen mit Hilfe von multispektralen Scanner-Aufnahmen im Küstengebiet. FMP.

Konecny G. (1972): Geometric Aspects of Remote Sensing. ISP.

Konecny G. (1976): Mathematical Models and Procedures for the Geometric Restitution of Remote Sensing Imagery. ISP.

Konecny G. (1977): Zum gegenwärtigen Stand der Fernerkundung. FMP.

Schuhr W. (1976): Digital Rectification of Multispectral Imagery. ISP.

Schuhr W. (1977): Geometrische Entzerrung multispektraler Abtastaufnahmen. FMP.

SFB 149 (1976 a): Vermessungs- und Fernerkundungsverfahren an Küsten und Meeren. Jahresbericht 1974. Wiss.A. Nr.68.

SFB 149 (1976 b): Vermessungs- und Fernerkundungsverfahren an Küsten und Meeren. Jahresbericht 1975. Wiss.A. Nr. 69.

SFB 149 (1976 c): Vermessungs- und Fernerkundungsverfahren an Küsten und Meeren. Jahresbericht 1976. Wiss.A. Nr. 70.

International Society of Photogrammetry
Commission III Symposium
Stuttgart, September 2nd to 6th, 1974

Presented Paper

Interpolation and Filtering of ERTS-Imagery

by H.P. Bähr, Hannover, Germany
Technische Universität
Institut für Photogrammetrie und Ingenieurvermessungen

Zusammenfassung

Filterung und Interpolation nach kleinsten Quadraten werden auf ein ERTS-Bild in Kanal 5 und 7 angewandt. Die Kovarianzfunktionen errechnen sich aus den Restklaffungen nach einer Helmerttransformation. Trotz der wenigen und ungünstig gelegenen Stützpunkte erhält man gute Resultate. Diese werden mit den Ergebnissen aus einer Interpolation mit Polynomen 2. Ordnung verglichen.

Abstract

Least-squares filtering and interpolation is applied to an ERTS frame in channel 5 and 7. Covariance functions are determined from residual errors of a 4-parameter fit. Though there is only a small number of reference points, results come out well. Results from least-squares interpolation are compared with residual errors from second-order polynomial interpolation.

1) Investigated Imagery

An ERTS-1 bulk photo from September 21st, 1972, showing parts of northern German lowlands was investigated (scale approx. 1 : 1.000.000). Though there is 40 % cloud cover, it is the most cloud-free photo available of this region.

Results by polynomial interpolation of this frame have been published (BÄHR/SCHUHR in /1/). Continuing these works, independent measurements have been carried out in channel 7 (o.8 ... 1.1 m) at 41 new points, which again are all related to water bodies. Additional observations were made at 20 points in channel 5 (o.6. ... 0.7 m) which nearly all are related to forest features. Interpretation of reference points was a sophisticated task, as they are of no symmetric shape; beside this, cloud cover in NE and SW and atmospheric haze prevent recording of more and better situated points. Image coordinates, measured at the Zeiss-PSK-Stereocomparator were related by a 4-parameter-fit ("Helmert-transformation") to terrain coordinates extracted from 1 : 50.000 scale maps.

Fig. 1 shows the result of this transformation for channel 7. All observations have been introduced as reference points. The root mean square errors, calculated from the residual errors, are

$$m_{x5} = \pm 109 \text{ m} \quad \text{(channel 5)}$$
$$m_{y5} = \pm 127 \text{ m} \quad \text{(channel 5)}$$
$$m_{x7} = \pm 131 \text{ m} \quad \text{(channel 7)}$$
$$m_{y7} = \pm 136 \text{ m} \quad \text{(channel 7)}$$

The vector diagrams show similar behavior of error distribution in both channels including the independent results from /1/. Finite regions indicate characteristical trends. Reasons for this may be effects from data processing, from atmospheric refraction or from inaccurate orientation data, i.e. parameters, which are identical for all channels at first-order approximation.

2) Determination of Covariance Function

The results in Fig. 1 indicate presence of both correlated(l_s, "systematic") and uncorrelated (l_r, "observational") error components. Summation of these components give the vectors shown in Fig. 1

$$l_i = (l_s + l_r)_i$$

By least-squares filtering both parts can be separated; by least-squares interpolation, both parts can be predicted at any point, if suitable reference points are available.

To prepare filtering and interpolation, a covariance function is to be determined from residuals after the 4-parameter adjustment, where all 41 points were introduced as reference points (Fig.1). This is the most appropriate way to find out the stochastic conditions of the ERTS-frame. After the covariance function is determined that way, it is used for all further calculations. Empirical determination of covariance functions interval by interval leads to discontinuous functions. They must be approximated by a continuous function.

In Fig. 2 covariance functions have been found independent for x and y in terms of 1,0 cm- and 2,0 cm-intervals. Size of the ERTS-frame was 18 by 18 cm. Fig. 2 shows that the extend of interval size may be of importance for the function which has to be determined, because of the small quantity of points. Though it is not absolutely necessary, a Gauß function often is used to describe the covariance conditions:

$$C\,\overline{(P_i\;P_k)} = C\,(0)\,e^{-k^2 s^2}$$

HereinC (0) and k^2 have to be determined. C (0), vertex of the curve, represents the v a r i a n c e of the l_s-components V_s. Theoretically, V_s is samller than the variance of the total error component V by the amount of V_r, variance of the l_r-components

$$\frac{1}{n} \sum_{i=1}^{n} (l_i\;l_i) = V = V_s + V_r$$

In Fig. 2 the amounts of V, which may be calculated from residuals after the 4-parameter adjustment, have been marked above the vertexes of the curves. The unit of the residuals is in kilometers. The k^2-parameter influences on the "bandwidth" of the curve and indicates up to which distance s correlation between error components may be found.

3) Results from Least-Squares Filtering and Interpolation

The covariance function includes the whole information of the error distribution. It allows to estimate the portion of l_s-compoments by following equations (see /3/:

$$l_{si} = c^t_i\; C^{-1}\; l$$

where

$$c_i = \begin{bmatrix} C\,\overline{(P_1\;P_i)} \\ \vdots \\ \\ C\,\overline{(P_n\;P_i)} \end{bmatrix}, \quad C = \begin{bmatrix} V & C\,\overline{(P_1\;P_2)} & \ldots & C\,\overline{(P_1\;P_n)} \\ & V & \ldots & C\,\overline{(P_2\;P_n)} \\ & & & \vdots \\ & & & V \end{bmatrix}$$

The $C\,\overline{(P_i\ P_k)}$ elements may be calculated from the covariance function. This function must be continuous. If we use the covariance values calculated for certain intervals, we get identical lines in the C matrix, i.e. singularity in case that 2 points lie within the same interval.

V is known a priori from the residual errors in Fig. 1. Though the values for $l_i\ l_i$ differ from point to point, the mean square value V has been introduced into C. Its amount is about 0,018 for both x and y. As the determination of the covariance function out of 41 points, which configuration is poor, remains uncertain, investiagations with different parameters have been carried out:

$$C\,\overline{(P_i\ P_k)} = F\,V\,e^{-k^2 s^2}\ , \qquad F\,V = C\,(0)$$

We call F the filtering coefficient. Regarding Fig. 2, we find $F_x \sim 0.5$ and $F_y \sim 0.7$. These numbers, empirically found, should give the best estimated values for l_s. If we use F = 1.0, we get larger l_s values: the whole l is interpreted as l_s-component and is filtered away. If F is smaller than the calculated values, we filter less than we should do. To improve the error distribution of the 4-parameter adjustment, we subtract the estimated l_s-components from the residual errors and get estimated random components l_{xr}, l_{yr}. Respectively, we have V_{xr}, V_{yr} and V_{xs}, V_{ys} for variances, which include values at the reference points.

In Fig. 3 variances calculated that way show, that the behavior of errors is a function of F. In particular, we see the effect from F = 1, where $V_{rx} = V_{ry} = 0$ and the effect from F = 0, where $V_{sx} = V_{sy} = 0$. We find that the accuracy is not very sensitive down to values of F = 0.5 and does hardly differ in x and y. It is for this reason, that all examples for filtering and interpolation published here have been calculated with F = o.75, both for x and for y. Beside this we read from Fig. 3, that V_r and V_s do not sum up to V as it should do theoretically. This will not happen, because the l_s-components have not been determined exactly, since the true variance - covariance-conditions remain unknown (see /4/).

Fig. 4 shows the result after filt[illegible] the residual errors from Fig. 1 with F = o.75. Fig. 5 gives the result from filtering and interpolation by 10 reference points for channel 7. The result shown in Fig. 5 is similar to Fig. 4, for there is not much change in error distribution if less than 41 reference points are introduced. However, this is not true for isolated points (see lower and upper left), which are hardly touched by the covariance function. For channel 5, we get the same variances V_r as in channel 7; this is because of accumulation of reference points. Error distribution after filtering is better in channel 7, where a larger number of points (41 versus 20) and a better configuration contributes to better stochastic conditions.

In the diagrams, orientation is towards grid north, corresponding to the reference meridian of the 3rd Gauss-Krüger-System. Consequently, the ERTS frames appear in oblique sense.

To give a rough idea of the improved results, see Table 1. Here, residual errors from 4-parameter fit and from least-squares interpolation have been listed. We get the M values in meter by taking the roots of corresponding V values and by multiplication with 10^3. Though they can not strictly be interpreted as root mean square errors, they indicate the magnitude of the residual errors.

Channel 1	Reference points 2	Interpolated points 3	M_x [m] 4	M_{xr} [m] 5	M_y [m] 6	M_{yr} [m] 7	P 8	k^2 9
7	41	-	131	50	136	45	0.75	0.05
	31	10	134	57	134	58	0.70	0.10
	10	31	138	79 71	145	88 77	0.75	0.10 0.01
	5	36	134	91	141	101	0.70	0.10
5	20	-	109	41	127	60	0.75	0.02
	9	11	134	80	122	88	0.70	0.02
	4	17	152	103	126	96	0.70	0.02

Table 1

First, M_x, M_y, i.e. residuals after 4-parameter adjustment, show the excellent quality of the ERTS image, which has a theoretical resolution of about 79 m per image point. The more reference points introduced, the Letter is the result, which lies about the value of theoretical resolution. An interesting detail is the influence of the k^2 parameter. For $k^2 = 0.01$ the M values go down a little bit compared with the value M from $k^2 = 0.1$. This is only because of the 2 isolated points at the left side of the frame. These points are improved if $k^2 = 0.01$, whereas they don't get corrections $k^2 = 0.1$.

4) <u>Interpolation by Polynomials</u>

Least-squares interpolation is just one method for interpolation. In /1/, polynomials have been sucessfully applied to evaluate ERTS imagery. Comparison of the results obtained by this two methods seems useful.

For interpolation, we take second-order polynomials:

$$x' = a_o + a_1 x + a_2 y + a_3 xy + a_4 x^2 + a_5 y^2$$
$$y' = b_o + b_1 x + b_2 y + b_3 xy + b_4 x^2 + b_5 y^2$$

with 6 unknowns for each coordinate. The result of the adjustment for channel 7 with 10 reference points is listed in Fig. 6. Comparison with results from the same point configuration after least squares interpolation in Fig. 7 show very good accordance. Differences can be observed at the 2 isolated points at the left side of the frame, where polynomials extrapolate, whereas least-squares interpolation does not transfer any information, if the covariance function is determined properly.

Table 2 lists the magnitudes of the residual errors after polynomial interpolation corresponding to Table 1 (r stands for "residual"):

Channel	Reference points	Interpolated points	M_x [m]	M_{xr} [m]	M_y [m]	M_{yr} [m]
7	10	31	138	59	145	87
5	9	11	134	59	122	77

Table 2

In conclusion we find, that both interpolation methods give roughly the same results. However polynomials are easier to process than least-squares interpolations. On the other hand, this method is more flexible and can be applied to a lot of further problems.

More sophisticated error analysis like KRAUS suggests in /4/ can not be carried out here because of small number and poor configuration of the reference points. Anyhow, the results obtained encourage to contimie work into this direction.

References

/1/ Bähr, H.P. and Schuhr, W.: Versuche zur Ermittlung der geometrischen Genauigkeit von ERTS-Multispektral-Bildern BuL 42, S. 22-24, 1974

/2/ Kraus, K.: Interpolation nach kleinsten Quadraten in der Photogrammetrie BuL 40, S. 4-12, 1972

/3/ Kraus, K. and Mikhail, E.M.: Linear Least-Squares Interpolation Photogrammetric Engineering 38, S. 1016-1029, 1972

/4/ Kraus, K.: Untersuchung zur Genauigkeit der Interpolation nach kleinsten Quadraten ZfV 1974, S. 198-205

Fig. 1

ERTS Channel 7

Residual errors after 4-parameter-fit.

Reference points shown by solid spots (41)

Variances of residual errors:
$V_x = 0{,}0171$
$V_y = 0{,}0185$

Scale:

10 km (situation)
100 m (vectors)

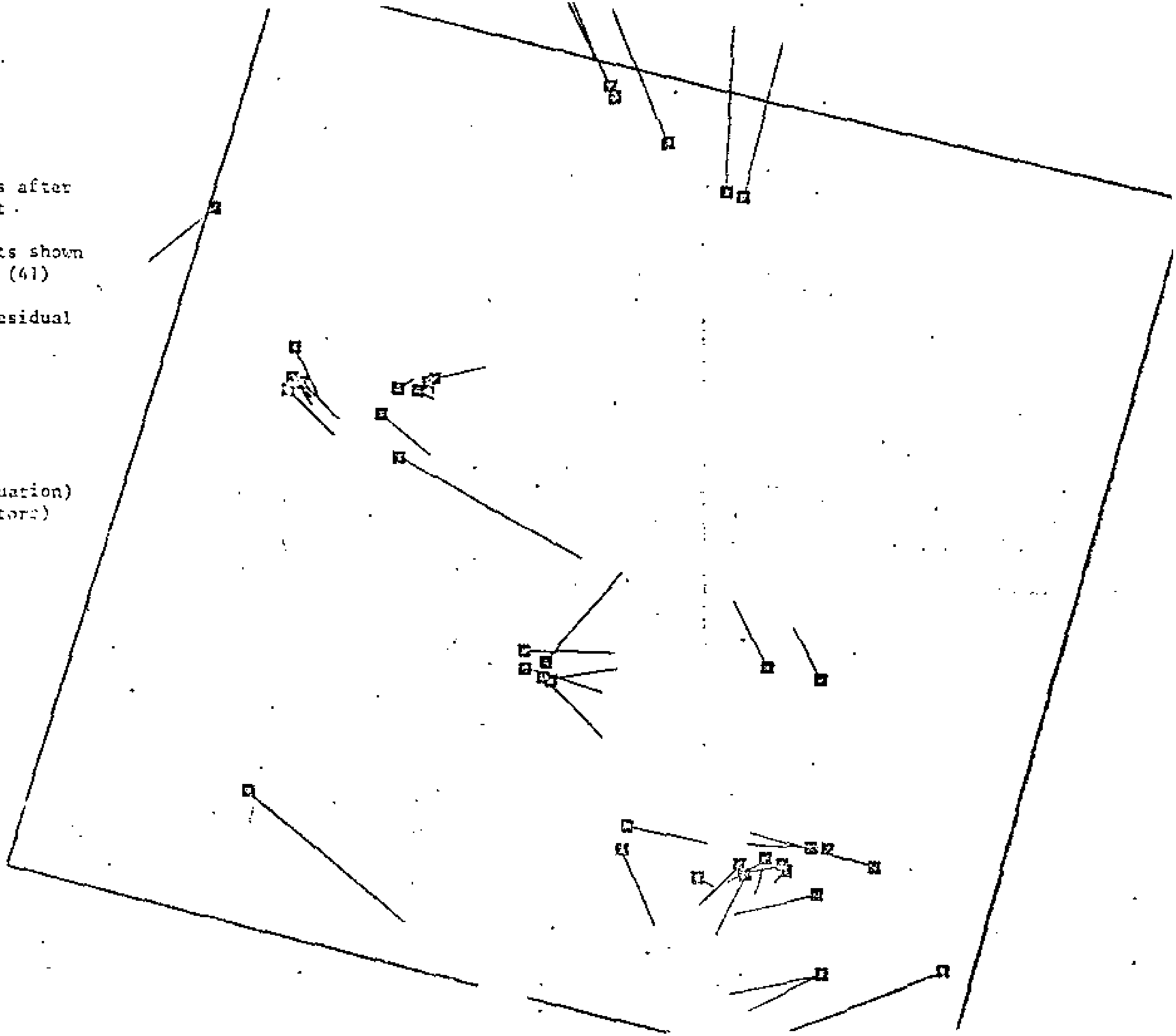

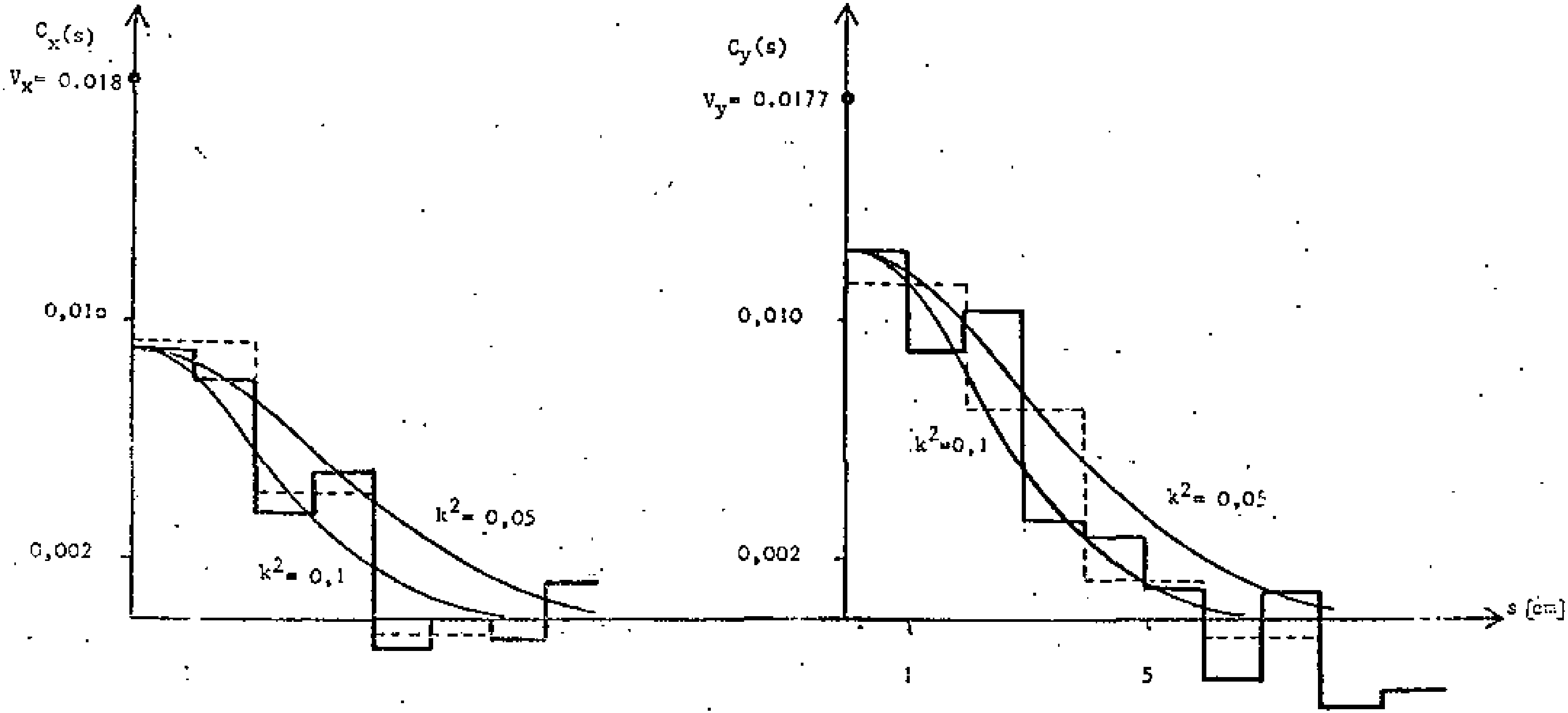

Fig.2

Determination of covariance functions

The dashed lines represent values for a 2cm-interval
For s > 10cm the values can show large discontinuities

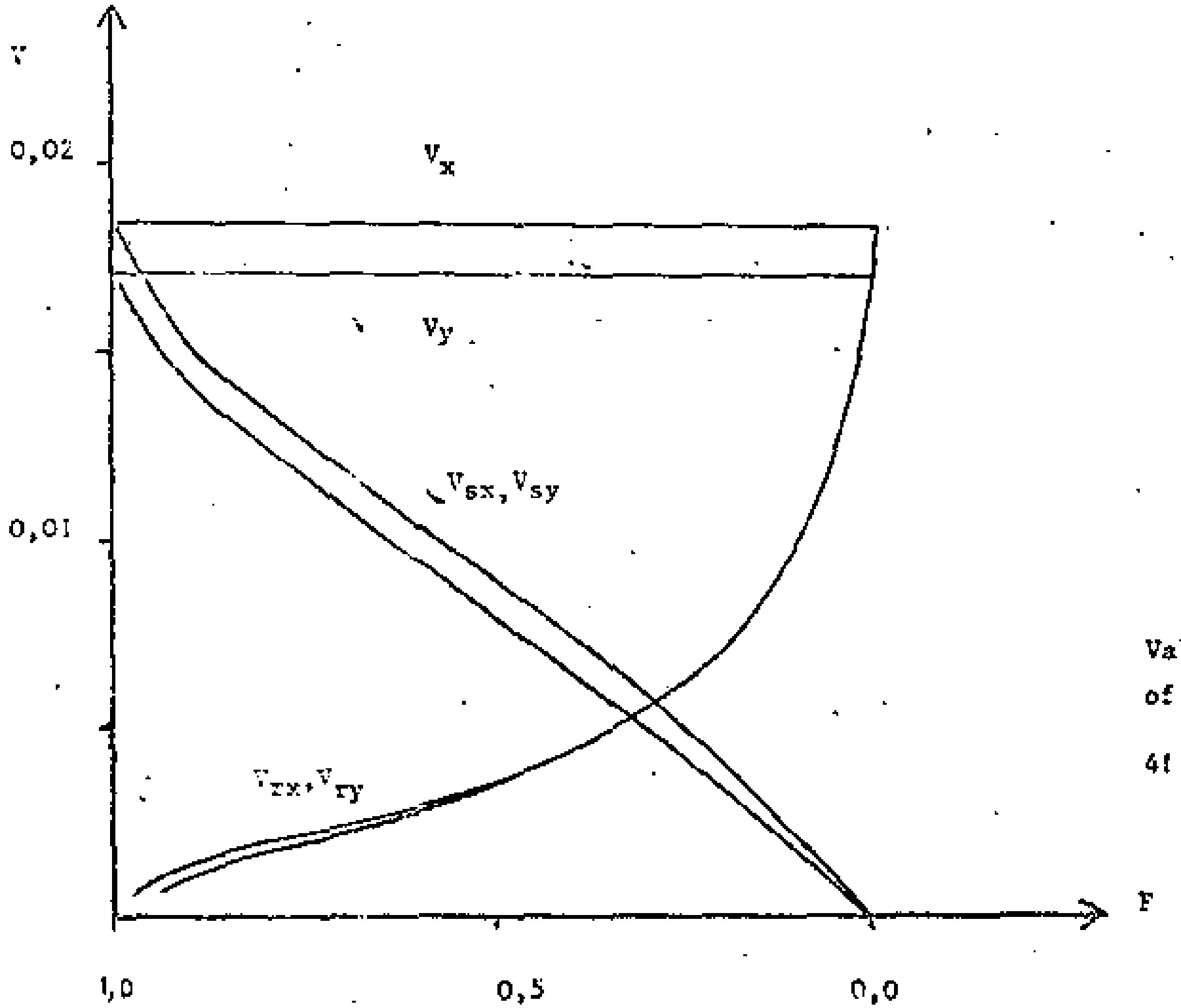

Fig. 3

Values of variances as a function of the filter coefficient F

41 reference points

Fig. 4

ERTS Channel 7

l_r - components

Reference points shown by solid spots (41).

V_2 = 0,018
K^2 = 0,05
F = 0,75

Variance of l_r:
V_{xr} = 0,0025
V_{yr} = 0,0021

Scale:

10 km (situation)
100 m (vectors)

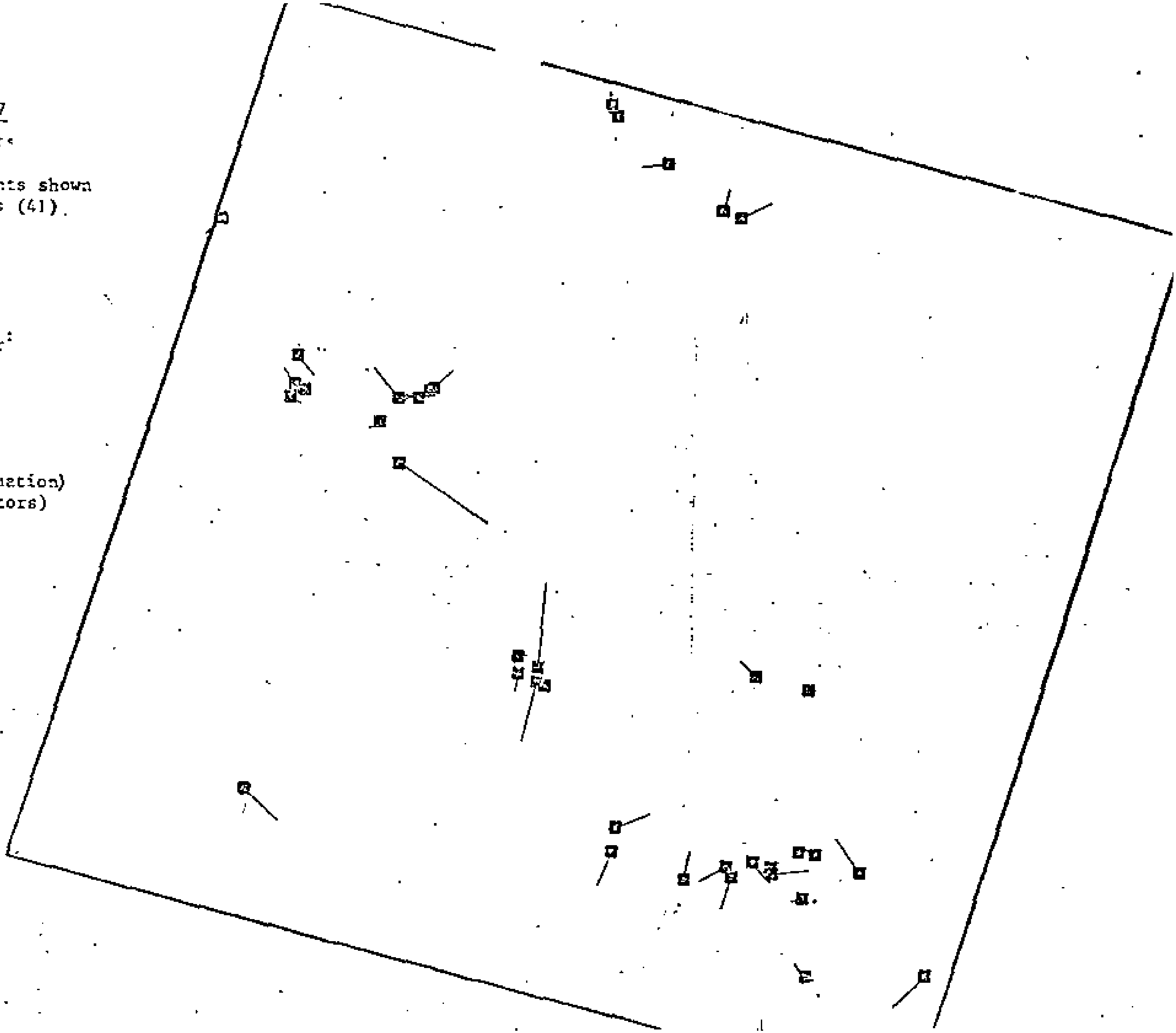

Fig. 5

ERTS Channel 7

l_r - components

Reference points shown by solid spots (10)

$V_2 = 0{,}018$
$K^2 = 0{,}1$
$F = 0{,}75$

Variances of l_r:
$V_{xr} = 0{,}0063$
$V_{yr} = 0{,}0077$

Scale:

10 km (situation)
100 m (vectors)

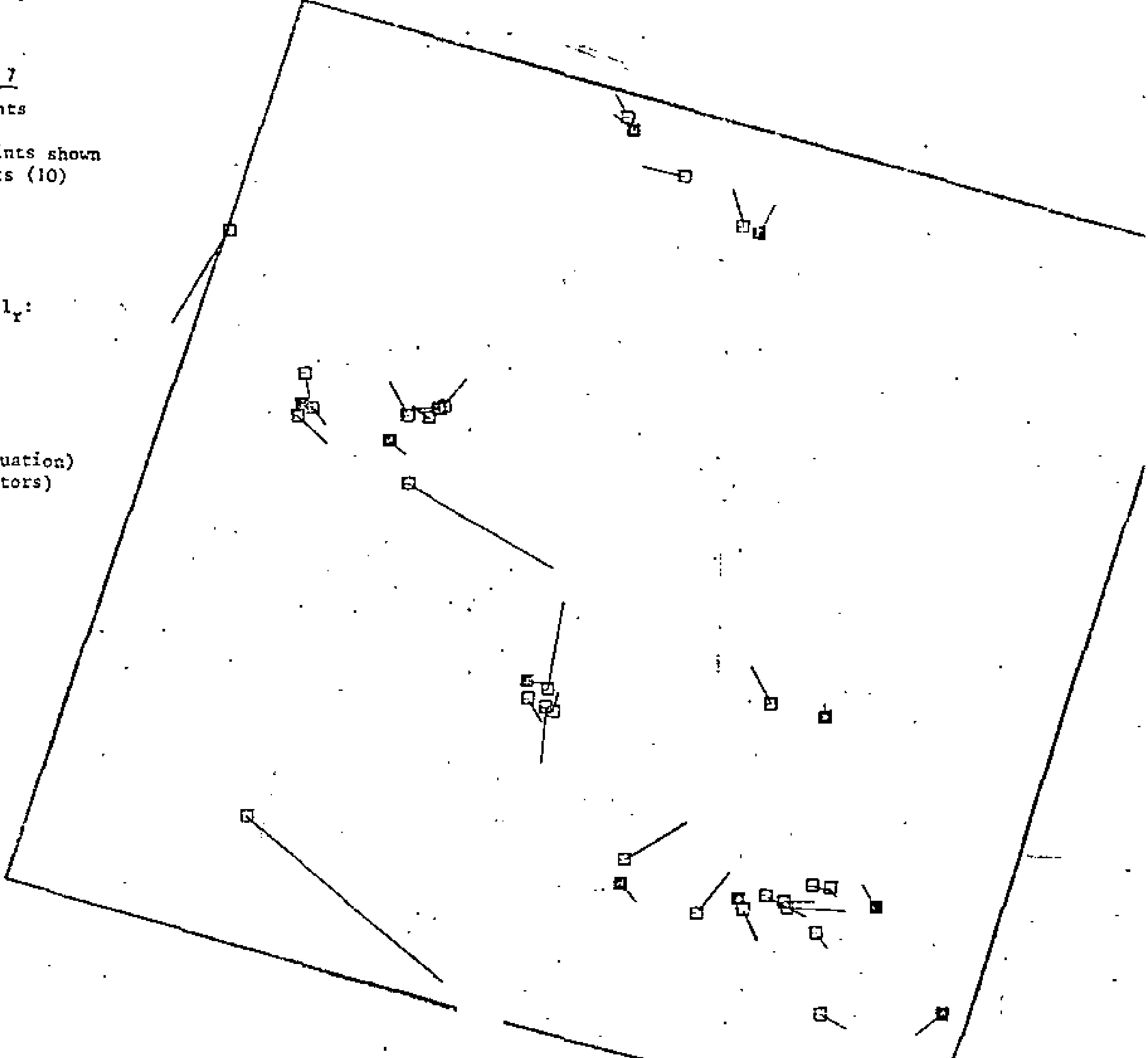

Fig.

ERTS Channel 7

Residual errors after second-order polynomial adjustment

Reference points shown by solid spots (10)

Variances of residual errors:
v_x = 0,00349
v_y = 0,00759

Scale:

10 km (situation)
100 m (vectors)

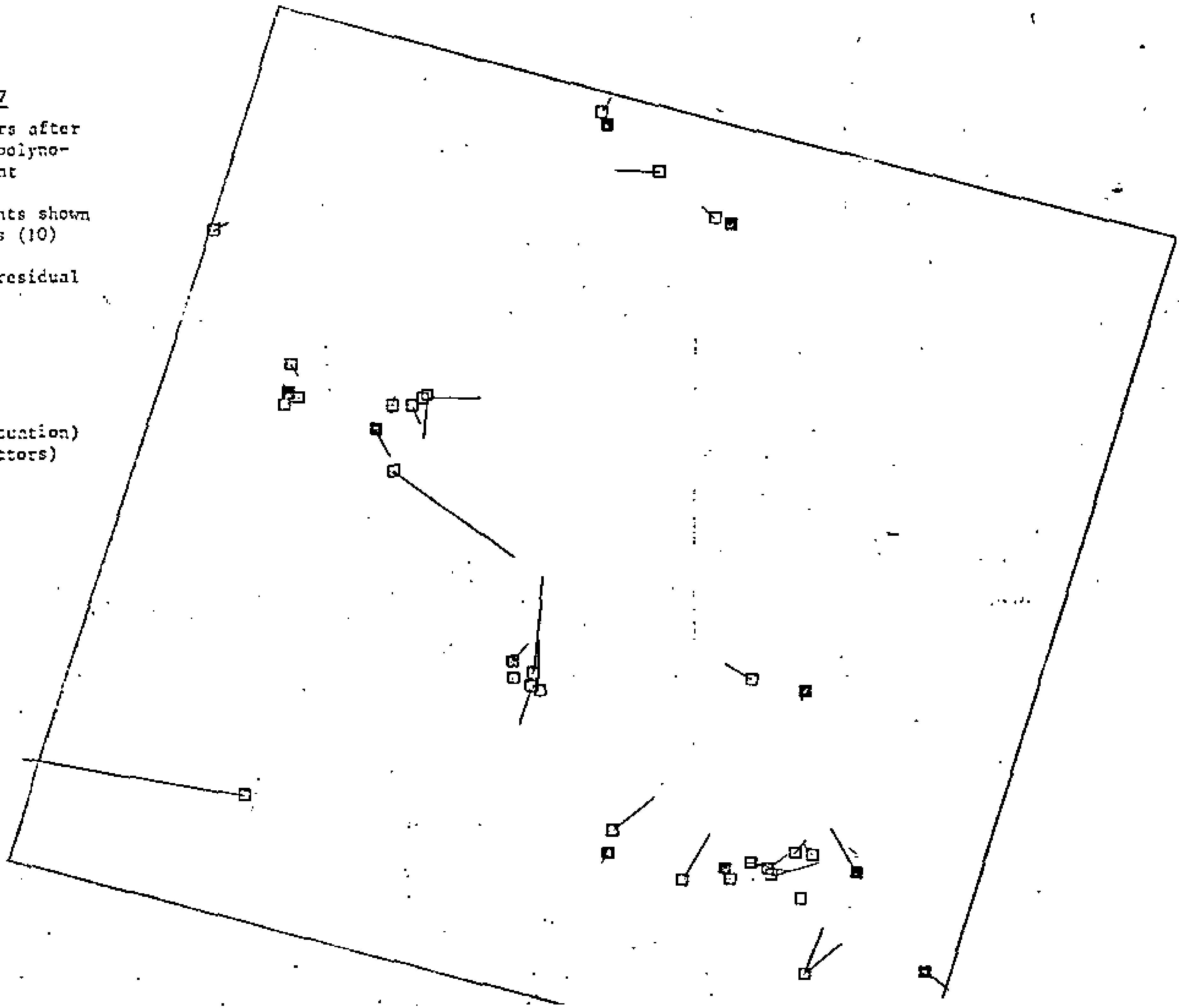

TIDAL LAND MAPPING FROM LANDSAT

by

H.-P. BÄHR and E. DENNERT-MÖLLER

Universität Hannover, Institut für Photogrammetrie und Ingenieurvermessungen

Federal Republic of Germany

RESUME

Une correction géométrique digitale a l'haute précision est executée pour un image LANDSAT (MSS), montrant les marées frisonnes au bord de la mer du nord. L'erreur moyenne sur les écartes résiduels atteint $m_x = \pm 25{,}7$ m, $m_y = \pm 51{,}3$ m. La classification multispectrale appliqué à 7 classes donne une précision plus de 89 %.

ABSTRACT

Precise digital geometrical rectification of LANDSAT MSS data leading to $m_x = \pm 25{,}7$ m and $m_y = \pm 51{,}3$ m rms was executed in order to prepare multispectral classification of the North Fresian tidal flats at the German North Sea coast. The maximum likelihood method was applied to 7 classes resulting in an accuracy better than 89 %.

1. Remote Sensing at German North Sea Coast

In general, remote sensing can be applied successfully

1. to extended areas
2. to regions to which access is difficult

and 3. if repetition of data collection is desired.

For mapping tidal flats of the North Sea coast all three aspects are valid simultaneously:

1. The North Fresian tidal flats, which are subject of this report, cover an area of about 30 km x 60 km. This is why in the past mapping from the ground by conventional methods could only be executed in a piecewise manner, leading to heterogeneous results from different authors and different interpretation keys.
2. By nature, access to the amphibian tidal landscape is difficult. The change from high tide to low tide twice a day and water level differences of 3 m normally imply significant limitation to ground work, apart from the fact, that this is possible only from May to September because of weather conditions.
3. Tidal flats are characterized by extreme temporal change of topography and hydrology. Sediment transportation can be taken as an indicator for flood conditions, on which seaways

depend. Moreover, construction of dams for coastal protection causes extensive change of the ecological balance. Consequently, frequent repetition of mapping is essential. Data have to be homogeneous, concerning season, tide and atmospheric conditions.

Considering all these aspects remote sensing seems to be very well appropriate for mapping tidal flats of the North Sea coast, an important and actual task.

With LANDSAT MSS data a well suited, relatively low-cost tool is available: the North Fresian terrain is recorded during not more than 9.7 seconds. The 79 m x 79 m resolution element on the ground, too large for many land-use-applications, corresponds well to the specific situation for tidal flats, where poorer resolution than for agricultural areas may be sufficient. A disadvantage of LANDSAT is the fixed flight plan: for 1975 until 1977 only three scenes are available showing the complete North Fresian tidal land both at low tide and cloud-free.

Mapping methods which entirely use conventional photointerpretation do not represent the international level of scientific development any more. On the contrary, computer-assisted multispectral classification procedures supply results statistically controlled, which incorporate less individual interpretation and which are largely reproducable. This aspect is very important when objective data are needed as a base for further decisions touching the ecological balance of that region.

Since 1971 the Institute for Photogrammetry at Hannover University concentrates on remote sensing activities on coastal environment. Supported by the German Government and the German Research Agency, a test site was established at the North Sea coast (Jade area near Wilhelmshaven), where different sensors were applied for monitoring sediment transport, water temperature, tidal land classification, water pollution etc. (see publications BÄHR, DENNERT-MÖLLER, KOLOUCH et al., KONECNY).

2. Rigorous Digital Geometrical Rectification of Satellite MSS Data

Geometrical rectification of imagery is essential in order to obtain data, which can be referred to ground information overlaying the rectified image on existing topographic maps. This is a supposition for tidal land classification, especially when change detection and multistage processing is desired.

Basis of the rectification procedure is a mathematical model, which expresses the ground coordinates x,y,z as a function of image coordinates x',y':

$$x,y,z = f(x',y') \qquad (1)$$

The most general analytical formulation expressing geocentric coordinates as a function of Satellite scanner imagery coordinates may be written in terms of collinearity equations:

$$\begin{pmatrix} x \\ y \\ z \end{pmatrix} = \underline{\underline{D}}_{u,i,\Omega} \left(\underline{\underline{D}}_{\phi,\omega,\kappa} \; \underline{\underline{R}}_{\Theta} \begin{pmatrix} 0 \\ 0 \\ -d \end{pmatrix} + \begin{pmatrix} 0 \\ 0 \\ r \end{pmatrix} \right) \qquad (2)$$

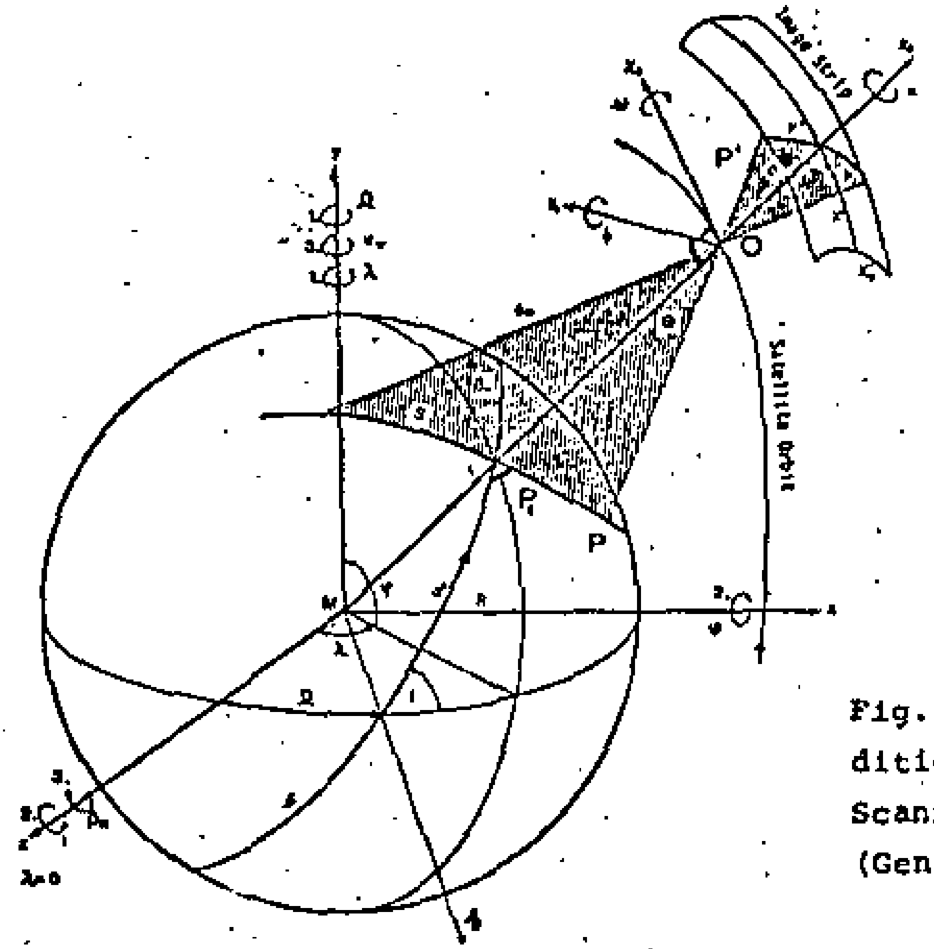

Fig. 1: Geometrical Conditions for Satellite Scanner Imagery (General Case)

According to Fig.1, $\underline{\underline{D}}_{u,i,\Omega}$ represents the rotation matrix containing the orbital parameters Ω (right ascension of ascending mode), i (inclination) and u (path length from ascending mode). The parameters can be computed out of orbital elements available for every satellite. $\underline{\underline{D}}_{\phi,\omega,\kappa}$ introduces the orientation angles of the sensor, not known a priori. $\underline{\underline{R}}_{\Theta}$ rotates the system by the scanning angle Θ. All elements are time dependant. Θ is proportional to the image ordinate y', whereas the image abscissa x' is porportional to the time and consequently affects a l l elements on the right side of (2).

This general model applied to NIMBUS scanner imagery for instance (BÄHR 1976), is valid for the forthcoming earth observation satellites too. It can be simplified for LANDSAT MSS data without loosing accuracy (BÄHR 1978). Because of small Θ (max. $\pm$ 5.5°) we may write

$$\begin{aligned} x &= a_o + a_1x' + a_2y' + a_3x'^2 + a_yy'^2 + a_5x'y' \\ y &= b_o + b_1x' + b_2y' + b_3x'^2 + b_4y'^2 + b_5x'y' \end{aligned} \qquad (3)$$

for precision processing of LANDSAT MSS imagery. The parameters a, b of the second-order-polynomial have to be determined applying least-squares adjustment procedures, introducing ground control coordinates (at least 9 well distributed points per scene). Image coordinates should be measured in a comparator ground control coordiates in a topographic map of at least 1:50 000 scale.

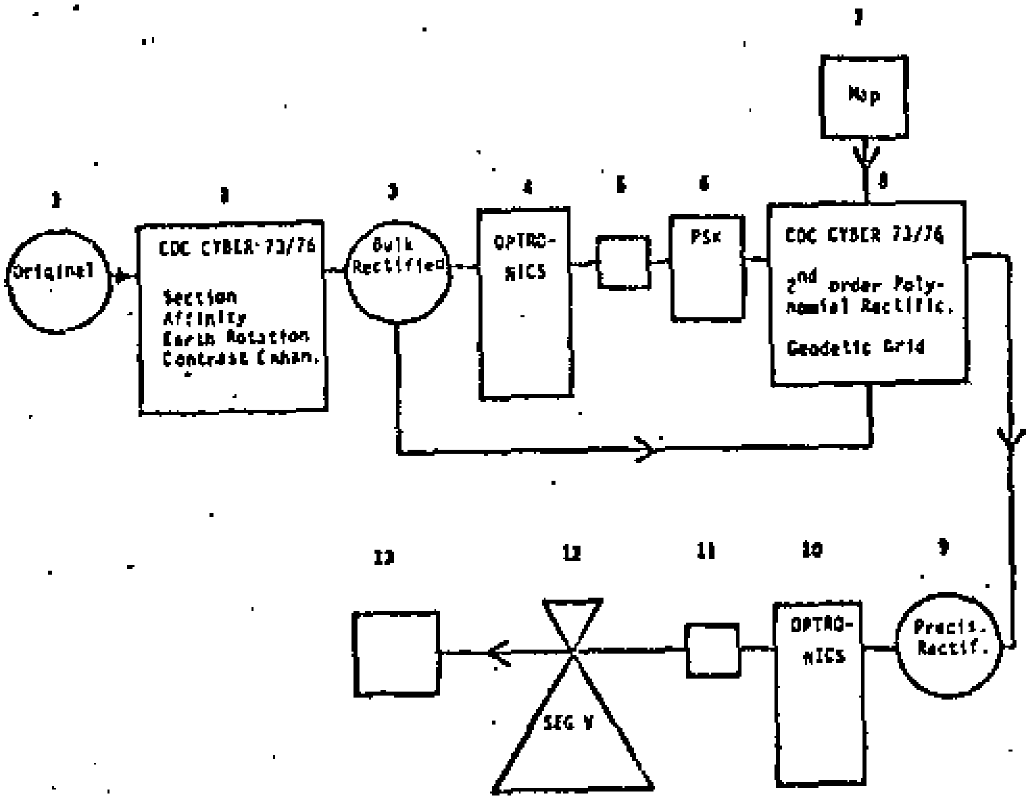

Fig. 2: Geometrical Rectification of LANDSAT-MSS-imagery at Hannover Institute for Photogrammetry (schematically)

1 Original CCT
2 Bulk processing by digital computer
3 Bulk processed CCT
4 Display at OPTRONICS
5 Bulk processed image
6 Image coordinate measurement at ZEISS-PSK Comparator
7 Measurement of ground control coordinates in topographic map 1:50 000
8 Precision rectification by digital computer
9 Precision processed CCT
10 Display at OPTRONICS
11 Precision rectified image, arbitrary scale factor
12 Enlargement by ZEISS-SEG V rectifier
13 Result, exact scale factor

We have to discriminate the "geometrical analysis" as described above and the "geometrical rectification". The latter is executed digitally, as schematically shown in Fig. 2. Digital image processing at the Institute for Photogrammetry is executed on a CDC CYBER 73/76 computer using the modular digital image processing package "MOBI" developed there (see BÄHR 1977). As measurement of ground control coordinates is impossible when taking the original data, the imagery has to be prepared applying an affinity factor (approx. 79/56 = 1.41), the earth rotation effect

$$\tan \gamma = \frac{\sqrt{\sin^2 i - \sin^2 \varphi}}{1400/U_T - \cos i} \qquad \text{(4; see BÄHR 1976)}$$

U_T = revolution period (minutes)

and contrast enhancement by histogram linearization (see Fig.2, number 2) all steps are processed by "MOBI". The imagery is displayed using an OPTRONICS MARK 17 digital writing device. Precision rectification takes place in a second step (number 8). The exact scale factor is introduced by analog means, using a precision rectifier (number 12).

For mapping the North Fresian tidal lands, a LANDSAT scene from August 11th, 1975 has been selected. Only 16 % of the whole frame was necessary for covering the desired area. The geometric accuracy of the image after application of affinity factor and earth rotation effect is shown by the vector plot Fig. 3a. The error vectors have been determined taking the conformal transformation

$$x = a_o + a_1x' - a_2y' \qquad (5)$$
$$y = b_o + a_2x' + a_1y'$$

and comparing the resulting x,y with the 30 control point coordinates. The differences correspond to the best fit possible by an ordinary enlarger. From the error vectors $\varepsilon_{x,y}$ the mean square root error $m_{x,y}$ is obtained by

$$m_{x,y} = \sqrt{\frac{\sum_{i=1}^{n} (\varepsilon_i \varepsilon_i)_{x,y}}{n-1}} \qquad n = 30 \qquad (6)$$

$$m_s = \sqrt{m_x^2 + m_y^2} \qquad (7)$$

which yields

$$m_x = \pm 89.7 \text{ m} \qquad m_s = \pm 119.4 \text{ m}$$
$$m_y = \pm 78.8 \text{ m}$$

x points north, y east. This good result depends on the small section processed.

Application of second-order polynomials (equation 3) improves the result again. Fig.3b shows that the error vectors are not any more effected by correlation. The root mean square error now is

$$m_x = \pm 25.7 \text{ m} \qquad m_s = \pm 57.4 \text{ m}$$
$$m_y = \pm 51.3 \text{ m}$$

The final result is displayed in Fig.4. MOBI allows overlay of an exact grid, which in this case corresponds to UTM coordinates. For the purpose of classification, data without grid were preferred.

The geometric accuracy obtained is in the order of magnitude of ± 50 m. Theoretically, the threshold of ± 1/3 resolution element (~ ± 25 m) cannot be surpassed. As our experience shows, ± 50 m accuracy can generally be expected for LANDSAT MSS processing. This is an excellent value compared to results for airborne scanner rectification, which are in the order of magnitude of ± 3 resolution elements.

The following classification procedure takes 79 m x 79 m units. Consequently, the obtained result for geometric rectification is in good correspondence.

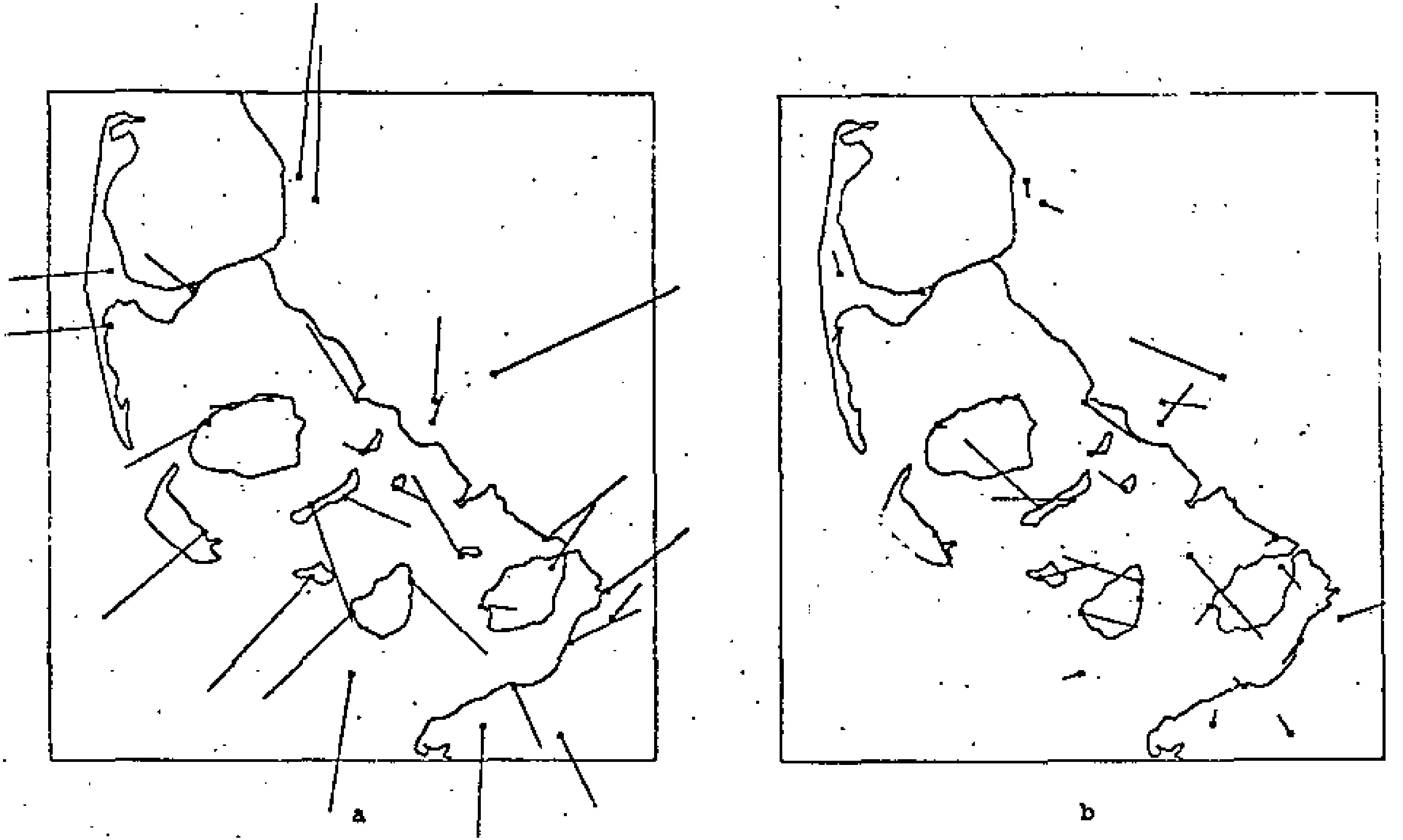

a b

Fig. 3 : Residuals at Control Points after Geometrical Rectification

Left: Bulk Processing Right: Precision Processing

⊢—⊣ Corresponds to 10 km on the Ground, to 100 m as a Vector

3. Digital Multispectral Classification Procedure

The most common supervised classification technique is the "Maximum Likelihood Method". During the last years it has been applied to various areas of earth observation.

The classification concept corresponds to the following statistical model: to each pixel belongs a pattern vector $\underline{x}$ whose n components are the grey levels of the pixel in the n different spectral bands. The assumption is made that the pattern vectors of each of the m classes taken by itself are events of random variables with multivariate density functions. Supposing the Maximum Likelihood method, these density functions are assumed to be Gaussian functions. The parameters describing a Gaussian function, the mean vector $\underline{m}_i$ and the covariance matrix C_i are estimated by the pattern vectors in the training fields. The discriminant functions of this method

$$p_i(\underline{x}) = p(w_i)\cdot\left(\frac{1}{2}\right)^{\frac{n}{2}}\cdot(\det(C_i))^{-\frac{1}{2}}\cdot\exp\left(-\frac{1}{2}(\underline{x}-\underline{m}_i)^T \cdot C_i^{-1}\cdot(\underline{x}-\underline{m}_i)\right),\quad i = 1,\ldots,m \qquad (8)$$

specify the probability $p_i(\underline{x})$ that the pattern vector $\underline{x}$ belongs to the class w_i.

Each pixel is assigned to the class w_i if the probability $p_i(\underline{x})$ that the adjoint pattern vector $\underline{x}$ belongs to w_i is greater than $p_j(\underline{x})$ for any other class w_j:

$$\underline{x} \in w_i \iff p_i(\underline{x}) > p_j(\underline{x}) \quad \forall j \neq i,\quad j = 1,\ldots,m \qquad (9)$$

Setting (8) equal to a constant, one obtains hyperellipsoids as "lines" of equal probability. A rejection class can be introduced by defining a "maximum hyperellipsoid" for each class: all pattern vectors which are outside of the union of all maximum hyperellipsoids are rejected as "not belonging to any of the classes". The size of the maximum ellipsoids is determined by a threshold value which has to be appropriately chosen.

The functions (8) show the importance of the parameters "mean vector" and "covariance matrix". As they are estimated by training fields, the classification results depend strictly on good and precise selection of the training fields. When selecting a training field which contains others than elements of one class the estimation results in falsified parameters and consequently in incorrect discriminant functions. Tidal lands are natural landscapes; thus the limits of different structures cannot be defined clearly. This circumstance makes selection of appropriate training fields difficult. Often there are only a few homogeneous, sufficiently large areas for "calibrating" the classification system. That is why supervised classification of tidal lands needs assistance by an expert being familiar with the terrain.

The computing time of the adjoint algorithm increases quadratically with the numbers of channels used. As the channels 4 and 5 as well as 6 and 7 are highly correlated it is convenient to execute classification using only two of the four LANDSAT-spectral bands. One approach is the linear transformation equivalent to a rotation of the original pattern space to the principle components as a new set of coordinate vectors. Selecting those features which

Fig. 4: Result from Precision Rectification
Scale 1: 567 000
Grid width corresponds to 10 km
(UTM System)

Fig. 5: Training and Control Areas
Sand (1), Dried Sand (2), Mud Flat (3)
Fore Shore (4), Land (5), Water (6)

are the eigenvectors corresponding to the largest eigenvalues of the covariance matrix results in a dimensionality reduction with minimal loss of information.

4. Execution of Classification and Results

In the LANDSAT-scene of 11/8/75 the following classes are to be discriminated:

1. Sand
2. Dried Sand
3. Mud Flat
4. Foreshore
5. Land
6. Water
7. Remaining areas

The analysis of principle components of the geometrically rectified LANDSAT-scene shows that the main directions of information contained in the picture are near the channels 5 and 6. The same statement is valid for the training fields in tidal land (classes number 1-4). Execution of the transformation to the principle components is not convenient in this case. Each of the three kinds of surfaces in the picture "tidal land", "land" and "water" has its own principal components. The principal components of the whole picture are linear combinations of them. As discriminating tidal land surfaces is the main task of the classification, the transformation could only support it, if the principal components of the whole picture and those of the tidal land areas were identical.

Some available training fields for the first six classes mentioned above were selected co-operating with an expert for this region. Fig.5 shows their location in the picture. The numbers 1-6 indicate the location of the training fields selected for classification, the numbers $\overline{1}$-$\overline{6}$ are within test areas which were used in order to control the classification result. Final selection of the training fields was done with respect to statistical aspects. The number of pixels should be as large as possible and the frequency distribution of the grey level values should be unimodal with a small variance. These criteria lead to an optimum estimation of the statistical parameters by the training fields and the adaption to the mathematical model. For the class "mud flat" two training areas were selected because the mean vectors of these two areas differed from each other. For the description of each of the other classes one training field seemed to be sufficient.

Fig. 6 shows the location of the lines of equal probability which result from the discriminant functions, set equal to a constant. The two ellipses of the class "mud flat" and that of "sand" show that the selection of two training fields for one class and only one for all other classes for this case can lead to overrating this class. If only the training field with the smaller mean vect would have been chosen, the percentage of mud flat in the classified picture would be smaller, whereas that of sand would increase. On the other hand omitting the training field with the smaller mean vector would probably enlarge the number of unclassified pixels.

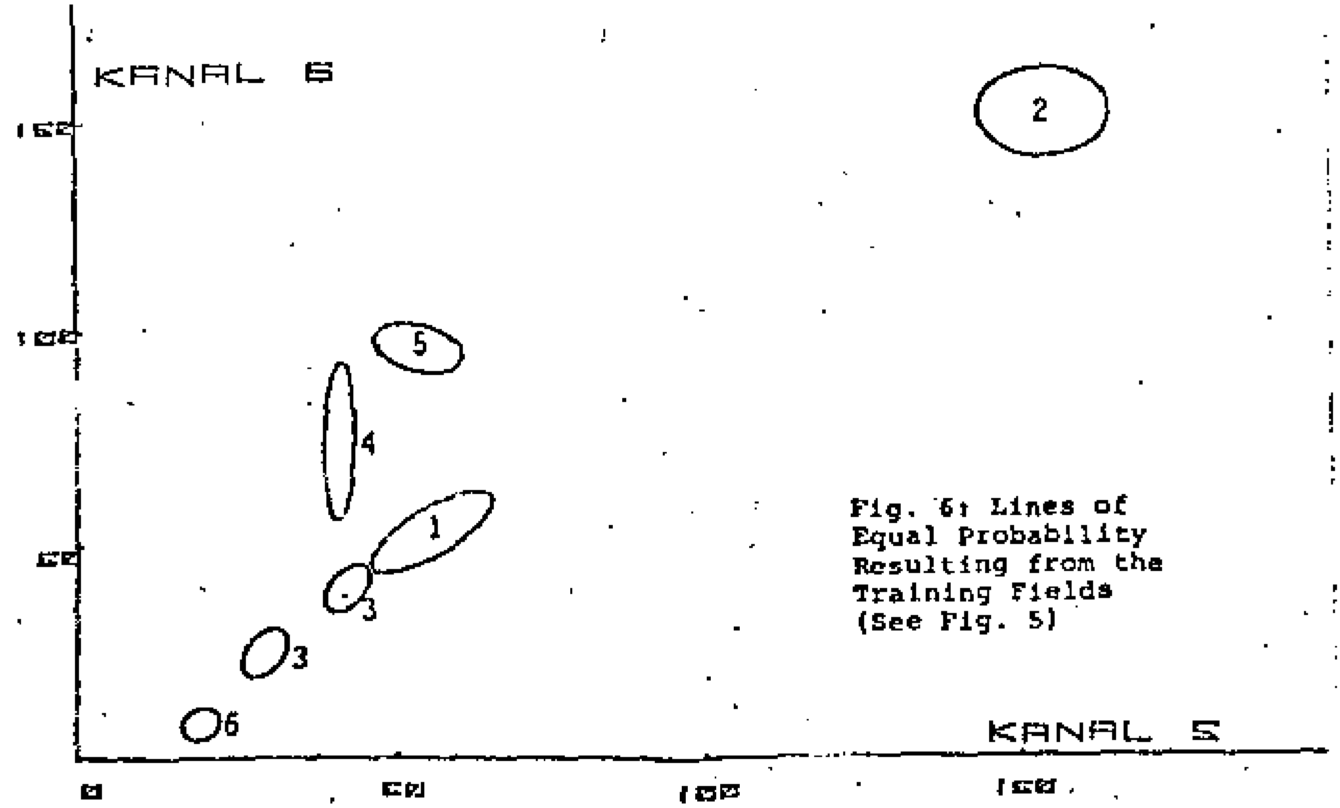

Fig. 6: Lines of Equal Probability Resulting from the Training Fields (See Fig. 5)

Fig. 7:

Classification of

Sand,
Dried Sand,
Mud Flat
Foreshore
Land
Water
(see Fig. 5)

and Remaining Areas

Fig. 8 : Separate Display of "Mud Flat"

Fig. 9 : Separate Display of ~~"Mud"~~ Sand

The classified picture presents the following distribution of the areas of the seven classes:

Class	area in km^2
Sand	828
Dried Sand	51
Mud Flat	1353
Land and Foreshore	4774
Water	1697
Remaining areas	1765

The class "remaining areas" contains the rejected pixels.

The classification results are shown in fig. 7-9. Principally, classification results ought to be displayed by thematic maps. This is possible for all classes simultaneously on a unique map, as well as on several maps separately for different classes. Advantage of separate display is a quick and clear overview of spatial distribution, going together with the disadvantage of lost relative orientation between the different classes. Practical experience shows that both types of display are needed. A c o l o u r e d map will improve the possibility for discrimination of the different classes for simultaneous presentation. Further interpretation as well as detailed analysis in order to draw practical consequences is task of the users.

Tha quality of the classification result was measured using the training fields and additional test areas (see 1-6 and $\bar{1}$-$\bar{6}$ in fig. 5). The accuracy of classification within an area can be defined as the percentage of correctly recognized pixels in the total number of pixels. The following two tables contain these accuracy values in the main diagonal. The other values in the table specify the percentage of pixels belonging to the class in the left, but assigned to the class in the top of the table. For example, "90.3" in the first line means that 90.3 of pixels in the training field "Sand" are correctly classified. 9.5 % of pixels are incorrectly assigned to "mud flat", 0.22 % to "Foreshore".

assigned to / training field	Sand	Dried Sand	Mud Flat	Foreshore	Land	Water	unclassified
Sand	90.3	–	9.5	0.22	–	–	–
Dried Sand	–	100.0	–	–	–	–	–
Mud Flat	2.5	–	97.3	0.2	–	–	–
Foreshore	–	–	8.1	89.6	2.3	–	–
Land	–	–	–	10.6	89.4	–	0.04
Water	–	–	–	–	–	100.0	–

Table 1: Accuracy of Classification Measured by Trainig Fields

assigned to / control area	Sand	Dried Sand	Mud Flat	Fore-shore	Land	Water	unclassified
Sand	93.8	-	2.7	3.1	-	-	0.4
Dried Sand	-	100.0	-	-	-	-	-
Mud Flat	-	-	99.4	0.6	-	-	-
Fore-shore	-	-	4.8	92.9	1.2	-	1.0
Land	-	-	-	13.9	85.9	-	0.2
Water	-	-	-	-	-	100.0	-

Table 2: Accuracy of Classification Mesured by Control Areas
The sums of the lines are 100 % each.
Summarizing the columns in the tables one can see that the class "Mud Flat" contains too many pixels, whereas the percentage of "Sand" is too small. The sums of the columns "Foreshore" and "Land" in the control-area-table show the same effect.
Defining a weighted accuracy by the ratio of the number of correctly classified pixels to the number of all pixels in the training fields or control area yields the accuracy values 0.94 in the training fields and 0.96 in the control areas.

This good result obtained by digital multispectral classification procedures would practically not be surpassed by mapping techniques from the ground.

Literature

NDREWS, H.C.: Introduction to Mathematical Techniques in Pattern Recognition. J.Wiley & Sons, New York 1972

BÄHR, H.-P.: Erfahrungen mit Methoden der Fernerkundung für Fragen der Küstengewässer. Symposium Erderkundung, DFVLR, Köln 1975

Geometrical Models for Satellite Scanner Imagery. IGP Komm. III, Helsinki 1976

Analyse der Geometrie auf Photodetektoren abgetasteter Aufnahmen von Erderkundungssatelliten. Schriftenreihe des Niedersächsischen Landesverwaltungsamtes - Landesvermessung -, Hannover 1976

Vom Satellitenbild zur Reihenmeßkammeraufnahme: das Jadegebiet im Vergleich unterschiedlicher Sensoren. Symposium Flugzeugmeßprogramm, Hannover 1977, edited by Bundesministerium für Forschung und Technologie 1978

Digital Image Processing Experience at Hannover Institute for Photogrammetry. IGP Symposium Komm.III, Arbeitsgruppe 4, Graz 1977

Geometric Analysis and Rectification of LANDSAT MSS Imagery: Comparison of Different Methods. IGP Komm. III, Moskau 1978

ENNERT-MÖLLER, E.: Multispectral Classification of Tidal Land. Mitteilungen der geodätischen Institute der Technischen Universität Graz, Folge 29, 1977

KOLOUCH, D. et al.: Spektrale Reflexionsmessungen von belastetem Wasser zur Analyse der Wasserqualität aus multispektralen Aufnahmen. IGP Helsinki, 1976

KONECNY, G.: Approach and Status of Geometric Restitution for Remote Sensing Imagery. BUL 1/1975

Digitale Entzerrung der Daten von Zeilenabtastern. BUL 4/1975

Mathematische Modelle und Verfahren zur geometrischen Auswertung von Zeilenabtaster-Aufnahmen. BUL 5/1976

BUL : Bildmessung und Luftbildwesen

IGP : International Society for Photogrammetrie

Digital Rectification of a Facade

H.-P. Bähr, Technische Universität Hannover

Presented at the International Society of Photogrammetry
Symposium Commission III, Moscow 1978

Abstract

A cylindrical-shaped facade of a castle was to display unrolled onto a tangential plane. After simplification of a general approach, the analytical relations were used for digital conversion of the original image.

Zusammenfassung

Die zylinderförmige Fassade eines Schlosses sollte auf eine Tangentialebene abgerollt dargestellt werden. Ausgehend von einer allgemeinen Lösung werden dazu vereinfachte analytische Beziehungen hergeleitet und zur digitalen Umbildung der Originalaufnahme verwendet.

Résumé

l'auteur présente le dévellopement sur un plan tangential d'une facade historique de forme cylindre. A partir d'une solution très générale, sont déduites des équations simplifiées pour la transformation digitale du cliché original.

A three - dimensional object can rigorously be described geometrically by a single frame, if additional geometrical parameters are introduced (see GRÜN /5/). For the specific object discussed here this means, that we have to provide the geometrical parameters of the facade. If we generally admit a second - order surface for the castle walls, we may write (/3/):

$$\mathcal{F} = a_{11} X^2 + a_{22} Y^2 + a_{33} Z^2 + 2a_{12} XY + 2a_{23} YZ + 2a_{31} ZX + \ldots$$
$$+ 2a_{14} X + 2a_{24} Y + 2a_{34} Z + a_{44} = 0 \quad (1)$$

This surface is defined within a local coordinate system X, Y, Z, and the parameters a_{11} ... a_{44} have to be determinded "somehow", e. g. by conventional surveying and adjustment procedures.

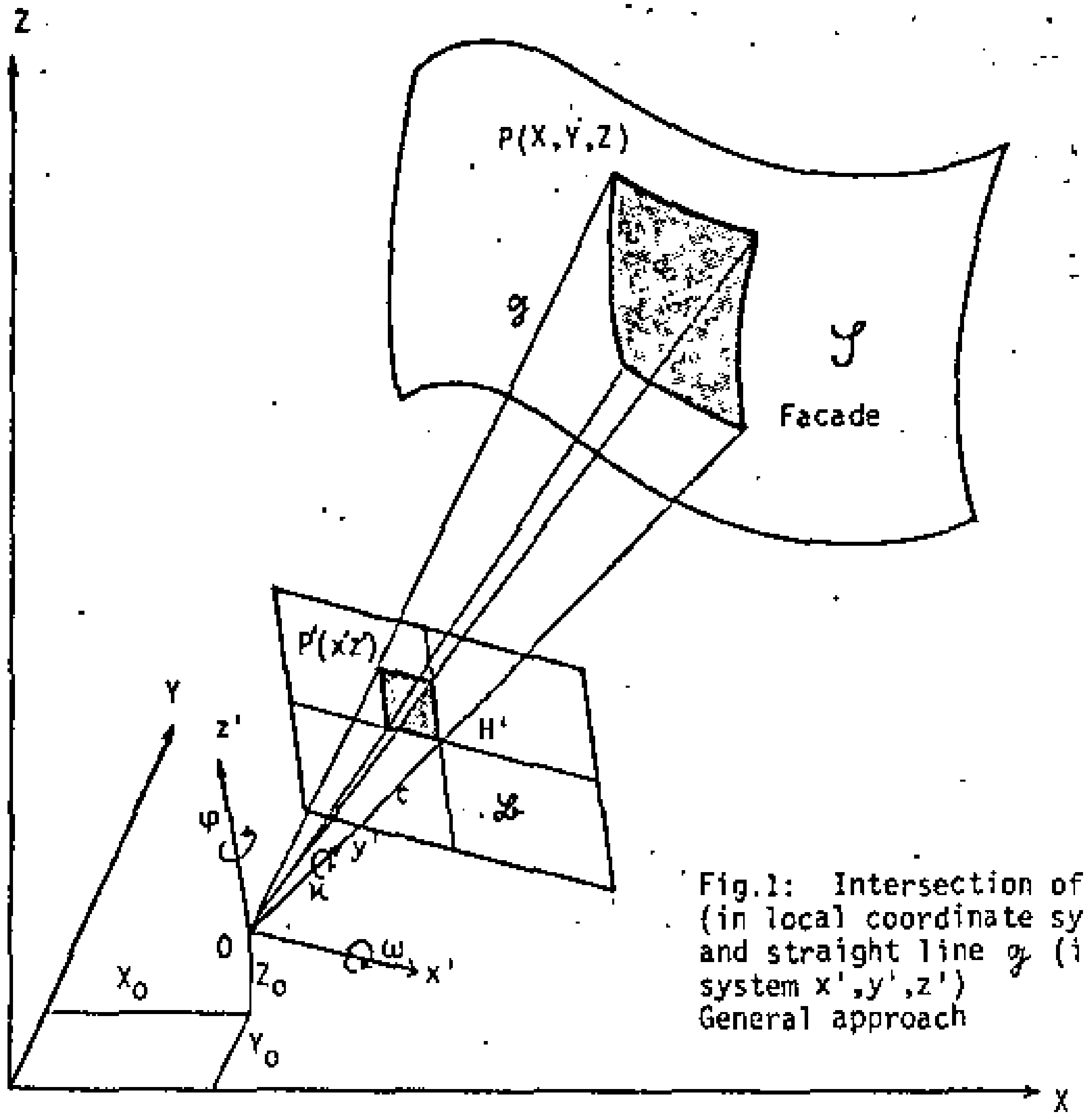

Fig.1: Intersection of surface $\mathcal{F}$ (in local coordinate system X,Y,Z) and straight line g (in camera system x',y',z') General approach

Fig. 1 illustrates the geometrical conditions when taking the imagery. This disposition leads to the well-known collinearity equations

$$g_i \equiv \begin{pmatrix} X \\ Y \\ Z \end{pmatrix}_i = \lambda \, D_{\varphi,\omega,\kappa} \begin{pmatrix} x' \\ c \\ z' \end{pmatrix}_i + \begin{pmatrix} X_o \\ Y_o \\ Z_o \end{pmatrix} \quad (2)$$

Digital Rectification of a Facade

H.-P. Bähr, Technische Universität Hannover

Presented at the International Society of Photogrammetry
Symposium Commission III, Moscow 1978

1. Background

New image processing techniques in photogrammetry are not restricted to single fields. Like "analytical" procedures have been successfully used for aerotriangulation as well as for terrestrial photogrammetry (ELLENBECK / WROBEL /4/) and non-conventional imagery (KONECNY /6/), pure digital methods will get increasing importance for all areas of photogrammetry in the near future.

In photogrammetry, digital image processing has been propagated originally for remote sensing applications, when scanner data was available in digital form (CCT's). In the meantime photogrammetrists became aware of the enormous possibilities offered by digital components for both acquisition and processing of imagery (see HANNOVER SYMPOSIUM 10/). Digital image processing therefore is an actual and challenging task, also with respect to conventional imagery and conventional applications.

Many users desire rectified imagery instead of line maps for final results because the photographs provide full semantic information in non-interpreted form, frequently relatively cheap. A common field for this type of data is the architecture, where rectification methods are operationally used for facades (WROBEL /9/). SEEGER /8/ shows, that even conventional orthophoto techniques can principally be applied to "architectural" objects. KRAUS /7/ finally, sucessfully uses modern orthophoto devices in order to rectify developable surfaces. His examples are similar to the task described here. However, the purely digital approach applied here, differs entirely from KRAUS's hardware-oriented procedure and is based on the general digital image processing concept.

Object of the investigation reported here is the Oelber castle near Hildesheim (Fed. Rep. of Germany), which dates back to the 15th century. The building is characterized by a circular groundplan. Consequently, imagery obtained from the facades show large distortions, i. e. nonlinear variation of scale within the whole frame (see Fig.4). Quantitative measurements within this type of imagery is impossible. Therefore it was desired to "unroll" the facade onto a tangential reference plane.

2. Analytical Relations

For digital rectification, an analytical formulation of the object to be rectified is necessary. This means, an explicite mathematical function of the corresponding surface has to be determined in advance +). We call this task "geometrical analysis", which we have to separate strictly from the rectification procedure which follows (see BÄHR /1/).

+) A related problem is the use of a digital terrain model supposed for digital rectification of single airborne scanner strips

Intersection of surface $\mathcal{S}$ (1) and straight line g_i (2) would finally yield

$$P\ (X,\ Y,\ Z) \equiv f\ (x',\ z',\ c,\ X_o,\ Y_o,\ Z_o, \varphi,\ \omega,\ \kappa,\ a_{11}\ \dots\ a_{44}) \qquad (3)$$

This is a very complicated expression, which would lead to costy digital rectification procedures. Therfore some restrictions are defined here in order to simplify the general formulas (1) and (2):

1. The facade is supposed to be vertical ($a_{33} = a_{23} = a_{31} = a_{34} = 0$)
2. The groundplan of the facade is supposed to be circular ($a_{12} = 0$; $a_{11} = a_{22}$)

From (1) we therefore get

$$\mathcal{S} \equiv a_{11}\ X^2 + a_{11}\ Y^2 + 2a_{14}\ X + 2a_{24}\ Y + a_{44} = 0 \qquad (4)$$

or may write

$$\mathcal{S} \equiv (X - X_M)^2 + (Y - Y_M)^2 = R^2 \qquad (5)$$

where X_M, Y_M and R are the parameters for a circle, which is the trace of the facade (see Fig. 2).

Further simplifications may be introduced for the collinearity equations (2):

3. $\underline{\underline{D}} = \underline{\underline{E}} = 1$, because $\kappa = \omega = 0$ is obtained by level vials, and $\varphi = 0$ by taking the direction defined by the image center as the local Y.
4. $X_o = Y_o = Z_o$, when shifting the local coordinate system X, Y, Z to 0. In practise it makes no difficulty to determine the ground coordinates directly in the X, Y, Z - system, containing 0 as origin and c on the Y-axis.

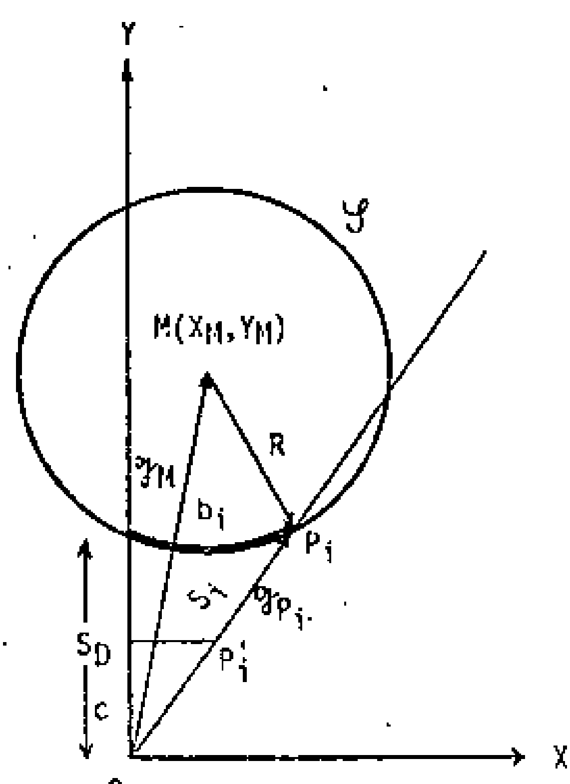

Fig.2:

Surface $\mathcal{S}$ and straight line g_P in X/Y plane after introduction of restrictions 1...4

From (2) we then get

$$\mathfrak{r}_i = \begin{pmatrix} X \\ Y \\ Z \end{pmatrix}_i = \lambda \begin{pmatrix} x' \\ c \\ z' \end{pmatrix}_i \qquad (6)$$

Fig. 2 shows the geometrical conditions after simplifications 1 ... 4 in the X / Y plane. The geometrical position of P can be defined here by

$$R^2 = (\mathfrak{r}_P - \mathfrak{r}_M)^2 = \left(\begin{pmatrix} X \\ \frac{X}{x'} c \end{pmatrix} - \begin{pmatrix} X_M \\ Y_M \end{pmatrix} \right)^2 \qquad (7)$$

taking (5) and (6) after elimination of λ. Equations (6) and (7) lead to the desired solutions, where the object coordinates are explicitely expressed as functions of x', z', c, X_M, Y_M and R:

$$X_i = \frac{X_M + \frac{c}{x'_i} Y_M \pm \sqrt{R^2 \left(1 + \frac{c^2}{x'^2_i}\right) - \left(Y_M - X_M \frac{c}{x'_i}\right)^2}}{1 + \frac{c^2}{x'^2_i}}$$

(positive root for $x' < 0$; negative root for $x' > 0$) (8)

$$Y_i = \frac{c}{x'_i} X_i$$

$$Z_i = \frac{y'_i}{c} z'_i$$

3. Rectification Procedure

Rectification is executed within a digital modular image processing package. This package has been designed by members of the Institut für Photogrammetrie und Ingenieurvermessungen (IPI) and installed at the CDC CYBER 73/76 computer of the Technical University Hannover. It is a multi - purpose package, containing 60 modules at the moment (see BÄHR /2/). For the specific task discussed here, a new version of the existing "DEHN" module was developed by cand. geod. A. BRANDT, whereas read / write and image enhancement procedures were already existing.

Read / write device is an OPTRONICS MARK 17 for A / D and D / A conversion, available at the IPI. The image processing data flow can schematically be illustrated as follows:

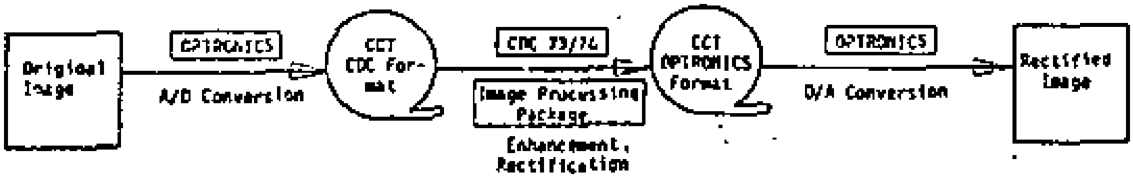

If one admits the restrictions defined in paragraph 2, adding $X_M=0$ as approximate value, rectification can be processed in two separate steps, as illustrated by Fig. 3: Firstly, the displacement of any point P_i' in z' -direction can be executed within a single image row , taking

$$\bar{z}_i = z' \frac{S_i}{S_D} \qquad (9)$$

where $\bar{z}_i$ is the correct position and S_i/S_D a scale factor (see Fig. 2 observing $X_M=0$). Secondly, a stretch in x'- direction has to be added, taking single image columns. For the purpose of unrolling the cylindrical surface on a tangential plane, one has to equalize $\bar{x}_i \mathrel{\hat{=}} b_i$ (see Fig. 2) and gets

$$\bar{x}_i = R \frac{c}{S_i} \arcsin \left(\frac{x_i'}{R} \right) \qquad (10)$$

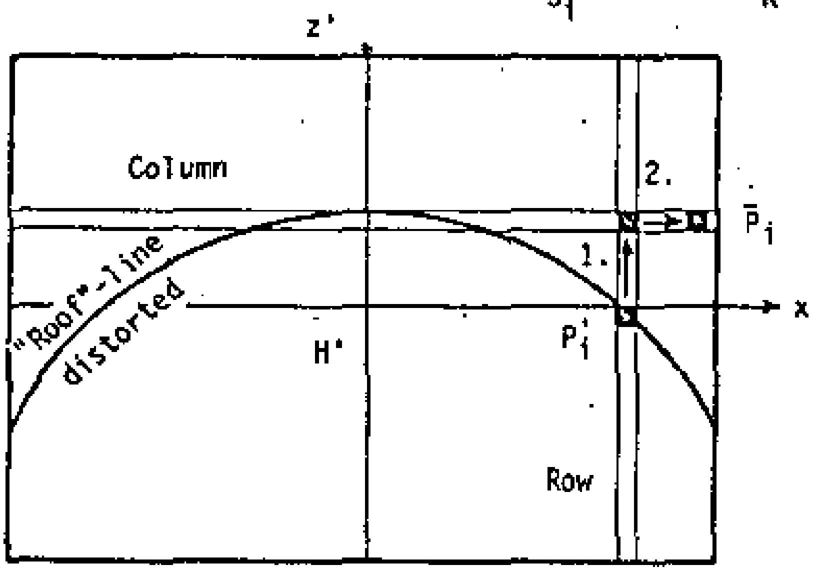

Fig.3:

Two-step principle for displacing a point P'_i (pixel) into its correct position $\bar{P}_i$

In practise, the rectification was mastered using the "indirect" method, for which good results were obtained from satellite imagery correction (BÄHR /1/). This means, that the distorted image values have to be available as functions of the corrected ones, which does not lead to any problems taking (9) and (10). The procedure then runs as follows:

1. R, X_M, Y_M, S_D, and c are known a priori
2. Computation of $(X,Y,Z)_i$ by (8)
3. Determination of $S_i = +\sqrt{X_i^2 + Y_i^2}$
4. Computation of $(x',z')_i$ coordinates in the distorted image ((9) and (10))

4. Results

Fig. 4 shows the original frame, used for digitization at the OPTRONICS Mark 17 taking 0.1mm x 0.1mm pixel size. This is the poorest resolution possible for the OPTRONICS, chosen in order to have low computing costs during the test phase. Digitization had to be executed taking the image verticals as rows, observing the scheme in Fig. 3.

The rectified result is shown by Fig. 5, unrolling the wall on a tangential plane, parallel to the image plane, touching the wall in the vertical line through the image center. Fig. 5 should not be considered as the final result, because both image quality and image geometry are not yet fully satisfactory:

As far as the image quality is concerned, discrete 0.1mm steps are obvious, particularly at horizontal lines. Moreover, the processed image does not contain the full original information, which leads to a poorer contrast, though histogram linearisation was applied. These disadvantages can be avoided simply by taking smaller resolution elements (e.g. 0.0125mm by 0.0125mm). This will of course drastically raise the computing costs, which are for this example about double of geometrical processing a corresponding LANDSAT section (see BAHR /1/).

As far as the image geometry is concerned, it can be checked thoroughly using 35 control points at the window frames. Point coordinates had been determined with reference to the wall surface. A conformal transformation ("HELMERT"- transformation), using two translations, a rotation and a scale factor, leads to $\pm$ 5.3 cm rms in x and $\pm$ 7.3 cm rms in z for the residuals, displayed in Fig. 6. The geometrical quality suffers very much from the restrictions introduced in paragraph 2. For instance, the wall is not simply a uniform cylinder, but changes its radius from the left to the right side of the image (see Fig. 4). Additional information like this has to be added to the analytical model, which does not lead to any problems.

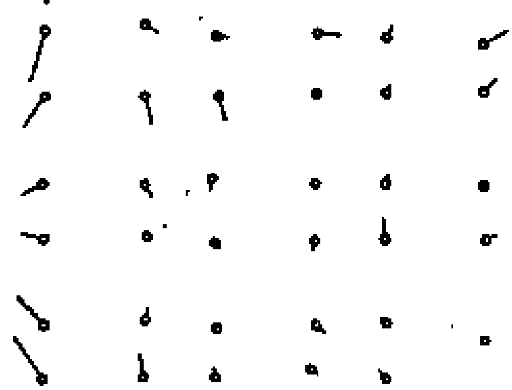

Fig. 6:

Residuals from conformal transformation of the result to 35 ground control points

⊢⊣ Corresponds to 2o cm error

The terminology "rectification" does not fully describe the approach applied here. The point in question is the g e n e r a l g e o m e t r i c a l t r a n s f o r m a t i o n of an image by purely digital techniques. The range of applications can hardly be overlooked and reaches from fitting LANDSAT imagery to arbitrary map projections to supporting design in the field of architecture, industry or engineering.

Digital image processing beyond the "classical" remote sensing applications generally offers all the well-known sophisticated techniques, like image enhancement and classification. Depending on the specific task, the operator has to arrange the steps following the geometrical transformation. For the castle wall discussed here, digital analysis of stone composition for example, would support the expert's further investigations.

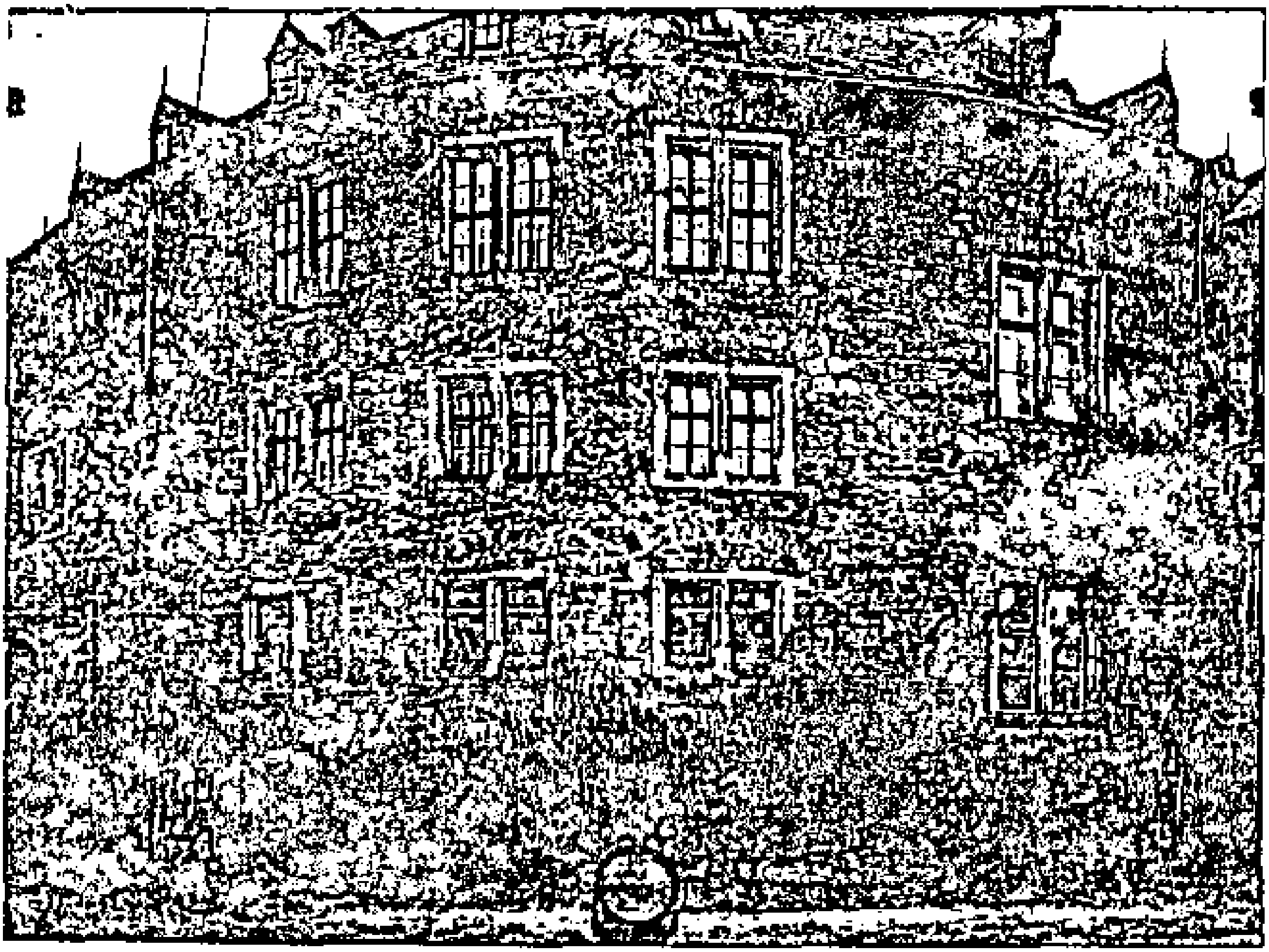

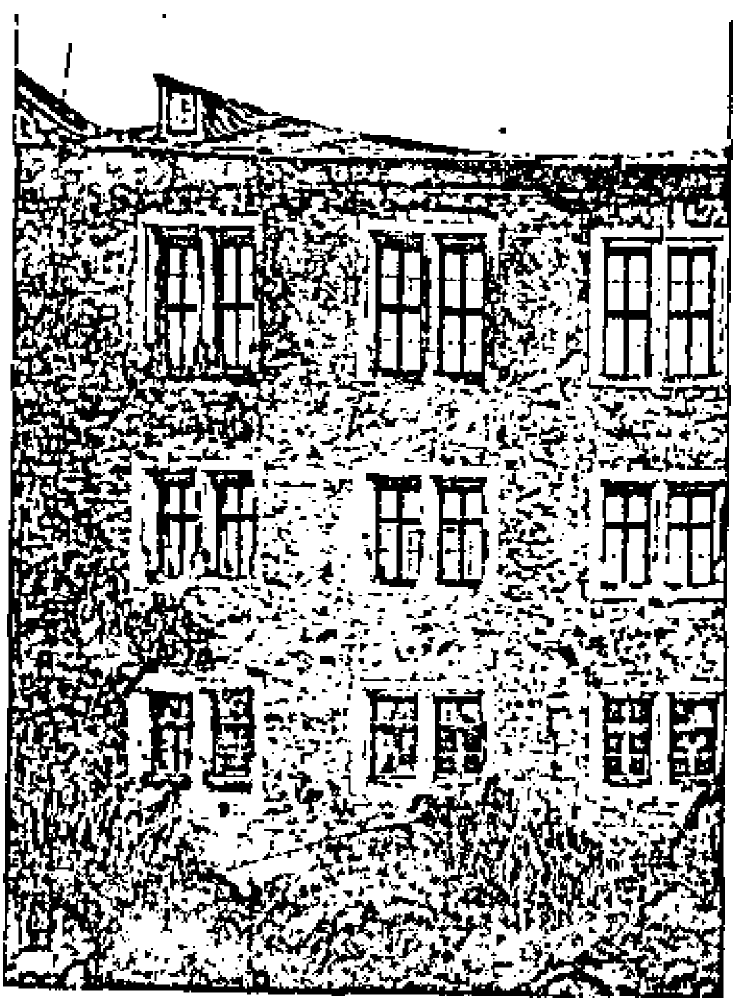

Fig. 4 (above): Original image, obtained from a FINSTERWALDER TAF camera (c= 15 cm , 13x18 cm format). Scale in image center approx. 1:100

Fig. 5 (left): Result: Facade (section) unrolled on a tangential plane (pixel size 0.1 mm)

Literature

/1/ BÄHR, H. P. : Geometrical Analysis and Rectification of LANDSAT MSS Imagery: Comparison of Different Methods. ISP, Symposium Comm. III, Moscow 1978

/2/ BÄHR, H. P. : Digital Image Processing Experience at Hannover Institute for Photogrammetry (IPI). ISP, Comm. III WG 2, Symposium Graz 1977

/3/ BRONSTEIN, I. N., SEMENDJAJEW, K. A.: Taschenbuch der Mathematik. Leipzig 1962

/4/ ELLENBECK, K. H.; WROBEL, B. : Zur Leistungssteigerung der terrestrisch - photogrammetrischen Punktbestimmung. Bildmessung und Luftbildwesen, 1977, S. 69 - 77

/5/ GRÜN, A. : Photogrammetrische Rekonstruktion von Rotationsflächen aus Einzelbildern. Deutsche Geodätische Kommission, Reihe C, Heft 212, München 1975

/6/ KONECNY, G. : Geometrical Aspects of Remote Sensing. ISP Ottawa 1972

/7/ KRAUS, K. : Zur photographischen Entzerrung abwickelbarer Regelflächen. Bildmessung und Luftbildwesen, 1976, p. 168-170

/8/ SEEGER, E : Orthophotography in Architectural Photogrammetry. ISP Helsinki 1976

/9/ WROBEL, B. : Photogrammetrische Bestandsaufnahme des Klosters Walkenried im Harz. Landeskonservator Rheinland, CIPA- Symposium 1976

/10/ : Symposium "Digital Componentsin Photogrammetry". Hannover, 16/17. Feb., 1978 (see Bildmesssung und Luftbildwesen 3/1978; proceedings to be published)

Dr.-Ing.habil. Hans-Peter Bähr

Seminario sobre la teledetección
Universidad nacional autónoma de México

3 al 7 de marzo de 1980

Lista de Libros de Referencia

Avery, T.E.	Interpretation of Aerial Photographs. Burgers Publishing Company, Minneapolis 1977 (sencillo)
Castleman, K.R.	Digital Image Processing. Prentice Hall, Englewood Cliffs 1979 (Jet Propulsion Laboratory, Pasadena)
Colwell, R.N. et al.	Basic Matter and Energy Relationships Involved in Remote Reconnaissance. Photogrammetric Engineering 1963 (elementos fundamentos)
Way, D.S.	Terrain Analysis (Aerial Photography, Geomorphology). McGraw-Hill, New York 1978
Konecny, G.	Geometrical Aspects of Remote Sensing. Proceedings of International Society of Photogrammetry Congress Ottawa 1972 (elementos fundamentos de geometría)
Peel et al.	Remote Sensing of the Terrestrial Environment. Butterworths, London 1976 (Contribuciones de un Seminario en Bristol)
Pratt, W.K.	Digital Image Processing. John Wiley and Sons, New York 1978 (Elementos básicos de la teoría de información)
Rudd, R.D.	Remote Sensing, a better View. Duxbury Press, North Scituate 1974. (Introducción sencilla)
Sabins, F.	Remote Sensing, Principles and Interpretation. W.H. Freeman and Company, San Francisco 1977. (Geología)
Swain, P.H./Davies, S.M.	Remote Sensing: The Quantitative Approach. McGraw-Hill, NY. 1979
erstappen; H.Th.	Remote Sensing in Geomorphology. Elsevier, Amsterdam 1977 (ITC)
	Manual of Remote Sensing. American Society of Photogrammetry 1975 (detallado, voluminoso)

centro de educación continua
división de estudios de posgrado
facultad de ingeniería unam

CURSO: P E R C E P C I O N R E M O T A

DR. HANS PETER BAHR

3 - 7 Marzo, 1980

4. Sistemas de coordenadas (método indirecto)

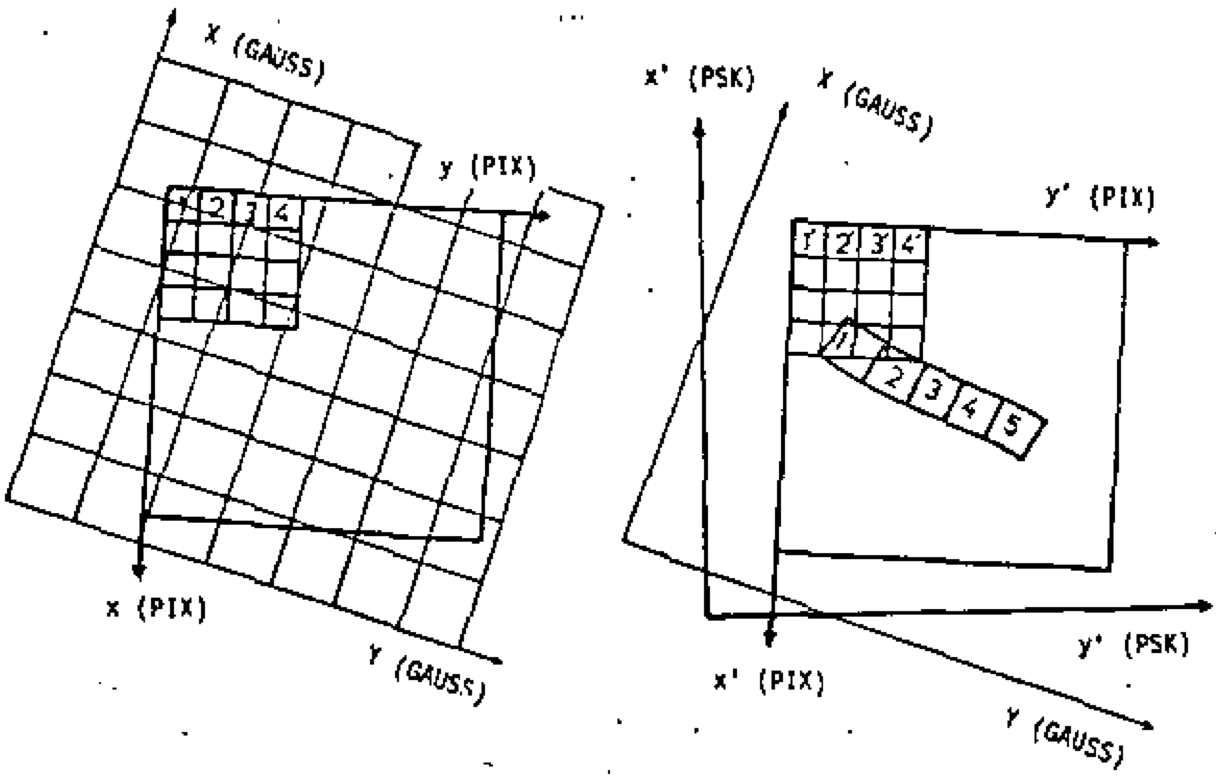

5. LANDSAT : trabajos preparativos geométricos

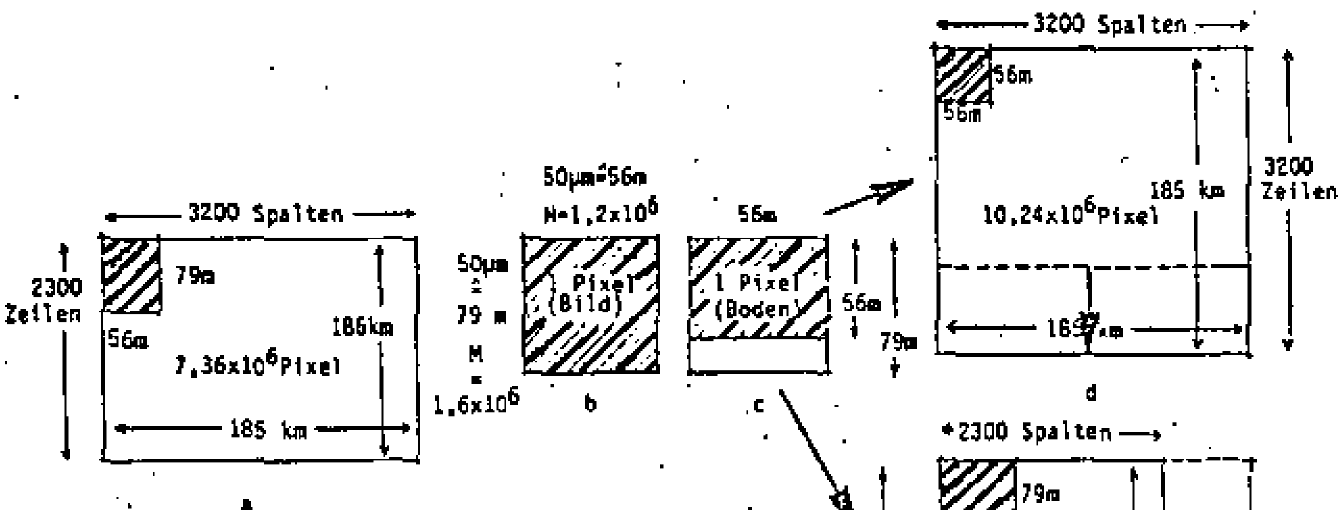

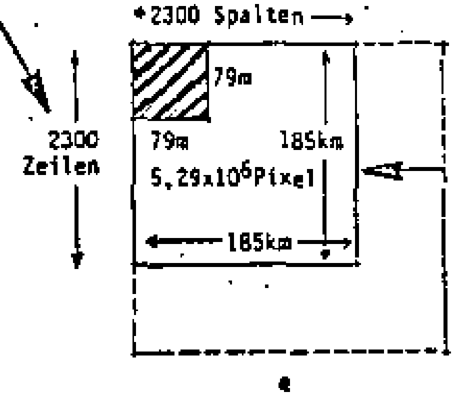

Bildelementgröße und Maßstab (schematisch)

- a Gesamte Originalaufnahme pro Magnetband
- b Bildelement bei Abspielung mit 50 µm
- c Bildelement am Boden
- d Elimination der Affinität durch Dehnung in Flugrichtung
- e Elimination der Affinität durch Stauchung in Abtastrichtung

GREY LEVEL ASSIGNMENT
(Interpolación)

1. Direct

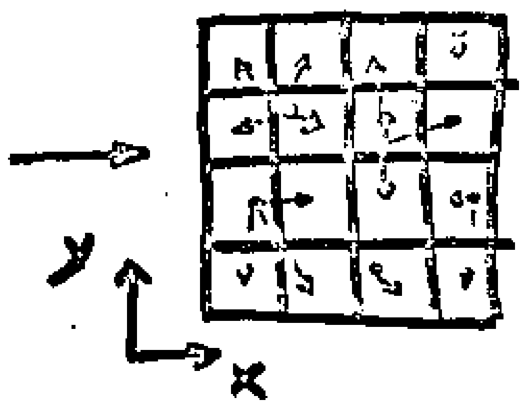

a. NEAREST NEIGHBOUR

2. Indirect

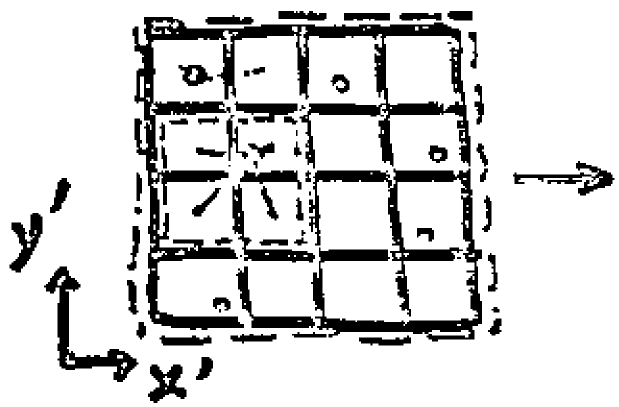

o = nearest neighbour

[4 pixels] = bilinear interpolation

[16 pixels] = cubic convolution

bilinear interpolation:

$$d(x',y') = p_1' \cdot d(u',v'+1) + p_2' \cdot d(u',v') + p_3' \cdot d(u'+1,v'+1) + p_4' \cdot d(u'+1,v')$$

$$p_i' = \frac{1}{d_i'}$$

cubic convolution

$$d(x',y') = p_1' \cdot d(u'-1,v'-1) + \dots p_{16}' d(u'+2,v'+2)$$

2. Rectificación numérica

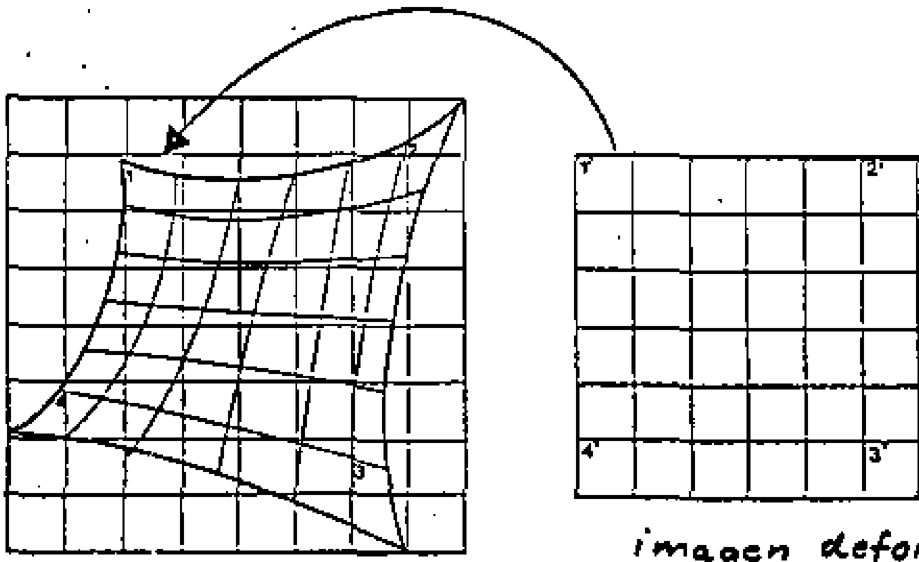

imagen deformada

Entzerrtes Bild
imagen rectificada

Verzerrtes Bild

Prinzip der direkten Entzerrungsmethode
Rectificación directa

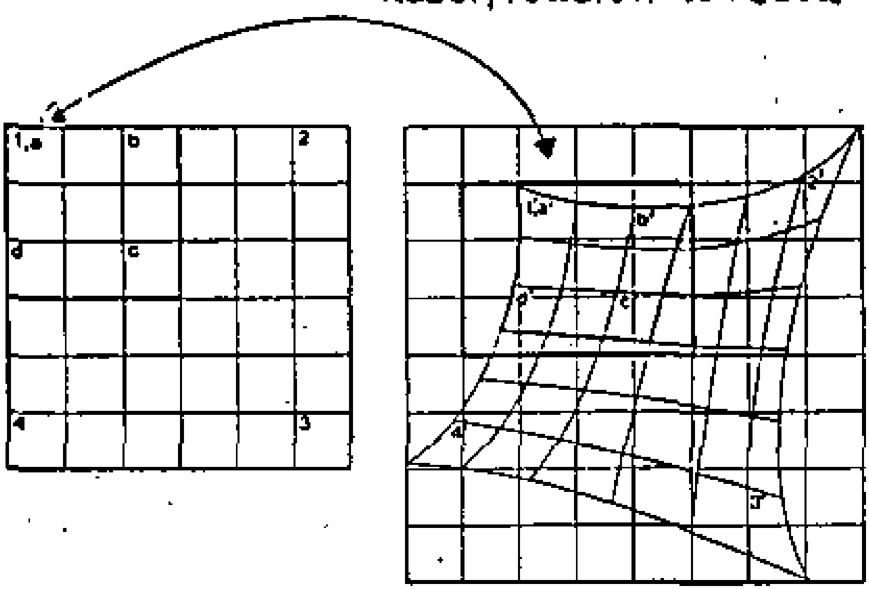

Entzerrtes Bild

Verzerrtes Bild

Prinzip der indirekten Entzerrungsmethode
Rectificación indirecta

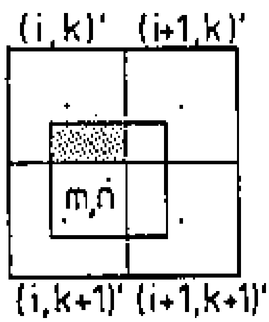

Interpolation des entzerrten Bildelements m,n aus vier benachbarten verzerrten Bildelementen

3. Interpolación de los valores

Reflecciones geométricas

1. Limitación de la exactitud geométrica por las dimensiones de los pixels

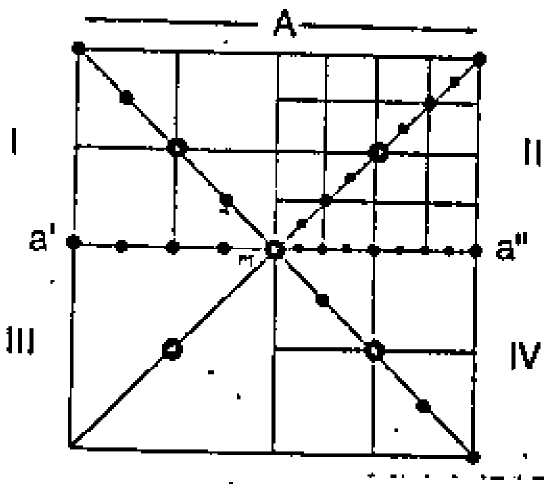

Ableitung der mittleren zufälligen Verschiebung

Formación de la translación media

$$M_v = \sum_{i=1}^{n} \frac{\overline{M_A M}_{n_i}}{n} \quad , \text{ für } n \rightarrow \infty$$

$$SU_{max} = \frac{A\,(1 + 3 + 5 + \ldots + (2n-1))}{n\sqrt{8n^2}} \doteq \pm \frac{A}{\sqrt{8}}$$

$$M_v \approx \pm \frac{\frac{A}{4} + \frac{A}{\sqrt{8}}}{2} = \pm \frac{A}{8}\,(1 + \sqrt{2}) \sim \boxed{\pm\, 0{,}3\, A}$$ **resultado**

"Sampling"

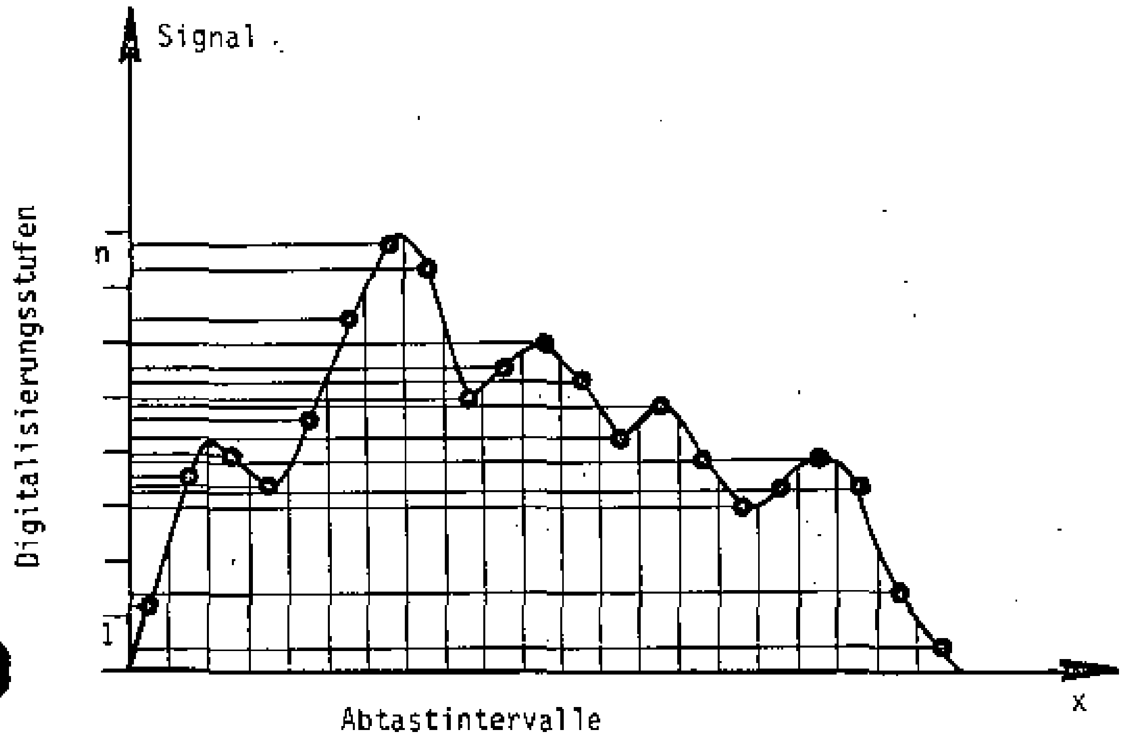

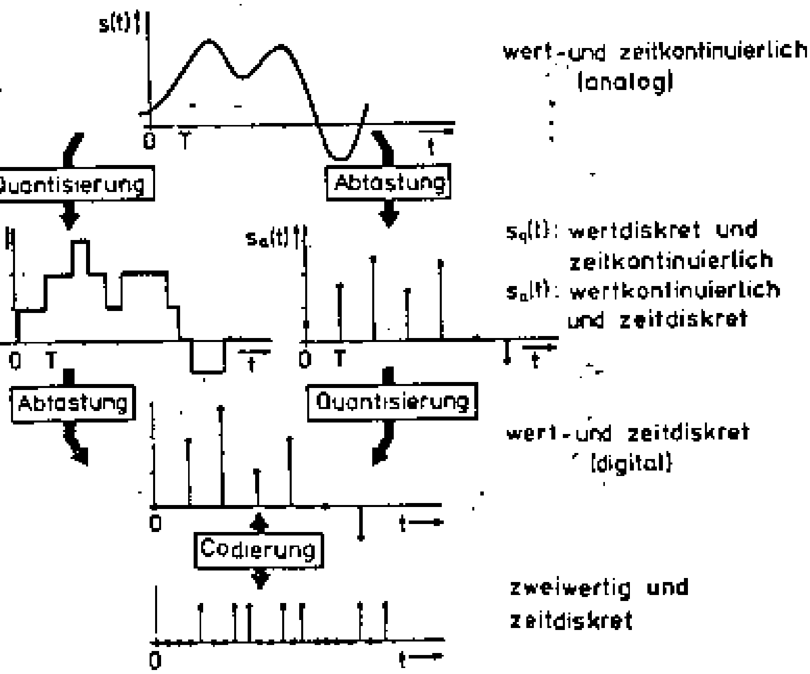

método análogo

método numérico

Datenmenge (Anzahl Bildelemente) bei Digitalisierung klassischer photogrammetrischer Aufnahmen

Cuantidad de pixels después de la numerisación de imágenes fotogramétricas

Sensor:	RMK 30/23 (Luftbildkamera)	TAF (Terrestrische Kamera)	MKF 6 (Weltraumkamera)	para comparación Zum Vergleich: LANDSAT
Bildformat (cm) Tamaño	23 x 23	13 x 18	5,5 x 8,1	16 x 16 (bei 50 μ)
Auflösung (Lp/mm) Resolución	30	50	80	6 (bei 50 μ)
Bildelemente bei korrekter Abtastung (Faktor 3) Cuantidad (Factor:3)	428,5 10^6	526,5 10^6	256,6 10^6	5,3 10^6

5.

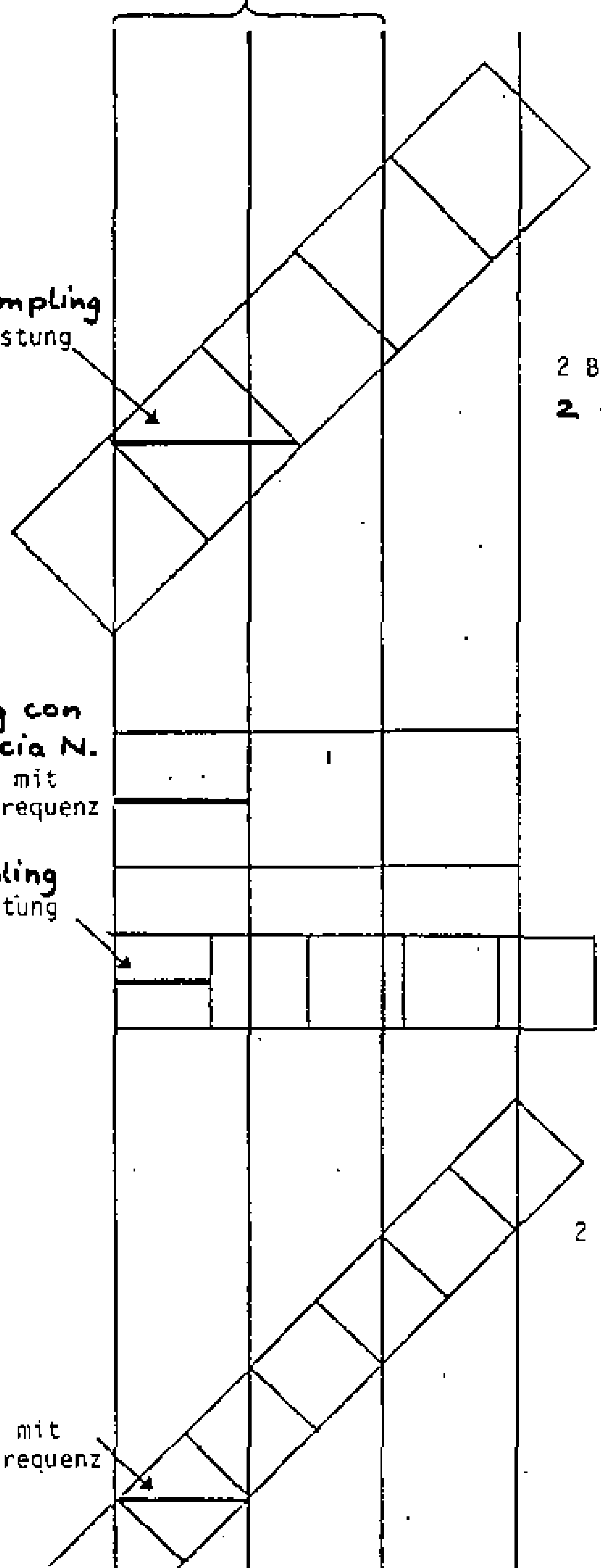
par de líneas
1 Linienpaar
undersampling
Unterabtastung
2 Bildelemente/Linienpaar
2 pixel / par de líneas
sampling con frecuencia N.
Abtastung mit NYQUIST-Frequenz
oversampling
Überabtastung
2 √2 Bildelemente/ Linienpaar
Abtastung mit NYQUIST-Frequenz

Suposiciones por reproducción del

7a.

Voraussetzungen für Wiederherstellung des

Eingangsignals f(x) ohne Informationsverlust

Señal entrado f(x) sin perdida de información

cualidad 1. Eigenschaft des Eingangsignals f(x)	Bandbegrenzung ν
cualidad de la reacción 2. Eigenschaft der Stoßantwort g(x)	Periode $\tau \leq \frac{1}{2\nu}$
3. Eigenschaft des Ausgangsignals f(x)	Interpolation sinc $(2\pi\nu x)$

Interpolationsfehler (nach PRATT)

Sinc - Funktion	0%
Treppenfunktion(Interpolation nullter Ordnung)	15,7%
Dreiecksfunktion (Interpolation erster Ordnung)	3,7%

Praktische Möglichkeit für Interpolation

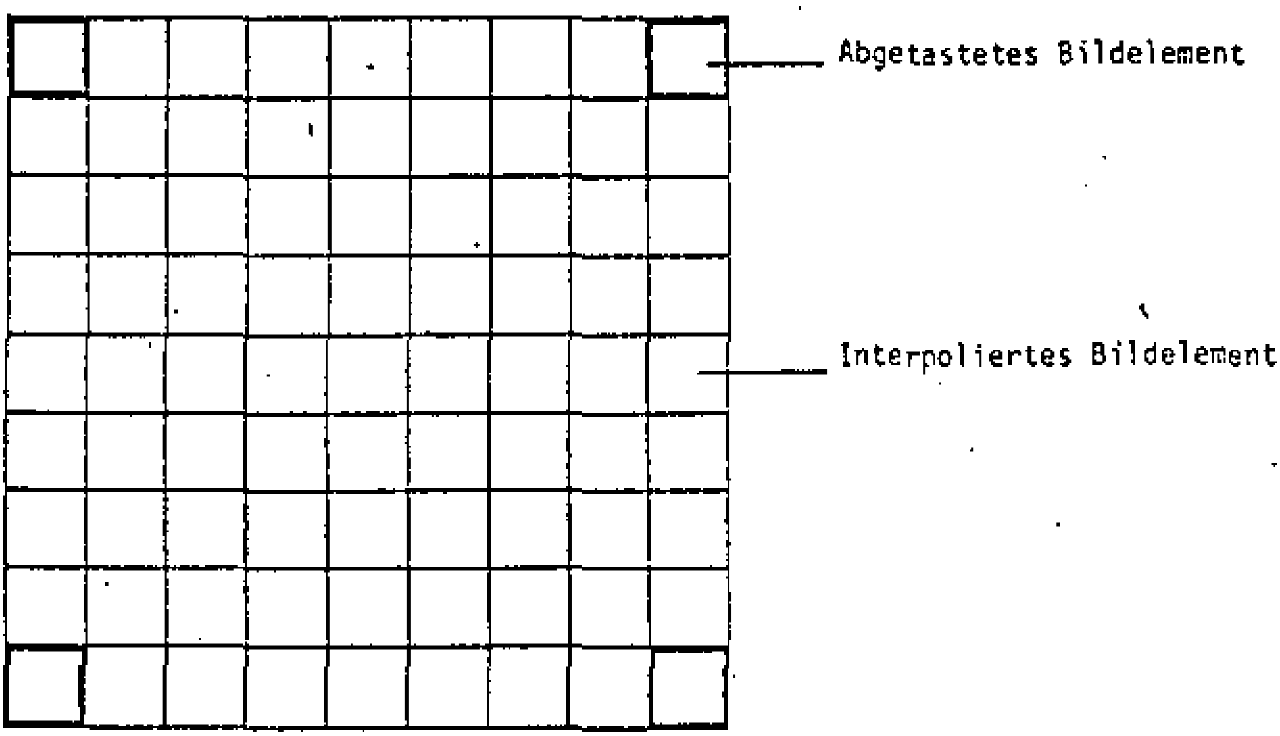

Erhöhung der Datenmenge
um den Faktor 64

Reproducción del señal entrado

4. Wiederherstellung des Eingangssignals f(x)

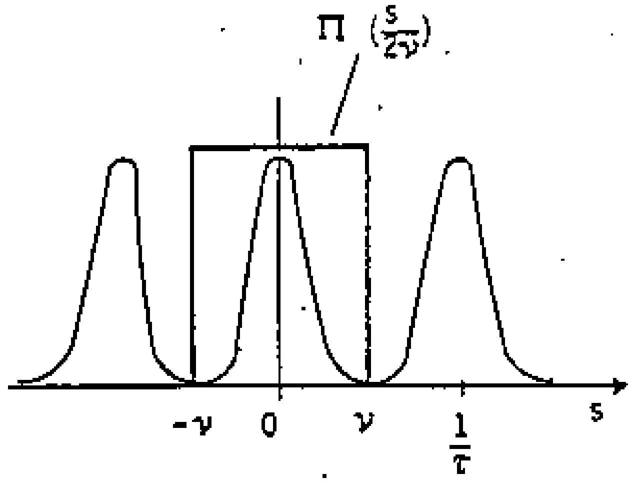

" Tiefpaßfilterung"
Filtro

$$F(s) = G(s)\, \Pi\left(\frac{s}{2\nu}\right)$$

$$\tau \leq \frac{1}{2\nu}$$

Periodo de "sampling"
Abtastperiode
2ν =NYQUIST-Frequenz

$$f(x) = \mathcal{F}^{-1}\left\{G(s)\, \Pi\left(\frac{s}{2\nu}\right)\right\}$$ Inverse Fouriertransformationen

$$= g(x) * \frac{\sin(2\pi \nu x)}{2\pi \nu x}$$ Faltungstheorem

$$= \int_{-\infty}^{+\infty} g(x) \frac{\sin(2\pi\nu\, x-\tau)}{(2\pi\nu\, x-\tau)}\, d\tau$$ Faltungsintegral

$$f(x) = \sum_{n=-\infty}^{n=+\infty} f(n\tau) \boxed{\frac{\sin\left(\frac{\pi x}{\tau} - n\pi\right)}{\left(\frac{\pi x}{\tau} - n\pi\right)}}$$

Interpolationsfunktion
(Sinc - Funktion)

ver pág. 2.1.3 - 110 y - 160

Beispiel für Wiederherstellung

Ejemplo:

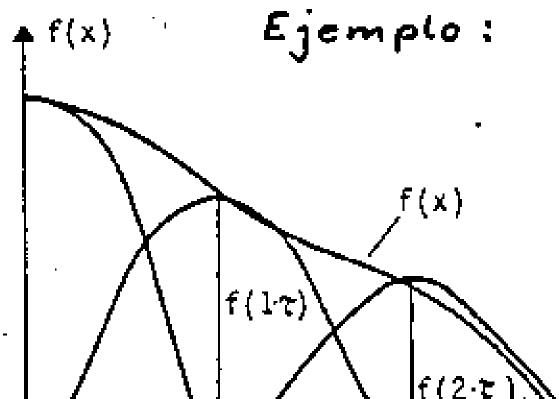

$$R(x,y) = \frac{\sin\left(\frac{\pi x}{t_x} - n\pi\right)}{\frac{\pi x}{t_x} - n\pi} \cdot \frac{\sin\left(\frac{\pi y}{t_y} - n\pi\right)}{\frac{\pi y}{t_y} - n\pi}$$

Interpolación en dos dimensiones

Abtasttheorem *Sampling theorem*

1. Wichtige Funktionen und ihre Fourier-Transformationen

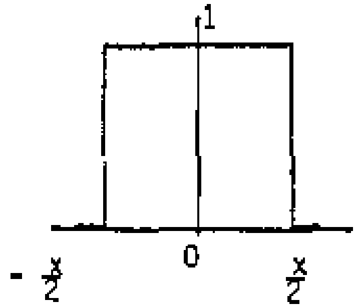

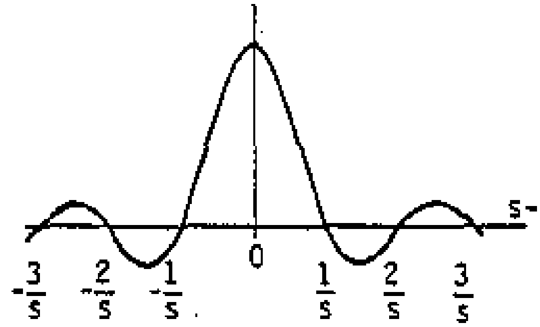

Rechteckimpuls $\Pi(x)$ ←----→ sinc (s)

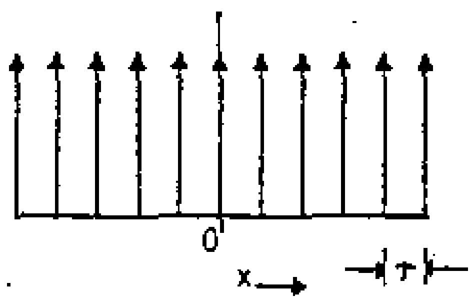

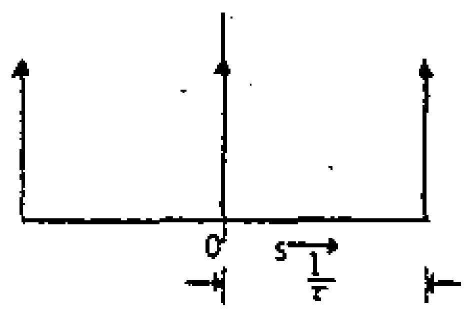

Scha - Funktion $III\left(\frac{x}{\tau}\right)$ ←--------→ Scha - Funktion $\tau III(\tau s)$

2. Bandbegrenzung *Limitación de la banda*

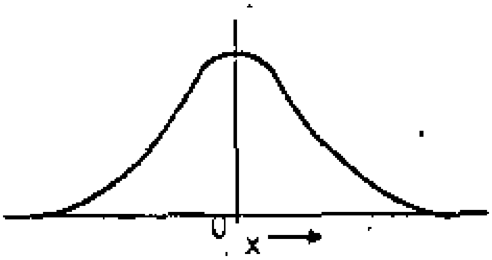

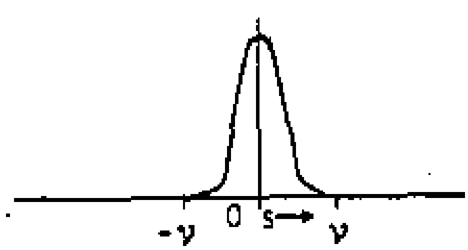

f(x) ←------------ F(s)

$F(s) = 0$
für $|s| \geq \nu$

3. Abtastung

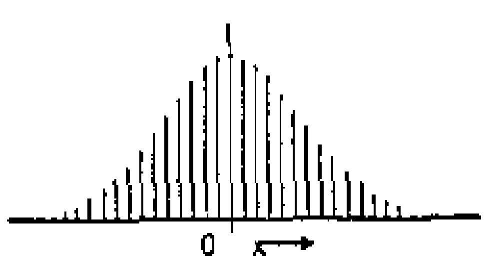

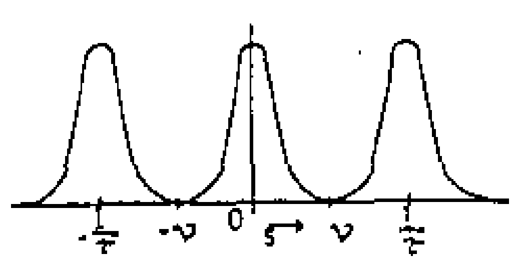

$g(x) = III\left(\frac{x}{\tau}\right) f(x)$ $G(s) = \tau III(\tau s) * F(s)$

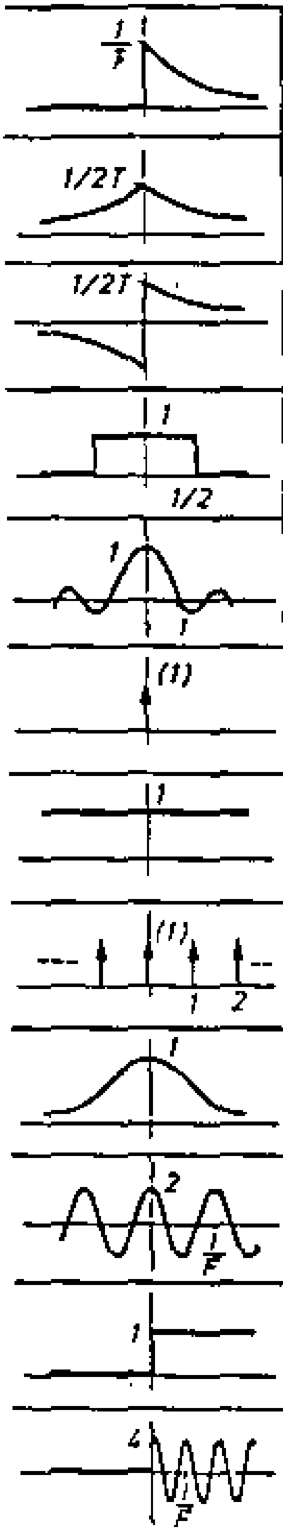

$f(x)$	$F(s)$
$\frac{1}{T}\varepsilon(t)e^{-t/T}$ $(T>0)$ Exponentialimpuls	$\frac{1}{1+j2\pi Tf}$
$\frac{1}{2T}e^{-\lvert t\rvert/T}$ $(T>0)$ Doppelexponentialimpuls	$\frac{1}{1+(2\pi Tf)^2}$
$\frac{1}{2T}\,\mathrm{sgn}(t)\,e^{-\lvert t\rvert/T}$	$-j\,\frac{2\pi Tf}{1+(2\pi Tf)^2}$
$\mathrm{rect}(t)$ Rechteckimpuls	$\mathrm{si}(\pi f)$
$\mathrm{si}(\pi t)$ si – Funktion	$\mathrm{rect}(f)$
$\delta(t)$ Diracstoß	1
1 Gleichstrom	$\delta(f)$
Ш(t) Diracstoßfolge	Ш(f)
$e^{-\pi t^2}$ Gaußimpuls	$e^{-\pi f^2}$
$2\cos(2\pi Ft)$ cos – Funktion	$\delta(f+F)+\delta(f-F)$
$\varepsilon(t)$ Sprungfunktion	$\frac{1}{2}\delta(f)-j\,\frac{1}{2\pi f}$
$4\varepsilon(t)\cdot\cos(2\pi Ft)$ geschaltete cos-Funktion	$\delta(f+F)+\delta(f-F)-\frac{j}{\pi}\,\frac{2f}{f^2-F^2}$

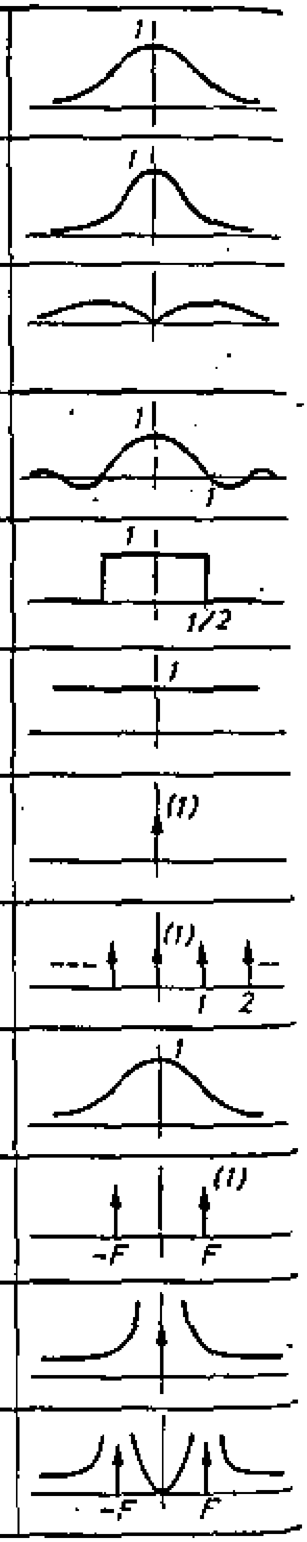

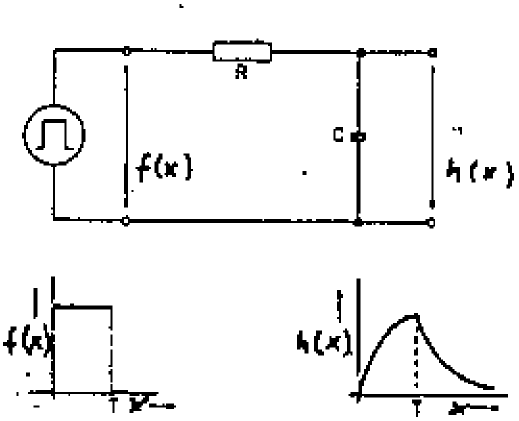

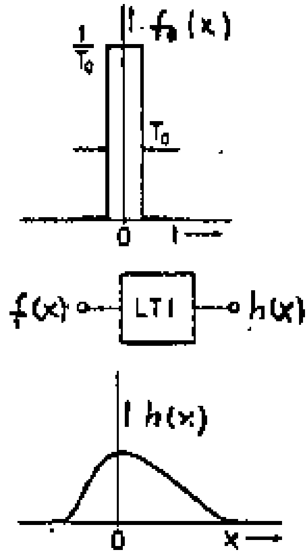

Reacción de un sistema lineal por un señal rectángulo

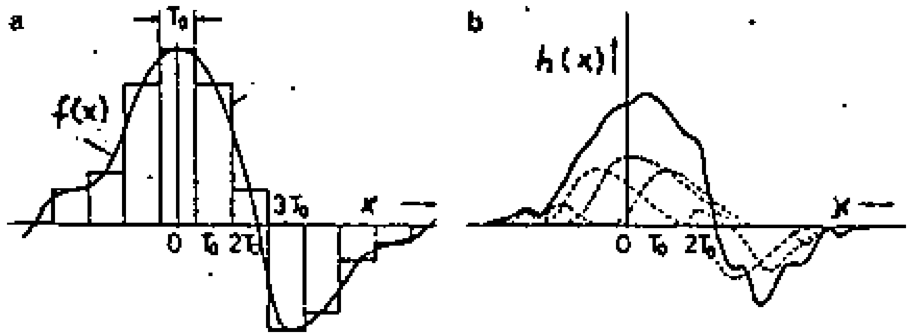

Aproximación de una función con señales rectángulos

$h(x) = f(x) * g(x)$
$H(s) = F(s) \quad G(s)$

für lineare Systeme

$$h(x) = \int_{-\infty}^{+\infty} f(\tau) \; g(x - \tau) \, d\tau$$

Faltungsintegral *Integral de convolución*

$$\mathcal{F}\{h(x)\} = H(s) = \int_{-\infty}^{+\infty} h(x) \, e^{-j2\pi sx} \, dx$$

Fouriertransformation von h(x) *Transformación de Fourier*

$$\mathcal{F}^{-1}\{F(s) \; G(s)\} = f(x) * g(x)$$

Faltungstheorem *Teorema de convolución*

↑ *función inversa*

Procedemiento numórica de las imagenes
— Sistemas lineales —

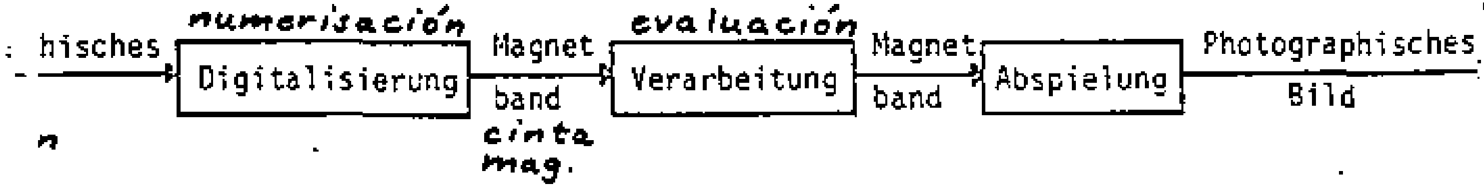

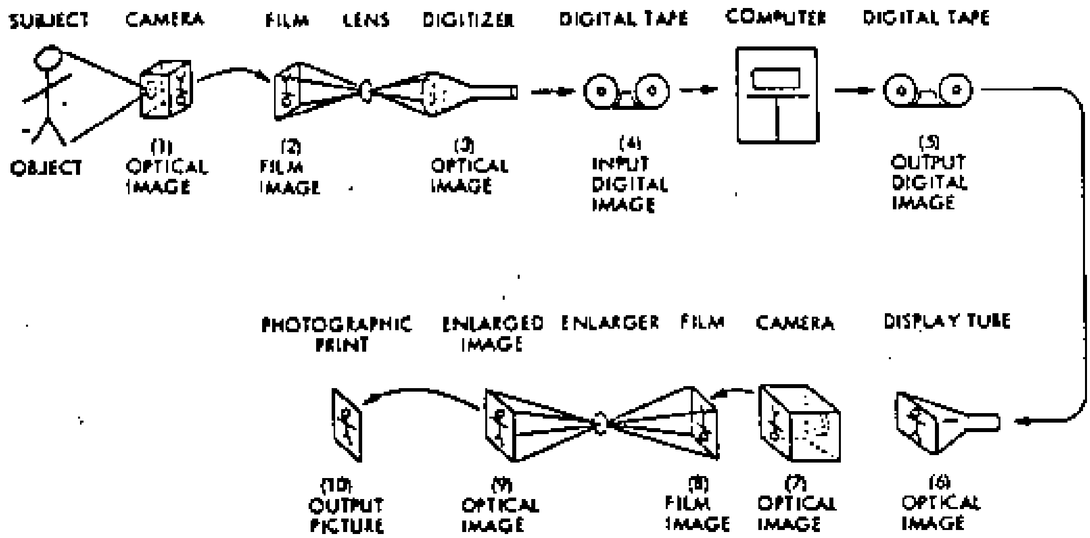

señal entrado		contestación		señal salido	
f(x)	Eingangssignal	g(x)	Stoßantwort	h(x)	Ausgangssignal
F(s)	Spektrum des Eingangssignals	G(s)	Übertragungsfunktion	H(s)	Spektrum des Ausgangssignals

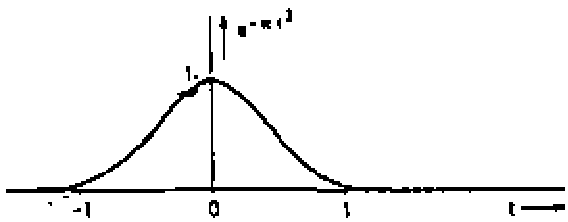

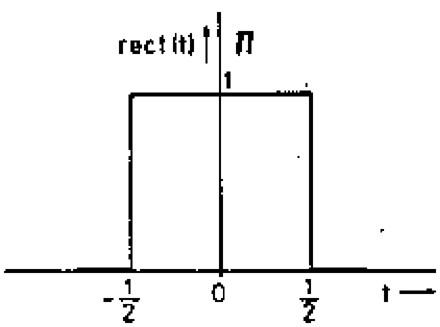

Señales elementarios

4. Forma

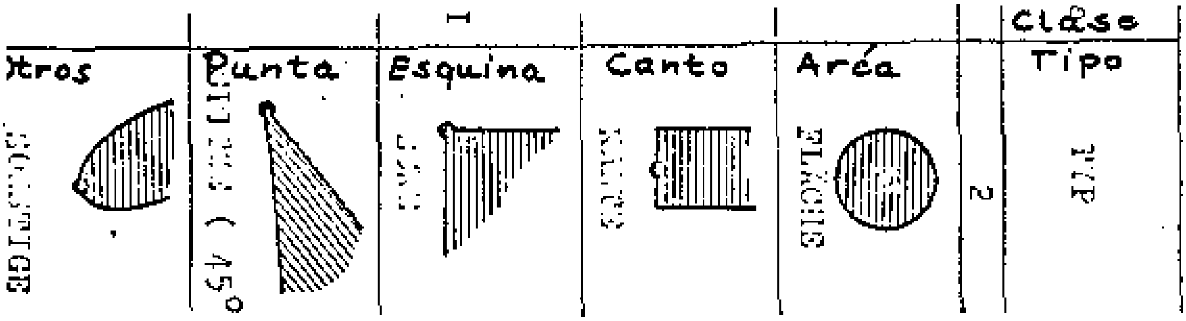

	Klasse	I	II	III	IV	V
	Bezeichnung	Flächen	Kanten	Ecken	Spitzen	Sonstige
Cantidad absoluta	Anzahl der Punkte	17	25	166	12	14
Frecuencia	Häufigkeit in %	7	11	71	5	6
Error standard	mittlerer Fehler m_x/m_y (Mittel)	46,7/44,9 (45,8)	43,5/47,5 (45,5)	42,0/46,1 (44,0)	62,2/63,9 (63,1)	74,9/41,5 (58,2)

Análisis estadístico de significancia	Hypothese gegen	Alternative	Freiheitsgrade m	n	c aus der Tabelle der Fisher-Verteilung für α = 5% (vgl. KREYSZIG)	$v_o = \frac{m_i^2}{m_j^2}$	$v_o \leq c$	$v_o > c$
	$m_V^2 = m_I^2$	$m_V^2 > m_I^2$	13	16	2,40	1,61	$v_o < c$	
	$m_I^2 = m_{II}^2$	$m_I^2 > m_{II}^2$	16	24	2,09	1,01	$v_o < c$	
	$m_I^2 = m_{III}^2$	$m_I^2 > m_{III}^2$	16	165	1,71	1,08	$v_o < c$	
	$m_{IV}^2 = m_I^2$	$m_{IV}^2 > m_I^2$	11	16	2,46	1,90	$v_o < c$	
	$m_V^2 = m_{II}^2$	$m_V^2 > m_{II}^2$	13	24	2,16	1,63	$v_o < c$	
	$m_{II}^2 = m_{III}^2$	$m_{II}^2 > m_{III}^2$	13	165	2,79	1,75	$v_o < c$	
	$m_{IV}^2 = m_V^2$	$m_{IV}^2 > m_V^2$	11	13	2,64	1,18	$v_o < c$	
	$m_{II}^2 = m_{III}^2$	$m_{II}^2 > m_{III}^2$	24	165	1,59	1,07	$v_o < c$	
	$m_{IV}^2 = m_{II}^2$	$m_{IV}^2 > m_{II}^2$	11	24	2,22	1,92	$v_o < c$	
	$m_{IV}^2 = m_{III}^2$	$m_{IV}^2 > m_{III}^2$	11	165	1,85	2,05		$v_o > c$
	$m_A^2 = m_B^2$	$m_A^2 > m_B^2$	233	233	1,32	1,05	$v_o < c$	
	$m_G^2 = m_B^2$	$m_G^2 > m_B^2$	233	233	1,32	1,10	$v_o < c$	

que ne

Puntos de apoyo

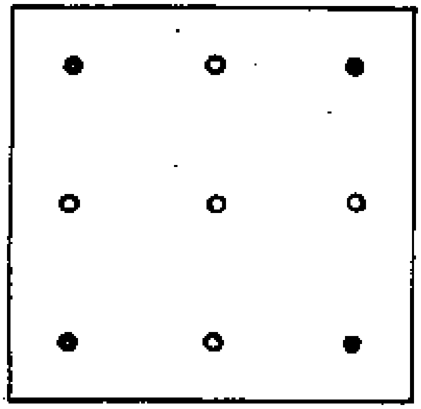

Observar

1. La cuantidad
2. La posición

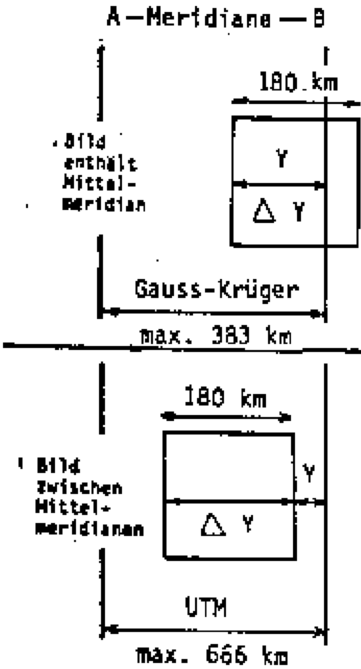

3. El sistema de coordenadas

Ejemplos

a) Gauss-Krüger

Y [km]	0	10	50	76	100	150	180	200	234
ΔY [m]	0	0	0.5	2	4	14	24	-	-
ΔY [m]	24	28	49	67	86	133	168	192	239

b) UTM

$$m_d = \pm\sqrt{\frac{\sum_{i=1}^{n} d_i d_i}{2n-1}}$$

Error standard de mediciones dobles

Imagen (cantidad puntos) / Bild (Punkte)	Bayern (234)			Norddeutschland (82)	
Observatore / Beobachter	A	B	G	B	J
$m_d(x/y)\pm$	2.8/2.7	8.4/9.1	4.9/5.4	7.5/7.5	7.4/5.3

(Imagen LANDSAT)

Kombination	A-B	A-G	B-G	B-J
$M(x/y)\pm$	17.2/18.6	21.1/20.5	20.8/20.7	12.3/11.2

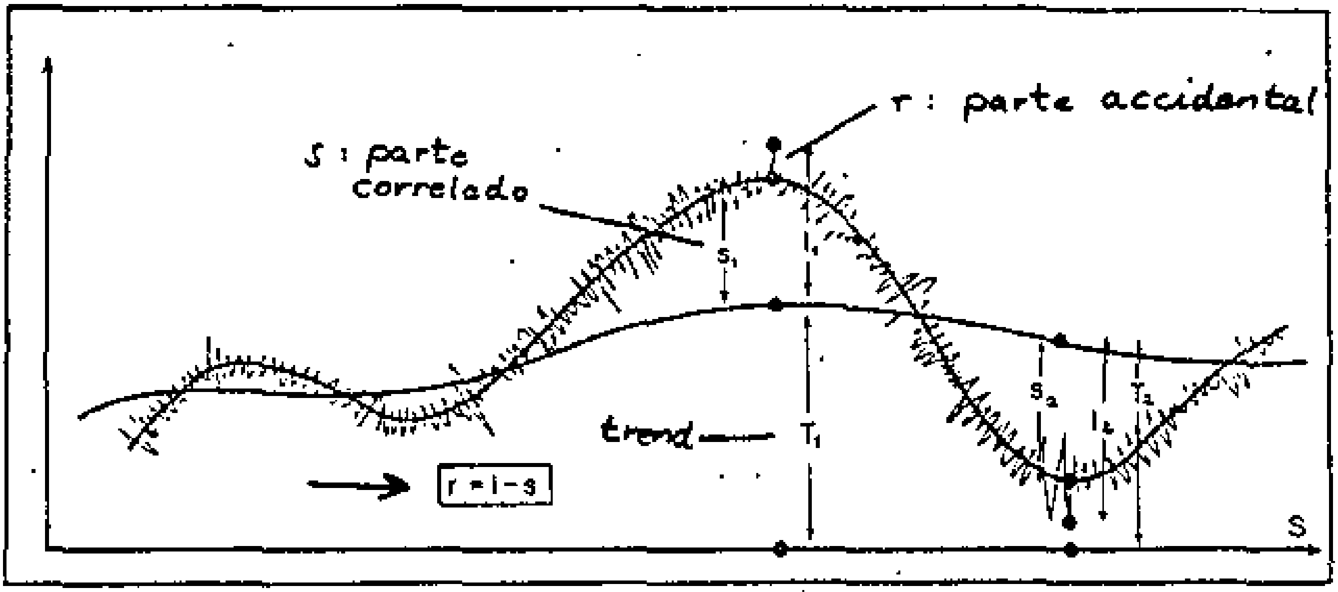

Trend T und Restfehler l, mit korreliertem Anteil s und zufälligem Anteil r

$$\tilde{l}_i = a_1\, l_1 + a_2\, l_2 + \ldots + a_n\, l_n$$

$$m_p^2 = \frac{[(l_p - \tilde{l}_p)]}{n} \longrightarrow \text{Min}$$ *método de cuadrados mínimos*

$$l_i = (s + r)_i \quad , \quad \text{falls} \quad E\{0\}$$

$$\tilde{l}_i = \underline{c}_i^T \left(\underline{\underline{C}}_{ss} + \underline{\underline{C}}_{ss} \right)^{-1} \underline{l}$$ *C : ecuación de correlación*

$$\tilde{l}_i = \begin{pmatrix} C(\overline{P_1P_i}) \\ C(\overline{P_2P_i}) \\ \vdots \\ C(\overline{P_nP_i}) \end{pmatrix} \begin{pmatrix} V & C(\overline{P_1P_2}) & \ldots & C(\overline{P_1P_n}) \\ & V & \ldots & C(\overline{P_2P_n}) \\ & & & \vdots \\ & & & V \end{pmatrix} \begin{pmatrix} l_1 \\ l_2 \\ \vdots \\ l_n \end{pmatrix}$$

$$\left.\begin{aligned} C_{i,k} &= C\,(0)\; e^{-k^2S^2} \\ V &= V_s + V_r = \frac{1}{n} \sum_{i=1}^{n} (l_i l_i) \\ C_{i,k} &= F\; V\; e^{-k^2S^2} \end{aligned}\right\}$$ *V : vertices*

Métodos simplificados

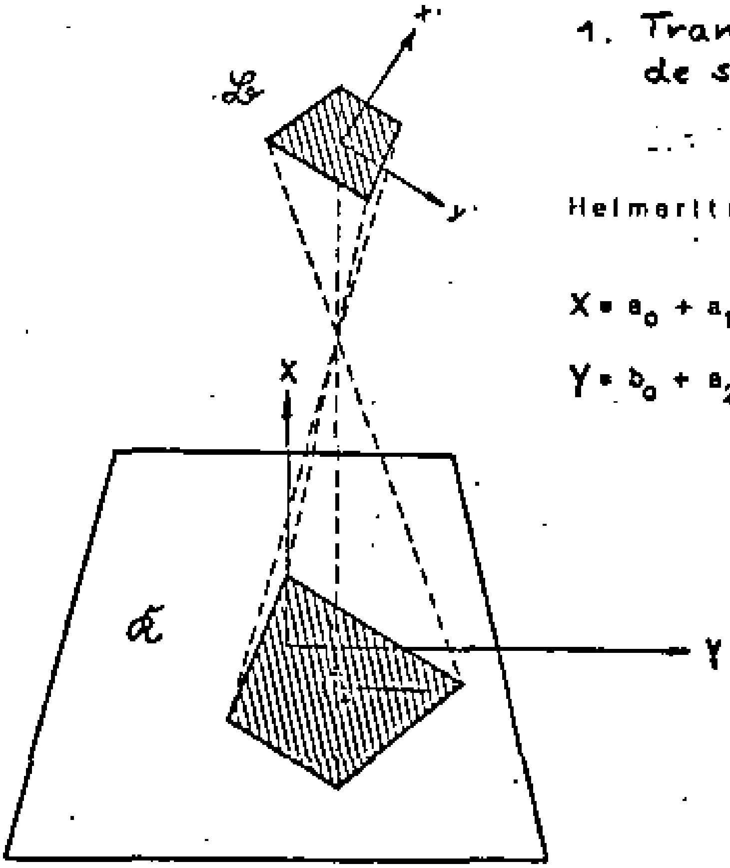

1. Transformación plana de semejanza

Helmerttransformation

$$X = a_0 + a_1 x' - a_2 y'$$

$$Y = b_0 + a_2 x' + a_1 y'$$

Escala:

$$M = \sqrt{a_1^2 + a_2^2}$$

Translación:

a_0, b_0

Rotación:

$$\alpha = \arctan\left(\frac{a_2}{a_1}\right)$$

2. Transformación afín

$$X = a_0 + a_1 x' + a_2 y'$$

$$Y = b_0 + b_1 x' + b_2 y'$$

mit dem Affinitätsfaktor

$$F_A = \frac{a_1^2 + a_2^2}{b_1^2 + b_2^2}$$

(Proporción de las escalas)

sowie Polynome 2. Grades der Form

3. Polínomos de segundo grado

$$X = a_0 + a_1 x' + a_2 y' + a_3 x'^2 + a_4 y'^2 + a_5 x' y'$$

$$Y = b_0 + b_1 x' + b_2 y' + b_3 x'^2 + b_4 y'^2 + b_5 x' y'$$

Ecuaciones de compensación rigurosas

9a

$$v_x = dx - (x_{gemessen} - x)$$
$$v_y = dy - (y_{gemessen} - y)$$
$$v_z = dz - (z_{gemessen} - z)$$

$$dx = \frac{\partial x}{\partial r} dr + \frac{\partial x}{\partial \theta} d\theta + \frac{\partial x}{\partial u} du + \frac{\partial x}{\partial i} di$$
$$dy = \frac{\partial y}{\partial r} dr + \frac{\partial y}{\partial \theta} d\theta + \frac{\partial y}{\partial u} du + \frac{\partial y}{\partial i} di$$
$$dz = \frac{\partial z}{\partial r} dr + \frac{\partial z}{\partial \theta} d\theta + \frac{\partial z}{\partial u} du + \frac{\partial z}{\partial i} di$$

$$r = r_T + dr = r_T + a_0 + a_1 T + a_2 T^2 + \ldots$$
$$\theta = \theta_T + d\theta = \theta_T + b_0 + b_1 T + b_2 T^2 + b_3 T^3 + \ldots$$
$$u = u_T + du = u_T + c_0 + c_1 T + c_2 T^2 + \ldots$$
$$i = i_T + di = i_T + d_0 + d_1 T + d_2 T^2 + \ldots$$

Primera formación

Desarollo polinominal de r, θ, u, i

$$dx = \frac{\partial x}{\partial R} dR + \frac{\partial x}{\partial \phi} d\phi + \frac{\partial x}{\partial \kappa} d\kappa + \frac{\partial x}{\partial \omega} d\omega$$
$$dy = \frac{\partial y}{\partial R} dR + \frac{\partial y}{\partial \phi} d\phi + \frac{\partial y}{\partial \kappa} d\kappa + \frac{\partial y}{\partial \omega} d\omega$$
$$dz = \frac{\partial z}{\partial R} dR + \frac{\partial z}{\partial \phi} d\phi + \frac{\partial z}{\partial \kappa} d\kappa + \frac{\partial z}{\partial \omega} d\omega$$

$$R = R_T + dR = R_T + a_0 + a_1 T + a_2 T^2 + \ldots$$
$$\phi = \phi_T + d\phi = \phi_T + b_0 + b_1 T + b_2 T^2 + \ldots$$
$$\kappa = \kappa_T + d\kappa = \kappa_T + c_0 + c_1 T + c_2 T^2 + \ldots$$
$$\omega = \omega_T + d\omega = \omega_T + d_0 + d_1 T + d_2 T^2 + d_3 T^3 + \ldots$$

Segunda formación

Desarollo polinominal de R, ϕ, ω, κ

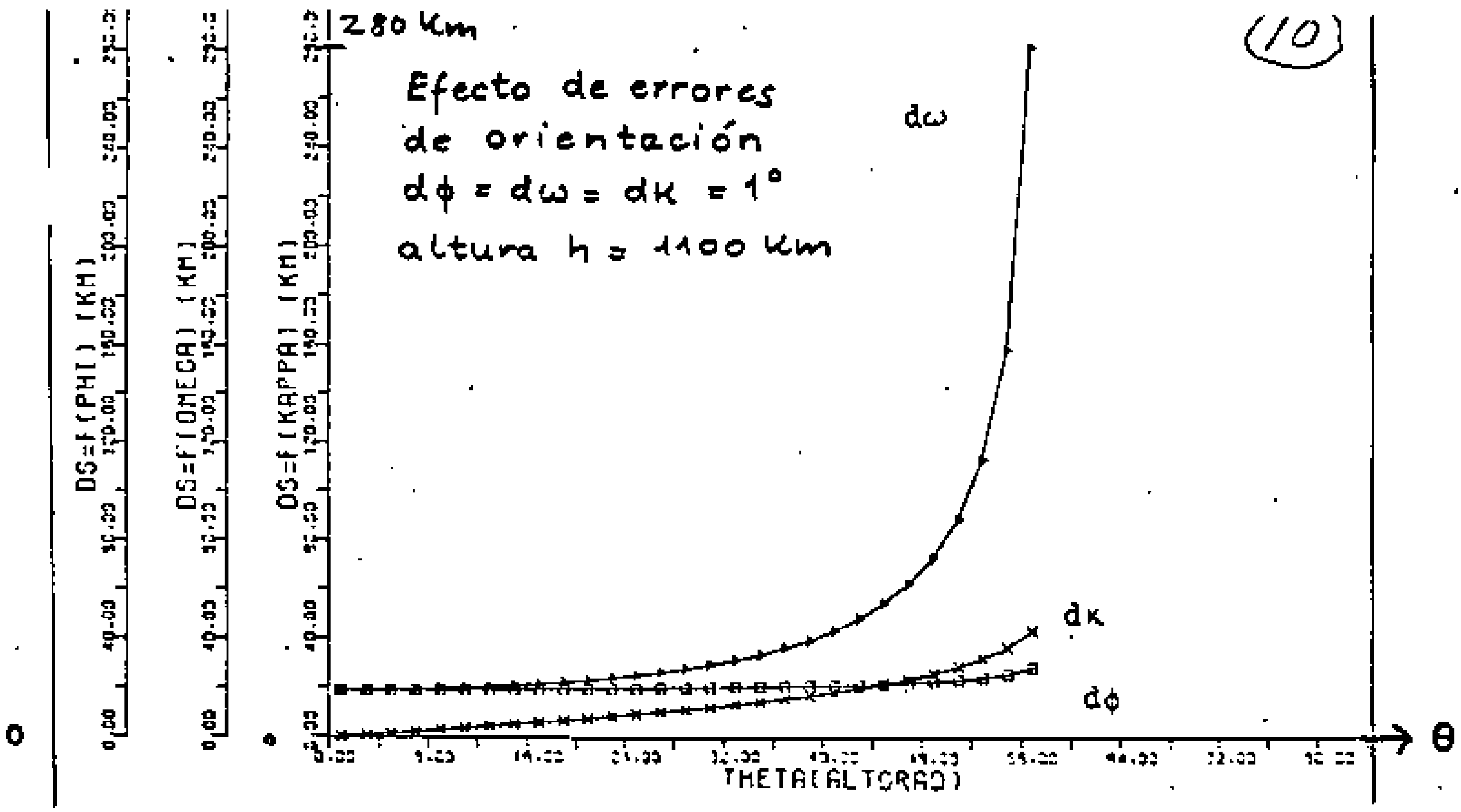
(10)
280 Km
Efecto de errores de orientación
dφ = dω = dκ = 1°
altura h = 1100 Km
dω
dκ
dφ
θ
DS=F(PHI) (KM)
DS=F(OMEGA) (KM)
DS=F(KAPPA) (KM)
THETA(ALTGRAD)

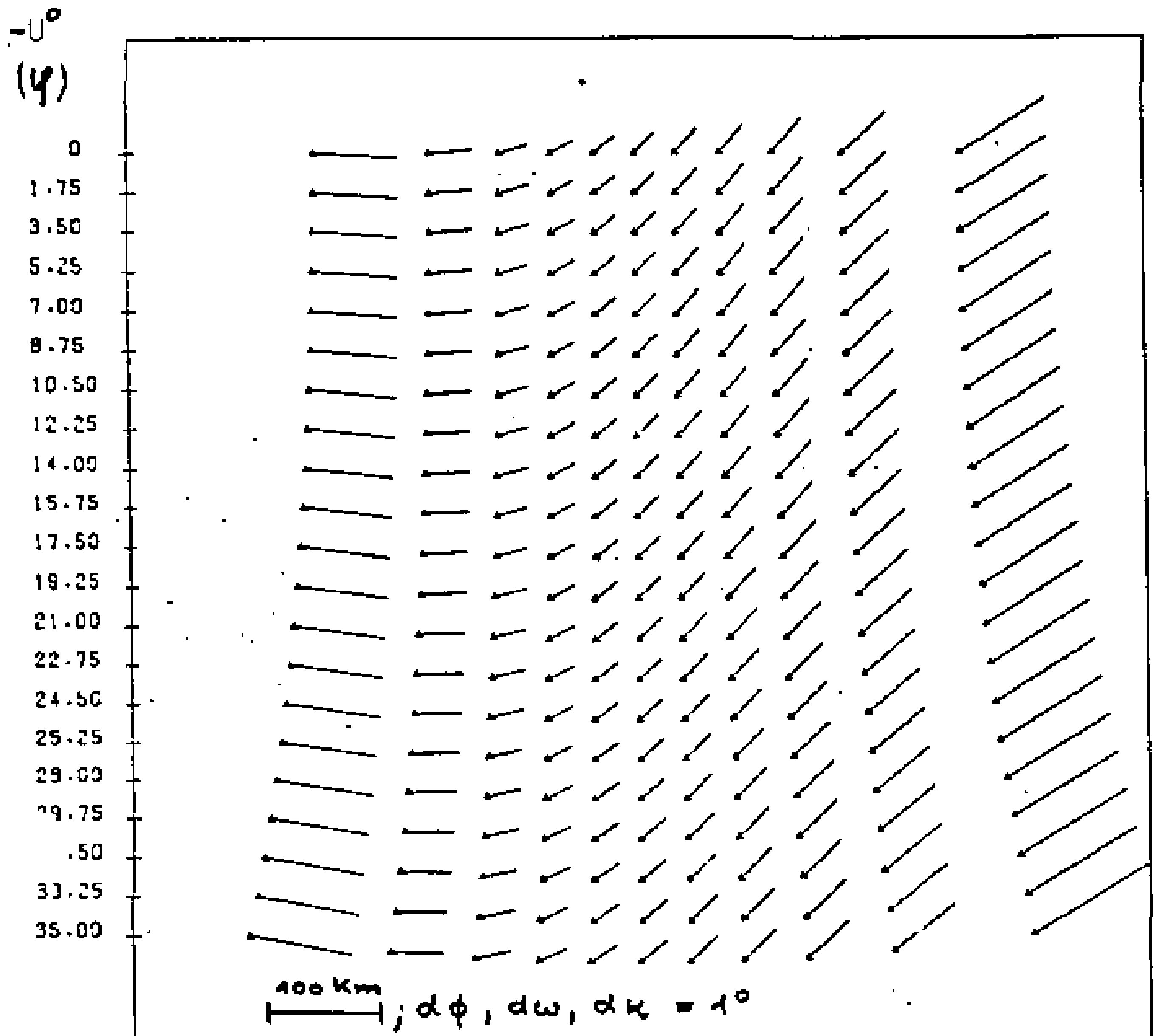
-U°
(ψ)
0
1.75
3.50
5.25
7.00
8.75
10.50
12.25
14.00
15.75
17.50
19.25
21.00
22.75
24.50
26.25
28.00
29.75
.50
33.25
35.00
400 Km ; dφ, dω, dκ = 1°

2 casos especiales

1. Satélito sobre el ecuador ($\varphi = \lambda = 0$)

S O N D E R F A L L 1 : Subsatellitenpunkt PS auf Äquator am Nullmeridian ($x_{PS} = y_{PS} = 0$)

$$u = 0^0,\quad i = 90^0,\quad \Omega = 0^0 \longrightarrow \underline{D} = \begin{pmatrix} 0 & -1 & 0 \\ 1 & 0 & 0 \\ 0 & 0 & 1 \end{pmatrix}$$

$$\begin{pmatrix} x \\ y \\ z \end{pmatrix} = \underline{D}^T\underline{k} = \begin{pmatrix} d'_\theta \sin\theta - d'_\theta \cos\theta\, d\omega \\ - d'_\theta \sin\theta\, d\kappa - d'_\theta \cos\theta\, d\phi \\ - d'_\theta \sin\theta\, d\omega - d'_\theta \cos\theta + r \end{pmatrix}$$

$$\Delta s = ((\underline{D}^T\underline{k})_{d\phi,d\omega,d\kappa\neq 0} - (\underline{D}^T\underline{k})_{d\phi,d\omega,d\kappa=0})^T ((\underline{D}^T\underline{k})_{d\phi,d\omega,d\kappa\neq 0} - (\underline{D}^T\underline{k})_{d\phi,d\omega,d\kappa=0})$$

$$\Delta s = \sqrt{(d'_\theta - d_\theta)^2 + d'^2_\theta\, d\omega^2 + (d_\theta \sin\theta\, d\kappa + d_\theta \cos\theta\, d\phi)}$$

	Fall 1a $\theta = 0$ $d\phi,\ d\omega,\ d\kappa \neq 0$	Fall 1b $d\kappa, \theta \neq 0$ $d\phi,\ d\omega = 0$	Fall 1c $d\omega, \theta \neq 0$ $d\phi,\ d\kappa = 0$	Fall 1d $d\phi,\ \theta \neq 0$ $d\omega,\ d\kappa = 0$
x	$-d d\omega$	$d\sin\theta$	$d\sin\theta - d'\cos\theta d\omega$	$d\sin\theta$
y	$-d d\phi$	$-d\sin\theta d\kappa$	0	$-d\cos\theta d\phi$
z	$-d+r$	$-d\cos\theta + r$	$r + d'\cos\theta - d'\sin\theta d\omega$	$-d\cos\theta + r$
Δs	$\sqrt{d^2 d\omega^2 + d^2\cos^2\theta d\phi^2}$	$d\sin\theta d\kappa$	$\sqrt{(d'-d)^2 + d'^2 d\omega^2}$	$d\cos\theta d\phi$

Efecto de errores de orientación

Auswirkung von Orientierungsfehlern auf die geozentrischen Koordinaten für Sonderfall 1

2. Movimiento del satélito a lo largo del meridio

S O N D E R F A L L 2 : Bewegung des Subsatellitenpunktes entlang des Nullmeridians $\lambda = 0$

$$i = 90^0,\quad \Omega = 0^0 \longrightarrow \underline{D} = \begin{pmatrix} 0 & -\cos u & \sin u \\ 1 & 0 & 0 \\ 0 & -\sin u & \cos u \end{pmatrix}$$

$$\underline{D}^T\underline{k} = \begin{pmatrix} x \\ y \\ z \end{pmatrix} = \begin{pmatrix} d'_\theta \sin\theta - d'_\theta \cos\theta\, d\omega \\ -d'_\theta \cos u \sin\theta\, d\kappa - d'_\theta \cos u \cos\theta\, d\phi + d'_\theta \sin u \sin\theta\, d\omega + d'_\theta \sin u \cos\theta - \sin u\, r \\ d'_\theta \sin u \sin\theta\, d\kappa + d'_\theta \sin u \cos\theta\, d\phi - d'_\theta \cos u \sin\theta\, d\omega - d'_\theta \cos u \cos\theta + \cos u\, r \end{pmatrix}$$

$$\begin{pmatrix} dx \\ dy \\ dz \end{pmatrix} = dR \begin{pmatrix} \bar{U} \sin\theta \\ -\sin u + \bar{U}\cos\theta \sin u \\ \cos u - \bar{U}\cos\theta\cos u \end{pmatrix},\quad \text{mit } \bar{U} = \frac{dd_\theta}{dR} = \cos\theta + \frac{r\sin^2\theta - R}{\sqrt{R^2 - r^2\sin^2\theta}}$$

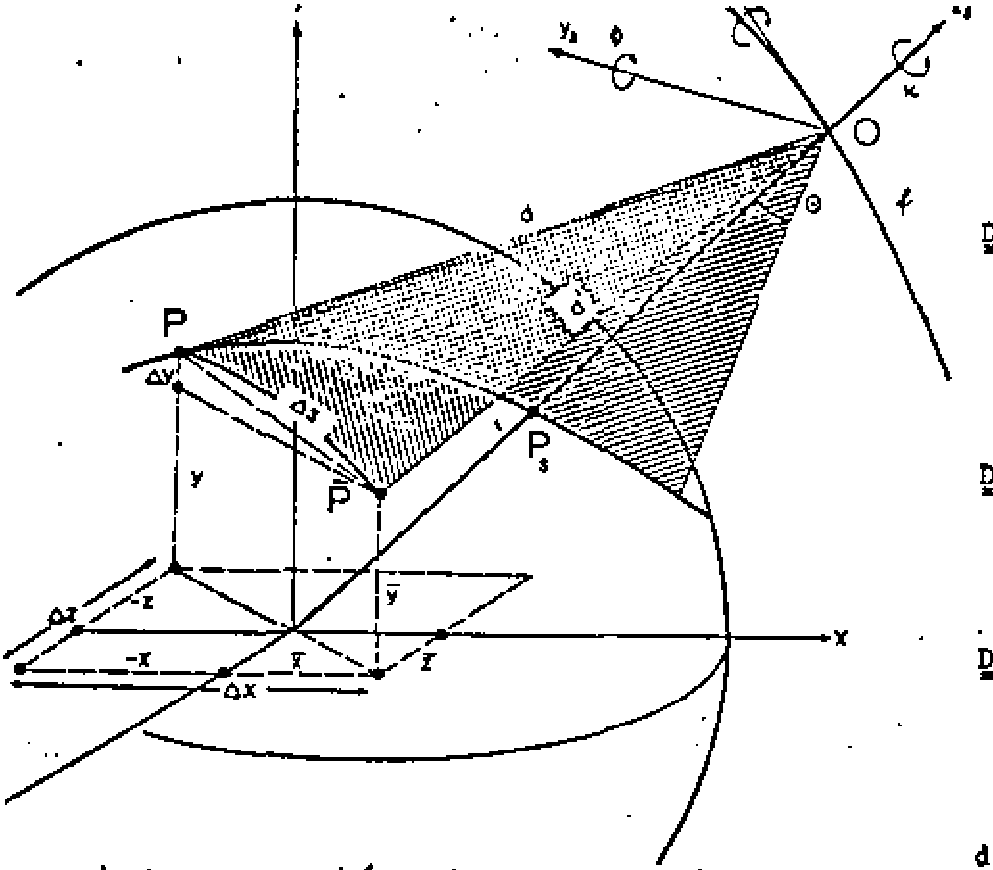

Introducción de errores de orientación (ϕ, ω, κ)

$$\underline{\underline{D}}_{\phi} = \begin{pmatrix} \cos\phi & 0 & \sin\phi \\ 0 & 1 & 0 \\ -\sin\phi & 0 & \cos\phi \end{pmatrix}$$

$$\underline{\underline{D}}_{\omega} = \begin{pmatrix} 1 & 0 & 0 \\ 0 & \cos\omega & -\sin\omega \\ 0 & \sin\omega & \cos\omega \end{pmatrix}$$

$$\underline{\underline{D}}_{\kappa} = \begin{pmatrix} \cos\kappa & -\sin\kappa & 0 \\ \sin\kappa & \cos\kappa & 0 \\ 0 & 0 & 1 \end{pmatrix}$$

$$d\underline{\underline{D}}_{\phi\omega\kappa} = \begin{pmatrix} 1 & -d\kappa & d\phi \\ d\kappa & 1 & -d\omega \\ -d\phi & d\omega & 1 \end{pmatrix}$$

↑ pequeños ángulos

$$\begin{pmatrix} x \\ y \\ z \end{pmatrix} = \underline{\underline{D}}^{T} \left(\underline{\underline{D}}^{T}_{\phi\omega\kappa} \; \underline{\underline{D}}^{T}_{\Theta} \begin{pmatrix} 0 \\ 0 \\ -d'_{\Theta} \end{pmatrix} + \begin{pmatrix} 0 \\ 0 \\ r \end{pmatrix} \right)$$

Resultado

$$\underline{k} = \underline{\underline{D}}^{T}_{\phi\omega\kappa} \; \underline{\underline{D}}^{T}_{\Theta} \begin{pmatrix} 0 \\ 0 \\ -d'_{\Theta} \end{pmatrix} + \begin{pmatrix} 0 \\ 0 \\ r \end{pmatrix} = \begin{pmatrix} d'_{\Theta} \sin\Theta \, d\kappa + d'_{\Theta} \cos\Theta \, d\phi \\ d'_{\Theta} \sin\Theta - d'_{\Theta} \cos\Theta \, d\omega \\ -d'_{\Theta} \sin\Theta \, d\omega - d'_{\Theta} \cos\Theta + r \end{pmatrix}$$

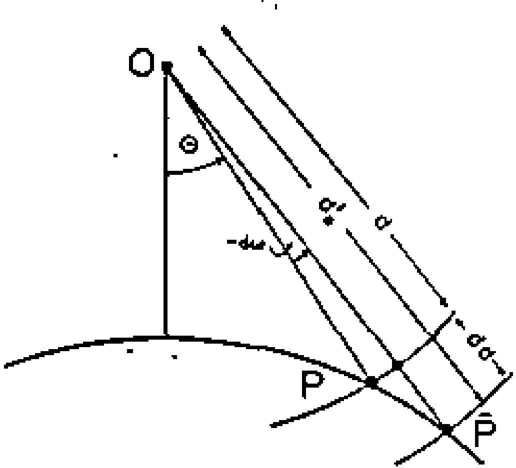

$$d'_{\Theta} = d_{\Theta} + dd = d_{\Theta} - \frac{d_{\Theta} \, r \sin\Theta}{r\cos\Theta - d_{\Theta}} \, d\omega$$

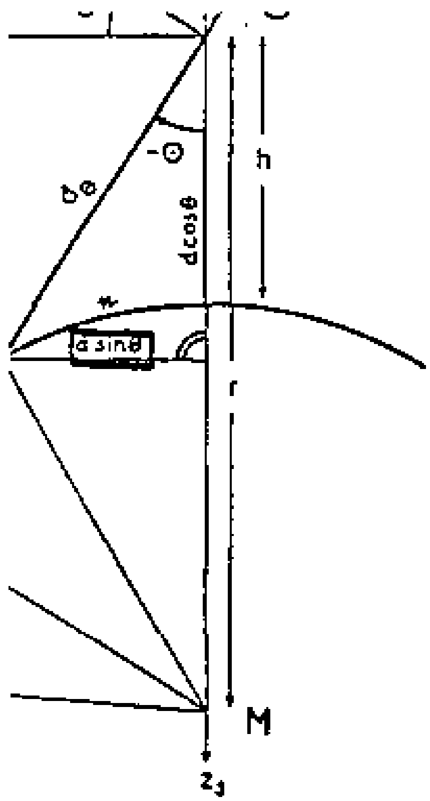

$$= r \cos \Theta - l_\Theta$$

$$\underline{\underline{D}}_\Theta = \begin{pmatrix} 1 & 0 & 0 \\ 0 & \cos\Theta & \sin\Theta \\ 0 & -\sin\Theta & \cos\Theta \end{pmatrix}$$

Entfernung vom Aufnahmezentrum O zum Punkt P auf der Erdoberfläche

Distancia $\overline{PO}$

$$\underline{\underline{D}}_\Theta^T \begin{pmatrix} 0 \\ 0 \\ -d_\Theta \end{pmatrix} + \begin{pmatrix} 0 \\ 0 \\ r \end{pmatrix} = \begin{pmatrix} 0 \\ \boxed{d_\Theta \sin\Theta} \\ -d_\Theta \cos\Theta + r \end{pmatrix}$$

Coordenadas del punto P

$$\begin{pmatrix} x \\ y \\ z \end{pmatrix} = \underline{\underline{D}}^T \left(\underline{\underline{D}}_\Theta^T \begin{pmatrix} 0 \\ 0 \\ -d_\Theta \end{pmatrix} + \begin{pmatrix} 0 \\ 0 \\ r \end{pmatrix} \right)$$

Resultado

$$\begin{pmatrix} 0 \\ 0 \\ -d_\Theta \end{pmatrix} = \underline{\underline{D}}_\Theta \underline{\underline{D}} \begin{pmatrix} x \\ y \\ z \end{pmatrix} - \underline{\underline{D}}_\Theta \begin{pmatrix} 0 \\ 0 \\ r \end{pmatrix}$$

$d_\Theta \sin\Theta \sin i \cos\Omega + r \sin u \cos i \cos\Omega + r \cos u \sin\Omega + \ldots$
$d_\Theta \cos\Theta \sin u \cos i \cos\Omega - d_\Theta \cos\Theta \cos u \sin\Omega$

$d_\Theta \sin\Theta \cos i + r \sin u \sin i - d_\Theta \cos\Theta \sin u \sin i$

$d_\Theta \sin\Theta \sin i \sin\Omega + r \cos\Omega \cos u - r \sin\Omega \cos i \sin u - \ldots$
$d_\Theta \cos\Theta \cos\Omega \cos u + d_\Theta \cos\Theta \sin\Omega \cos i \sin u$

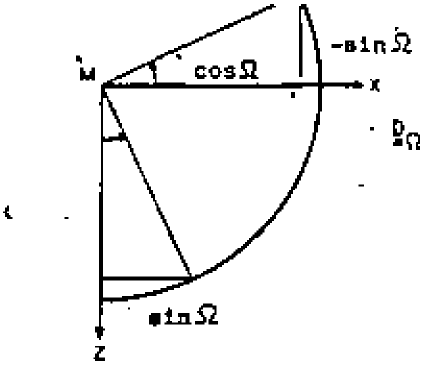

$$\underline{\underline{D}}_{\Omega} = \begin{pmatrix} \cos\Omega & 0 & \sin\Omega \\ 0 & 1 & 0 \\ -\sin\Omega & 0 & \cos\Omega \end{pmatrix}$$

1. Ω

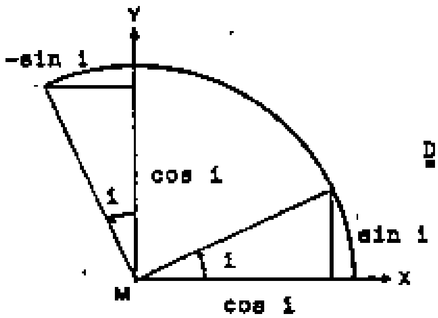

$$\underline{\underline{D}}_{i} = \begin{pmatrix} \cos i & -\sin i & 0 \\ \sin i & \cos i & 0 \\ 0 & 0 & 1 \end{pmatrix}$$

2. i

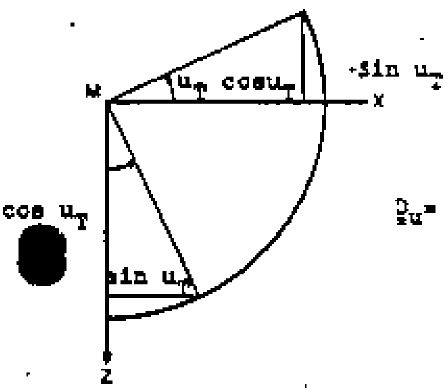

$$\underline{\underline{D}}_{u} = \begin{pmatrix} \cos u_T & 0 & \sin u_T \\ 0 & 1 & 0 \\ -\sin u_T & 0 & \cos u_T \end{pmatrix}$$

3. u

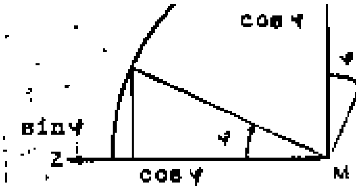

$$\underline{\underline{D}}_{\lambda} = \begin{pmatrix} \cos\lambda & 0 & \sin\lambda \\ 0 & 1 & 0 \\ -\sin\lambda & 0 & \cos\lambda \end{pmatrix} \qquad (2.51\text{-}8)$$

1. λ

$$\underline{\underline{D}}_{\varphi} = \begin{pmatrix} 1 & 0 & 0 \\ 0 & \cos\varphi & \sin\varphi \\ 0 & -\sin\varphi & \cos\varphi \end{pmatrix} \qquad (2.51\text{-}9)$$

2. φ

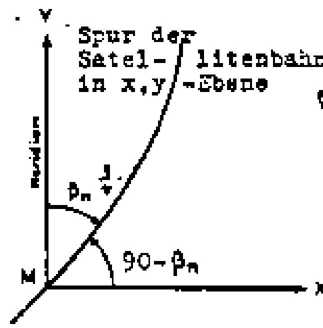

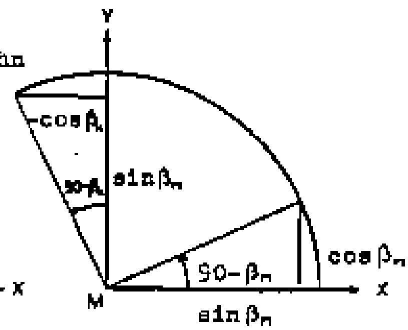

3. β_n

$$\underline{\underline{D}}_{\beta} = \begin{pmatrix} \sin\beta_n & -\cos\beta_n & 0 \\ \cos\beta_n & \sin\beta_n & 0 \\ 0 & 0 & 1 \end{pmatrix}$$

$$\underline{\underline{D}} = \underline{\underline{D}}_{u}\,\underline{\underline{D}}_{i}\,\underline{\underline{D}}_{\Omega} = \begin{pmatrix} \cos\Omega\cos i\cos u - \sin\Omega\sin u & -\cos u\sin i & \cos u\cos i\sin\Omega + \sin u\cos\Omega \\ \sin i\cos\Omega & \cos i & \sin i\sin\Omega \\ -\sin u\cos i\cos\Omega - \cos u\sin\Omega & \boxed{\sin u\sin i} & -\sin\Omega\cos i\sin u + \cos\Omega\cos u \end{pmatrix}$$

$$\underline{\underline{D}} = \underline{\underline{D}}_{\beta}\,\underline{\underline{D}}_{\varphi}\,\underline{\underline{D}}_{\lambda} = \begin{pmatrix} \cos\lambda\sin\beta + \sin\lambda\sin\varphi\cos\beta & -\cos\beta\cos\varphi & \sin\lambda\sin\beta - \cos\lambda\cos\beta\sin\varphi \\ \cos\lambda\cos\beta - \sin\lambda\sin\beta\sin\varphi & \cos\varphi\sin\beta & \sin\lambda\cos\beta + \cos\lambda\sin\beta\sin\varphi \\ -\sin\lambda\cos\varphi & \boxed{\sin\varphi} & \cos\lambda\cos\varphi \end{pmatrix}$$

$$\boxed{\sin\varphi \equiv \sin i\sin u}$$

$$\frac{-\sin\lambda\cos\varphi}{\cos\lambda\cos\varphi} = -\tan\lambda \equiv \frac{-\cos\Omega\cos i\sin u - \sin\Omega\cos u}{-\sin\Omega\cos i\sin u + \cos\Omega\cos u} \xrightarrow{\Omega = 0} \tan u\cos i$$

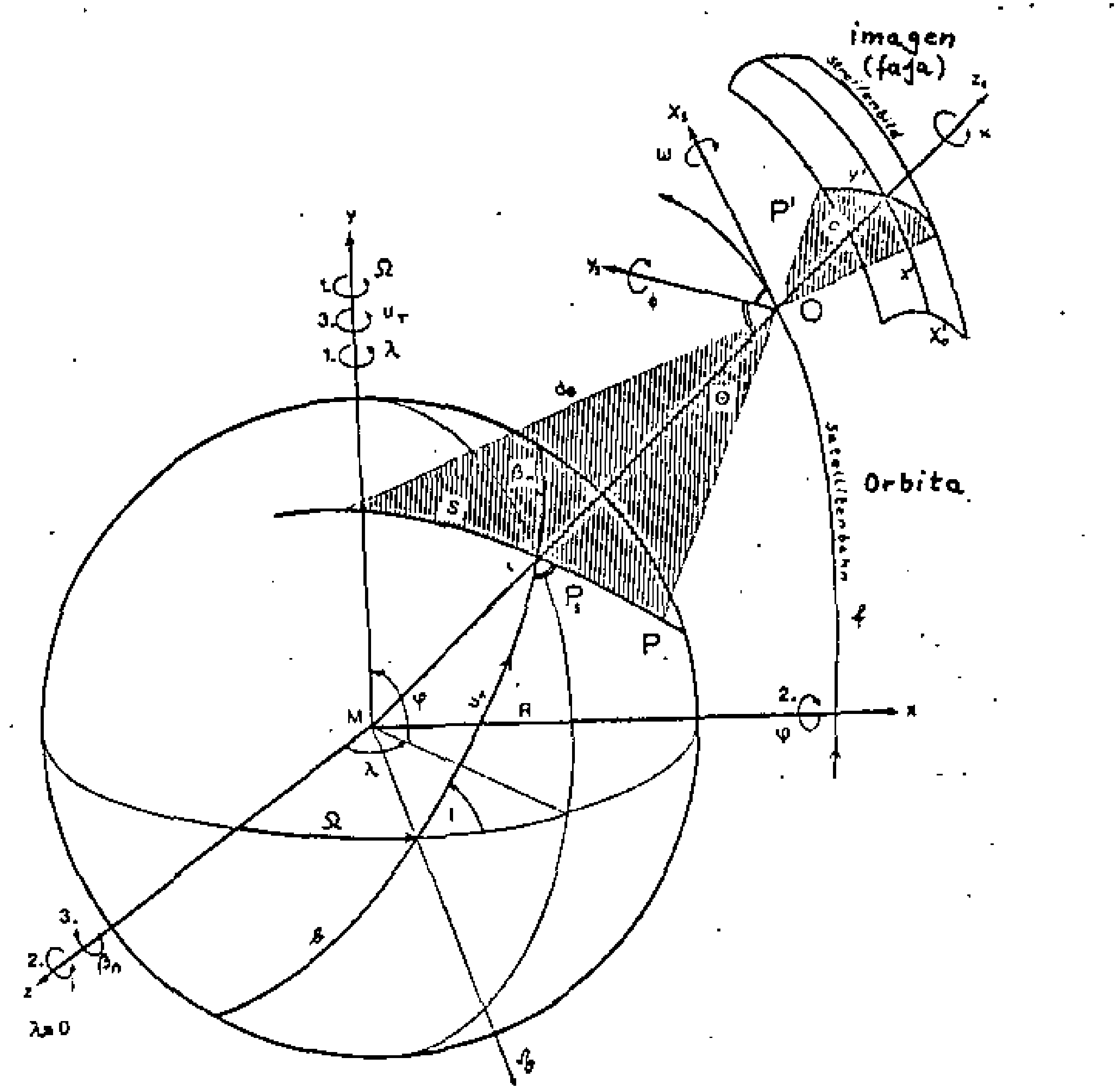

Transformación de las coordenadas geocéntricas x, y, z en el sistema de la imagen x', y'

$$\begin{pmatrix} x \\ y \\ z \end{pmatrix} = R \begin{pmatrix} \cos\varphi \sin\lambda \\ \sin \\ \cos\varphi \; \cos\lambda \end{pmatrix}$$

coord. geográficas/geocéntricas

$$r = a(1 - e \cos M_T \cdot \frac{e^2}{2} (\cos 2M_T - 1) - \ldots$$

$\overline{MO}$

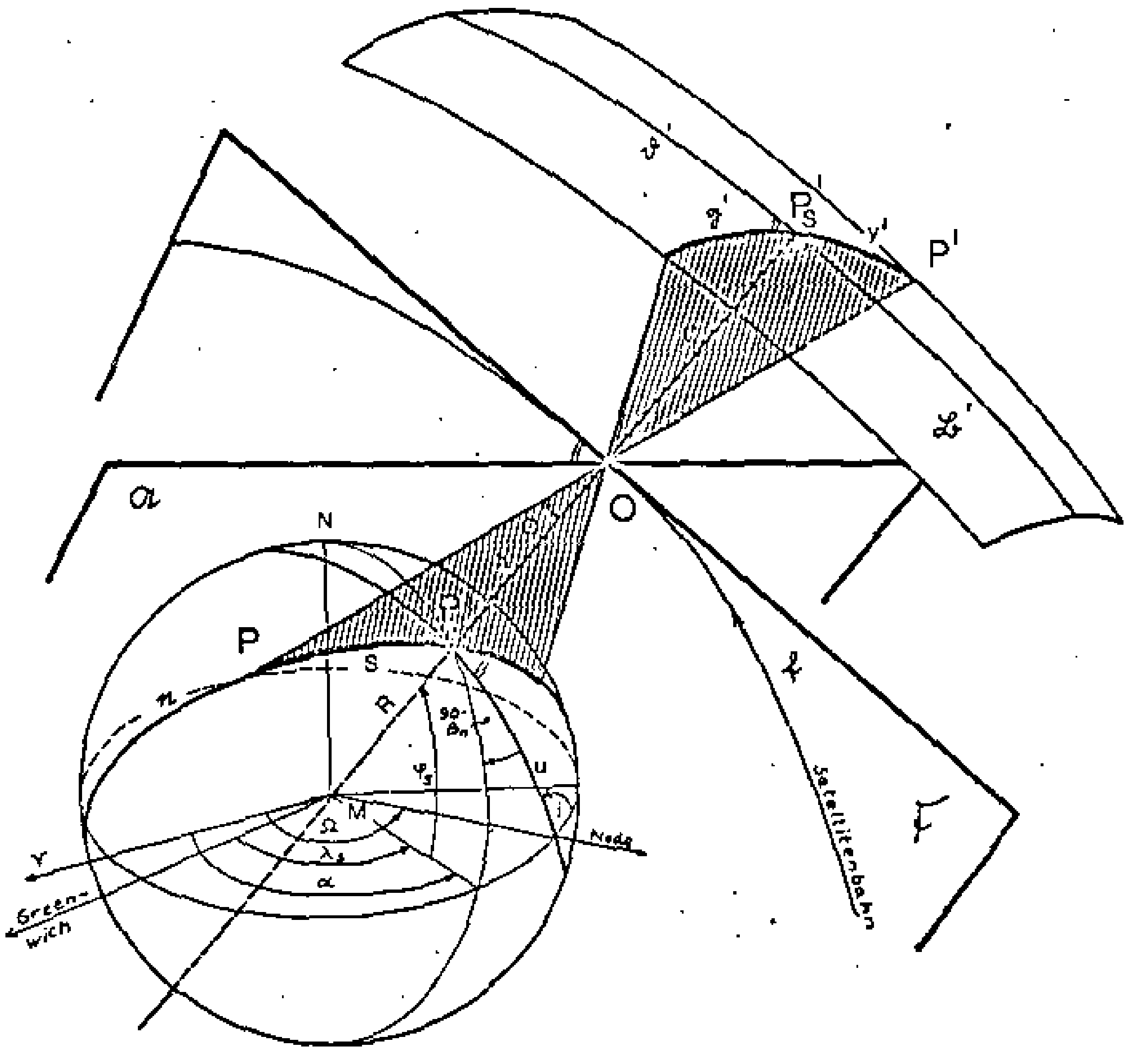

Scanners de satélitos : condiciones geométricas

Determinación de la orientación exterior de sistemas dinamicos

BESTIMMUNG DER ÄUSSEREN ORIENTIERUNG DYNAMISCHER AUFNAHMESYSTEME

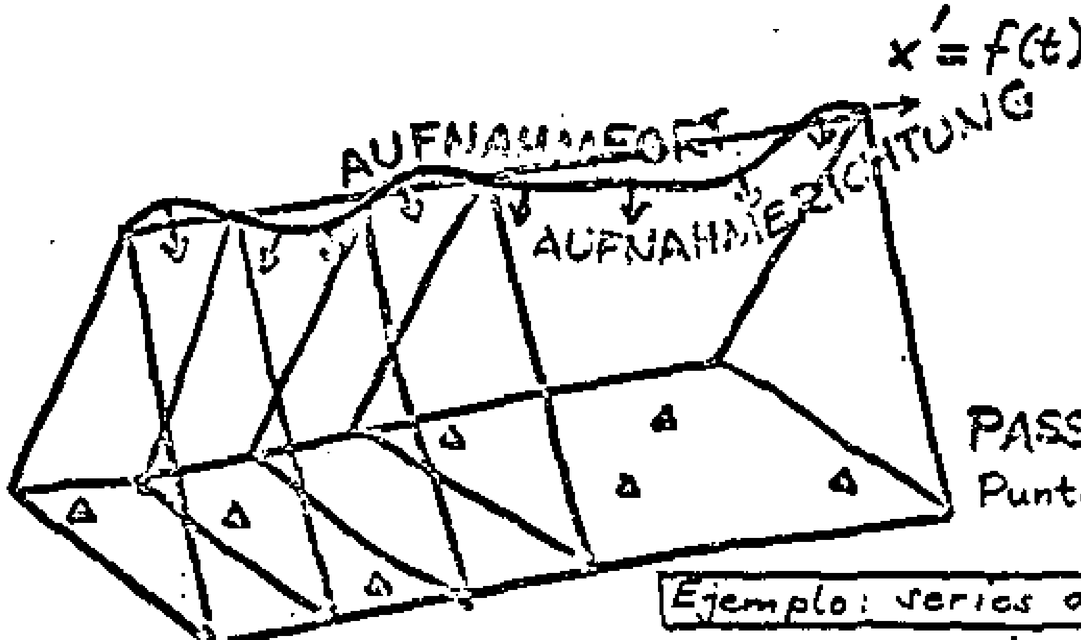

Ejemplo: series de Fourier

Ansatz für die Orientierungsparameter:

$$x_0 = x_{o_{gen}} + a_0 + a_1 \cos\frac{x'}{x'_m} + a_2 \sin\frac{x'}{x'_m} + a_3 \cos\frac{2x'}{x'_m} + a_4 \sin\frac{2x'}{x'_m} + \ldots$$

$$y_0 = y_{o\,gen} + b_0 + \ldots\ldots + b_4 \sin\frac{2x'}{x'_m}$$

$$z_0 = z_{o\,gen} + c_0 + \ldots\ldots + c_4 \sin\frac{2x'}{x'_m}$$

$$\omega = \omega_{gen} + d_0 + \ldots\ldots + d_4 \sin\frac{2x'}{x'_m}$$

$$\phi = \phi_{gen} + e_0 + \ldots\ldots + e_4 \sin\frac{2x'}{x'_m}$$

$$K = K_{gen} + f_0 + \ldots\ldots + f_4 \sin\frac{2x'}{x'_m}$$

3a. Gegenseitige Orientierung
Relative Orientation

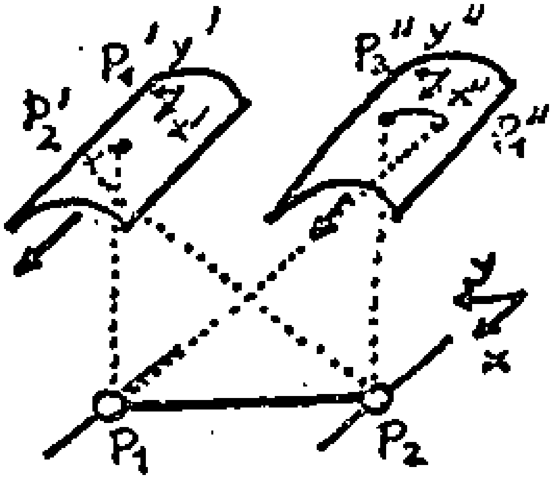

$$\begin{vmatrix} bx_{jk} & by_{jk} & bz_{jk} \\ u_i' & v_i' & w_i' \\ u_i'' & v_i'' & w_i'' \end{vmatrix} = 0$$

condición de complanaridad

$$\begin{pmatrix} u_i' \\ v_i' \\ w_i' \end{pmatrix} = \begin{pmatrix} a_{11j} & a_{12j} & a_{13j} \\ a_{21j} & a_{22j} & a_{23j} \\ a_{31j} & a_{32j} & a_{33j} \end{pmatrix} \begin{pmatrix} 0 \\ c \cdot \sin \frac{y_i'}{c} \\ -c \cdot \cos \frac{y_i'}{c} \end{pmatrix}$$

$$\begin{pmatrix} u_i'' \\ v_i'' \\ w_i'' \end{pmatrix} = \begin{pmatrix} a_{11k} & a_{12k} & a_{13k} \\ a_{21k} & a_{22k} & a_{23k} \\ a_{31k} & a_{32k} & a_{33k} \end{pmatrix} \begin{pmatrix} 0 \\ c \cdot \sin \frac{y_i''}{c} \\ -c \cdot \cos \frac{y_i''}{c} \end{pmatrix}$$

$$\begin{pmatrix} bx_{jk} \\ by_{jk} \\ bz_{jk} \end{pmatrix} = \begin{pmatrix} x_{0k}'' - x_{0j}' \\ y_{0k}'' - y_{0j}' \\ z_{0k}'' - z_{0j}' \end{pmatrix}$$

Linearisiert, in Modellkoord., gen. Senkrechtfall
Linearized, in model coords., approx. vert. case

Bestimmung der Äußeren Orientierung
Determination of Exterior Orientation

1. Plattform-stabilisierung	1. Platform stabilization
2. Registrierung der Orientierungsdaten	2. Recording of orientation parameters
3. Orientierungs-verfahren	3. Orientation procedures
3a. Gegenseitige Orientierung (streng nur möglich für ebenes Gelände, parallele Flugstreifen)	3a. Relative Orientation (strictly only possible for flat terrain, parallel strips)
3b. Absolute Orientierung (komplexes Blockausgleichungs-modell - Kollinearitätsgl.)	3b. Absolute Orientation (complex block adjustment model - collinearity eq's)
→ 3c. Interpolation mit Polynomen (zw. Paßpunkten)	3c. Interpolation with polynomials (betw. control)
4. Annahme eines stabilisierten Flugs	4. Assumption of straight and level flight

Innere Orientierungsparameter bei Scannern
Interior Orientation Parameters for scanners

a. Rand des Films (Zählung von y_i')

b. Zeitmarken in x_i' (Korrelation von Hilfsdaten zur Zeit t_j; Filmgeschwindigkeit v)

c. Sensorkonstante c (Verzeichnung dc)

a. Edge of Film (origin of y_i')

b. Timing Marks in x_i' (correlation of auxiliary data for t_j; film velocity v)

c. Sensor Constant c (Distortion dc)

Innere Orientierungsparameter beim Seitwärtsradar
Interior Orientation Parameters for S.L.A.R.

a. Verzögerung (Δt für linken Filmrand)

b. Zeitmarken in x_i' (Korrelation von Hilfsdaten zur Zeit t_j) (Filmgeschwindigkeit v)

c. Maßstabsfaktor m_o

d. bei Grundentfernungsaufzeichnung h_o

e. Zeitmarken in y_i' (Kathodenstrahlröhrenfehler)

f. Ausrichtung der Antennenebene

a. Delay (Δt for left film edge)

b. Timing marks in x_i' (correlation of auxiliary data for t_j) (film velocity v)

c. Scale factor m_o

d. for ground range recording h_o

e. Timing marks in y_i' (CRT errors)

f. orientation of antenna plane.

Radar-Punktbestimmung
Radar-Positioning

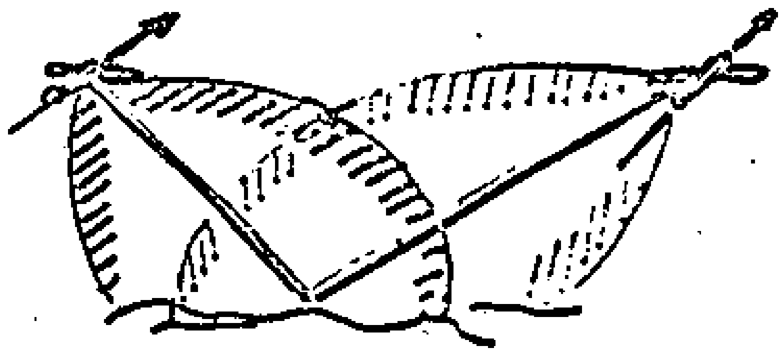

$$t_j = T_1 + \frac{x_i'}{V_1} \qquad t_k = T_2 + \frac{x_i''}{V_2}$$

$$s_{ij} = \frac{y_i'}{m_0} \qquad s_{ik} = \frac{y_i''}{m_0}$$

Kugelgleichungen Equations of spheres

(1) $(x_{0j}' - x_i)^2 + (y_{0j}' - y_i)^2 + (z_{0j}' - z_i)^2 = s_{ij}^2$

(2) $(x_{0k}'' - x_i)^2 + (y_{0k}'' - y_i)^2 + (z_{0k}'' - z_i)^2 = s_{ik}^2$

} Schnitt ≡ Kreis → circle

Antennenorientierungsebenen
Plane of antenna orientations

(3) $a_{11j}(x_i - x_{0j}') + a_{21j}(y_i - y_{0j}') + a_{31j}(z_i - z_{0j}') = 0$

$a_{11k}(x_i - x_{0k}'') + a_{21k}(y_i - y_{0k}'') + a_{31k}(z_i - z_{0k}'') = 0$

Schnitt ≡ 2 Punkte → 1 Pkt
→ 2 points → 1 pt.

ensoren
isradar)

Active Sensors
(S.L.A.R.)

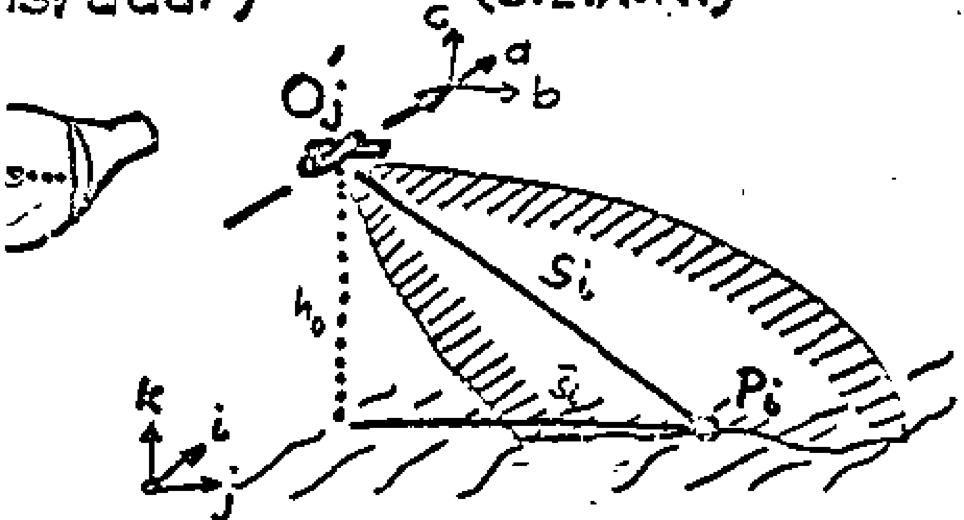

ngsgleichung Range equation :

$$\frac{\cdot \Delta t_{ij}}{2} \quad ; \quad y_i' = m_o \cdot S_i$$

factor de escala

arstellung Slant range representation

$$\sqrt{S_i^2 - h_0^2} \quad ; \quad \bar{y}_i' = m_o \cdot \bar{S}_i$$

arstellung Groundrange representation

$$x_{oj}' - x_i)^2 + (y_{oj}' - y_i)^2 + (z_{oj}' - z_i)^2$$

g der Antennenorientierungsebene :
of Antenna Orientation

$$\begin{pmatrix} a_{11} & a_{21} & a_{31} \\ a_{12} & a_{22} & a_{32} \\ a_{13} & a_{23} & a_{33} \end{pmatrix} \begin{pmatrix} \vec{i} \\ \vec{j} \\ \vec{k} \end{pmatrix} \quad ; \quad \vec{a} = \vec{b} \times \vec{c}$$

$$x_i - x_{oj}') + a_{21j}(y_i - y_{oj}') + a_{31j}(z_i - z_{oj}') = 0$$

Räumlicher Vorwärtsschnitt / Space Intersection

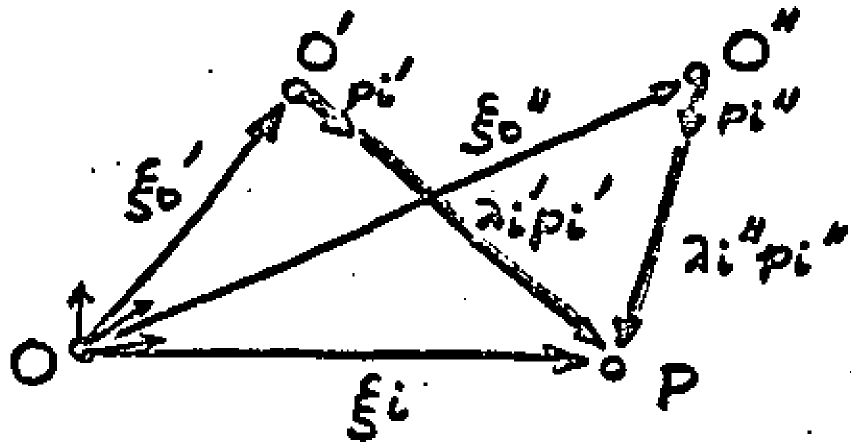

Determinacion de coordenadas

Gegeben Given :

$$\xi_{oj}' \qquad \xi_{ok}'' \qquad A_j' = f(\omega_j' \phi_j' \kappa_j') \qquad A_k'' = f(\omega_k'' \phi_k'' \kappa_k'')$$

$$\begin{pmatrix} x_{oj}' \\ y_{oj}' \\ z_{oj}' \end{pmatrix} \quad \begin{pmatrix} x_{ok}'' \\ y_{ok}'' \\ z_{ok}'' \end{pmatrix} \quad \begin{pmatrix} a_{11j} & a_{12j} & a_{13j} \\ a_{21j} & a_{22j} & a_{23j} \\ a_{31j} & a_{32j} & a_{33j} \end{pmatrix} \quad \begin{pmatrix} a_{11k} & a_{12k} & a_{13k} \\ a_{21k} & a_{22k} & a_{23k} \\ a_{31k} & a_{32k} & a_{3} \end{pmatrix}$$

$$\xi_i = \xi_{o_j}' + \lambda_i' p_{i_j}' = \xi_{o_k}'' + \lambda_i'' p_{i_k}''$$

$$\therefore \boxed{\xi_{ok}'' - \xi_{oj}' = \lambda_i' p_{ij} - \lambda_i'' p_{ik}''}$$

Scanner:

$$\begin{pmatrix} x_{ok}'' - x_{oj}' \\ y_{ok}'' - y_{oj}' \\ z_{ok}'' - z_{oj}' \end{pmatrix} = \lambda_i' \begin{pmatrix} a_{11j} & a_{12j} & a_{13j} \\ a_{21j} & a_{22j} & a_{23j} \\ a_{31j} & a_{32j} & a_{33j} \end{pmatrix} \begin{pmatrix} 1 & 0 & 0 \\ 0 & \cos\theta_i' & -\sin\theta_i' \\ 0 & \sin\theta_i' & \cos\theta_i' \end{pmatrix} \begin{pmatrix} 0 \\ 0 \\ -c \end{pmatrix}$$

$$- \lambda_i'' \begin{pmatrix} a_{11k} & a_{12k} & a_{13k} \\ a_{21k} & a_{22k} & a_{23k} \\ a_{31k} & a_{32k} & a_{33k} \end{pmatrix} \begin{pmatrix} 1 & 0 & 0 \\ 0 & \cos\theta_i'' & -\sin\theta_i'' \\ 0 & \sin\theta_i'' & \cos\theta_i'' \end{pmatrix} \begin{pmatrix} 0 \\ 0 \\ -c \end{pmatrix}$$

$$\theta_i' = \frac{y_i'}{c} \quad ; \quad \theta_i'' = \frac{y_i''}{c}$$

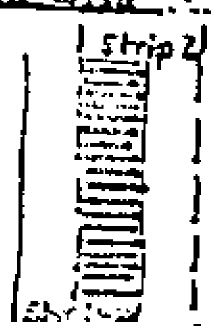

ollinearitätsgleichungen: Collinearity Equations:

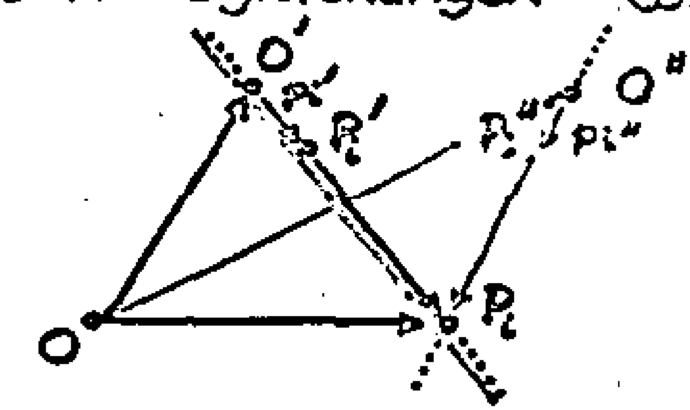

segundo centro de proyección

Determinación de las incógnitas
$a_{11} \dots a_{33}$
x_0', y_0', z_0'

uftaufnahmen Aerial Photos

$$x_i' = -c\,\frac{a_{11}(x_i-x_0')+a_{12}(y_i-y_0')+a_{13}(z_i-z_0')}{a_{31}(x_i-x_0')+a_{32}(y_i-y_0')+a_{33}(z_i-z_0')}$$

$$y_i' = -c\,\frac{a_{21}(x_i-x_0')+a_{22}(y_i-y_0')+a_{23}(z_i-z_0')}{a_{31}(x_i-x_0')+a_{32}(y_i-y_0')+a_{33}(z_i-z_0')}$$

treifenbilder Strip Photos

$$0 = -c\,\frac{a_{11j}(x_i-x_0')+a_{12j}(y_i-y_0')+a_{13j}(z_i-z_0')}{a_{31j}(x_i-x_0')+a_{32j}(y_i-y_0')+a_{33j}(z_i-z_0')}$$

$$y_i' = -c\,\frac{a_{21j}(x_i-x_0')+a_{22j}(y_i-y_0')+a_{23j}(z_i-z_0')}{a_{31j}(x_i-x_0')+a_{32j}(y_i-y_0')+a_{33j}(z_i-z_0')}$$

$$t_j = T + \frac{x_i'}{V}$$

Passive Abtastung Passive Scanning

$$0 = -c\,\frac{a_{11j}(x_i-x_{0j}')+a_{12j}(y_i-y_{0j}')+a_{13j}(z_i-z_{0j}')}{a_{31j}(x_i-x_{0j}')+a_{32j}(y_i-y_{0j}')+a_{33j}(z_i-z_{0j}')}$$

$$c\cdot \mathrm{tg}\frac{y_i'}{c} = -c\,\frac{a_{21j}(x_i-x_{0j}')+a_{22j}(y_i-y_{0j}')+a_{23j}(z_i-z_{0j}')}{a_{31j}(x_i-x_{0j}')+a_{32j}(y_i-y_{0j}')+a_{33j}(z_i-z_{0j}')}$$

$$t_j = T + \frac{x_i'}{V}$$

Bei $\dot{\Theta} \to \infty$	For $\dot{\Theta} \to \infty$	
Schnelle passive Abtastung	**Fast passive scanning**	$\Theta' \to \frac{y'}{c}$, multiplicación

$$\begin{pmatrix} 0 \\ c \cdot \sin \frac{y_i'}{c} \\ -c \cdot \cos \frac{y_i'}{c} \end{pmatrix} = \frac{1}{\lambda_i'} \begin{pmatrix} a_{11j} & a_{21j} & a_{31j} \\ a_{12j} & a_{22j} & a_{32j} \\ a_{13j} & a_{23j} & a_{33j} \end{pmatrix} \begin{pmatrix} x_i - x_{0j}' \\ y_i - y_{0j}' \\ z_i - z_{0j}' \end{pmatrix}$$

$$x_i' = \int_{t=T}^{t_j} \frac{dv}{dt} \cdot dt \approx (t_j - T) \cdot v \; ; \; v \approx \frac{c}{z_i - z_0'} \cdot V$$

escala → $\frac{c}{z_i - z_0'}$; película → v; avión → V

Luftaufnahme: Aerial Camera:

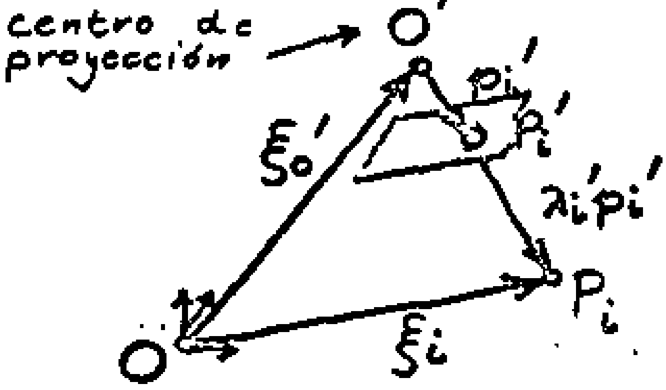

$$\xi_i = \xi_o' + \lambda_i p_i'$$

$$\begin{pmatrix} x_i \\ y_i \\ z_i \end{pmatrix} = \begin{pmatrix} x_o' \\ y_o' \\ z_o' \end{pmatrix} + \lambda_i' \begin{pmatrix} u_i' \\ v_i' \\ w_i' \end{pmatrix}$$

$$\begin{pmatrix} u_i' \\ v_i' \\ w_i' \end{pmatrix} = A \begin{pmatrix} x_i' \\ y_i' \\ -c \end{pmatrix}$$

Geometría analítica del espacio

$$\begin{pmatrix} x_i' \\ y_i' \\ -c \end{pmatrix} = \frac{1}{\lambda_i'} \begin{pmatrix} a_{11} & a_{21} & a_{31} \\ a_{12} & a_{22} & a_{32} \\ a_{13} & a_{23} & a_{33} \end{pmatrix} \begin{pmatrix} x_i - x_o' \\ y_i - y_o' \\ z_i - z_o' \end{pmatrix}$$

Streifenbilder: Strip Photos:

$$\begin{pmatrix} 0 \\ y_i' \\ -c \end{pmatrix} = \frac{1}{\lambda_i'} \begin{pmatrix} a_{11j} & a_{21j} & a_{31j} \\ a_{12j} & a_{22j} & a_{32j} \\ a_{13j} & a_{23j} & a_{33j} \end{pmatrix} \begin{pmatrix} x_i - x_{oj}' \\ y_i - y_{oj}' \\ z_i - z_{oj}' \end{pmatrix}$$

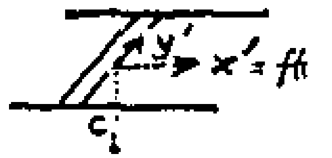

$$x_i' = \int_{t=T}^{t_j} \frac{dv}{dt} \cdot dt \approx (t_j - T) \cdot v \quad ; \quad v \approx \frac{c}{z_i - z_o'} \cdot V$$

(v: película; V: avión)

Passive Abtastung Passive Scanning

$$\begin{pmatrix} 1 & 0 & 0 \\ 0 & \cos\theta_i' & -\sin\theta_i' \\ 0 & \sin\theta_i' & \cos\theta_i' \end{pmatrix} \begin{pmatrix} 0 \\ 0 \\ -c \end{pmatrix} = \frac{1}{\lambda_i'} \begin{pmatrix} a_{11j} & a_{21j} & a_{31j} \\ a_{12j} & a_{22j} & a_{32j} \\ a_{13j} & a_{23j} & a_{33j} \end{pmatrix} \begin{pmatrix} x_i - x_{oj}' \\ y_i - y_{oj}' \\ z_i - z_{oj}' \end{pmatrix}$$

$$\theta_i' = \int_{t=t_j-\Delta t_j}^{t_j} \frac{d\theta}{dt} \cdot dt \approx -\Delta t_j \cdot \dot{\theta} \quad ; \quad y_i' = c \cdot \theta_i'$$

$$x_i' = \int_{t=T}^{t_j} \frac{dv}{dt} \cdot dt \approx (t_j - T) \cdot V$$

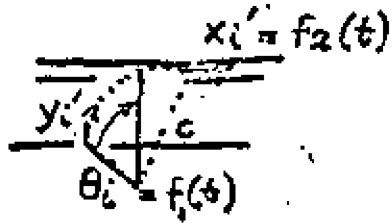

ACCURACY OF PHOTOGRAMMETRY

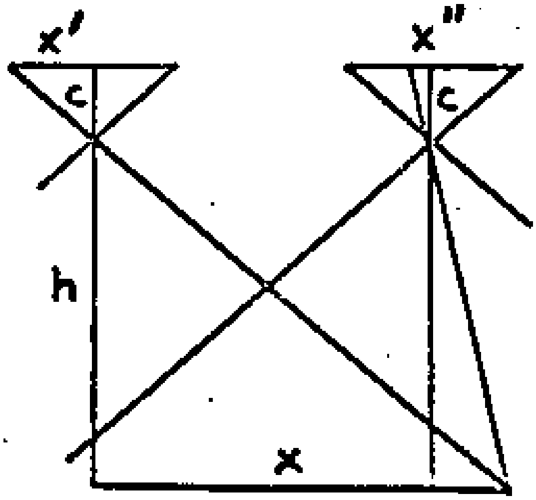

Image scale factor
height-base ratio
Image coordinate accuracy
Limits:

$$500 < \frac{h}{c} < 60\,000$$

$$1 < \frac{h}{b} < 6$$

10 – 20 μm

Single Model

$$x = \frac{h}{c} x'$$

$$y = \frac{h}{c} y'$$

$$h = \frac{b \cdot c}{x' - x''}$$

$$dx = \frac{h}{c} dx'$$

$$dy = \frac{h}{c} dy'$$

$$dh = \frac{h}{c} \cdot \frac{h}{b} (dx' - dx'')$$

Aerial Triangulation

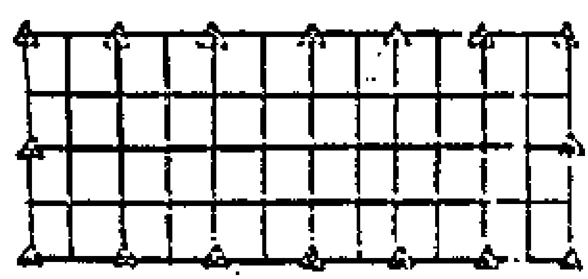

for position

5 – 10 μm

with statoscope data also for height in medium and small scales

(19)

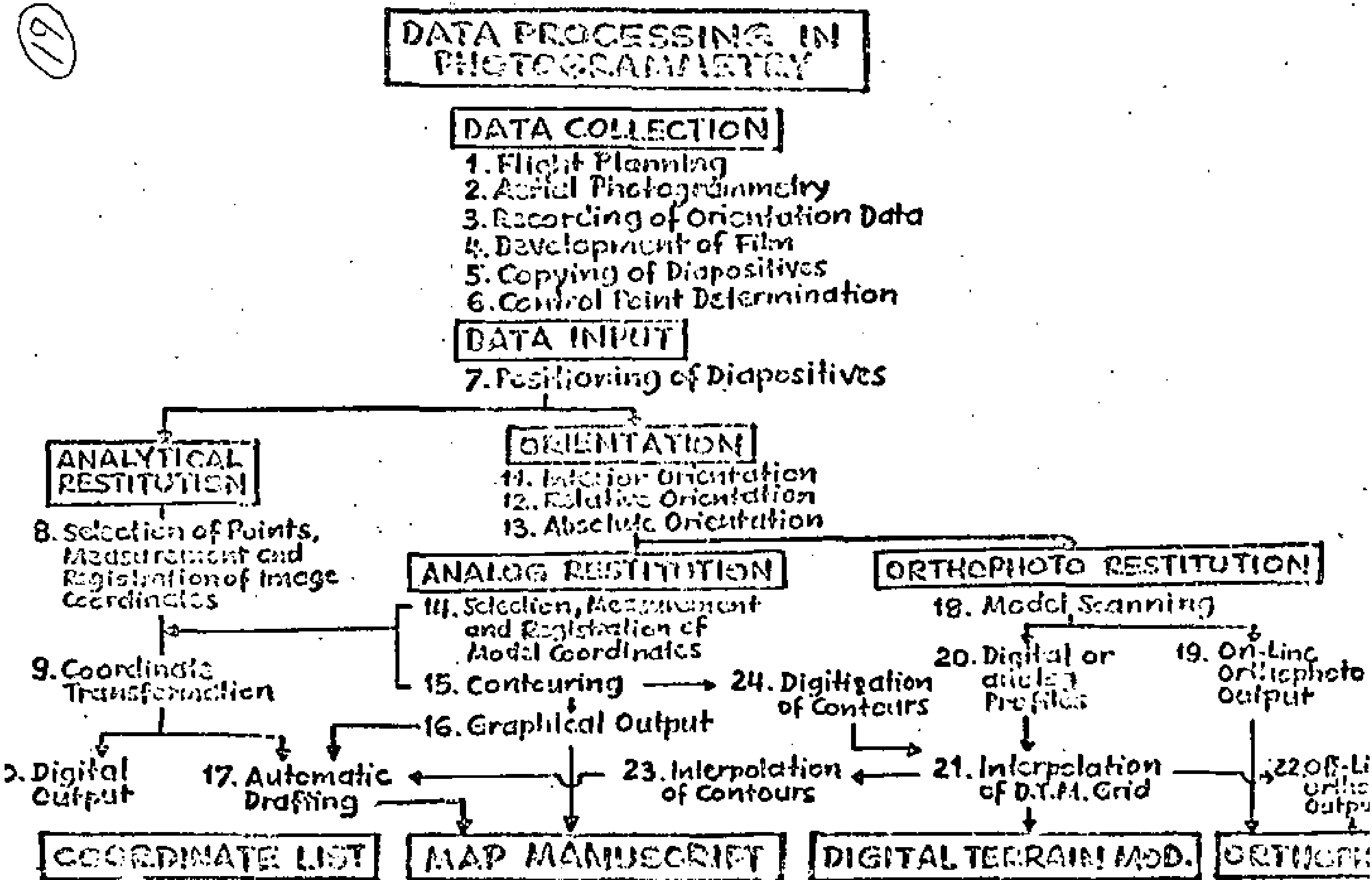
DATA PROCESSING IN PHOTOGRAMMETRY
DATA COLLECTION
1. Flight Planning
2. Aerial Photogrammetry
3. Recording of Orientation Data
4. Development of Film
5. Copying of Diapositives
6. Control Point Determination
DATA INPUT
7. Positioning of Diapositives
ANALYTICAL RESTITUTION
8. Selection of Points, Measurement and Registration of Image Coordinates
9. Coordinate Transformation
Digital Output
ORIENTATION
11. Interior Orientation
12. Relative Orientation
13. Absolute Orientation
ANALOG RESTITUTION
14. Selection, Measurement and Registration of Model Coordinates
15. Contouring
16. Graphical Output
17. Automatic Drafting
24. Digitization of Contours
23. Interpolation of Contours
ORTHOPHOTO RESTITUTION
18. Model Scanning
20. Digital or analog Profiles
19. On-Line Orthophoto Output
21. Interpolation of D.T.M. Grid
COORDINATE LIST
MAP MANUSCRIPT
DIGITAL TERRAIN MOD.

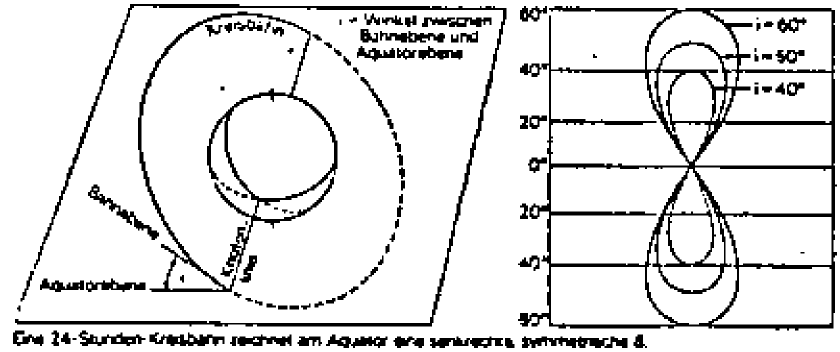

Eine 24-Stunden-Kreisbahn zeichnet am Äquator eine senkrechte, symmetrische 8.

orbita circular

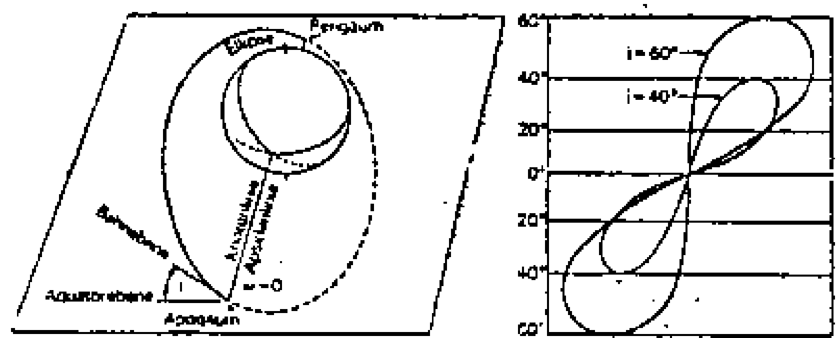

Eine elliptische 24-Stunden-Bahn ist um ihre Längsachse (Apsidenlinie) gekippt.

orbita elipse
ω = 0

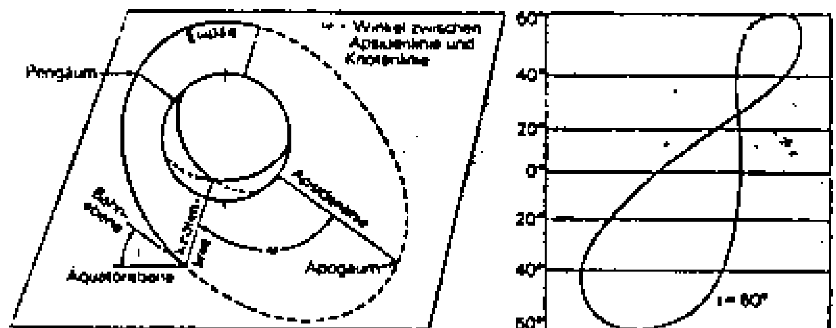

Die Längsachse der Ellipse liegt nicht in der Äquatorebene.

orbita elipse
ω ≠ 0

Verzerrungen der 24-Stunden-Spur

Distorciones = f(e) ; ω = 90°

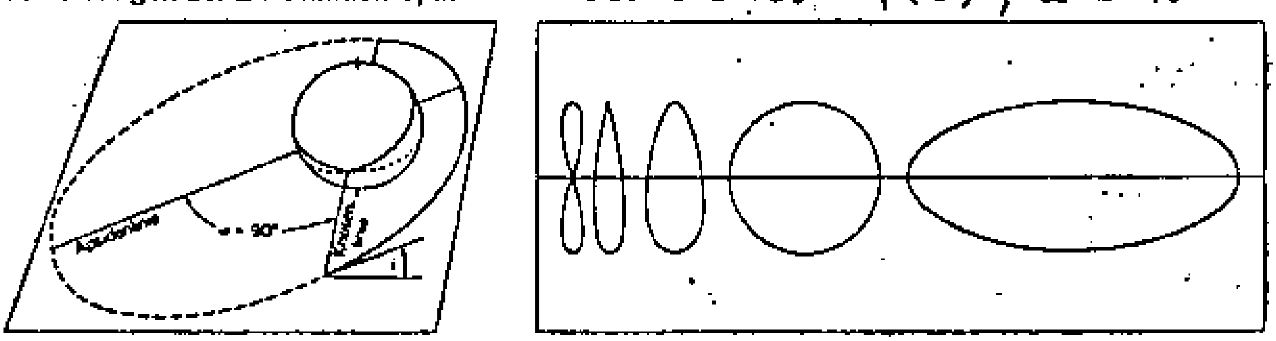

Liegt die Apsidenlinie senkrecht zur Knotenlinie, so deformiert sich die „Acht" mit steigender Exzentrizität.

System geostationärer Nachrichtensatelliten (oben) und ihre Bedeckung (unten).

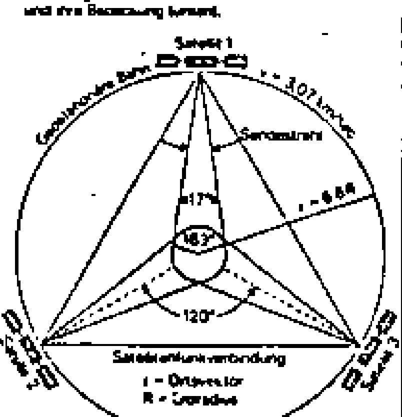

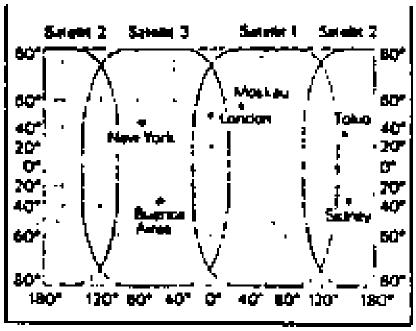

Orbita geo-estacionaric

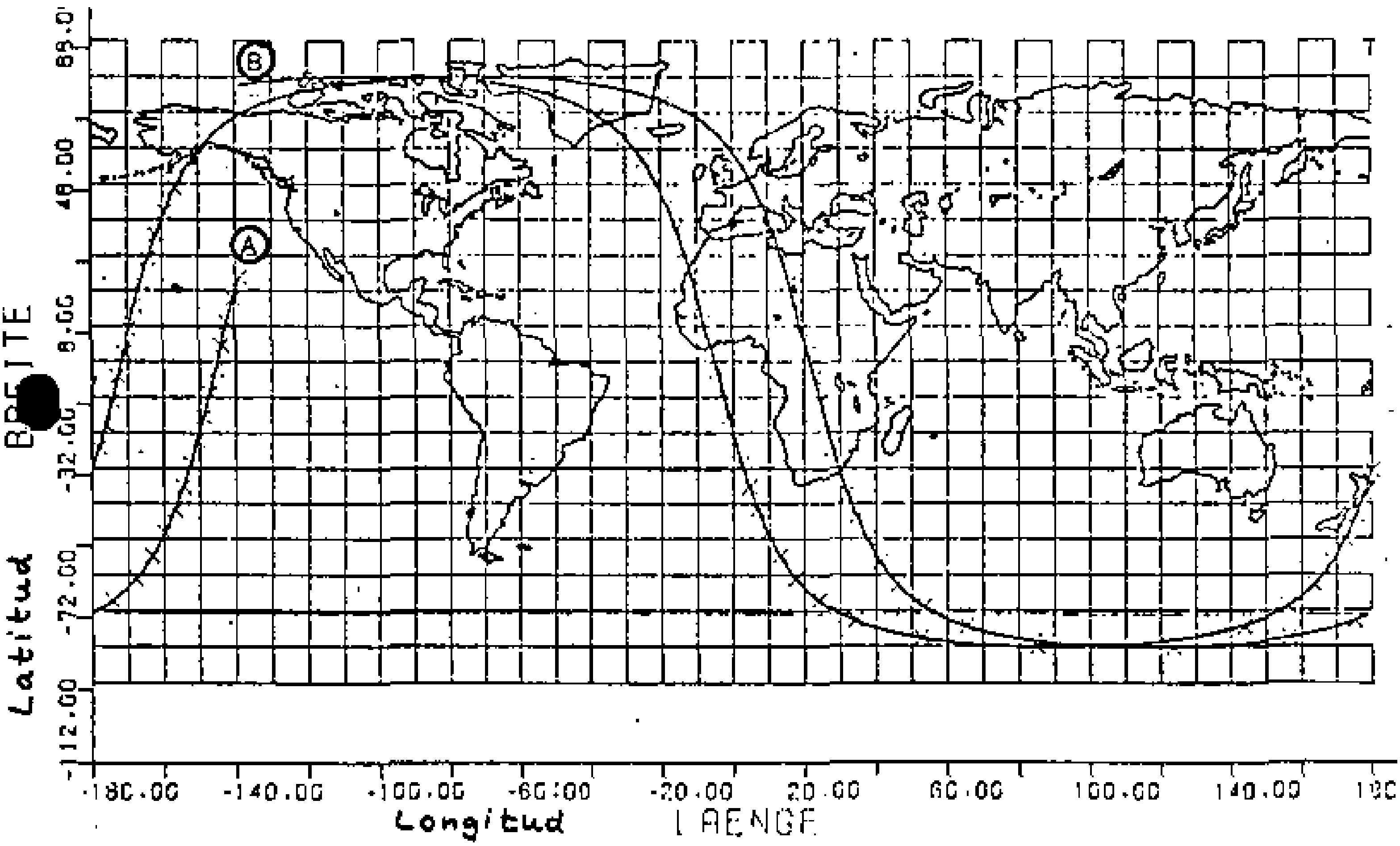

Proyección de la orbita contra la tierra (NIMBUS-3

A : 9.00ʰ
B : 12.17ʰ
} Tiempo Greenwich , 8 de junio 1969

Variación de los elementos de la órbita por día (NIMBUS-3)

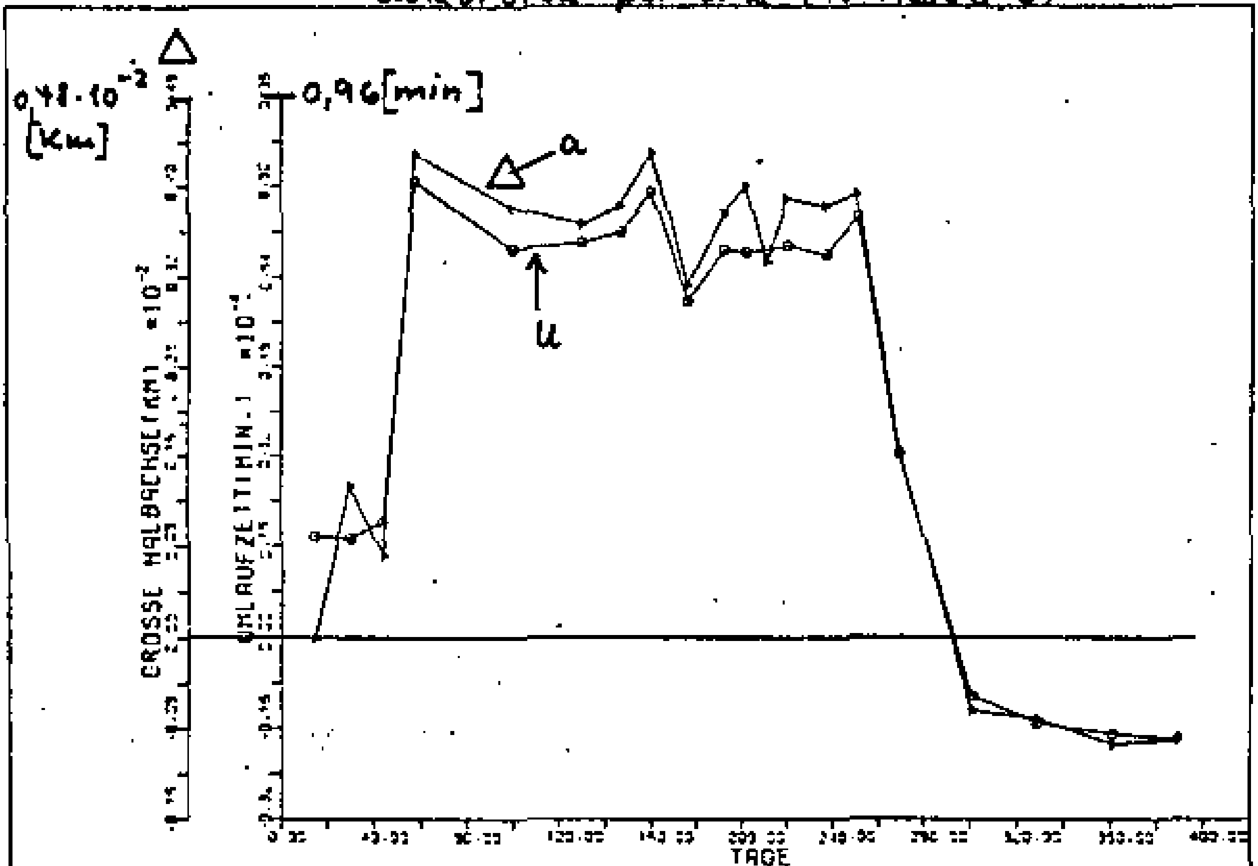

Abbildung 3.1- III AENDERUNG BAHNELEMENTE PRO TAG

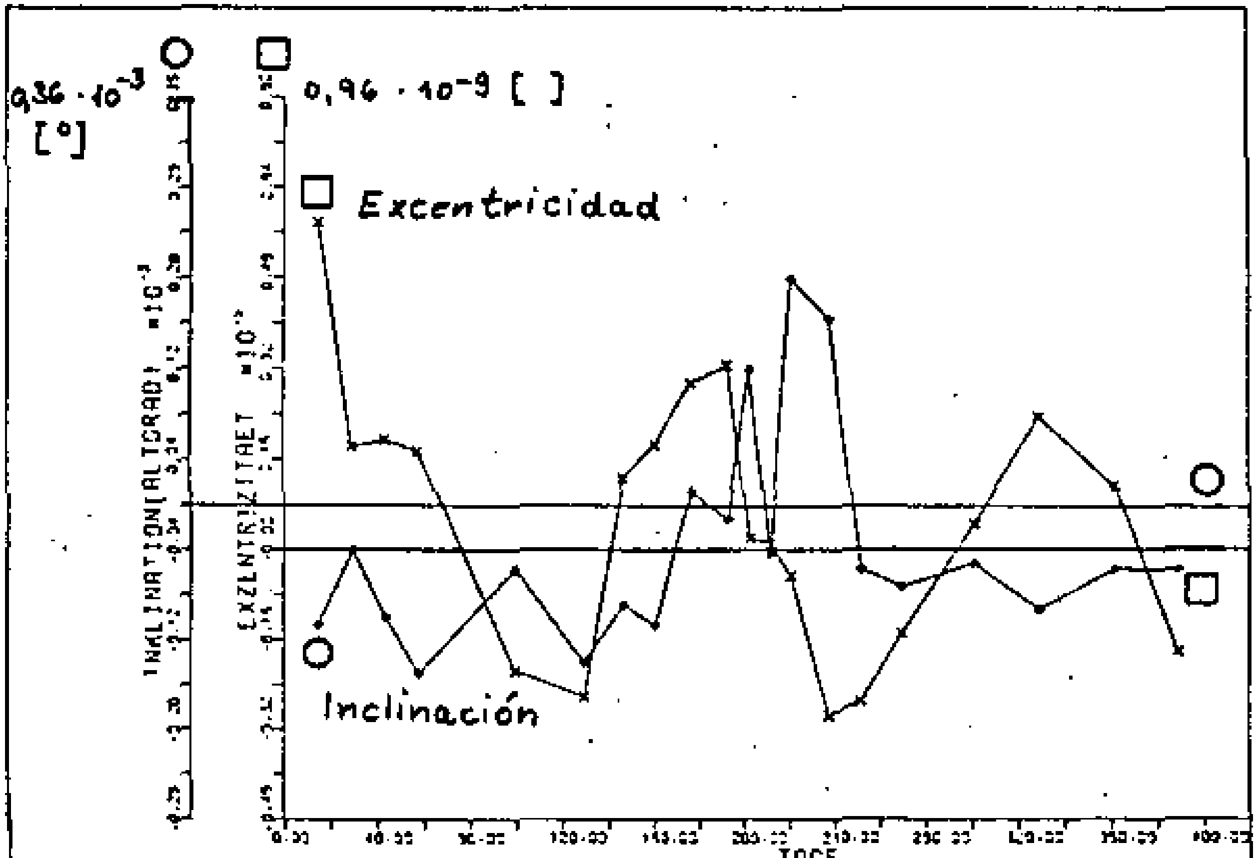

Abbildung 3.1-IV AENDERUNG BAHNELEMENTE PRO TAG

Valores absolutas de los elementos orbitales
(NIMBUS-3)

21

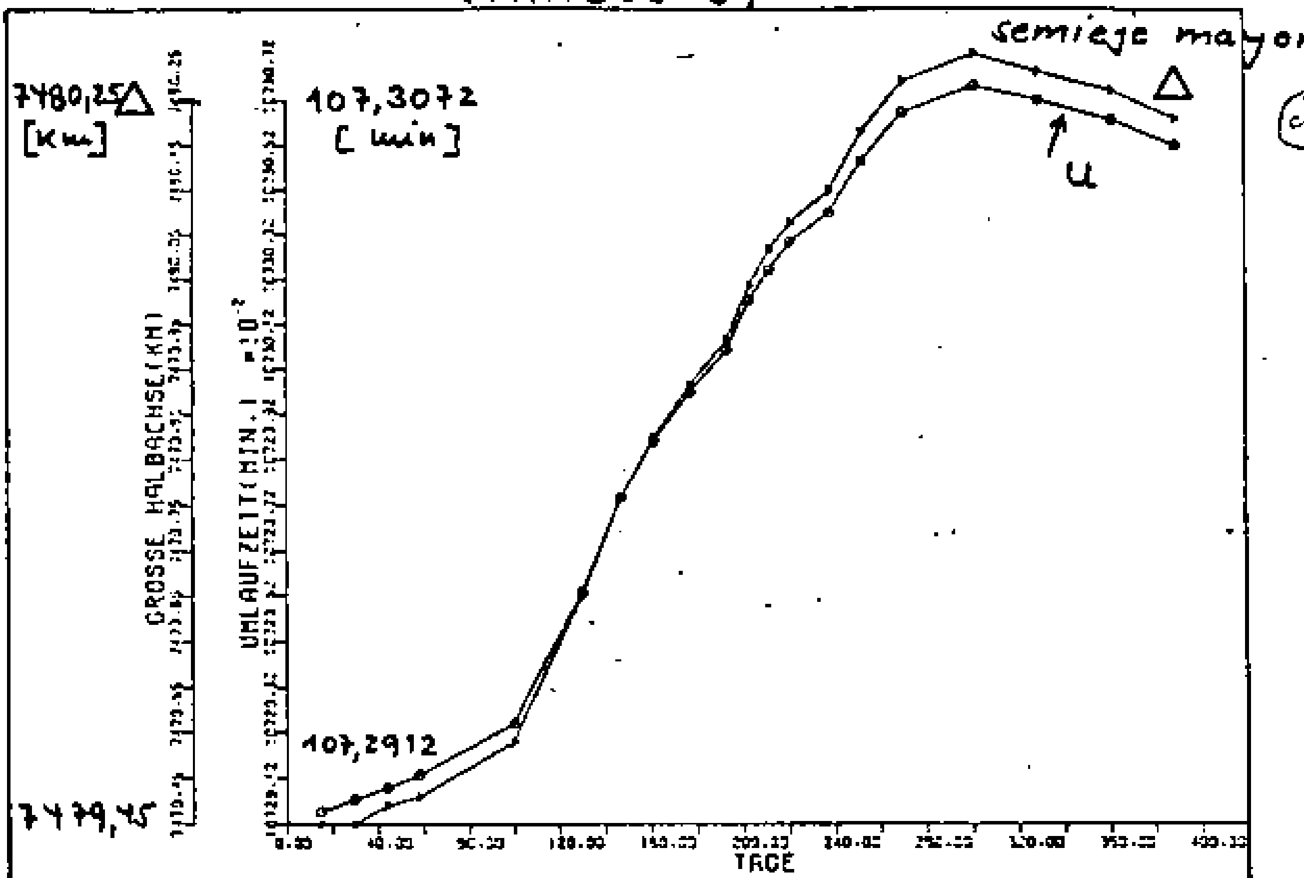

Abbildung 3.1-I GROESSE DER BAHNELEMENTE

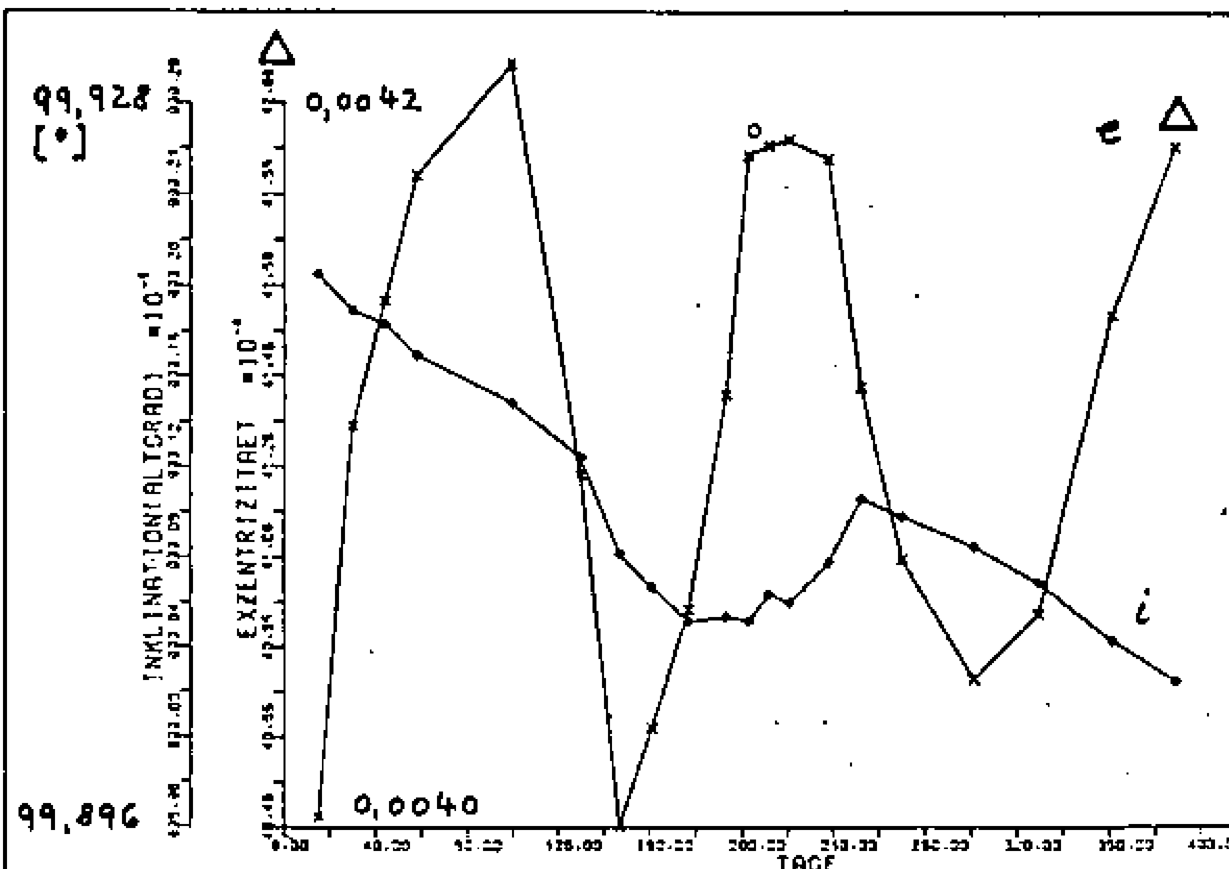

Abbildung 3.1-II GROESSE DER BAHNELEMENTE

N [U/Tag] 1	a [Km]	h [Km] 35807	a/R	U [min]	i [°]	Δλ [°] pro 1U für γ=0
10	9091	2719	1,427	144,0	110,0	36,1
11	8531	2159	1,339	130,9	105,9	32,8
12	8051	1679	1,263	119,9	102,9	30,1
13	7632	1260	1,198	110,8	100,7	27,8
14	7264	892	1,140	102,8	99,0	25,8
15	6938	566	1,089	96,0	97,6	24,1

acción recíproca de los elementos orbitales con condiciones de iluminación constantes (N^2 numeros cardinales)

Gegenseitige Abhängigkeiten von Flughöhe, Umlaufszeit, Inklination usw. nach 1.2-2...5 bei konstanten Beleuchtungsverhältnissen

Satellit	N [U/Tag]	a [km]	h [km]	a/R	U [min]	i [°]	Δλ [°]	e	Ortszeit Äquator-
NIMBUS-3	13,45	7479	1107	1,171	107,3	99,9	26,03	0,004	12^h
NIMBUS-4	13,41	7472	1100	1,173	107,1	99,9	26,77	0,0007	12^h
LANDSAT-1	13,95	7286	914	1,143	103,3	99,1	25,82	0,0006	9^h42m

↑ × 14 = 360°

Bahnelemente von NIMBUS- und LANDSAT-Satelliten

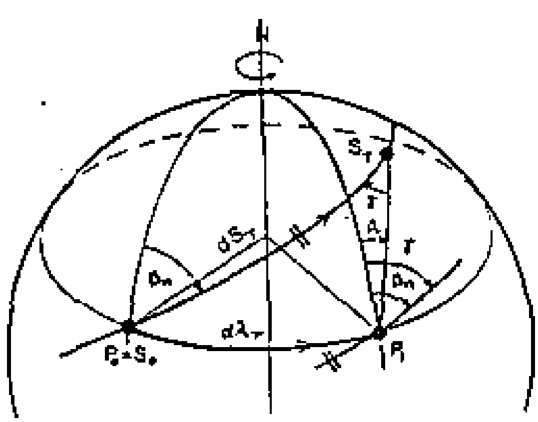

Determinación de la dirección del vuelo

β_n : nominal

β_r : real

$$\tan\gamma = \frac{\sqrt{\sin^2 i - \sin^2 \beta}}{\frac{1400}{U_T} - \cos i}$$

β°	β_n°	γ°	β_r°
0	9,10	4,01	13,11
50	14,24	2,53	16,77
80,9	90,00	0,00	90,00

LANDSAT

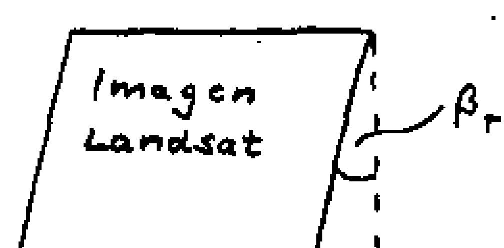

		a	e	i	ω	α	Ω	U
EPOCH	DT	GROSSE ACHSE	EXZENTRIZIT.	INCLINATION	PERIGAEUM	REKTASZENS.	MITTL.ANOMAL.	UMLAUFZEIT
21.04.69	15	7479.4632[km]	.0040484	99.9205[°]	229.0141[°]	21.0103[°]	76.91095[°]	107.2912[min]
6. 5.69	15	7479.4765	.0041352	99.9189	191.2441	35.7192	154.10040	107.2912
21. 5.69	14	7479.4895	.0041627	99.9183	155.2292	50.4279	230.34990	107.2916
4. 6.69	14	7479.5076	.0041901	99.9169	121.7972	64.1554	157.16550	107.2919
18. 6.69	42	7479.5602	.0042146	99.9148	88.2880	77.8785	83.74400	107.2930
30. 7.69	30	7479.7049	.0041243	99.9124	347.0004	119.0378	219.77074	107.2962
29. 8.69	17	7479.8100	.0040463	99.9082	273.8407	148.4272	5.17774	107.2984
15. 9.69	14	7479.8711	.0040443	99.9067	231.4310	165.0766	15.15282	107.2997
29. 9.69	16	7479.9263	.0040946	99.9052	192.3786	180.7442	234.54272	107.3009
15.10.69	16	7479.9741	.0041421	99.9054	158.2400	194.4512	155.77741	107.3019
31.10.69	10	7480.0291	.0041946	99.9057	119.8160	210.1173	12.93880	107.3031
10.11.69	9	7480.0633	.0041968	99.9064	95.9492	219.9077	58.09354	107.3039
19.11.69	9	7480.0943	.0041979	99.9060	74.0577	228.7217	314.85782	107.3045
28.11.69	17	7490.1266	.0041938	99.9078	52.7932	237.5339	210.73996	107.3052
15.12.69	14	7400.1834	.0041435	99.9106	11.8990	254.1823	214.04625	107.3065
29.12.69	19	7480.2256	.0041058	99.9098	337.9583	267.8937	131.61210	107.3076
16. 1.70	31	7480.2647	.0040772	99.9085	293.7771	285.5195	282.47695	107.3082
16. 2.69	28	7480.2490	.0040936	99.9069	217.5570	315.8716	202.52560	107.3078
16. 3.70	32	7480.2200	.0041598	99.9043	149.4984	343.2800	37.17762	107.3074
17. 4.70	28	7480.2009	.0041966	99.9025	72.6996	14.5954	105.09692	107.3068
15. 5.70	1	7480.1761	.0041466	99.9009	5.3537	41.9926	300.36760	107.3063

21.04.69	15	.0009	.0000058	-.0001	-2.4513	.9806	.11304	0.0000
6. 5.69	15	.0009	.0000018	-.0000	-2.4010	.9806	.21704	.0000
21. 5.69	14	.0010	.0000020	-.0001	-2.3880	.9805	.24156	.0000
4. 6.69	14	.0040	.0000018	-.0002	-2.3935	.9802	.22146	.0001
18. 6.69	42	.0034	-.0000022	-.0001	-1.8402	.9800	.76403	.0001
30. 7.69	30	.0035	-.0000026	-.0001	-2.4387	.9796	.15009	.0001
29. 8.69	17	.0036	.0000013	-.0001	-2.4947	.9794	.04010	.0001
15. 9.69	14	.0039	.0000019	-.0001	-2.7895	1.1191	4.26897	.0001
29. 9.69	16	.0030	.0000030	.0000	-2.1337	.8567	19.04071	.0001
15.10.69	16	.0034	.0000033	-.0000	-2.4015	.9791	.22742	.0001
31.10.69	10	.0034	.0000002	.0001	-2.3868	.9790	.25423	.0001
10.11.69	9	.0034	.0000001	-.0000	-2.4323	.9793	.16333	.0001
19.11.69	9	.0035	-.0000005	.0002	-2.3639	.9791	.30052	.0001
28.11.69	17	.0034	-.0000030	.0002	-2.4050	.9793	.21595	.0001
15.12.69	14	.0037	-.0000027	-.0001	-1.7101	.9794	.88905	.0001
29.12.69	19	.0016	-.0000015	-.0001	-2.4545	.9792	.12250	.0000
16. 1.70	31	-.0005	.0000005	-.0001	-2.4587	.9791	.10651	-.0000
16. 2.69	29	-.0009	.0000024	-.0001	-2.4307	.9789	.16081	-.0000
16. 3.70	32	-.0008	.0000012	-.0001	-2.4000	.7286	.22197	-.0000
17. 4.70	28	-.0009	-.0000018	-.0001	-2.4052	.9785	.21143	-.0000

1004 F KEIN NEWPLOT AUFRUF

Elementos orbitales de NIMBUS-3 y sus variaciones per día

Bahnelemente von NIMBUS-3 aus Katalogen /45/ und ihre Änderungen pro Tag

2.1.4-70

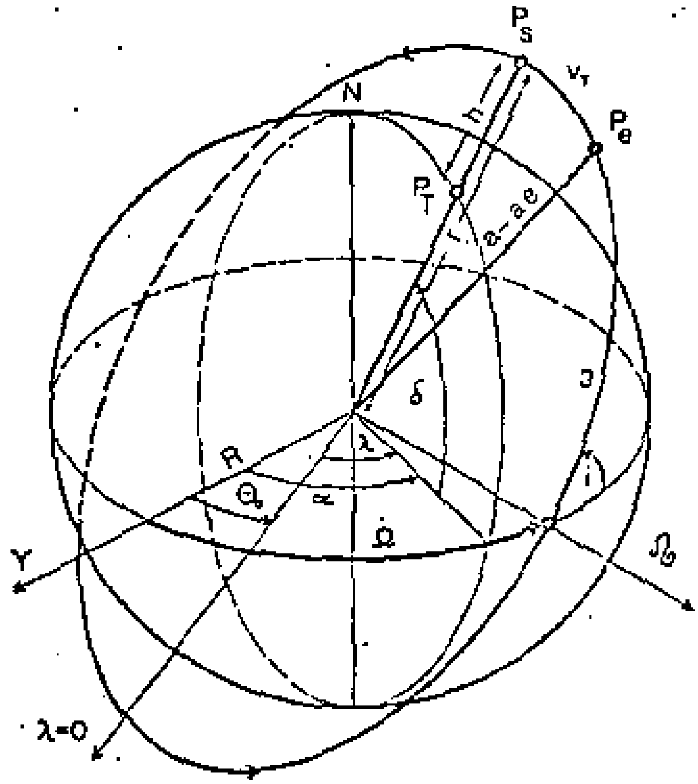

Elementos orbitales

Die Bahnparameter einer Satellitenbahn bezogen auf die Äquatorebene

$\ddot{x} = -\frac{G M x}{r^3}$; $\ddot{y} = -\frac{G M y}{r^3}$; $\ddot{z} = -\frac{G M z}{r^3}$; $G = 6{,}670 \cdot 10^{-11} [m^3/kg s^2]$

M = peso de la tierra

$U = 2\pi\sqrt{\frac{a^3}{GM}} \sim 1{,}659 \cdot 10^{-4} \sqrt{a^3_{[Km]}}$ período orbital

$N_{[Tag^{-1}]} = \sqrt{\frac{G M}{a^3}} \sim 17{,}042 \left(\frac{R}{a}\right)^{\frac{3}{2}}$ períodos per día

$\frac{\Delta\Omega}{Tag} = -3\pi J_2 \left(\frac{R}{p}\right)^2 \cos i \sim \frac{9^0{,}98}{\sqrt{\left(\frac{a}{R}\right)^7}(1-e^2)} \cos i$ prececión del nudo per día

$J_2 \sim 1082{,}64 \cdot 10^{-6}$

$p = r(1 + e\cos(v_T))$

$i \sim \text{Arccos}\left(-0{,}09877 \sqrt{\left(\frac{a}{R}\right)^7}\right)$ inclinación

	1	2	3	4	5	
	Konstante Wiederholungsperioden *periodos de repetición constantes*	Hohe Informationsauflösung *Resolución*	Lange Lebensdauer des Satelliten *duración de la vida del satélite*	Konstante Beleuchtungsverhältnisse *Condiciones de iluminación constantes*	Konstanter Aufnahmemaßstab *escala constante*	Lücke… Bedec… Erdob… *cubie… sin h…*
ückenlose Bedeckung der Erdoberfläche		X		X		*orbit…* Polar… i nahe… ße Str… breite…
onstanter Aufnahemaßstab					Kreisbahn e ~ 0° *orbita circular*	
onstante Beleuchungsverhältnisse	X			Sonnensynchrone Präzession, legt i fest; N=natürliche Zahl *orbita sincrona con el sol*		
nge Lebensdauer es Satelliten		X	Große Flughöhe *altura alta*			
he Informationsauflösung		Kleine Streifenbreite, niedrige Flughöhe. *altura baja*				
nstante Wiederlungsperioden	Variation der Umlaufzeit *variación del período orbital*					

Condiciones por un satélito …
por la percepción remota te…
X : contradicciones

Flughöhe in m altura del vuelo	Bodenauflösung in m		Cantidad de líneas pro km Anzahl der Scanlinien pro km und Kanal		Cantidad de las imagenes TV à 525 líneas Anzahl der TV Bilder mit 525 Linien pro km	
	M^2S	Super Cyclope	M^2S	Cyclope	M^2S	Cyclope
300	0,75	0,45	1.340	2.220	2,60	4,25
600	1,50	0,90	670	1.110	1,30	2,12
1.200	3,00	1,80	333	557	0,63	1,06
2.000	5,00	3,00	200	333	0,38	0,63
2.500	6,25	3,75	160	267	0,31	0,51
3.000	7,50	4,50	133	222	0,26	0,42
5.000	12,50	7,50	80	133	0,15	0,26

Anzahl der TV-Bilder pro km-Flugstreifen als Funktion
der Flughöhe für M^2S und Super-Cyclope

Misión, r avión
Scanner

	bandas	
Öffnungswinkel:	M^2S - lo - Kanal Scanner	Super Cyclope 4-Kanal IR Scanner
	100^{o}	30^{o} - 60^{o} (50^{o})
Auflösung:	2,5 mrad	1,5 mrad

Flughöhe in m	Resolución (pixel) [m] Auflösung in m		extensión de una faja abgescannte Breite in m		bei 20%iger Überdeckung	
	M^2S	Super Cyclope	M^2S	Super Cyclope	M^2S	Super Cyclope
300	0,75	0,45	715	280	430	170
600	1,50	0,90	1.430	560	860	336
1.200	3,00	1,80	2.850	1.150	1.710	690
2.000	5,00	3,00	4.767	1.865	2.860	1.120
2.500	6,25	3,75	5.950	2.350	3.580	1.400
3.000	7,50	4,50	7.150	2.800	4.290	1.680
5.000	12,50	7,50	11.918	4.660	7.150	3.000

Bodenauflösung, Scanbreite ohne und mit 20% Überdeckung für M^2S und Super-Cyclope als Funktion der Flughöhe

Misión por avión:
camera multiespect[i]

ciss MUK 8; Winkel 64°; *ángulo* 7 x 7 cm Film *película*

lughöhe in m	Erfaßte Breite in m	Erfaßte Breite bei 20% Überlappung in m	Erfaßte Breite bei 60% Überlappung in m	Erfaßte Breite bei 75% Überlappung in m
300	265	212	106	66
600	530	424	212	132
.200	1.060	848	424	265
.000	1.767	1.413	707	442
.500	2.206	1.764	882	552
.000	2.651	2.120	1.060	663
.000	4.419	3.535	1.768	1.105

Erfaßte Breite am Boden für verschiedene Überdeckungsgrade (Längsüberdeckung) als Funktion der Flughöhe für Multispektrale Kamera (MUK 8, Zeiss) male photogrammetrische Kamera (RMK); Winkel 125°; 24 x 24 cm Film *Misión por avión*

Camera fotogramétrica *ángulo* *película* *camera*

C = 15 cm

ura del elo ughöhe m	Erfaßte Breite in m, *extensión de las fajas en el suelo*	Erfaßte Breite bei 20% Überlappung in m *20% cubierta*	Erfaßte Breite bei 60% Überlappung in m	Erfaßte Breite bei 75% Überlappung in m
300	815	625	326	204
600	1.630	1.304	652	407
200	3.260	2.608	1.304	805
000	5.433	4.346	2.173	1.358
500	6.791	5.432	2.716	1.697
000	8.150	6.520	3.260	2.037
000	13.583	10.866	5.433	3.396

. Erfaßte Breite am Boden für verschiedene Überdeckungsgrade (Längsüberdeckung als Funktion der Flughöhe für Photogrammetrische Kamera [Zeiss])

Disposición de plataformas de una misión preparativa

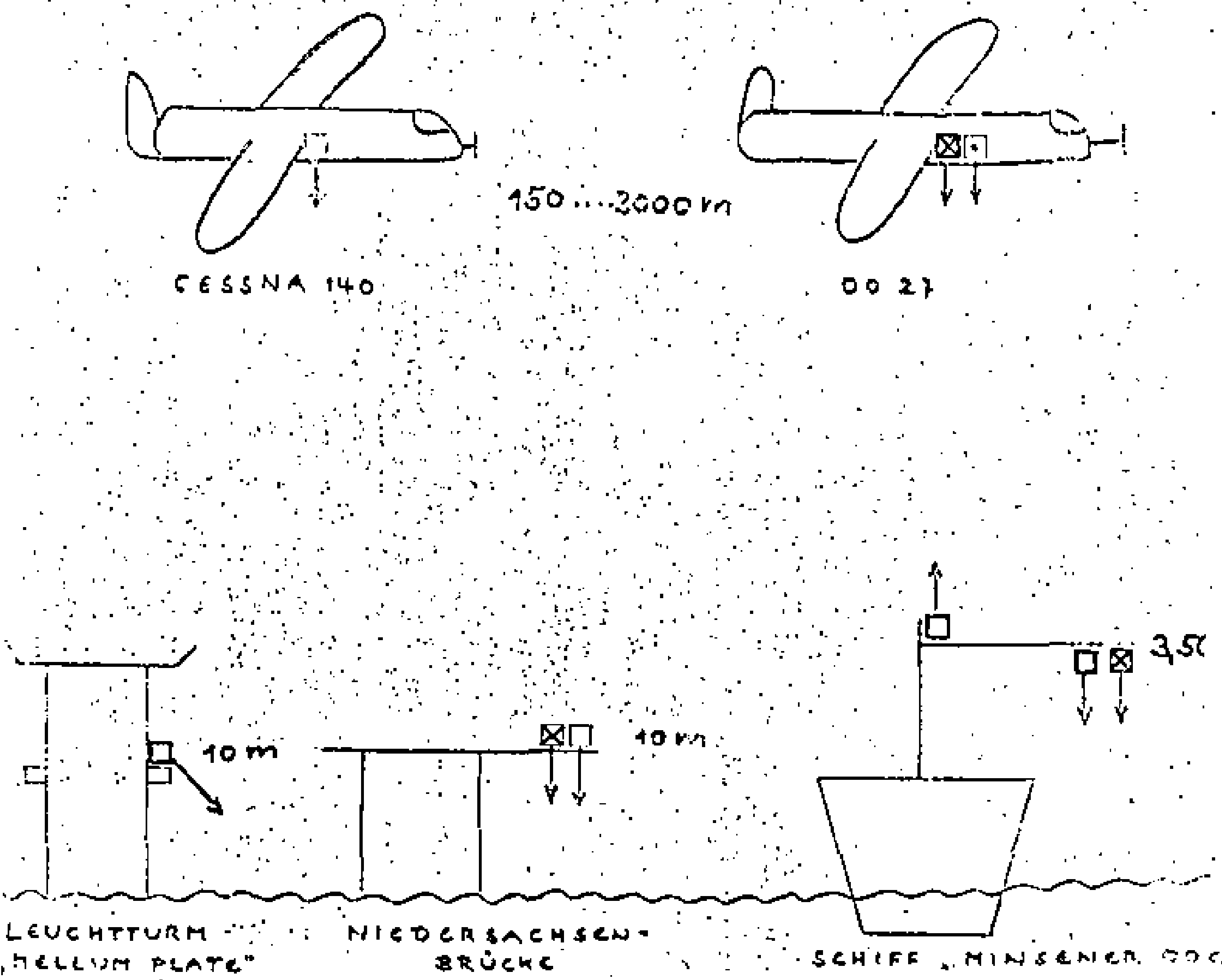

RADIOMETEREINSATZ JADEBUSEN 1974

☐ EXOTECH 100 4 Kanal/ERTS-kompatibel

☒ BARNES PRT5, HEIMANN KT4 thermal 8 ... 14 μ

⊡ Thermalscanner RECONOFAX XIII 8 ... 14 μ

Modulacion de un señal continuo

$f_e = \frac{1}{2\ell}$: Signalfrequenz,
frecuencia del señal

2ℓ : Wellenlänge einer Hell-Dunkel-Periode
periodo de un par de líneas

$f_s = \frac{1}{s}$: Abtastfrequenz, abgestimmt auf die Breite s eines Auflösungselementes
frecuencia del scanning, corespondiente a un pixel

$$\boxed{f_e \leq \frac{f_s}{2}} \qquad (s \leq \ell)$$

f_s : *frecuencia límite ("NYQUIST")*

Determinación empírica

Original

25 µm

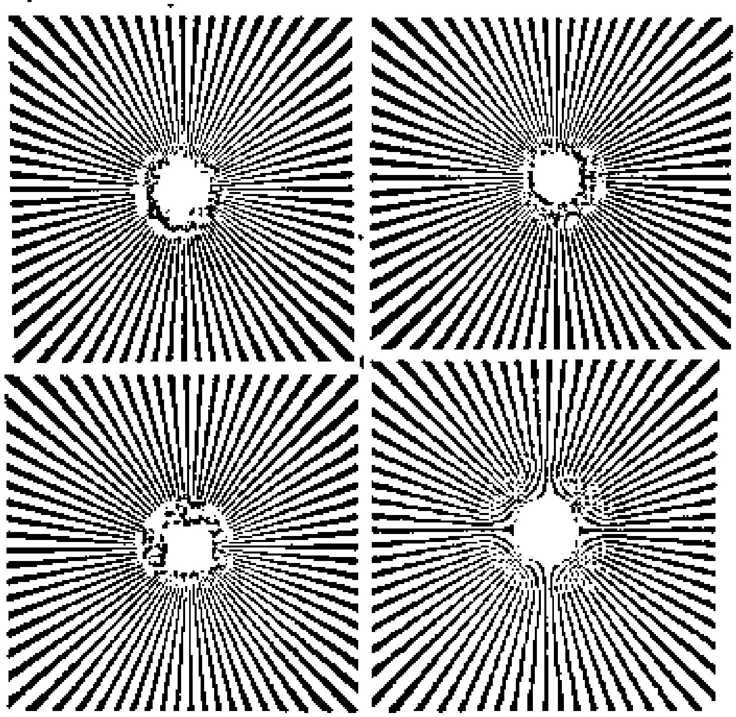

50 µm

100 µm

$$\frac{2\ell}{s} \sim 2{,}5 \ldots 3$$

Modulacion de un señal rectangulo

$$M_r = \frac{s^2 - 2(s^2 - s \cdot l)}{s^2} = 2 \cdot l/s - 1$$

s^2 : aréa de un pixel
$s \cdot l$: aréa cubierta

für $l \leq s$

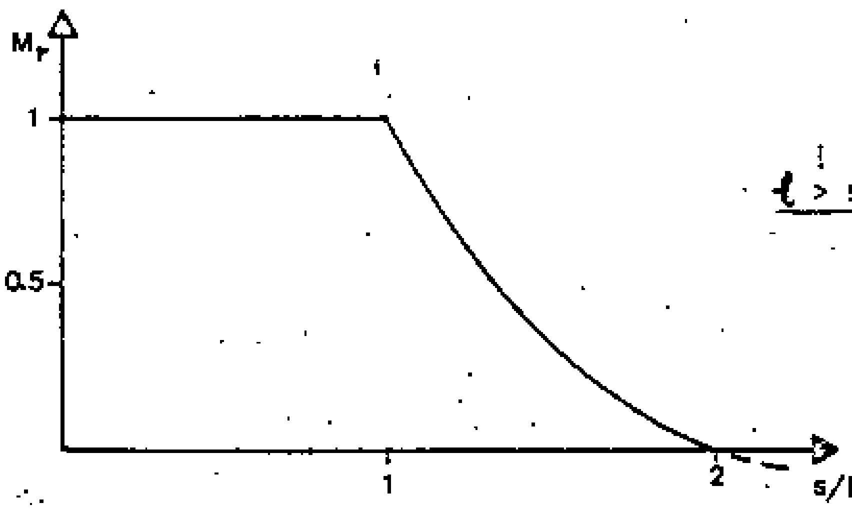

$l \overset{!}{>} s/2$

Modulación de un señal seno $i = J_0 \cos(2\pi f_e x)$

$$i'(x) = \frac{1}{s} \int_{x-s/2}^{x+s/2} i(\xi) d\xi = \frac{J_0}{s} \cdot \frac{1}{2\pi \cdot f_e} \cdot 2 \cdot \cos 2\pi f_e \cdot x \cdot \sin 2\pi f_e \cdot \frac{s}{2}$$

señal del detector (i')

$$MTF = \frac{\sin(\pi \cdot f_e \cdot s)}{\pi \cdot f_e \cdot s} = \frac{i'}{i}$$

, ver pág. 2.4.3-110

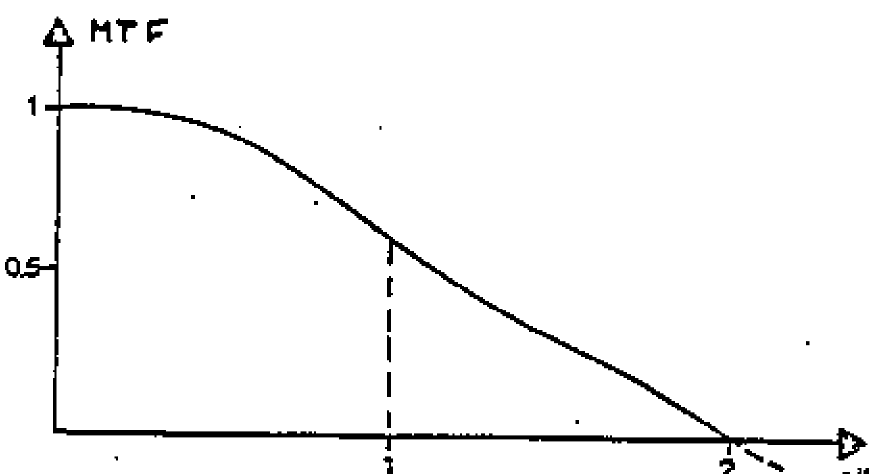

Z. 1.3 – 150

(27)

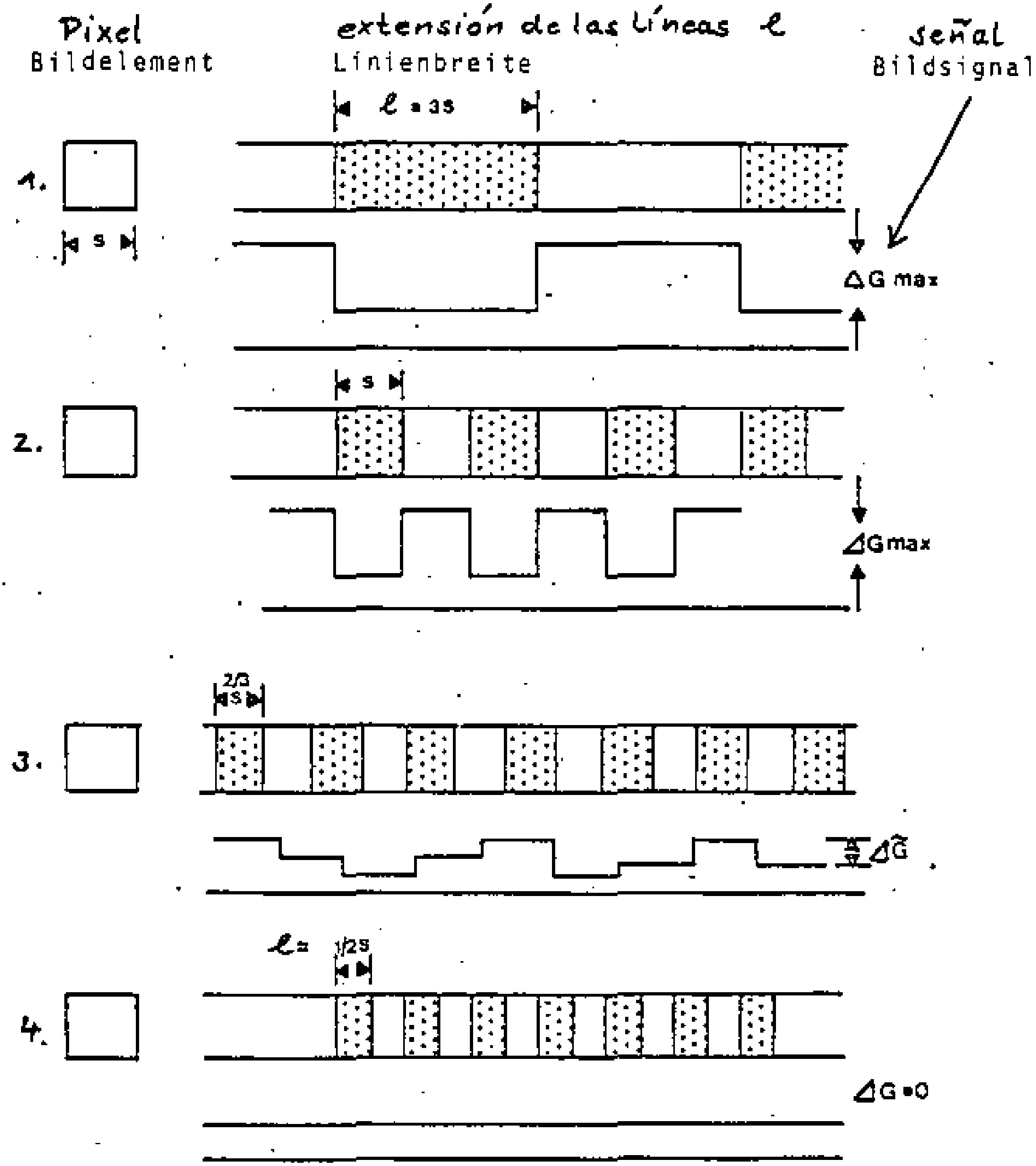

Scanning de líneas, variando la extensión de las líneas ℓ (4 casos)

Abtastung eines Strichrasters bei einer Variation der Rasterlinienbreite

In den Digitalbildern der Abtastsysteme sind neben elektronischen Störeinflüssen (Rauschen, Störungen bei der Aufzeichnung auf Magnetband) zwei Komponenten ausschlaggebend für mögliche Verzerrungen des Bildsignals:

1) die endliche Größe eines Bildelements (1)
2) Abtastung des kontinuierlichen Signals (2)

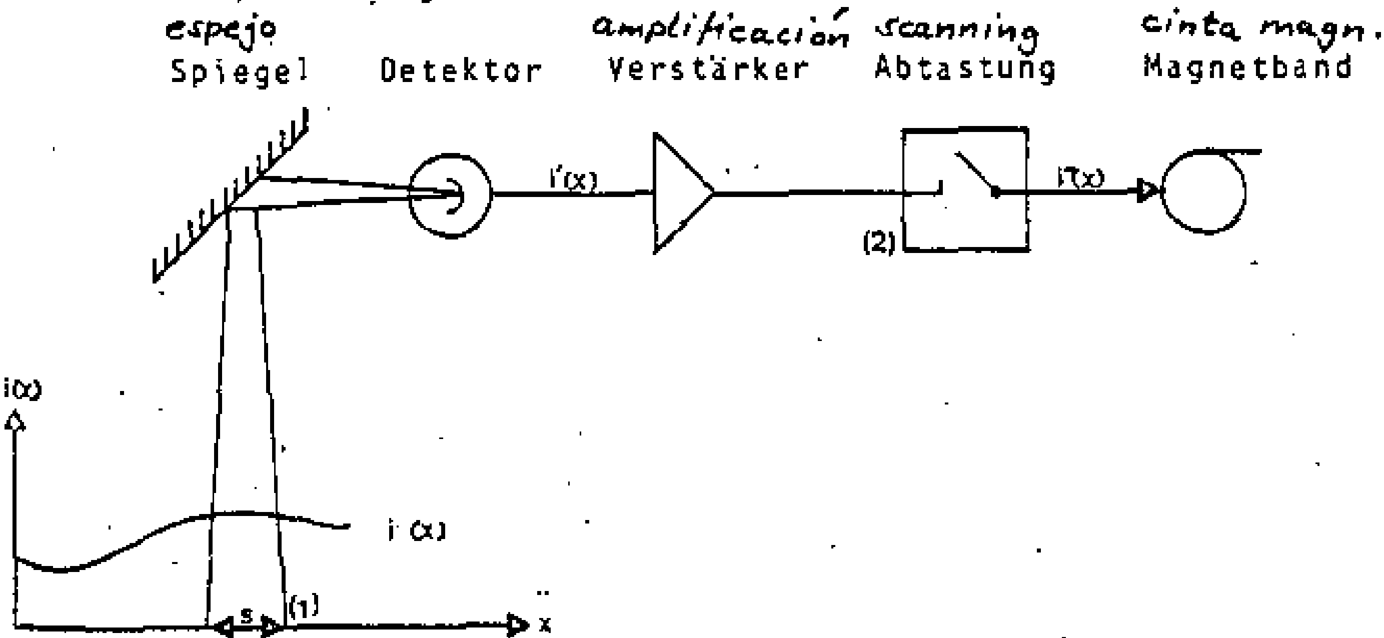

Perturbaciones de los señales
Störeinflüsse im Übertragungsweg des Bildsignals
(nach Nowak)

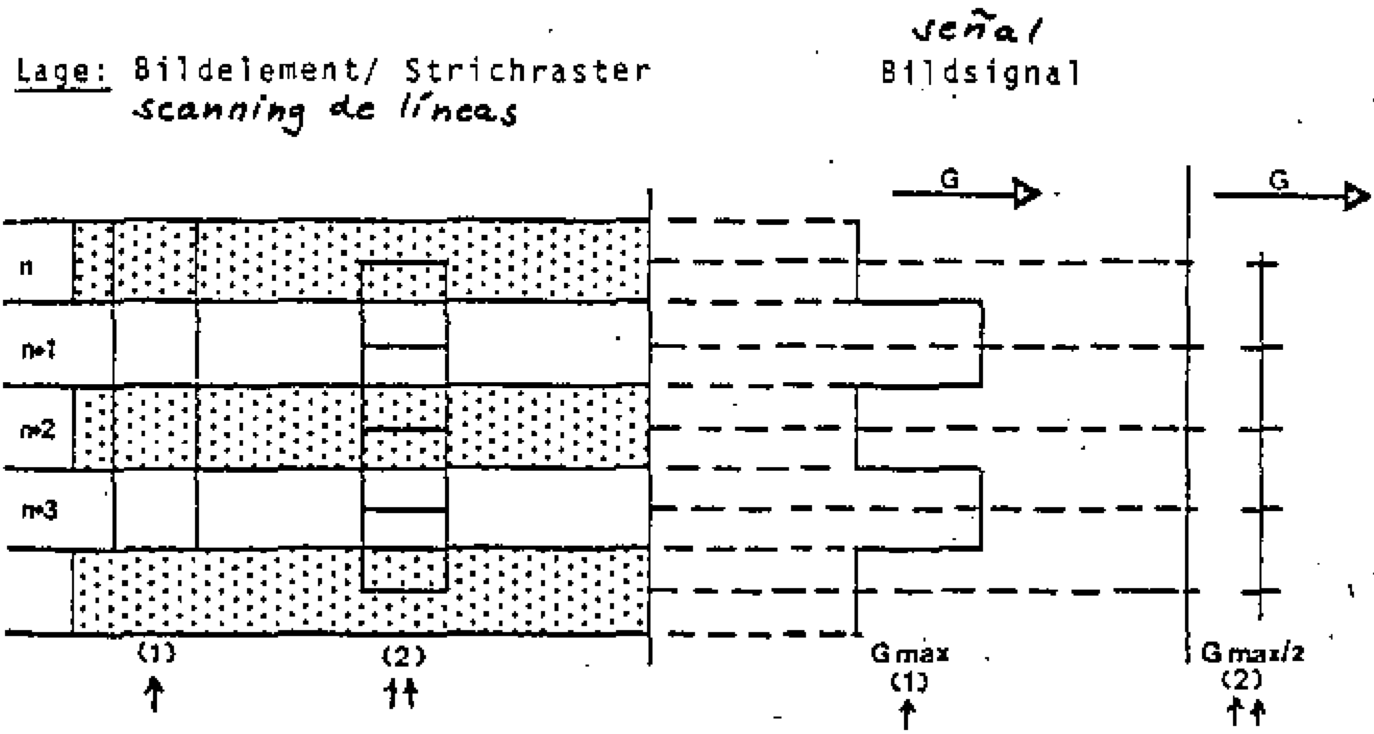

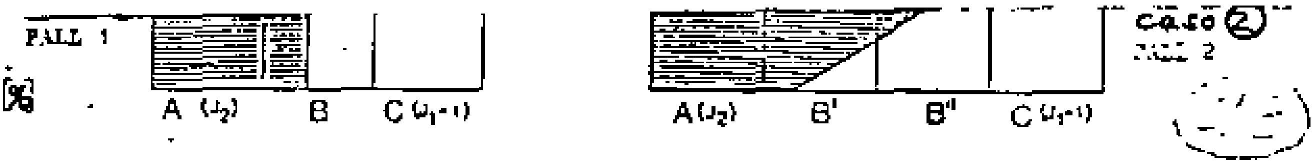

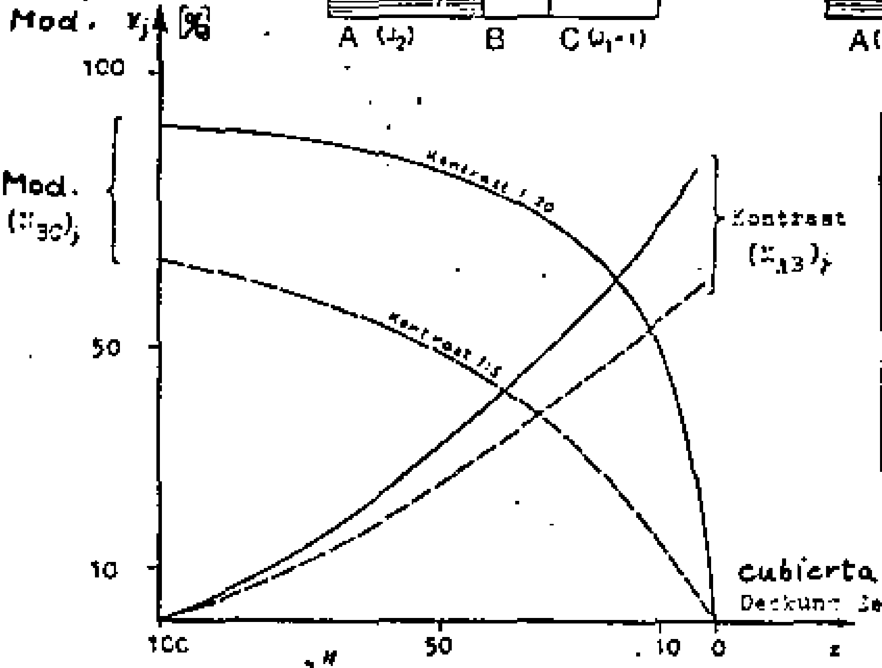

$$(M_{AB})_j = \frac{J_2 - (1 + \frac{z}{100}(J_2 - 1))}{J_2 + (1 + \frac{z}{100}(J_2 - 1))} \quad (1)$$

$$(M_{B'B''})_j = \frac{z'(J_2-J_1) - z''(J_2-J_1)}{z'(J_2-J_1) + z''(J_2-J_1) + 200J_1} \quad (2)$$

Modulación (véan 2.1.3-70)

cubierta de la area del sensor [%]

Deckung Sensorfläche [%]

z'' ↑ / z' →	0	10	20	30	40	50	60	70	80	90	100
100	67	56	47	39	32	25	19	14	9	4	0
90	64	53	44	35	28	21	15	10	5	0	
80	62	50	40	31	24	17	11	5	0		
70	58	46	36	27	19	12	6	0			
60	55	42	31	21	13	6	0				
50	50	36	25	15	7	0					
40	44	30	18	8	0						
30	37	22	10	0							
20	29	12	0								
10	17	0									
0	0										

Modulación entre z' y z'' [%] por C = 5:1 (agua / campos)

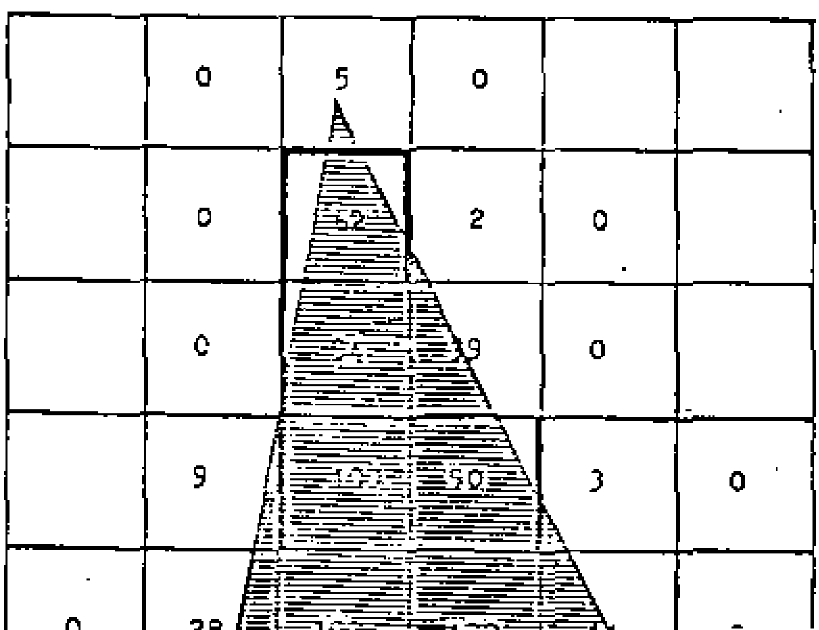

En vecino de un "punto" de apoyo el contraste varia casualmente

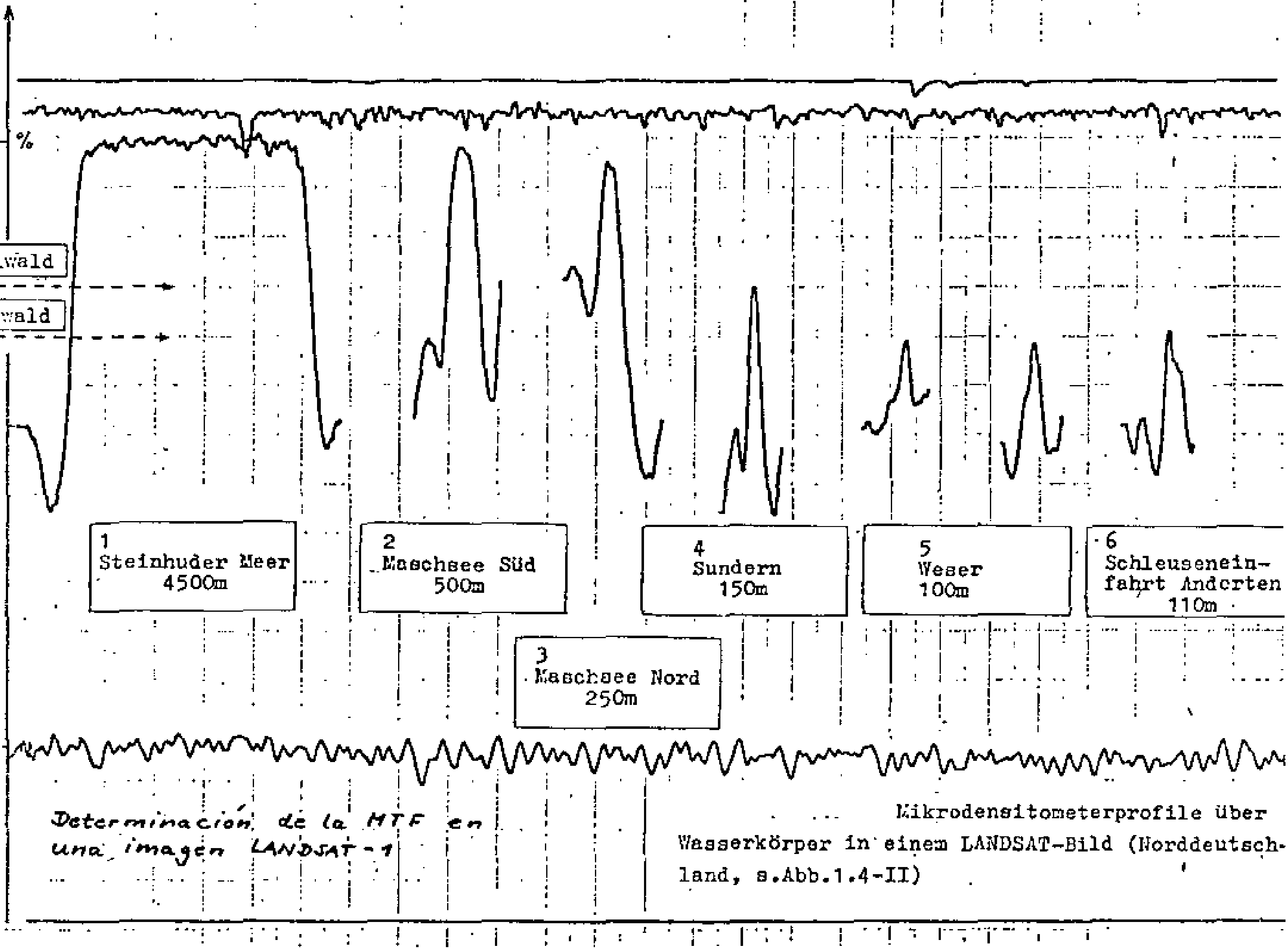

Determinación de la MTF en una imagen LANDSAT-1

Mikrodensitometerprofile über Wasserkörper in einem LANDSAT-Bild (Norddeutschland, s.Abb.1.4-II)

Parámetros de calidad por imagenes numéricas

$$MTF_s = S_\flat t \frac{\sin \frac{\pi S_\flat}{\lambda}}{\frac{\pi S_\flat}{\lambda}}$$; statisch – dirección del vuelo

λ : dimensión de los objetos

$$MTF_d = S_\flat t \frac{\sin \frac{\pi S_\flat}{\lambda}}{\frac{\pi S_\flat}{\lambda}} \cdot \frac{\sin \frac{\pi t v}{\lambda}}{\frac{\pi t v}{\lambda}}$$; dynamisch – dirección del scanning

SATELLIT	Brennweite Abtaster [cm] *distancia focal*	Flughöhe h [km] *Altitud del vuelo*	Differentielle Öffnung (?) [mrad]	Spiegelfrequ. (f) [U/sec]	Größe einer Detektorzelle S_D [mm] *Dimens. detector*	Bildel. am Bod. in Flugr. [km] (D)	Fluggeschwind. v_L [km/sec] *velocidad del vuelo*	Scangeschwind. v_q [km/sec] *v. del scanning*	Belichtungszeit t [µs] *tiempo de la exposición*	Bildelement am Boden in Abtast-richt. [km]
NIMBUS-3	10	1112	8,7	0,80	0,635 × 0,635	9,5	6,23	8733,6	1,11	9,5
LANDSAT-1	46	913	0,086	13,62	0,04 × 0,04	0,078	6,47	78131,8	0,00072	0,056

Ejemplos por componentes para determinación teorética de la MTF en 2 direcciones

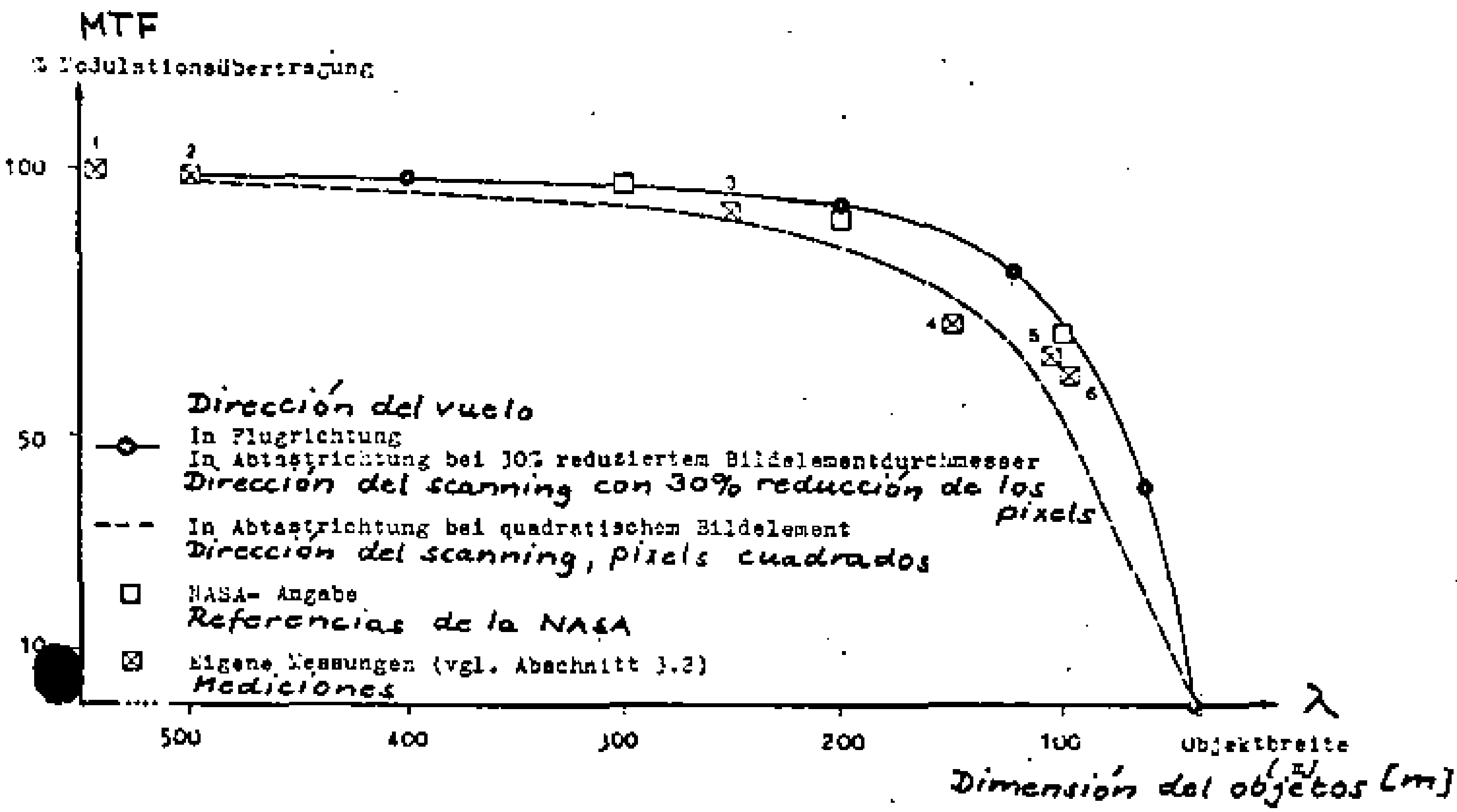

MTF teorética del scanner LANDSAT 1-3

Resolución

Ergebnis:
Resultado:

Auflösungsvermögen

Hoher Kontrast — 52 lp/mm

Niedriger Kontrast — 37 lp/mm

Resolución de tipos de cameras disponibles
Auflösungsvermögen verfügbarer Kameratypen

Kameratyp	Auflösung
Zeiss RMK 15/23	40 lp/mm
Zeiss RMK 30/23	40 lp/mm
Zeiss RMK 60/23	25 lp/mm
Zeiss TRb 60/24	75 lp/mm
Itek LFC 30	80 lp/mm
Wild RC10 15/23	40 lp/mm
Wild RC10 30/23	25 lp/mm

Emulsion: 32 lp/mm - 50 lp/mm
Spezialemulsion: 100 lp/mm

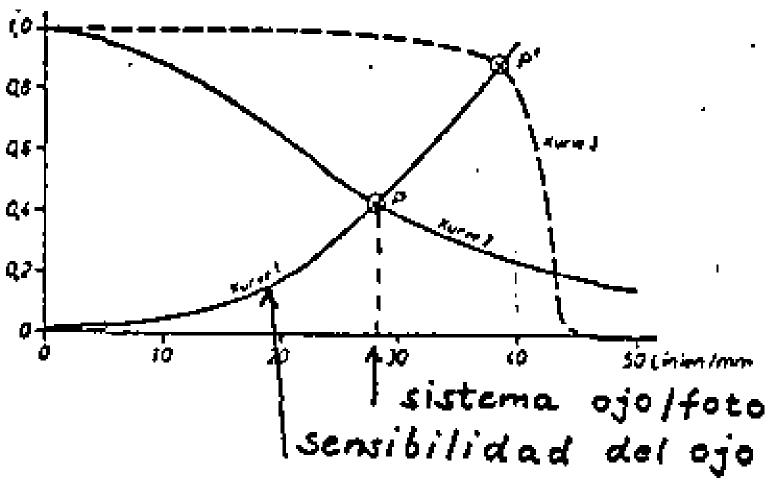

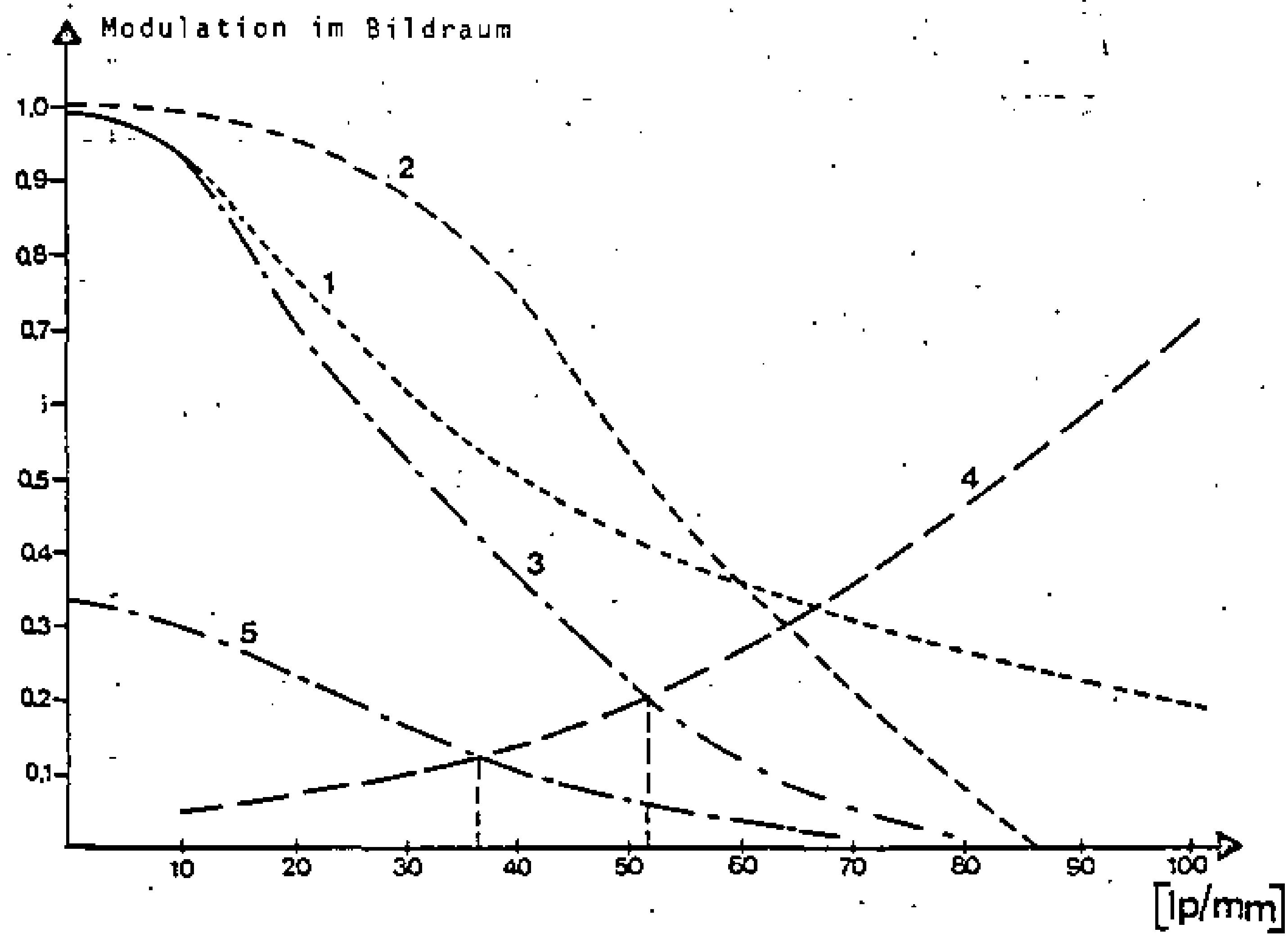

1) MTF de un objetivo, contraste 1000:1

2) MTF por movemiento de la imagen (12 µm)

3) Función total de 1) y 2)

4) Sensibilidad del ojo

5) Función 3) transformada por contraste 2:1

$$MTF = \frac{M_A}{M_E} \; ; \; 0 \leq MTF \leq 1 \quad ; \quad M_A < M_E$$

$$MTF = f(f_\lambda)$$

La capacidad de películas, objetivos y otros elementos ópticos para reproducir los detalles de un objeto puede definirse por la función de transferencia de contraste MTF. Esta indica la relación entre el contraste . del objeto y el contraste . de la imagen en la reproducción. La razón . . es una función de la frecuencia espacial N, es decir, de la densidad de las estructuras del objeto, medida en líneas por milímetro (L/mm).

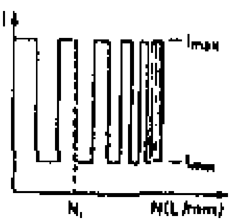

Objekt
Object

Bild
Image

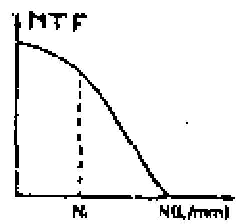

Photographische Schicht
Photographic emulsion
Émulsion photographique
Emulsión fotográfica

- - - - - 15 DIN
——— 20 DIN
········ 25 DIN

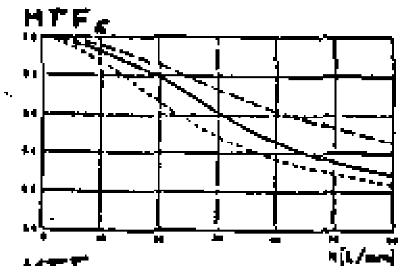

Objektiv
Lens
Objectif
Objetivo

c_k = 150 mm 1 : 5.6

- - - - - τ = 0°
——— τ = 22.5°
········ τ = 45°

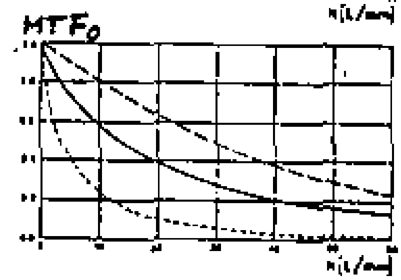

Modulationsübertragungsfunktion für die Bildwanderung

Movemiento de la imagen

w: Bildwanderung in [mm]

f_λ: Ortsfrequenz [lp/mm]

frecuencia espacial

$$W(f_\lambda) = \frac{1}{f_\lambda \cdot w \cdot \pi} \cdot \sin f_\lambda \cdot w \cdot \pi$$

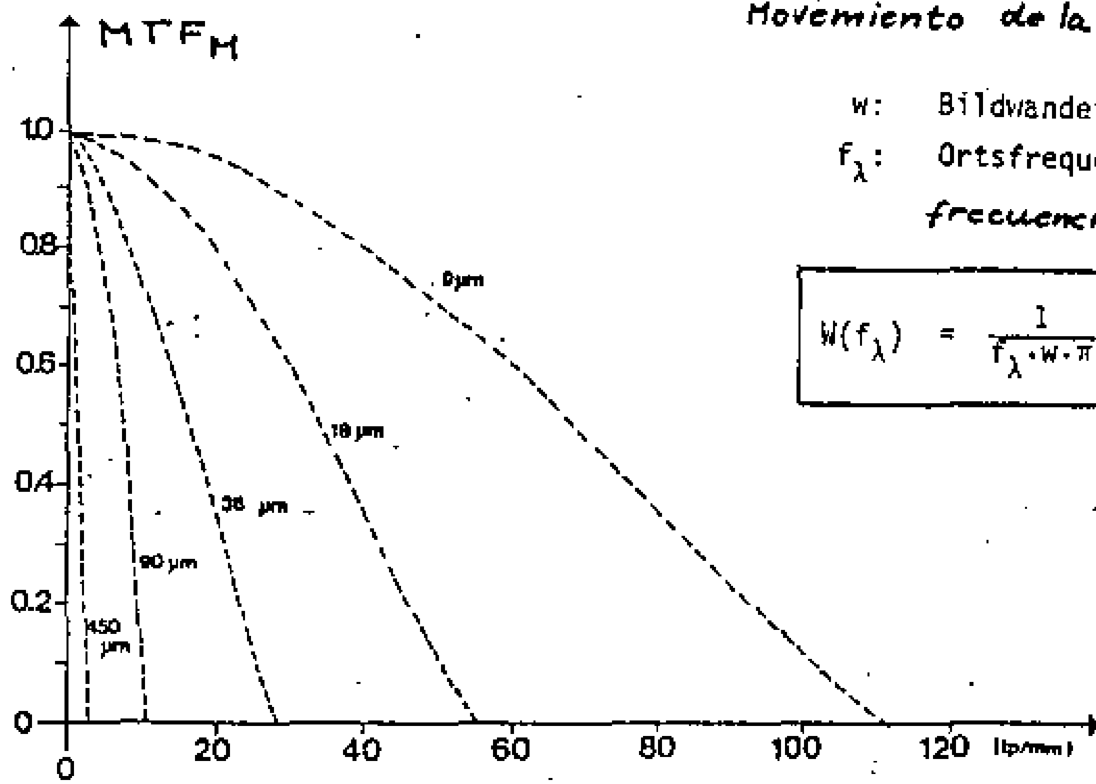

Gesamtfunktion
Optical transfer function
Fonction de transfert globale
Función total

20 DIN
τ = 22.5°
w = 0.023 mm

$$MTF = MTF_E \cdot MTF_O \cdot MTF_H$$

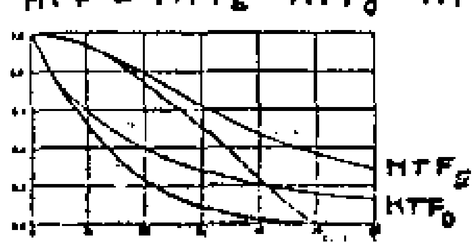

El contraste

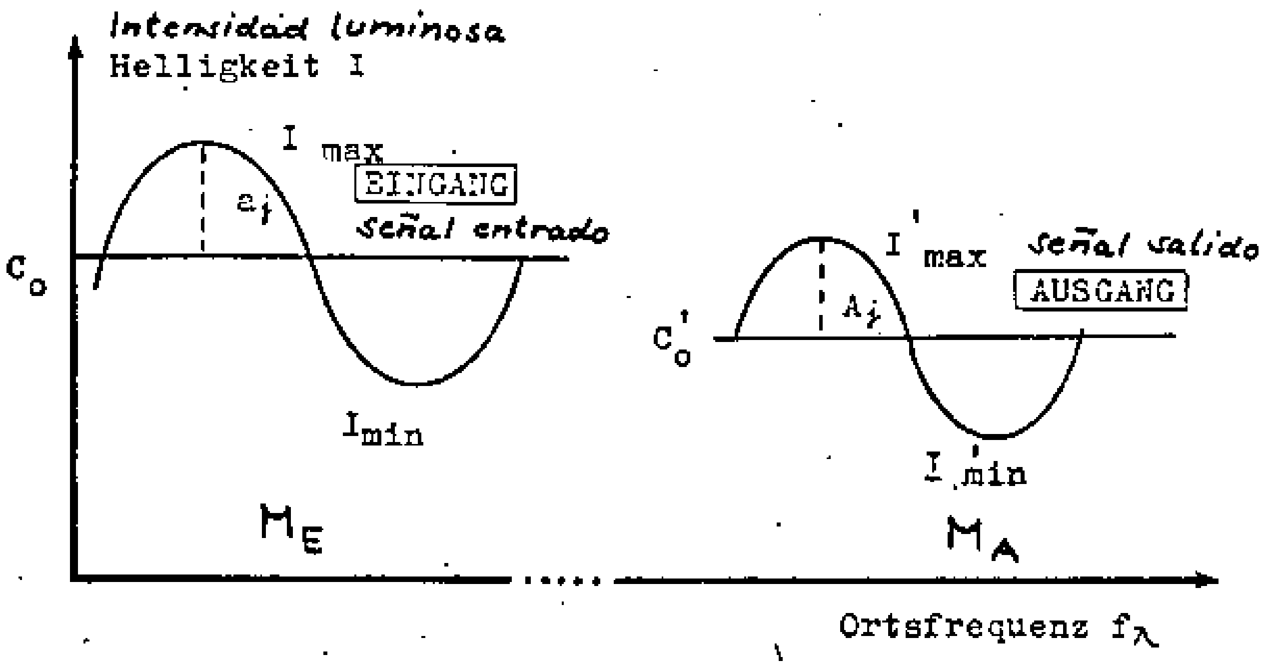

- $C = \frac{I_{max}}{I_{min}}$ Verhältnis von maximaler zu minimaler Helligkeit, $I_{min} = 1$. **contraste**

- $D = \log(\frac{I_{max}}{I_{min}})$ Dichtedifferenz, Logarithmus von C

- Modulation-(Kontrast-)umfang

$$M = a/C_o = \frac{(I_{max}-I_{min})/2}{(I_{max}+I_{min})/2} = \frac{I_{max}-I_{min}}{I_{max}+I_{min}}$$ *Modulación*

$$M = \frac{C-1}{C+1} = \frac{10^D-1}{10^D+1} \quad (I_{min} = 1)$$

C	Dichtedifferenz D	Modulation M
1000 : 1	3,0	1,0
100 : 1	2,0	0,98
32 : 1	1,5	0,94
10 : 1	1,0	0,82
8 : 1	0,9	0,78
5 : 1	0,7	0,66
4 : 1	0,6	0,60
3 : 1	0,5	0,50
2 : 1	0,3	0,33
1,6 : 1	0,2	0,23

RESOLUTION

2. OPTICS

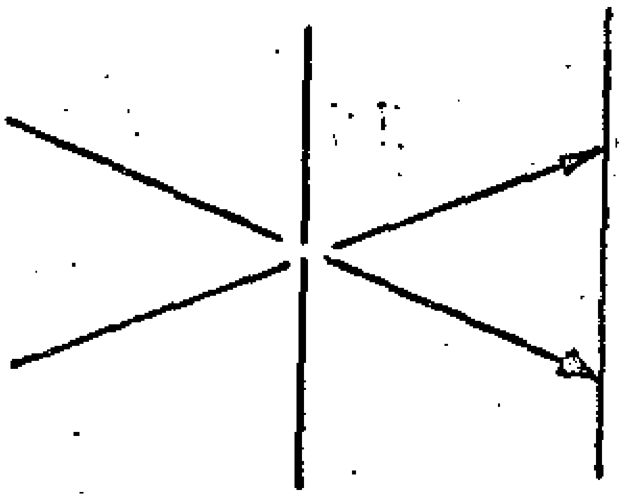

ideal mathematical
image by
pin hole camera

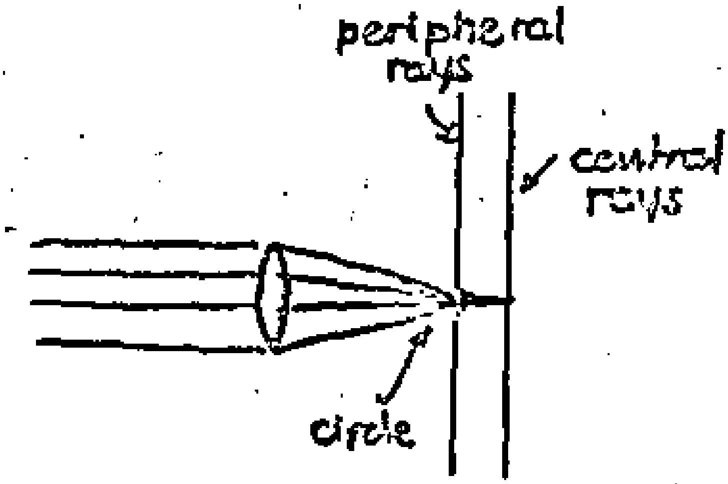

lens errors:

1) photogrammetric cameras
format 23 x 23 cm
20 - 60 lp/mm
2) small format cameras
format 70 x 70 mm
to 100 lp/mm
3) panoramic cameras
to 200 lp/mm

3. IMAGE MOTION, VIBRATIONS

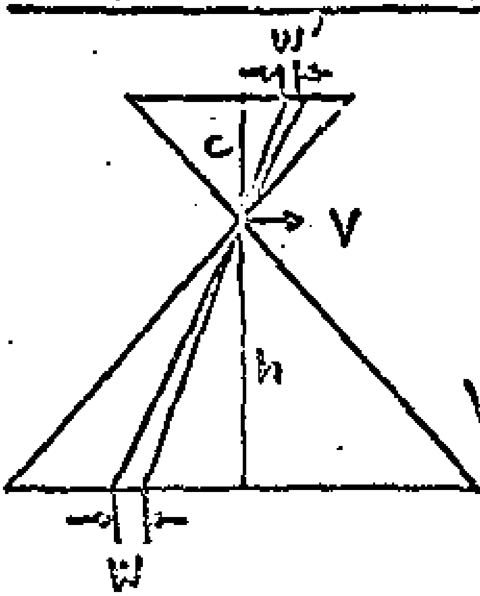

image scale $= \frac{c}{h} = \frac{1}{\text{scale factor } m_B}$

T = exposure time

$V_{km/h} \Rightarrow$ in m/sec

$$W' = \frac{h}{c} \cdot W$$

limit is T = 1/1000 or 1/2000
to 1/250 sec

sensitivity
23/10 DIN – 17/10 DIN

RESOLUTION

1. FILM

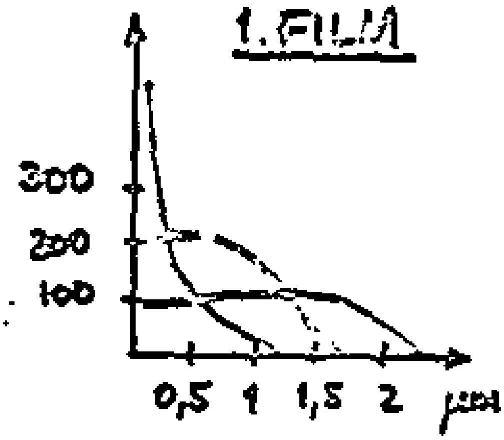

- hard fine grain emulsion, low sensitivity
- normal emulsion, ave. grain ave. sensitivity
- soft coarse grain emulsion high sensitivity

2. DIFFUSION

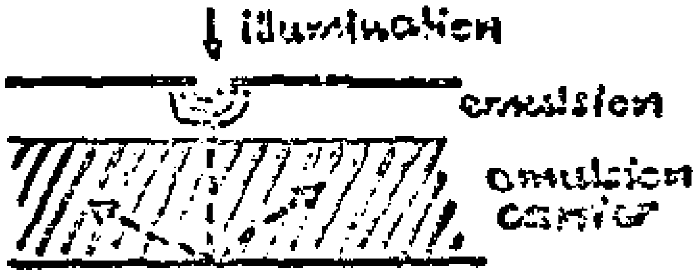

} during exposure colored to avoid reflexions
during development removed

normal emulsions have :

for contrast	1 : 1000	90 – 100 lp/mm
for contrast	1 : 2	30 – 60 lp/mm

copying emulsions have : up to 4000 lp/mm

D-LOG E CURVE

9. EXPOSURE

$$E = S_\omega \cdot T \cdot \tau \cdot \frac{\frac{\pi}{4}}{\left(\frac{c}{d}\right)^2}$$

$\frac{c}{d} = \frac{\text{camera const.}}{\text{aperture}} = \text{f-stop}$

T = exposure time

τ = transmission coeff. of optics

S_ω = radiation (reflection & diffuse)

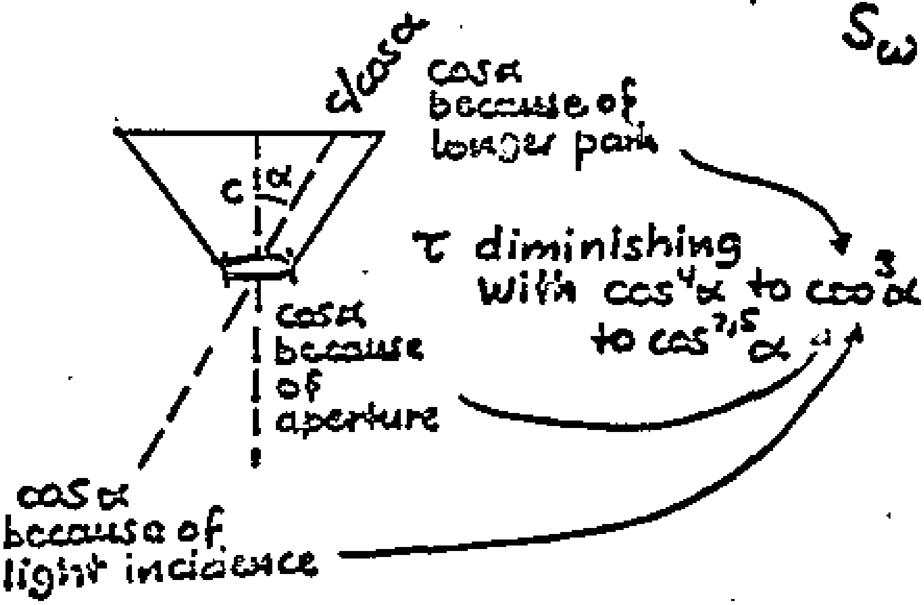

$$D = \frac{D_0}{2}\left[1 + \text{erf}\left(\gamma \log \frac{E - E_0}{E_G - E_0}\right)\right]$$

$$\text{erf}\, y = \frac{1}{\sqrt{\pi}} \int_{-\infty}^{+y} e^{-y^3} dy$$

γ = Slope
E_0 = min. Energy
D_0 = base + fog
E_G = max. Energy to obtain max. density

(constant of film & development)

D - LOG E CURVE

7. Film Sensitivity as Function of Temperature

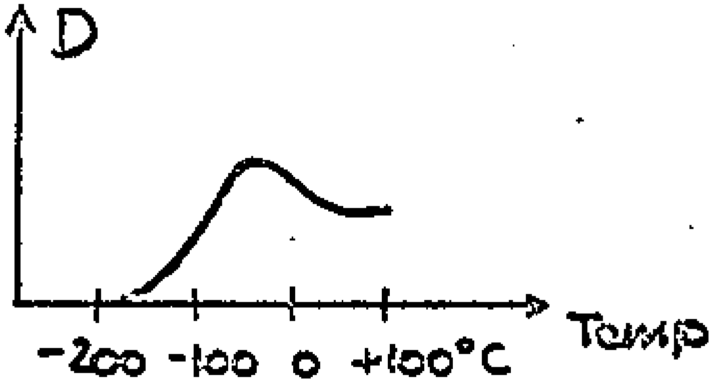

8. γ-curve for different developing times, developer

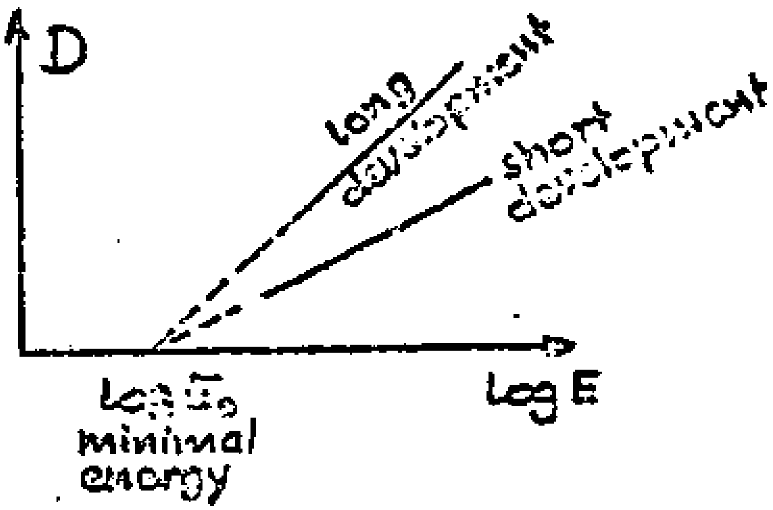

5. OBJECT RANGE

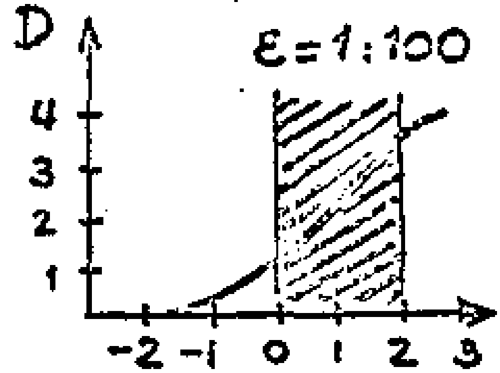

$$\varepsilon = \frac{E_1}{E_2}$$

$$\log \varepsilon = \log E_1 - \log E_2$$

correct illumination in linear part of curve

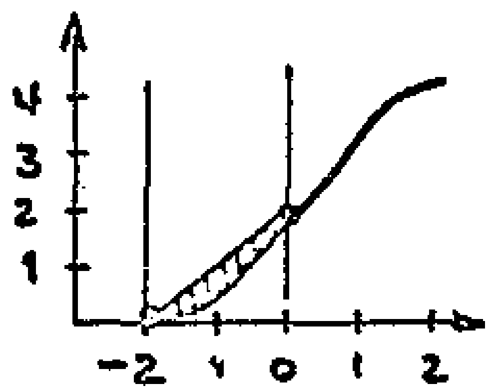

underexposure

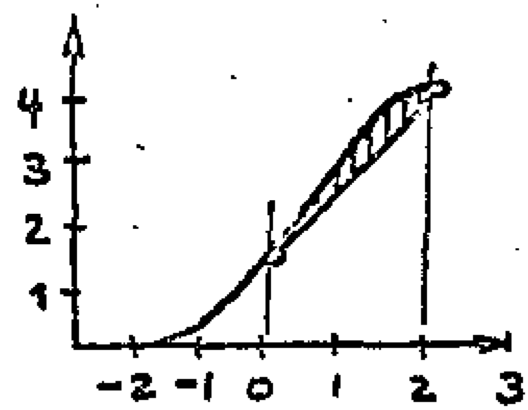

overexposure

6. γ

$$\frac{dD}{d(\log E)} = tg\,\alpha = \gamma$$

Film characteristics:

$\gamma = 1$ ordinary $\varepsilon = 1:100$

$\gamma > 1$ to $\varepsilon = 1:2000$

Nature:

landscape 1:40
aerial photos 1:10
[illegible] 1 : 10^7

D-LOG E CURVE

1. $E = I \cdot t$ Energy = Intensity · Time

2. Equal Energy → Equal Density Change
approximation

3. $\frac{I}{I_0} = T$ T = transparency
I_0 = incoming intensity
I = transmitted intensity

$\frac{1}{T}$ = opacity

4. $D = \log \frac{1}{T} = -\log T$

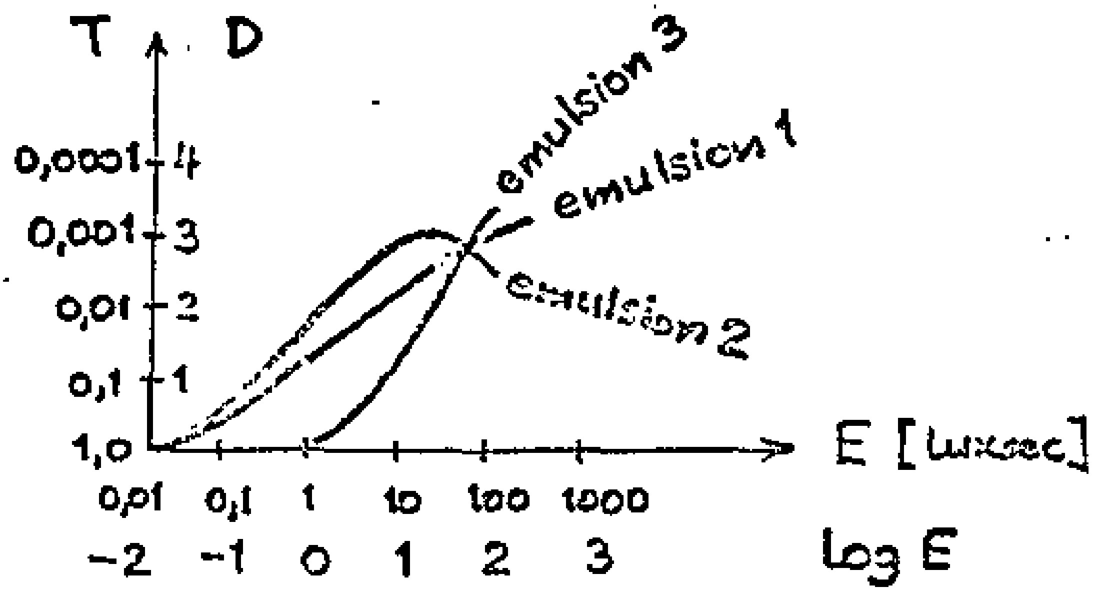

3 Beispiele für S.S.S. - Aufnahme 34 A

S.S.S.
Geom

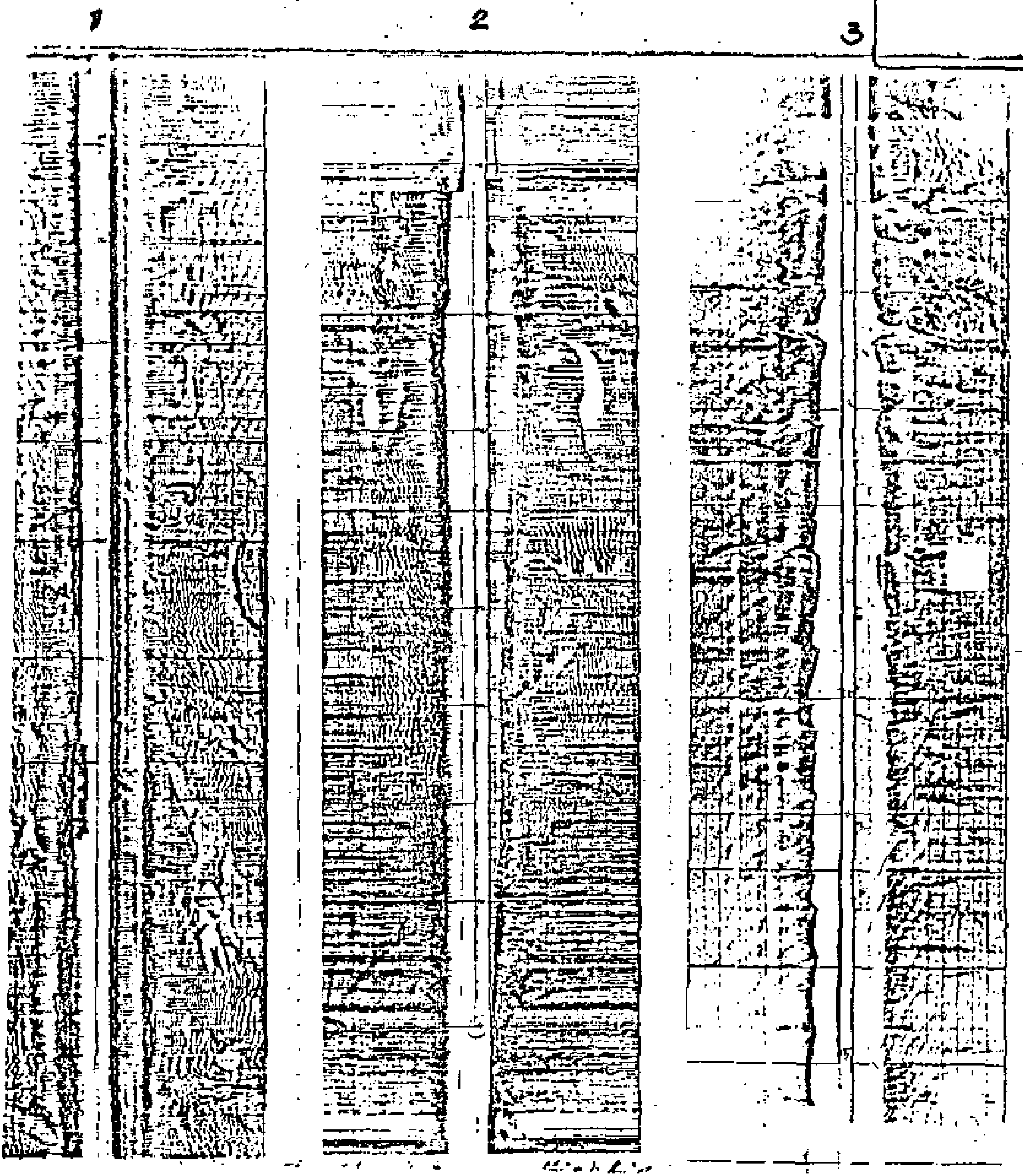

Aufzeichnung:
Formación de los imágenes

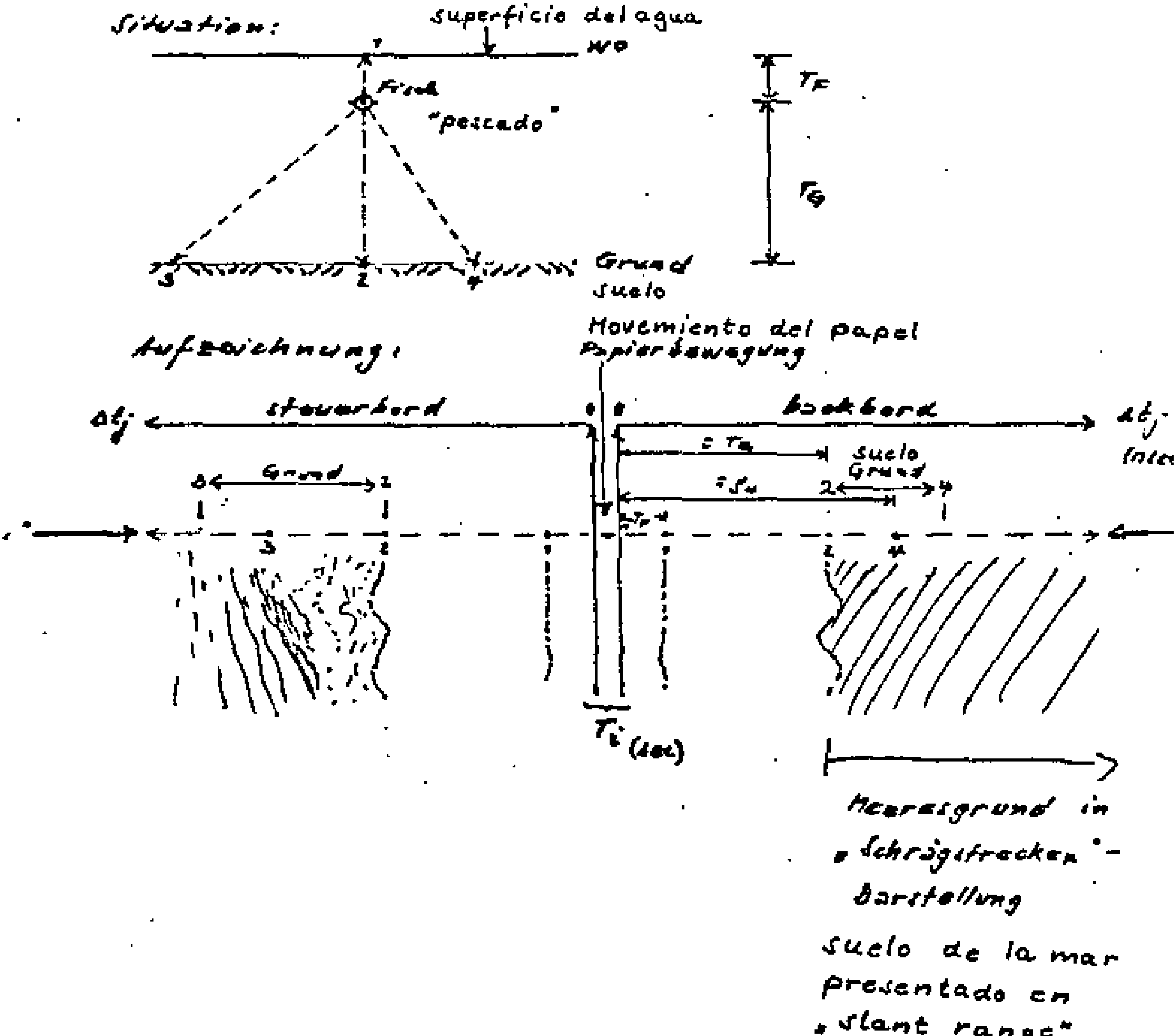

35A

Sistema de Sonar

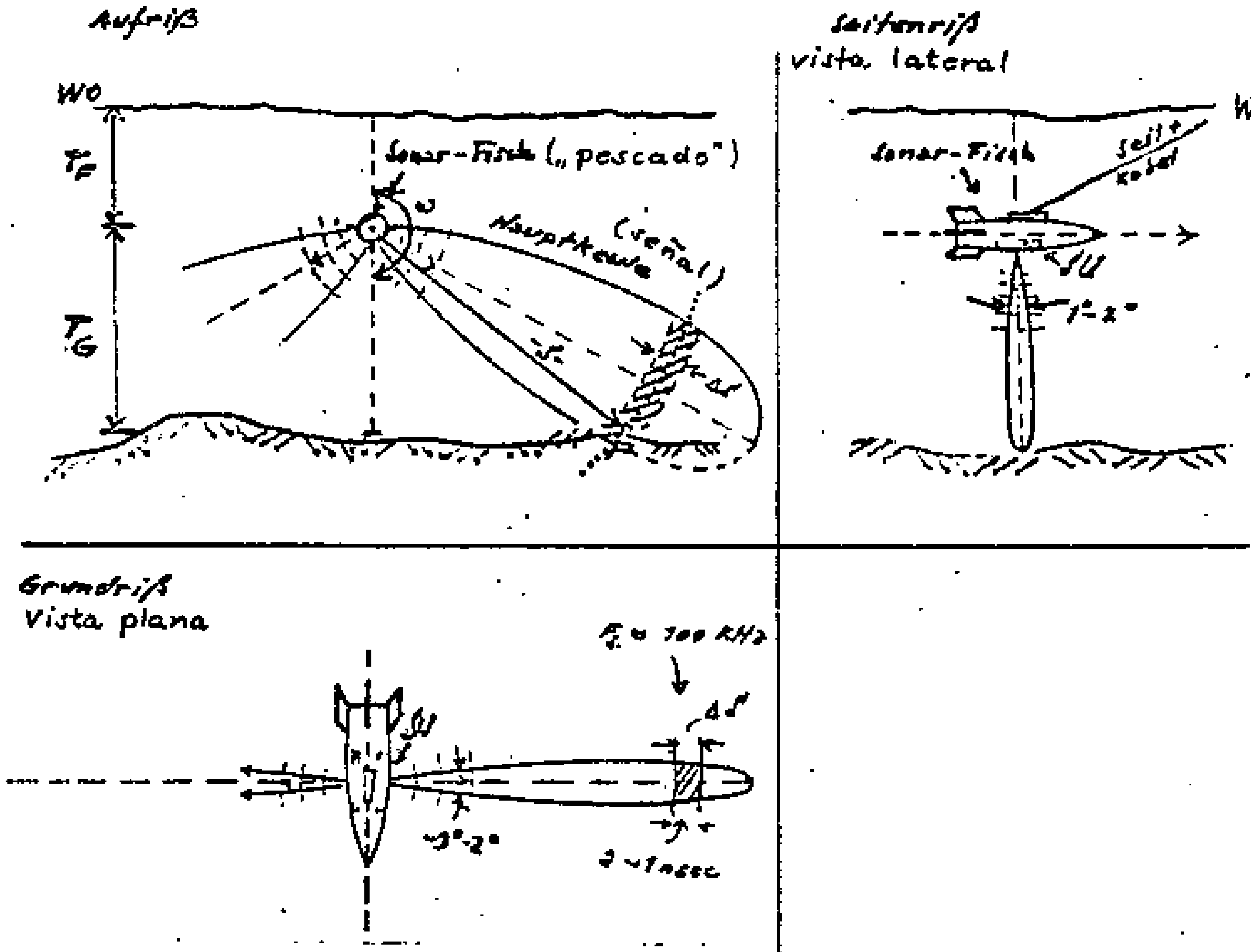

SU: emisor y receptora

Principios de emisión y recepción

Parámetros importantes

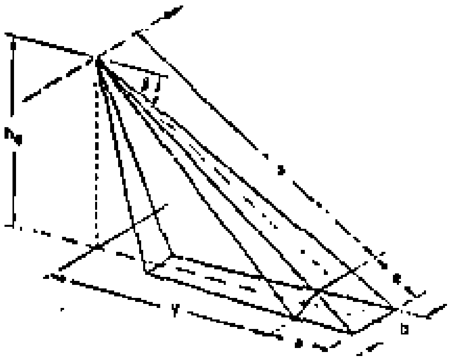

Flughöhe über Grund Flying height above ground Hauteur du vol au-dessus du sol Altura de vuelo sobre el terreno	h_g	Lichtgeschwindigkeit Velocity of light Vitesse de la lumière Velocidad de la luz	c
Schrägentfernung Slant range Distance oblique Distancia oblicua	s	Wellenlänge Wavelength Longueur d'onde Longitud de onda	λ
Horizontale Entfernung Ground range Distance au sol Distancia horizontal	y	Wirksame Antennenlänge Eff. length of antenna Longueur eff. de l'antenne Longitud efectiva de la antena	l
Depressionswinkel Depression angle Angle de dépression Angulo de depresión	β	Zeitdauer eines Pulses Duration of pulse Durée d'une impulsion Duración del impulso	Δt
Auflösung in der Schrägentfernung Slant range resolution Définition dans la distance oblique Resolución en la distancia oblicua			$e \approx \frac{c \cdot \Delta t}{2}$
Geländeauflösung quer zur Flugrichtung Ground range resolution Définition perpendiculairement à la direction du vol Resolución transversalmente a la dirección de vuelo			$a \approx \frac{c \cdot \Delta t}{2 \cdot \cos \beta}$
Geländeauflösung in Flugrichtung Azimuth resolution Définition au sol dans la direction du vol Resolución acimutal			$b \approx \frac{s \cdot \lambda}{l} \approx \frac{h_g \cdot \lambda}{l \cdot \sin \beta}$

Lagefehler eines Geländepunktes mit der Höhe Δh
Horizontal error of a ground point of elevation Δh
Erreur planimetrique d'un point du terrain de hauteur Δh
Error planimetrico de un punto del terreno de altura Δh

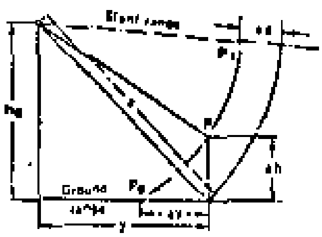

Slant range

$\Delta s = s - \sqrt{y^2 + (h_g - \Delta h)^2}$

$\Delta s \approx \frac{h_g}{s} \cdot \Delta h$

Ground range

$\Delta y = y - \sqrt{y^2 - 2\Delta h \cdot h_g + \Delta h^2}$

$\Delta y \approx \frac{h_g}{y} \cdot \Delta h$

Einflüsse der Geländeneigung
Effect of ground slope
Influence de la pente du terrain
Efectos de la pendiente del terreno

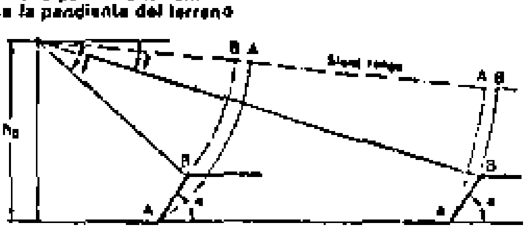

α > 90° − β	Umklappung im Radarbild Radar layover Rabattement dans l'image radar Abatimiento del haz	α < 90° − β	Keine Umklappung No radar layover Pas de rabattement Sin abatimiento

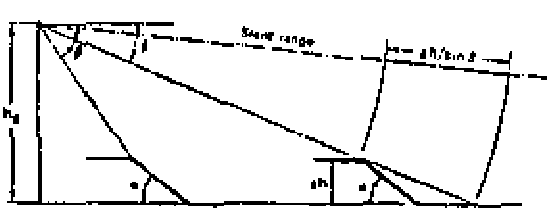

α < β	Kein Schatten No shadow Pas d'ombres radar	α > β	Radarschatten Radar shadow Ombres radar

Reproducción

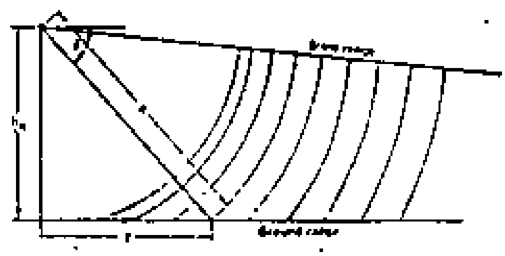

Bei der Abbildung durch Seitwärtsradar (SLAR) werden auf einer Kathodenstrahlröhre Laufzeitdifferenzen registriert, die proportional zur Schrägentfernung s sind (»slant range«). Durch Ablenkung des Kathodenstrahls kann für eine Bezugshöhe h_g die Abbildung proportional zur Horizontalentfernung y gemacht werden (»ground range«). Zwischen diesen Abbildungsarten bestehen folgende Beziehungen:

Side-looking radar (SLAR) records differences in traveling time proportional to the slant range s on a cathode ray tube. By deflecting the cathode ray, the resulting image can be made proportional to the ground range y for a certain datum h_g. These types of image formation are governed by the following relationships:

Les images du radar incliné (SLAR) apparaissent sur l'écran d'un tube à rayons cathodiques, comme différences du temps de propagation des impulsions émises et réfléchies. Ces différences sont proportionnelles à la distance oblique s (»slant range«). Par déflexion du pinceau d'électrons en fonction du temps, elles peuvent être rendues proportionnelles à la distance au sol y (»ground range«) pour une altitude de référence h_g. Il existe entre ces modes de représentation les relations suivantes:

En la reproducción por radar lateral (SLAR) se registran en un tubo de rayos catódicos diferencias de tiempos de recorrido proporcionales a la distancia oblicua s (»slant range«). Desviando el rayo catódico es posible hacer la imagen proporcional a la distancia horizontal "y" (»ground range«) para una altura de referencia h_g. Entre estos tipos de reproducción existen las siguientes relaciones:

$$s = \sqrt{y^2 + h_g^2} \qquad y = \sqrt{s^2 - h_g^2} \qquad \frac{y}{s} = \cos\beta$$

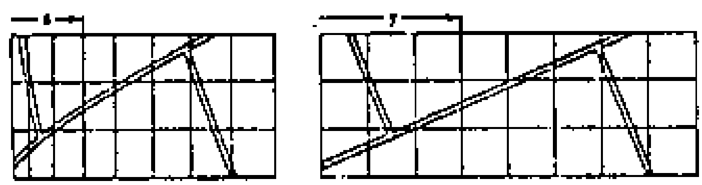

Slant range   Ground range

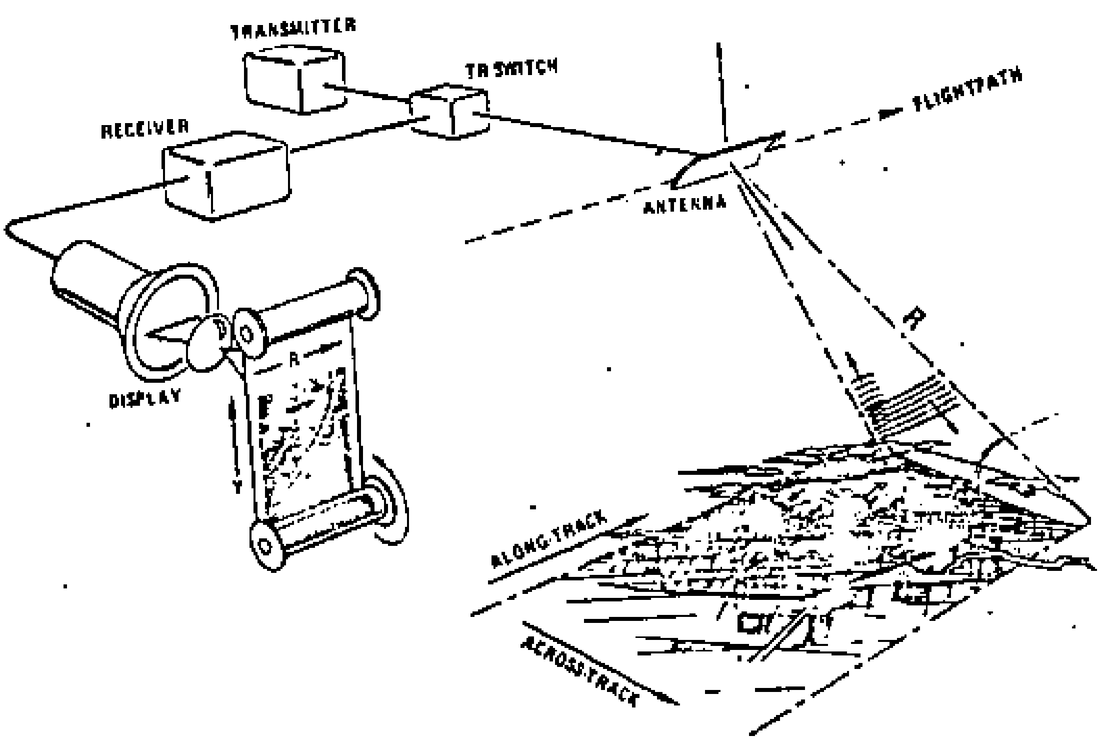

Sistema de Radar

Frequenzbereiche
Frequency bands
Bandes de fréquences
Gamas de frecuencia

Herkömmliche Radarverfahren arbeiten mit Frequenzen zwischen 230 und 40000 MHz. Zur Bezeichnung einzelner Frequenzbereiche wird ein Buchstaben-Code benutzt, der ursprünglich aus militärischen Sicherheitsgründen willkürlich festgelegt worden war.

Conventional radars utilize the frequency range from 230 to 40000 MHz. A letter code of frequency bands was arbitrarily selected to ensure military security in the early developmental stages of radar, and has continued in use.

Les systèmes radar traditionnels travaillent avec des fréquences comprises entre 230 et 40000 MHz. Les différentes bandes de fréquences sont désignées par des lettres-code, choisies arbitrairement lors des premières applications militaires, à des fins de sécurité.

Los métodos convencionales de radar aprovechan frecuencias entre 230 y 40000 MHz. Para designar las distintas gamas de frecuencia se emplea un código de letras arbitrarias, originalmente elegidas para satisfacer las exigencias de seguridad militar.

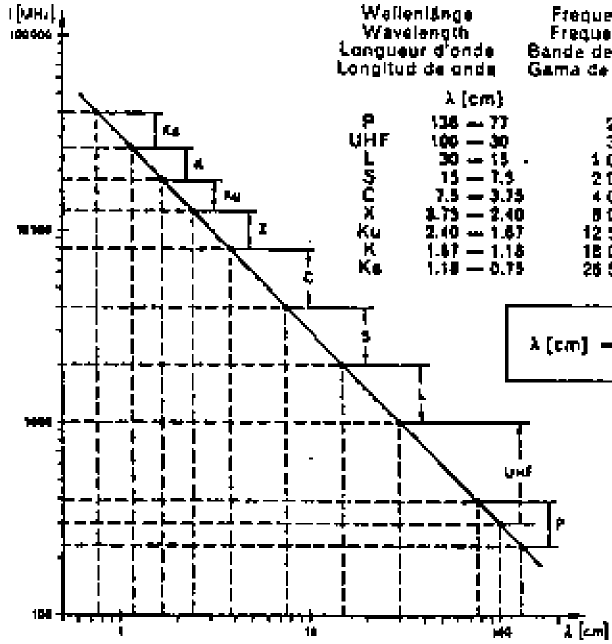

	Wellenlänge / Wavelength / Longueur d'onde / Longitud de onda λ [cm]	Frequenzbereich / Frequency range / Bande de fréquences / Gama de frecuencias f [MHz]
P	130 — 77	230 — 390
UHF	100 — 30	300 — 1 000
L	30 — 15	1 000 — 2 000
S	15 — 7.5	2 000 — 4 000
C	7.5 — 3.75	4 000 — 8 000
X	3.75 — 2.40	8 000 — 12 500
Ku	2.40 — 1.67	12 500 — 18 000
K	1.67 — 1.13	18 000 — 26 500
Ka	1.13 — 0.75	26 500 — 40 000

$$\lambda\,[\mathrm{cm}] = \frac{30\,000}{f\,[\mathrm{MHz}]}$$

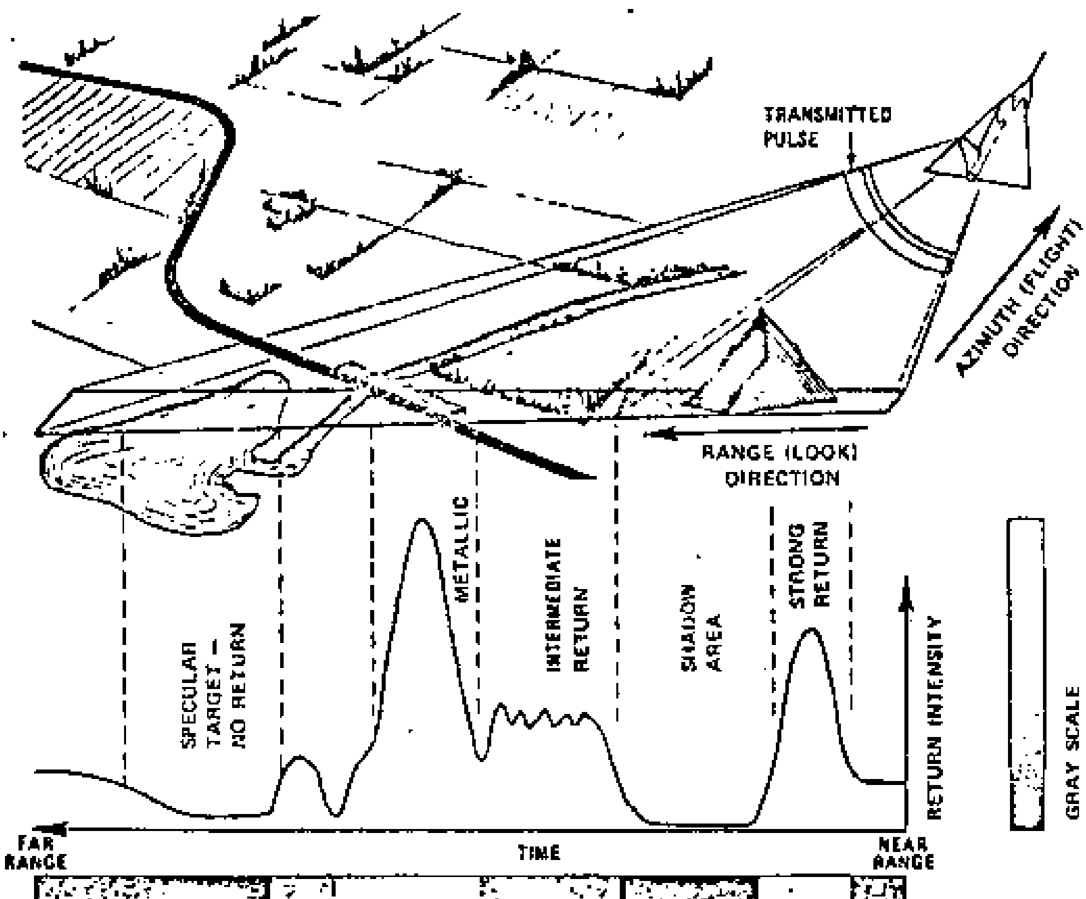

Ejemplos

h_v (m)	s [m] Ω = 77°20'	90°	100°	120°	s [m] α = 0 ω = 2.5 mrad	b_{max} [m] α = Ω/2 ω = 2.5 mrad Ω = 77°20'	90°	100°	120°	b_{min} [m] α = Ω/2 ω = 2.5 mrad Ω = 77°20'	90°	100°	120°
200	320	400	477	693	0.5	0.8	1.0	1.2	2.0	0.6	0.7	0.8	1.0
400	640	800	953	1 386	1.0	1.6	2.0	2.4	4.0	1.3	1.4	1.6	2.0
600	960	1 200	1 430	2 078	1.5	2.5	3.0	3.6	6.0	1.9	2.1	2.3	3.0
800	1 280	1 600	1 907	2 771	2.0	3.3	4.0	4.8	8.0	2.6	2.8	3.1	4.0
→ 1 000	1 600	2 000	2 384	3 464	→ 2.5	4.1	5.0	6.1	10.0	3.2	3.5	3.9	5.0
1 200	1 920	2 400	2 860	4 157	3.0	4.9	6.0	7.3	12.0	3.8	4.2	4.7	6.0
1 400	2 241	2 800	3 337	4 850	3.5	5.7	7.0	8.5	14.0	4.5	4.9	5.4	7.0
1 600	2 561	3 200	3 814	5 543	4.0	6.6	8.0	9.7	16.0	5.1	5.7	6.2	8.0
1 800	2 881	3 600	4 290	6 235	4.5	7.4	9.0	10.9	18.0	5.8	6.4	7.0	9.0
2 000	3 201	4 000	4 767	6 928	5.0	8.2	10.0	12.1	20.0	6.4	7.1	7.8	10.0
2 200	3 521	4 400	5 244	7 621	5.5	9.0	11.0	13.3	22.0	7.0	7.8	8.6	11.0
2 400	3 841	4 800	5 720	8 314	6.0	9.8	12.0	14.5	24.0	7.7	8.5	9.3	12.0
2 600	4 161	5 200	6 197	9 007	6.5	10.7	13.0	15.7	26.0	8.3	9.2	10.1	13.0
2 800	4 481	5 600	6 674	9 699	7.0	11.5	14.0	16.9	28.0	9.0	9.9	10.9	14.0
3 000	4 801	6 000	7 151	10 392	7.5	12.3	15.0	18.2	30.0	9.6	10.6	11.7	15.0
3 500	5 601	7 000	8 343	12 124	8.8	14.4	17.5	21.2	35.0	11.2	12.4	13.6	17.5
4 000	6 402	8 000	9 534	13 856	10.0	16.4	20.0	24.2	40.0	12.8	14.1	15.6	20.0
4 500	7 202	9 000	10 726	15 588	11.3	18.5	22.5	27.2	45.0	14.4	15.9	17.5	22.5
5 000	8 002	10 000	11 918	17 321	12.5	20.5	25.0	30.3	50.0	16.0	17.7	19.4	25.0
5 500	8 802	11 000	13 109	19 053	13.8	22.6	27.5	33.3	55.0	17.6	19.4	21.4	27.5
6 000	9 602	12 000	14 301	20 785	15.0	24.6	30.0	36.3	60.0	19.2	21.2	23.3	30.0
6 500	10 403	13 000	15 493	22 517	16.3	26.7	32.5	39.3	65.0	20.8	23.0	25.3	32.5
7 000	11 203	14 000	16 685	24 249	17.5	28.7	35.0	42.4	70.0	22.4	24.7	27.2	35.0
7 500	12 003	15 000	17 876	25 981	18.8	30.8	37.5	45.4	75.0	24.0	26.5	29.2	37.5
8 000	12 803	16 000	19 068	27 713	20.0	32.8	40.0	48.4	80.0	25.6	28.3	31.1	40.0
8 500	13 603	17 000	20 260	29 445	21.3	34.9	42.5	51.4	85.0	27.2	30.1	33.1	42.5
9 000	14 404	18 000	21 452	31 177	22.5	36.9	45.0	54.5	90.0	28.8	31.8	35.0	45.0
9 500	15 204	19 000	22 643	32 909	23.8	39.0	47.5	57.5	95.0	30.4	33.6	36.9	47.5
10 000	16 004	20 000	23 836	34 641	25.0	41.0	50.0	60.5	100.0	32.0	35.4	38.8	50.0

Relative spektrale Empfindlichkeit von Detektoren
Relative spectral response of detectors
Sensibilité spectrale relative des détecteurs
Sensibilidad espectral relativa de detectores

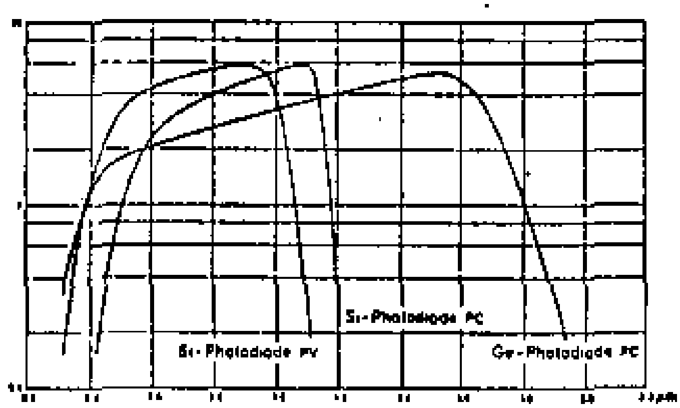

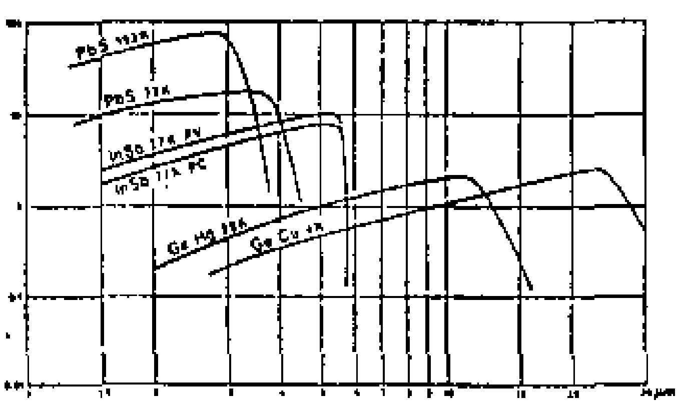

PV Photovoltaisch / Photovoltaic / Photovoltaïque / Fotovoltáico

PC Photokonduktiv / Photoconductive / Photoconductrice / Fotoconductivo

4K Gekühlt auf 4 Kelvin / Cooled to 4 Kelvin / Refroidie sur 4 Kelvin / Refrigerado a 4 Kelvin

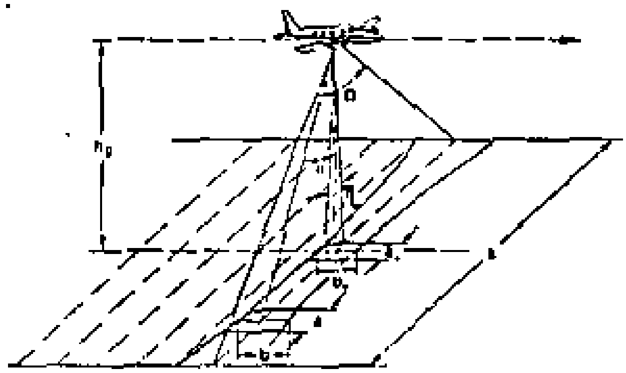

Flughöhe über Grund Flying height above ground Hauteur de vol au-dessus du sol Altura de vuelo sobre el terreno	h_g	Abtastfrequenz Scan rate Fréquence de balayage Frecuencia de exploración	f
Öffnungswinkel der Abtastoptik Instantaneous field of view Angle de champ de l'optique Angulo de abertura de la óptica	η	Gesamtöffnungswinkel Field of view Angle de champ global Angulo total de abertura	Ω
Länge einer Abtastlinie Length of a scan line Longueur d'une ligne Longitud de una línea	$s = 2\,h_g \cdot \tan\frac{\Omega}{2}$	Fluggeschwindigkeit Flying speed Vitesse de vol Velocidad de vuelo	v
Ausdehnung der Abtastfläche quer zur Flugrichtung Extension of scan area at right angles to line of flight Extension de la surf. explorée au droit de la dir. du vol Extensión de la superf. de expl. transv. a la dir. de vuelo			$a = \frac{\omega \cdot h_g}{\cos^2 \alpha}$
Ausdehnung der Abtastfläche in Flugrichtung Extension of scan area in line of flight Extension de la surface explorée en direction du vol Extensión de la superf. de expl. en la dirección de vuelo			$b = \frac{\omega \cdot h_g}{\cos \alpha}$
Verhältnis Geschwindigkeit zu Höhe, bei dem gerade noch lückenlos abgetastet wird Maximum speed-to-height ratio for scanning without gaps Rapport vitesse/altitude pour lequel il ne se produit encore aucun manque de balayage Relación entre velocidad y altura, en la cual la exploración aún no presenta lagunas			$\frac{v}{h_g} = \omega \cdot f$

Parámetros importantes

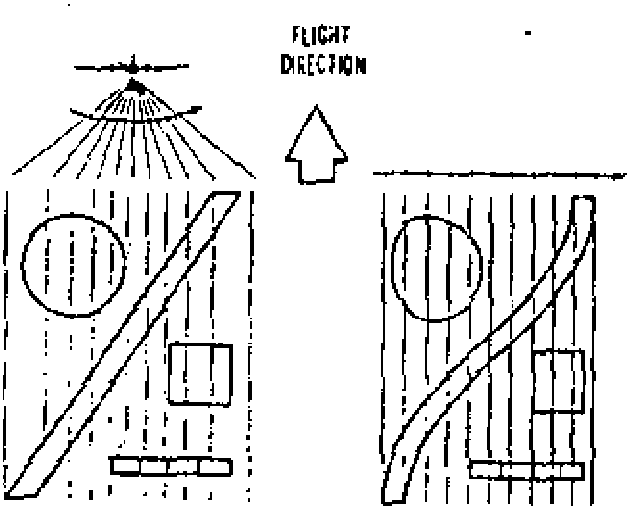

A TERRAIN FEATURES WHICH ARE SCANNED AT CONSTANT ANGULAR RATE.

B. RESULTING IMAGE DISTORTION CAUSED BY RECORDING AT CONSTANT LINEAR RATE.

Perturbaciones geométricas

Sistema Scanner

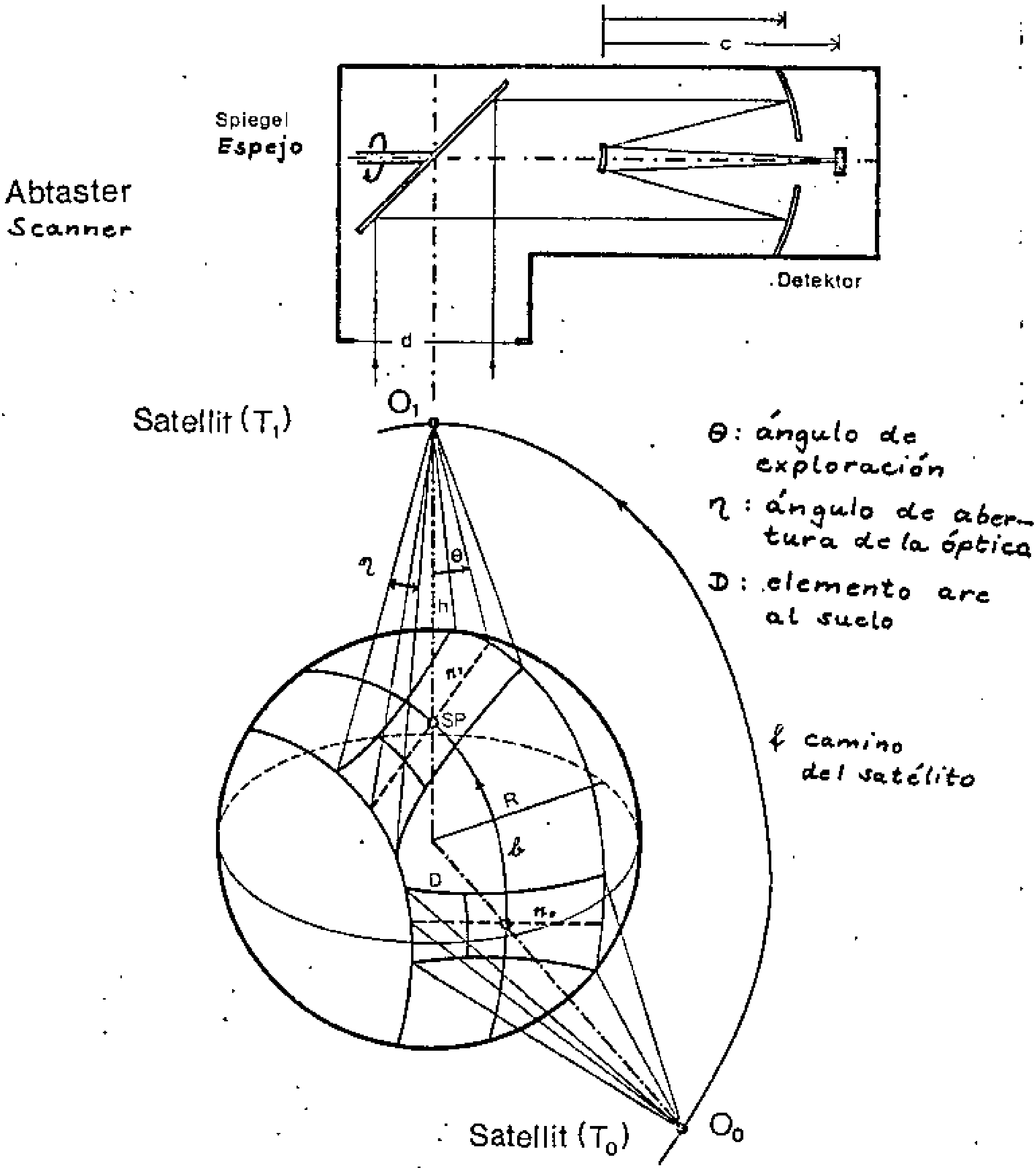

c = 15 cm, 30 cm, 60 cm
Format 23 cm x 23 cm

Bildfolge	Ü	b/h			m_z
		15 cm	30 cm	60 cm	15 cm, 30 cm, 60 cm
1.+2.Bild	80 %	0.3	0.15	0.075	± 54 m
1.+3.Bild	60 %	0.6	0.3	0.15	± 27 m
1.+4.Bild	40 %	0.9	0.45	0.2	± 18 m
1.+5.Bild	20 %	1.2	0.6	0.3	± 14 m

Bildfolge	stereoskop.auswertbare Fläche (km^2)		
	15 cm	30 cm	60 cm
1.+2.Bild	383x306	192x153	96x77
1.+3.Bild	383x229	192x115	96x58
1.+4.Bild	383x153	192x 76	96x38
1.+5.Bild	383x 77	192x 38	96x19

$$\frac{\text{Fläche } F_{15cm}}{\text{Fläche } F_{60cm}} = \frac{16}{1}$$

$$\frac{\text{Fläche } F_{30cm}}{\text{Fläche } F_{60cm}} = \frac{4}{1}$$

b) Large Format Camera LFC

c = 30 cm; 22,5 cm x 45 cm

Bildfolge	Ü	b/h	m_z	Fläche (km^2)
1.+2.Bild	80 %	0.3	± 27 m	188x300
1.+3.Bild	60 %	0.6	± 14 m	188x225
1.+4.Bild	40 %	0.9	± 9 m	188x150
1.+5.Bild	20 %	1.2	± 7 m	188x 75

c) Zeiss TRb 60/24

c = 61 cm; 23 cm x 11,5 cm

Bildfolge	Ü	b/h	m_z	Fläche (km^2)
1.+2.Bild	80 %	0.04	± 108 m	96x38
1.+3.Bild	60 %	0.075	± 54 m	96x29
1.+4.Bild	40 %	0.1	± 36 m	96x19

Manipulación del base

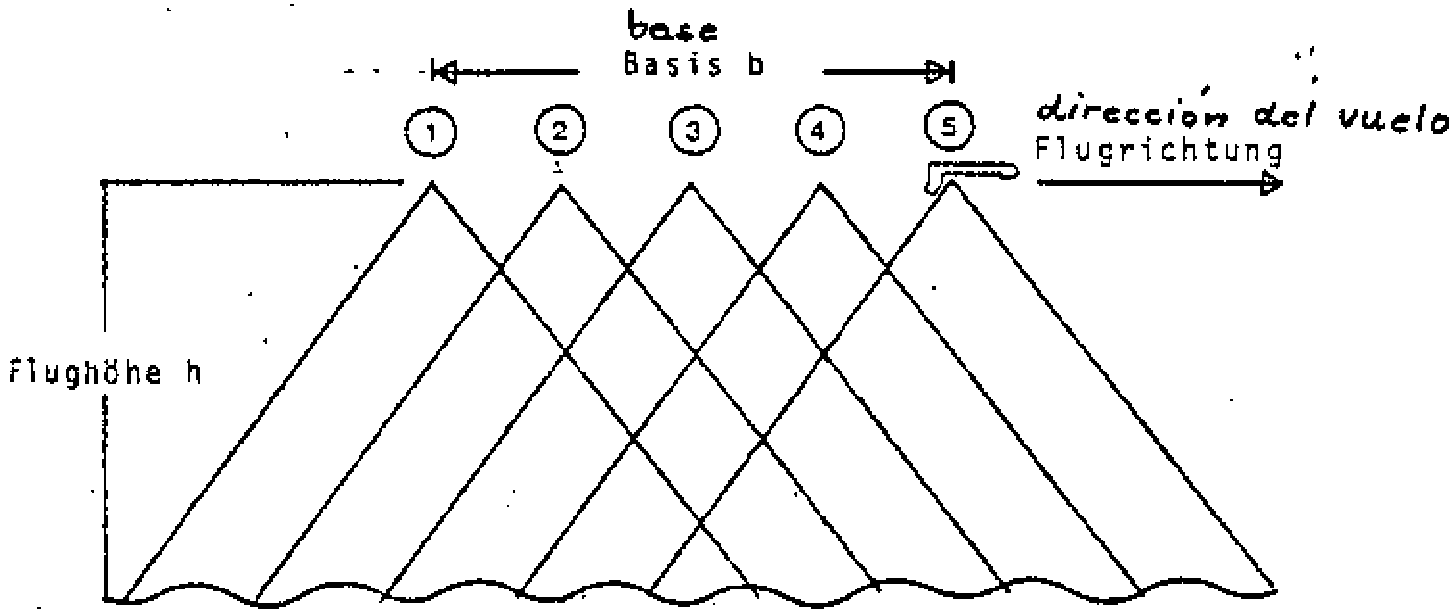

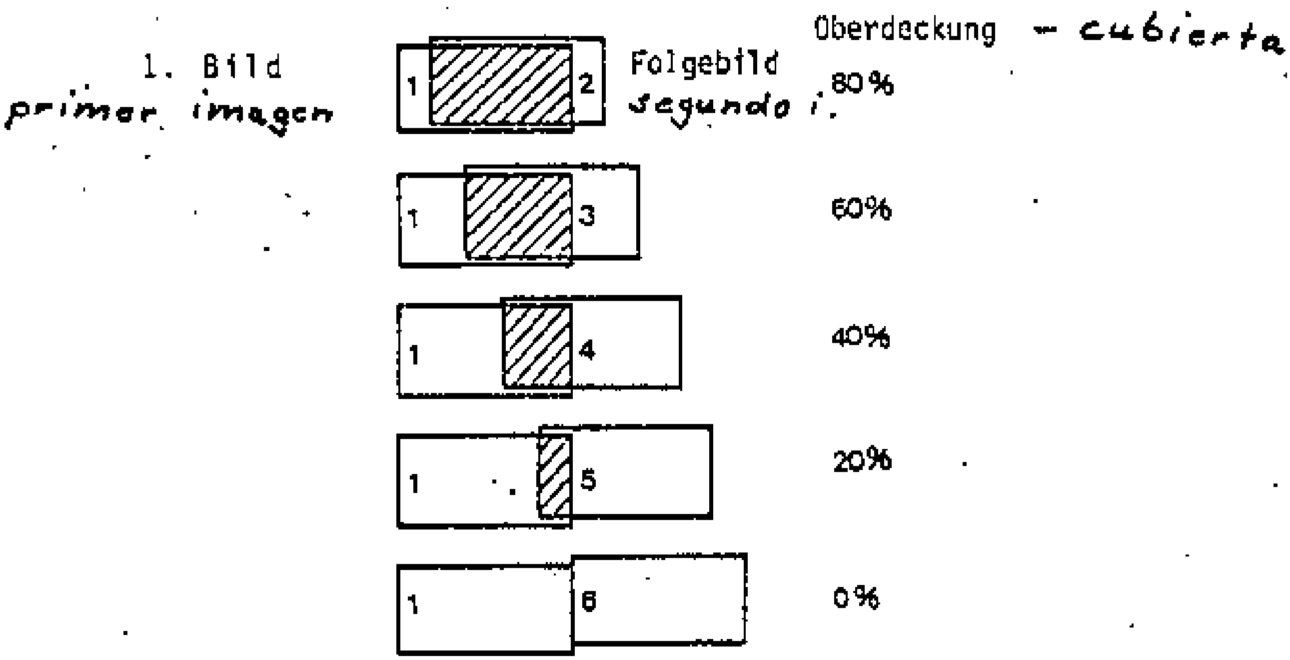

Cameras fotogramétricas (aplicación del espacio)

- Lagegenauigkeit (h = 250 km) *exactitud en el plano*

$$m_p = \frac{h}{c} \cdot m_{x'y'}$$

m : error standard

a) Reihenmeßkammer RMK
Format 23 cm x 23 cm

c	15 cm	30 cm	60 cm
m_p	± 16 m	± 8 m	± 4 m
área Fläche/Bild	383 km x 383 km	192 km x 192 km	96 km x 96 km

b) Large Format Camera LFC
c = 30 cm; Format 22,5 cm x 45 cm

m_p = ± 8 m	*área* Fläche/Bild = 188 km x 376 km

c) Zeiss TRb 60/24
c = 61 cm; Format 23 x 11,5 cm

m_p = ± 4 m	*área* Fläche/Bild = 96 km x 48 km

- Höhengenauigkeit (h = 250 km) *exactitud de altura*

$$m_z = \frac{h}{c} \cdot \frac{h}{b} \cdot m_{p_x}$$

b : base

40A

FLIGHT PLANNING

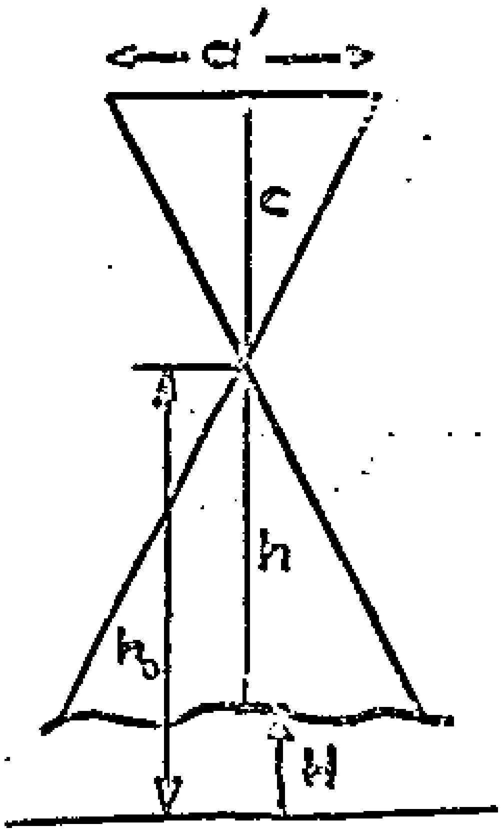

H = elev. above sea level

h = flying height above ground

c = camera constant

h_0 = flying height above sea level

a' = image format

a = ground coverage

$$a = \frac{h}{c} a'$$

$$a = m_B \cdot a'$$

$$m_B = \frac{h}{c}$$ image scale factor m_B

$$\frac{1}{M_B} = m_B$$ image scale M_B

Filtros

(91)

Agfa-Gevaert
1 CTO 1
2 [illegible]453
3 [illegible]77
4 [illegible]10
5 [illegible]599
6 L 731

Ilford
1 No. 104 Alpha
2 No. 109 Delta
3 No. 110 Minus Blue
4 No. 202 Micro 5
5 No. 204 Tricolour Red

Kodak Wratten
1 HF-3 (2B)
2 No. 3 (Aero 1)
3 No. 8 (K2)
4 No. 12 (Minus Blue)
5 No. 15 (G)
6 No. 25 (A)
7 No. 89 B (IR)

Wild
1 Sandwich Color
2 Hazefilter
3 Dark yellow
4 Light red
5 Infrared

Zeiss
1 B
2 D
3 E
4 F
5 I
6 K

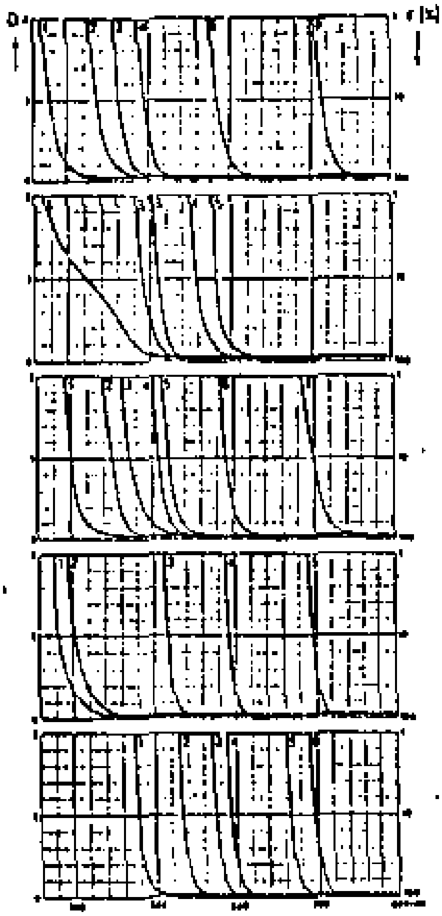

...missionsgrad / Transmittance / Transmittance / Transmitancia τ	Dichte / Density / Densité / Densidad D

	Bezeichnung / Designation / Désignation / Designación	Typ	Agfa-G. Pan 30 PE / Pan 33 PE	Agfa-G. Pan 36 PE	Ilford FP 3	Ilford HP 3	Kodak 2402	Kodak 2403	Kodak 2405	Kodak 3400, 3401	Kodak 3414	Kodak 2424
Agfa-G.	CTO 1	UV	.	.	.	.	.	.	.	.	.	.
	L 453	Y1	1.4	1.4	.	.	.	.	.	.	.	.
	L 477	Y2	1.8	1.5	.	.	.	.	.	.	.	.
	L 510	Y3	1.8	1.7	.	.	.	.	.	.	.	.
	L 599	R	3.8	2.5	.	.	.	.	.	.	.	.
	L 731	IR	.	.	.	.	.	.	.	.	.	.
Ilford	No. 104	Y1	.	.	1.5	1.5	.	.	.	.	.	.
	No. 109	Y2	.	.	2	2	.	.	.	.	.	.
	No. 110	Y3	1.8	1.7	2	2	2	1.5	2	2	2	1.5
	No. 202	O	.	.	4	3	.	.	.	.	.	.
	No. 204	R	.	.	6	4	.	.	.	.	.	.
Kodak	HF-3	UV	.	.	.	.	.	.	.	.	.	.
	No. 3	Y1	1.4	1.4	.	.	1.5	.	1.5	.	.	.
	No. 8	Y2	1.8	1.5	.	.	2	.	2	.	.	.
	No. 12	Y3	1.8	1.7	.	.	2	1.5	2.5	2	2	1.5
	No. 15	Y3	.	.	.	.	2	.	2.5	.	.	.
	No. 25	R	3.8	2.8	.	.	4	3	4	4	2.5	2
	No. 89 B	IR	.	.	.	.	.	.	.	.	.	3
Wild	Sandw. Color	UV	.	.	.	.	.	.	.	.	.	.
	Hazefilter	UV	.	.	.	.	.	.	.	.	.	.
	Dark yellow	Y3	.	.	.	.	.	.	.	.	.	.
	Light red	O	.	.	.	.	.	.	.	.	.	.
	Infrared	IR	.	.	.	.	.	.	.	.	.	.
Zeiss	B	Y2	.	.	.	.	.	.	.	.	.	.
	D	Y3	.	.	.	.	.	.	.	.	.	.
	E	O	.	.	.	.	.	.	.	.	.	.
	F	O	.	.	.	.	.	.	.	.	.	.
	I	IR	.	.	.	.	.	.	.	.	.	.
	K	IR	.	.	.	.	.	.	.	.	.	.

Gelbfilter für leichten Dunst / Yellow filter for light haze / Filtre jaune pour brume légère / Filtro amarillo para bruma ligera	Y1	Rotfilter für starken Dunst / Red filter for heavy haze / Filtre rouge pour brume épaisse / Filtro rojo para bruma densa	R
Gelbfilter für mittleren Dunst / Yellow filter for medium haze / Filtre jaune pour brume moyenne / Filtro amarillo para bruma media	Y2	Grünfilter / Green filter / Filtre vert / Filtro verde	G
Gelbfilter für starken Dunst / Yellow filter for heavy haze / Filtre jaune pour brume épaisse / Filtro amarillo para bruma densa	Y3	Filter für Infrarotaufnahme / Infrared filter / Filtre infrarouge / Filtro infrarrojo	IR
Orangefilter für starken Dunst / Orange filter for heavy haze / Filtre orange pour brume épaisse / Filtro naranjo para bruma densa	O	UV-Absorptionsfilter / UV filter / Filtre UV / Filtro UV	UV

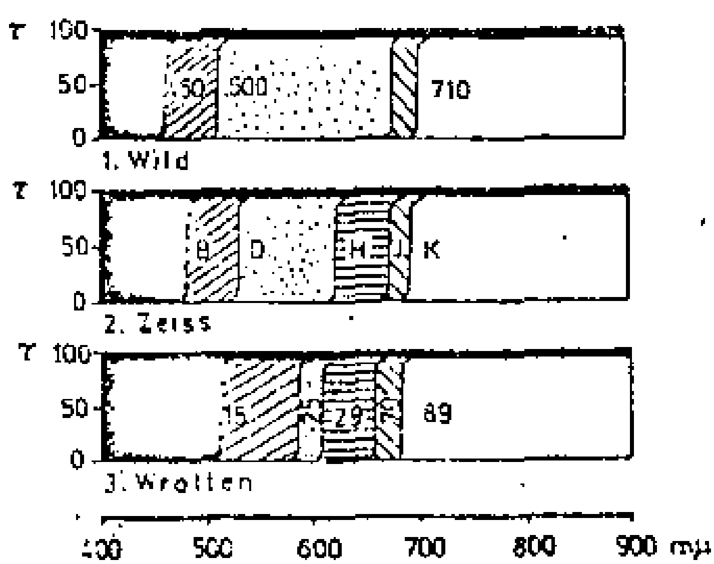

Películas aéreas

Hersteller Manufact. Producteur Fabricante	Bezeichnung Designation Désignation Designación	Typ Type Type Tipo	Rel. spektrale Empfindlichkeit Relative spectral sensitivity Sensibilité spectrale relative Sensibilidad espectral relativa	Schichtträger Base Support Portaemulsión	[mm]	Empfindlk. Speed Sensibil. DIN	ASA	AFS	Entwickler Developer Révélateur Revelador	Auflösung Resolution [L/mm] TOC 1000:1	TOC 1.6:1	RMS	Gamma	Anwendung Applicat.
Agfa-Gevaert	Aviphot Pan 30 PE	Pan		Polyester	0.10	20	80		G 2, G 5, Metinol U Refinal	133			1.55[3]) 1.50[3])	T
Agfa-Gevaert	Aviphot Pan 33 PE	Pan		Polyester	0.10	24	200		G 2, G 5, Metinol U Refinal	95			1.48[3]) 1.29[3])	T
Agfa-Gevaert	Aviphot Pan 36 PE	Pan		Polyester	0.10	27	400		G 5, Metinol U	83			1.20[3])	T
Agfa-Gevaert	Aviphot Color Neg.	Color Neg.		Triacetat	0.13	17	40		C 17-Process	85			0.6	
GAF	Anscopan Aerial Film	Pan	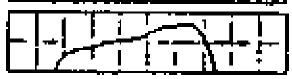	Triacetat (speziell)	0.13	20	80		D-19, D-76	110				H
GAF	Anscochrome D/200 Aerial Color Film	Color Pos.		Gafstar	0.15	24	200		Anscochrome AR-1	125	40		2.2	
Ilford	FP3 Aerial Film	Pan		Acetat Polyester	0.13 0.10	24	200		Microphen Phenisol	100[5])	75[5])	20 29	1.04[4]) 1.87[4])	T
Ilford	HP3 Aerial Film	Pan		Acetat Polyester	0.13 0.10	27	400		Microphen Phenisol	78[5])	52[5])	29 44	0.94[4]) 1.56[4])	T
Kodak	Plus-X-Aerographic 2402	Pan		Estar	0.10			250	D-19 Versamat A Versamat 641	100	50	18	2.4[4]) 2.3[4]) 1.0[4])	T
Kodak	Tri-X-Aerographic 2403	Pan		Estar	0.10			640	D-19 Versamat A Versamat 641	80	25	33	2.0[4]) 1.7[4]) 0.95[4])	T
Kodak	Double-X-Aerographic 2405	Pan		Estar	0.10			320	DK-50 Versamat A Versamat 641	100	50	28	— 1.65[4]) 1.0[4])	T
Kodak	Panatomic-X Aerial 3400	Pan	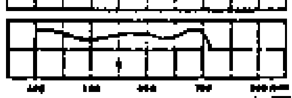	Estar	0.06			64	D-19 Versamat A Versamat 641	200	80	16	— 2.85[4]) 2.7[4])	H, A
Kodak	Plus-X Aerial 3401	Pan	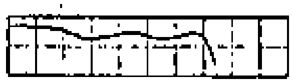	Estar	0.06			200	D-19 Versamat A Versamat 641	125	40	30	— 2.85[4]) 2.5[4])	A
Kodak	High Definition Aerial 3414/1414	Pan	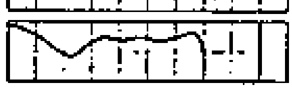	Estar	0.06 0.04			8	D-19 Versamat 641	630	250	9	— 2.8[4])	H, A
Kodak	Infrared Aerographic 2424	IR		Estar	0.10			200	D-19 Versamat A Versamat 641	80	40	33	1.5[4]) 1.6[4]) 1.35[4])	F
Kodak	Aerocolor Negative 2445	Color Neg.		Estar	0.10			100	Aero-Negativ Color Process	80	40	13		T
Kodak	Ektachrome-MS Aerographic 2448[1])	Color Pos.		Estar	0.10			32	EA-5	80	40	12		A
Kodak	Aerial Color SO-242/SO-255	Color Pos.		Estar	0.06 0.04			6	Versamat ME-4	200	100	11		H, A
Kodak	Ektachrome-EF Aerographic SO-397	Color Pos.		Estar	0.10			64	EA-5	80	40	13		A
Kodak	Aerochrome Infrared 2443/3443	False Color		Estar	0.10 0.06			40[7])	EA-5	63	32	17		F
Kodak	Water Penetration Color Film SO-224	Color Pos.		Estar	0.10			40	EA-5	125	80	24		

Sistemas de sensibilidad

(42)

DIN	ASA Exposure Index	ASA Speed Value	BSI (log)	General Electric	Weston	Scheiner (Europ.)	t
	0.6		9	0.8	0.5	10	64.00
	0.8		10	1.0	0.6	11	50.80
1	1.0		11	1.2	0.8	12	40.32
2	1.2		12	1.6	1.0	13	32.00
3	1.6		13	2.0	1.2	14	25.40
4	2.0		14	2.5	1.6	15	20.16
5	2.5		15	3	2.0	16	16.00
6	3		16	4	2.5	17	12.70
7	4		17	5	3	18	10.08
8	5		18	6	4	19	8.00
9	6	1.0	19	8	5	20	6.35
10	8	1.3	20	10	6	21	5.04
11	10	1.7	21	12	8	22	4.00
12	12	2.0	22	16	10	23	3.17
13	16	2.3	23	20	12	24	2.52
14	20	2.7	24	25	16	25	2.00
15	25	3.0	25	32	20	26	1.59
16	32	3.3	26	40	25	27	1.26
17	40	3.7	27	50	32	28	1.000
18	50	4.0	28	64	40	29	0.794
19	64	4.3	29	80	50	30	0.630
20	80	4.7	30	100	64	31	0.500
21	100	5.0	31	125	80	32	0.397
22	125	5.3	32	160	100	33	0.315
23	100	5.7	33	200	125	34	0.250
24	200	6.0	34	250	160	35	0.198
25	250	6.3	35	320	200	36	0.157
26	320	6.7	36	400	250	37	0.125
27	400	7.0	37	500	320	38	0.099
28	500	7.3	38	640	400	39	0.079
29	640	7.7	39	800	500	40	0.062
30	800	8.0	40	1000	640	41	0.050
31	1000	8.3	41	1250	800	42	0.039
32	1250	8.7	42	1600	1000	43	0.031
33	1600	9.0	43	2000	1250	44	0.025
34	2000	9.3	44	2500	1600	45	0.020
35	2500	9.7	45	3200	2000	46	0.016
36	3200	10.0	46	4000	2500	47	0.012
37	4000	10.3	47	5000	3200	48	0.010
38	5000	10.7	48	6400	4000	49	0.008
39	6400	11.0	49	8000	5000	50	0.006
40	8000	11.3	50	10000	6400	51	0.005

t — Relative Belichtungszeit
Relative exposure time
Temps d'exposition relatif
Tiempo de exposición relativo

AFS Aerial Film Speed (ANSI Standard PH2.34-1969)
Amerikanische Norm zur Bestimmung der Empfindlichkeit für Luftbildfilme.
American standard for determining the speed of aerial films.
Norme américaine définissant la sensibilité des films aériens.
Norma americana para determinar la sensibilidad de películas aéreas.

TOC Test Object Contrast
Helligkeitsumfang des Objekts — Gamme de luminosité du sujet
Brightness range of object — Alcance de contrastes del objeto

RMS Root-mean-square Granularity
Dieser Wert stellt ein objektives Maß für den subjektiven Eindruck der Körnigkeit dar. Er wird aus mikrophotometrischen Messungen ermittelt.
This value is an objective measure of the subjective impression given by granularity. It is determined by microphotometry.
Cette valeur constitue une mesure objective pour l'impression subjective de la granularité. Elle est déterminée par une méthode microphotométrique.
Este valor es una medida objetiva de la impresión subjetiva de la granularidad. Se determina mediante mediciones microfotométricas.

[1] Kann in modifiziertem C-22 Prozeß negativ entwickelt werden.
Negative development possible by modified C-22 process.
Peut être développé comme négatif par le procédé modifié C-22.
Puede revelarse como negativo mediante el proceso modificado C-22.

[2] Test Object Contrast 100 : 1/3 : 1

[3] Entwicklungszeit 5 min bei 20°C — Temps de dével. 5 min. à 20°C
Development time 5 min. at 20°C — Tiempo de revelado 5 min a 20°C

[4] Entwicklungszeit 10 min bei 20°C — Temps de dével. 10 min. à 20°C
Development time 10 min. at 20°C — Tiempo de revelado 10 min a 20°C

[5] Entwicklungszeit 12 min bei 20°C — Temps de dével. 12 min. à 20°C
Development time 12 min. at 20°C — Tiempo de revelado 12 min a 20°C

[6] Geschwindigk. 10 ft/min bei 90°F — Vitesse 10 ft/min à 90°F
Speed 10 ft/min at 90°F — Velocidad 10 ft/min a 90°F

[7] Mit Kodak Wratten Filter Nr. 12 — Avec filtre Wratten Kodak No. 12
With a Kodak Wratten Filter No. 12 — Con filtro Kodak Wratten núm. 12

T Für topographische Auswertungen — Pour restitutions topograph.
For topograph. plotting purposes — Para restitución topográfica

H Für große Flughöhen — Pour grandes altitudes de vol
For high altitudes — Para grandes alturas de vuelo

A Für Luftbildaufklärung — Pour reconnaissance aérienne
Aerial reconnaissance film — Para reconocimiento aéreo

Dichte
Density
Densité
Densidad
$D = \log \frac{1}{\tau}$

Opazität
Opacity
Opacité
Opacidad
$O = \frac{1}{\tau}$

Transparenz
Transparency
Transparence
Transparencia
$\tau = \frac{\Phi}{\Phi_0}$

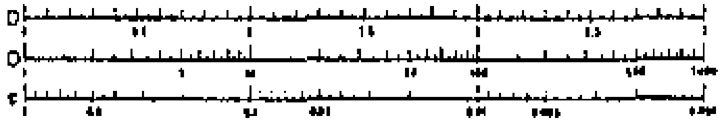

Die Schwärzungskurve gibt die Abhängigkeit der Schwärzung (Dichte) D einer Emulsion von der Belichtung E · t an.

The characteristic curve defines the relationship between the density D of an emulsion and exposure E · t.

La courbe caractéristique exprime la relation entre la densité D d'une émulsion et l'exposition E · t.

La curva característica indica la relación entre la densidad D de una emulsión y la exposición E · t.

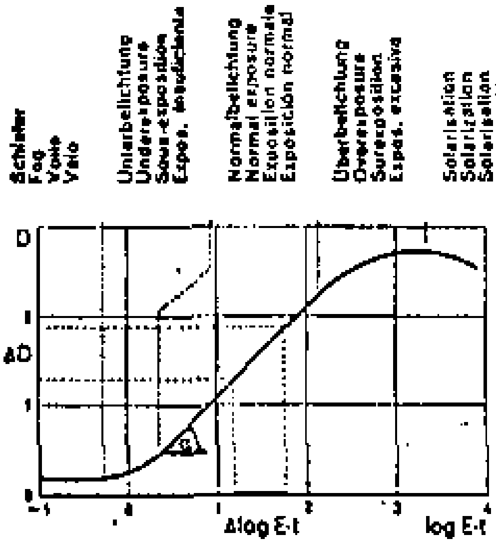

Gradation
Gradación
GAMMA

$$\gamma = \tan \alpha = \frac{\Delta D}{\Delta \log E \cdot t}$$

$\gamma =$ Negativdichteumfang / Density range of negative / Plage de densité du négatif / Margen de densidad del negat. — Originaldichteumfang / Density range of original / Plage de densité du sujet / Margen de densidad del original

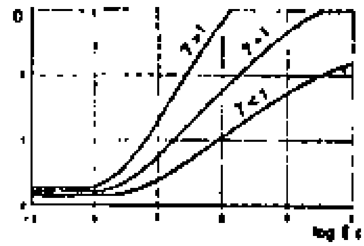

γ > 1 hart / hard / dur / duro

γ = 1 normal

γ < 1 weich / soft / doux / suave

Die Gradation hängt ab
Gradation depends on
La gradation dépend
La gradación depende

1. vom Entwickler
the developer
du révélateur
del revelador

2. von der Entwicklungszeit t
the development time t
du temps de développement t
del tiempo de revelado t

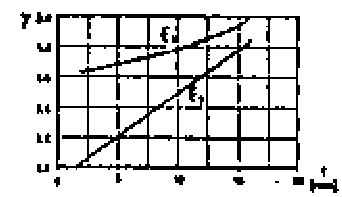

3. von der Entwicklertemperatur
the development temperature
de la température du révélateur
de la temperatura del revelador

4. vom photographischen Material
the photographic material
du matériel photographique
del material fotográfico

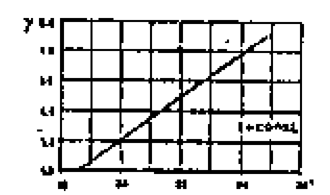

Objektbeleuchtung
Object illumination
Eclairage de l'objet
Iluminación del objeto

Objektreflexion
Object reflection
Réflexion de l'objet
Reflexión del objeto

Filterdurchlässigkeit
Filter transmission
Transparence du filtre
Transmisión del filtro

Filmempfindlichkeit
Film speed
Sensibilité de la pellicule
Sensibilidad de la película

Schwärzung
Density
Densité de l'émulsion
Densidad

$D(\lambda) = E(\lambda) \cdot \rho(\lambda) \cdot \tau(\lambda) \cdot S(\lambda)$

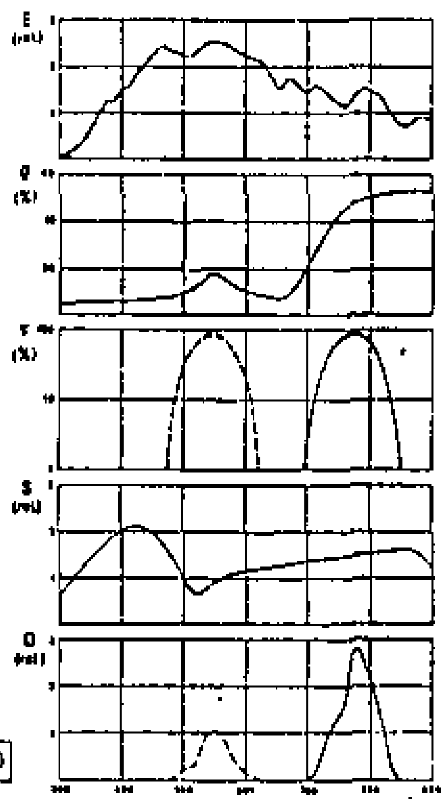

Die Schwärzung der photographischen Schicht ist proportional zu der Fläche unter der Kurve.

The density of a photographic emulsion is proportional to the area below the curve.

La densité de l'émulsion photographique est proportionnelle à la surface située au-dessous de la courbe.

La densidad de una emulsión fotográfica es proporcional a la área situada debajo de la curva.

Ein dunkles Objekt (z. B. dunkler Wald) remittiert ca. 1 % der auftreffenden Strahlung, ein helles Objekt (z. B. Sand) 30 %. Der abgehende Objektumfang ($L_{min} : L_{max}$) beträgt also 1 : 30. In Flughöhen um 3000 m werden ca. 3 % der Sonnenstrahlung am Aerosol reflektiert und als Luftlicht dem abgehenden Objektumfang überlagert. Dieser verringert sich dadurch auf 4 : 33 ≈ 1 : 8. Damit im Bild ein Helligkeitsumfang 1 : 30 entsteht, muß Photomaterial mit der Gradation γ = 1,6 verwendet werden.

A dark object (such as a dark forest) reflects about 1 % of the radiation incident on it, and a bright object (e. g. sand) 30 %. The object range transmitted ($L_{min} : L_{max}$) is thus 1 : 30. At flight heights around 3000 m, approx. 3 % of the solar radiation is reflected by aerosol and superimposed on the object range transmitted in the form of atmospheric haze. As a result, the object range is reduced to 4 : 33 ≈ 1 : 8. To obtain a brightness range of 1 : 30 in the photography, photographic material with a gradation of γ = 1,6 must be used.

Un objet sombre (p. ex. forêt) réfléchit environ 1 % du flux lumineux incident, un objet clair (p. ex. sable) 30 %. La plage des contrastes transmises par l'objet ($L_{min} : L_{max}$) est donc 1 : 30. A des altitudes de vol de 3000 m, approximativement 3 % de la radiation solaire est réfléchie par aérosol et superposée comme voile atmosphérique à la plage des contrastes transmise par l'objet. Il en résulte une réduction de cette plage de 4 : 33 ≈ 1 : 8. Pour obtenir une plage de contrastes de 1 : 30 dans la photographie, il faut adopter un matériel photogr. γ = 1,6.

Un objeto oscuro (por ejemplo, un bosque oscuro) refleja aprox. el 1 % de la radiación incidente, un objeto claro (por ejemplo, arena) el 30 %. El margen de contrastes transmitidos por el objeto ($L_{min} : L_{max}$) es, por lo tanto, 1 : 30. A alturas de vuelo de unos 3000 m, un 3 % de la radiación solar es reflejada por el aerosol y superpuesta al margen de contrastes transmitido por el objeto como eluz aérea. Dicho margen se reduce así a 4 : 33 ≈ 1 : 8. Para obtener un margen de contrastes de 1 : 30 en la foto, hay que emplear material fotográfico γ = 1,6.

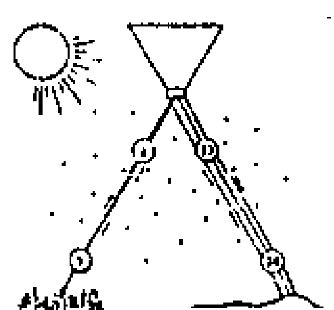

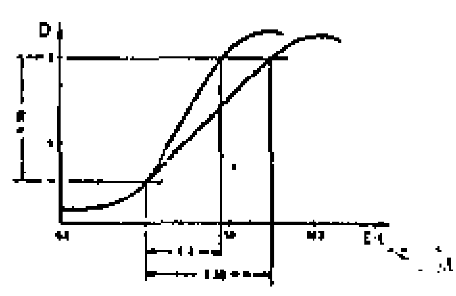

EXPOSURE, DENSITY & CONTRAST

$$\gamma = tg\alpha = \frac{\Delta D}{\Delta \log E}$$

$E_{max} : E_{min}$	K	$\log \frac{E_{max}}{E_{min}}$
1000 : 1	0,999	3,0
100 : 1	0,98	2,0
50 : 1	0,96	1,7
10 : 1	0,82	1,0
8 : 1	0,78	0,9
5 : 1	0,65	0,7
3 : 1	0,50	0,5
2 : 1	0,33	0,3
1,5 : 1	0,20	0,2

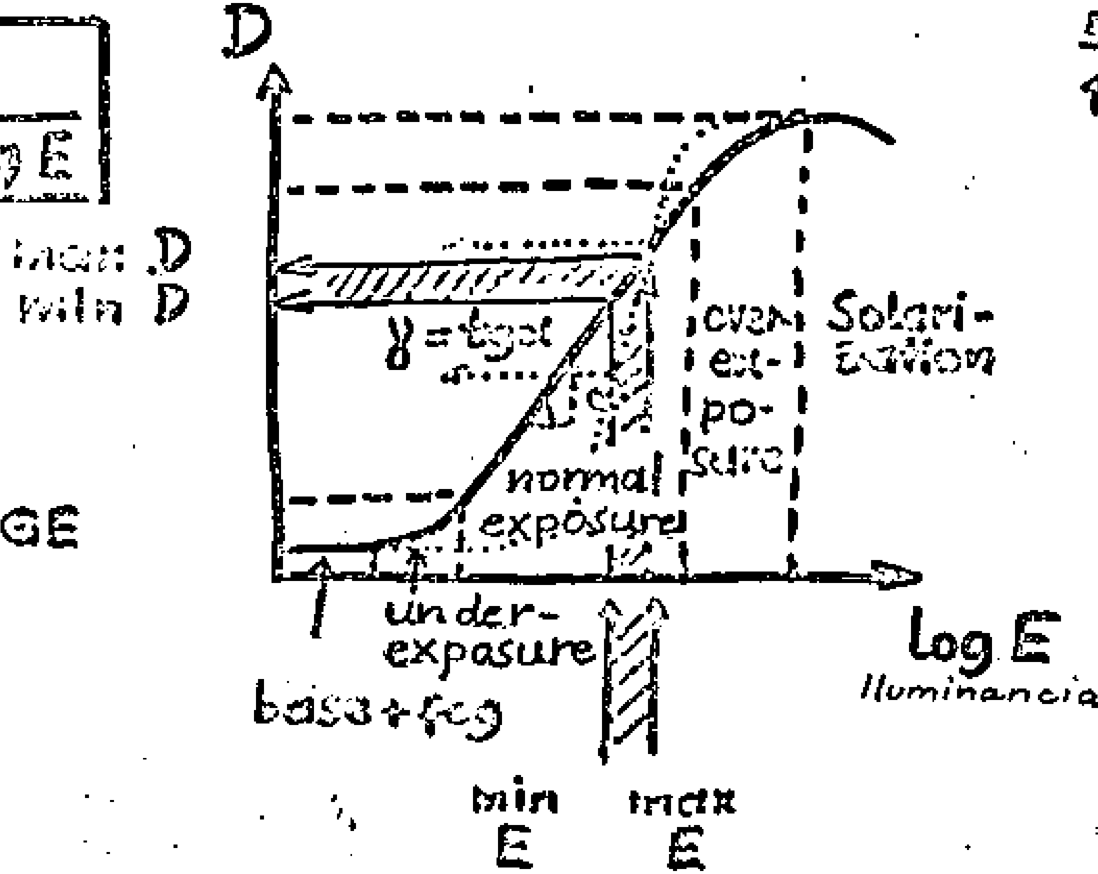

OBJECT RANGE

$$\frac{E_{max}}{E_{min}}$$

DENSITY RANGE

$$\log\left(\frac{E_{max}}{E_{min}}\right)$$

COLOR SENSITIVITY SENSIBILIZATION FILTERS

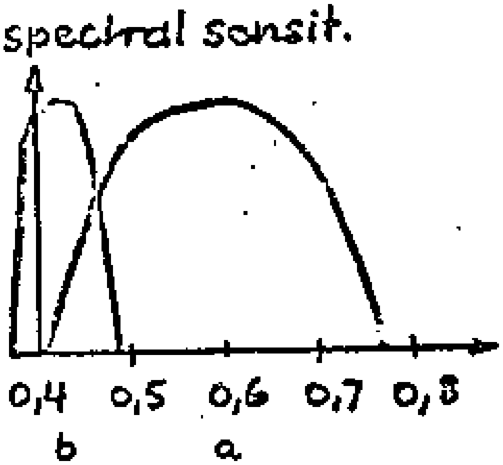

a Sensitivity of the eye
b Sensitivity of unsensitiood AgBr-layer

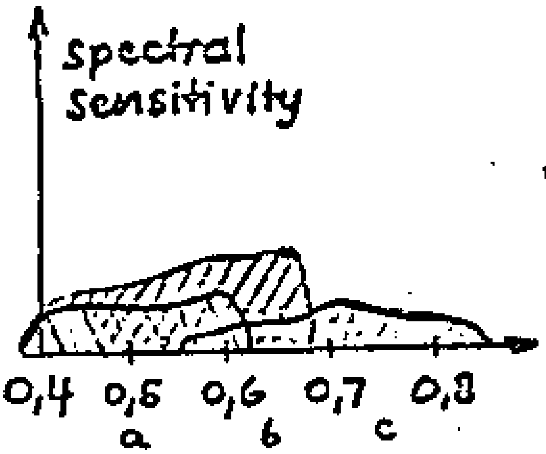

Sensibilization by tar particles

a orthochromatic
b panchromatic
c infrared

Orthochromatisch
Orthochromatic
Orthochromatique
Ortocromática

Panchromatisch
Panchromatic
Panchromatique
Pancromática

Infrarotempfindlich
Infrared sensitive
Sensible à l'infrarouge
Sensible al infrarrojo

Farbfilm (3 Schichten)
Color film (three-layer)
Film couleurs (trois couches)
Película en color (tres capas)

Farbinfrarotfilm
Color infrared film
Film infrarouge couleurs

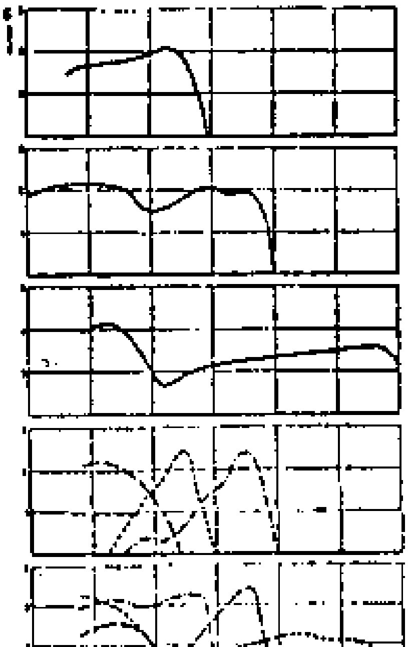

Die spektrale Empfindlichkeit einer photographischen Schicht gibt an, in welchem Maße sie für Licht verschiedener Wellenlängen des Spektrums empfindlich ist.

The spectral sensitivity of a photographic emulsion indicates to what extent the latter is sensitive to light of different wavelength in the spectrum.

La sensibilité spectrale d'une émulsion photographique indique combien cette

MEANING OF COLOR

PHYSICS	PSYCHO-PHYSICS	PSYCHO-LOGY
radiation	Light emission	color sense
1. intensity	1. light intensity	1. brightness
2. spectral composition	2. dominating wave length	2. tone
3. spectral purity (coherence)	3. purity	3. saturation
		MUNSELL-COLOR CHART

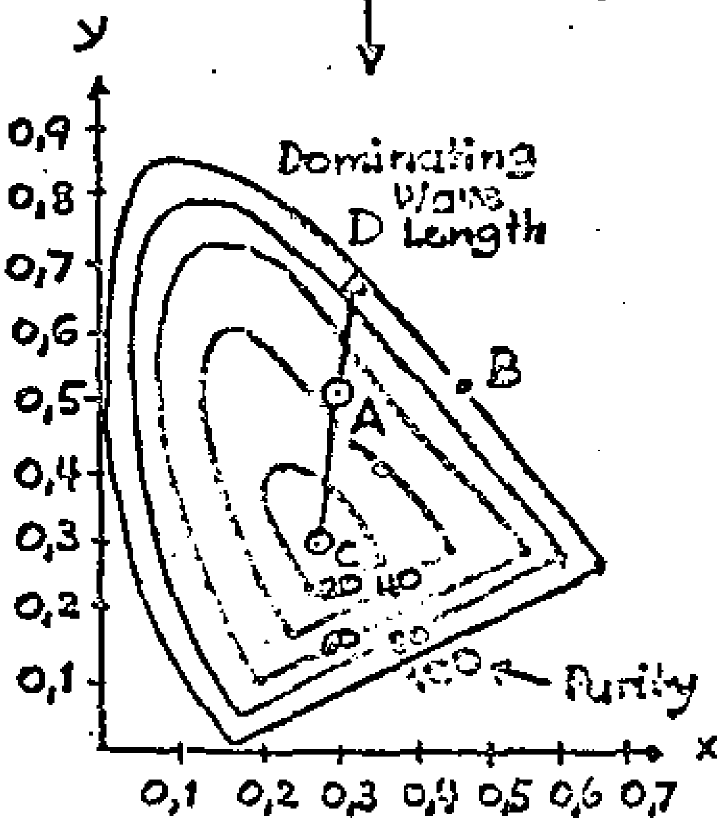

A = Tungsten Light
B = Sunlight at noon
C = Daylight

$$X = \int_0^\infty E_\lambda \cdot \rho_\lambda \bar{x}_\lambda \, d\lambda \; ;$$

$$Y = \int_0^\infty E_\lambda \cdot \rho_\lambda \bar{y}_\lambda \, d\lambda \; ;$$

$$Z = \int_0^\infty E_\lambda \cdot \rho_\lambda \bar{z}_\lambda \, d\lambda \; ;$$

↓ spectral sensitivity of standard observer

$$x = \frac{X}{X+Y+Z} \; ; \qquad x + y + z = 1$$

$$y = \frac{Y}{X+Y+Z} \; ;$$

COPYING

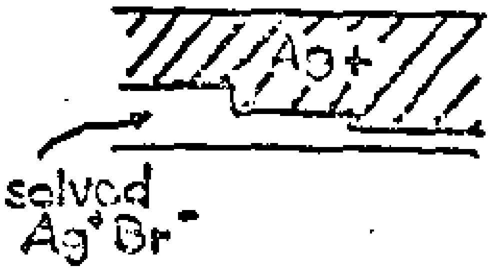

Negativ

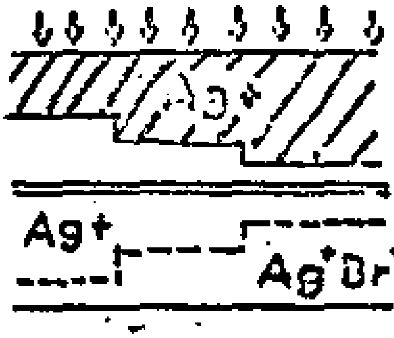

Exposure by
Contact
Copy

Development, Stop Bath,
Fixing & Drying

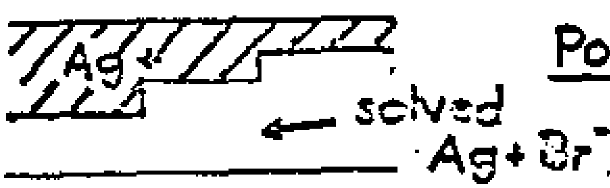

Positiv

PHOTOGRAPHIC PROCESS

1. EXPOSURE

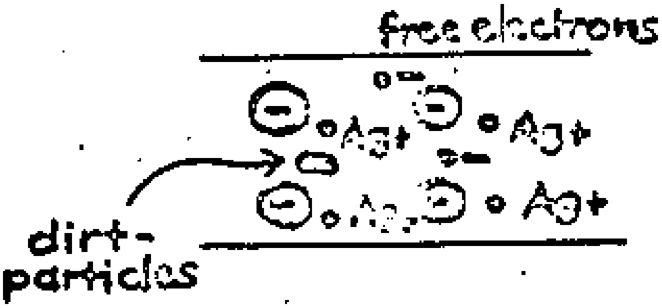

original film unexposed ①

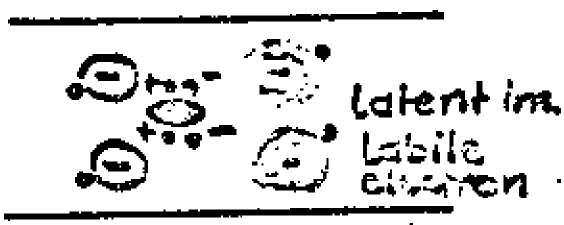

original film exposed ②

2. DEVELOPMENT

a. Developer = reducing substance (e.g. Hydrochinon) ③

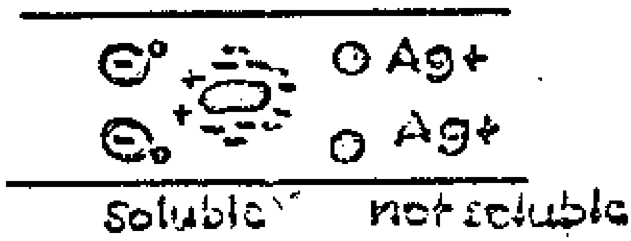

b. Stop-Bath H_2O - stop of development ④

c. Fixing

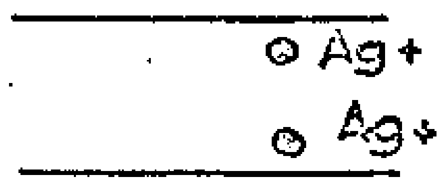

Solving of unreduced Ag^+Br^- ⑤

d. Drying ⑥

1/5

HISTORY OF COLOR PHOTOGRAPHY

1850	Niépce (Niephow) Hill	Paris England	Direct colours of halogens → volatile
1861	Maxwell Cros Du Hauron	London Paris Bordeaux	Color addition by projection Subtractive process
1893	Joly	Dublin	Color additive process, color chips on emulsion
	Lumière		[illegible]

HISTORY OF PHOTOGRAPHY

1727	Schulze	Altdorf (Nürnberg)	Silvernitrate turns violet from white in sun
1824	Niépce	Chalons s. Saône	"Heliogravure" Bitumen on Tin soluble when unexposed
	Daguerre	Paris	Silver on Copperplate, coated w. Jodiumvapour, developed in Hg-vapour → Hg where exposed
1839	Arago	French Acad. of Sciences	Lecture about works of Niépce & Daguerre
1839	Talbot	England	Negativ-Positivmethod Silver on Paper
1847	Niépce (nephew)	Paris	Emulsion with egg white on glass
1846	Ménard	Paris	"COLLODION"
1850	Bingham	England	Collodion applied to photogr. emulsion → "FILM"
1877-80	Eastman	U.S.A. (N.Y.)	Dryplate, Gelatine & AgBr
1887	Goodwin	USA (N.J.)	Patent for Roll Film
1898	Eastman	USA (Rochester)	KODAK Rollfilm ANSCO-Film Co.

Aplicaciones

- aplicaciones militares
- levantamiento de mapas de escala pequena en países con mucha cubierta de nubes
- análisis de regiones polares (evaluación de hielo)

Ventajas y desventajas de los sensores diferentes

Sistemas fotográficos

Ventajas

- técnica madura para tomar y labrar fotos
- muy buena calidad de la geometría
- depósito simple y barato de los datos

Desventajas

- fotografías en bandas espectrales largas
- depende de la cubierta de nubes

Aplicaciones

- levantamiento de mapas topográficas
- determinación de coordenadas de puntos geodéticas
- fotointerpretación

Sistemas scanner

Ventajas

- datos simultaneamente en diferentes frecuencias espectrales, incluido las radiaciones infrarojo, ultravioleta
- imágenes numéricos en cintas magnéticas, transmisión telemétrica

Desventajas

- perturbaciones por movemiento de la plataforma
- generalmente no evaluación esteroscopa
- depende de la cubierta de nubes

Aplicaciones

- percepción remota numérica: geología, agronomía, silvicultura, hidrología; tratamientos de clasificación

Sistemas radar

Ventajas

- no dependencia de las condiciones del tiempo y de la atmósfera
- transmisión telemétrica

Desventajas

- geometría depende mucho de la orientación de la plataforma y de la topografía
- no evaluación estereoscopa
- las condiciones de reflectancia de los objetos no estan estudiadas suficientemen

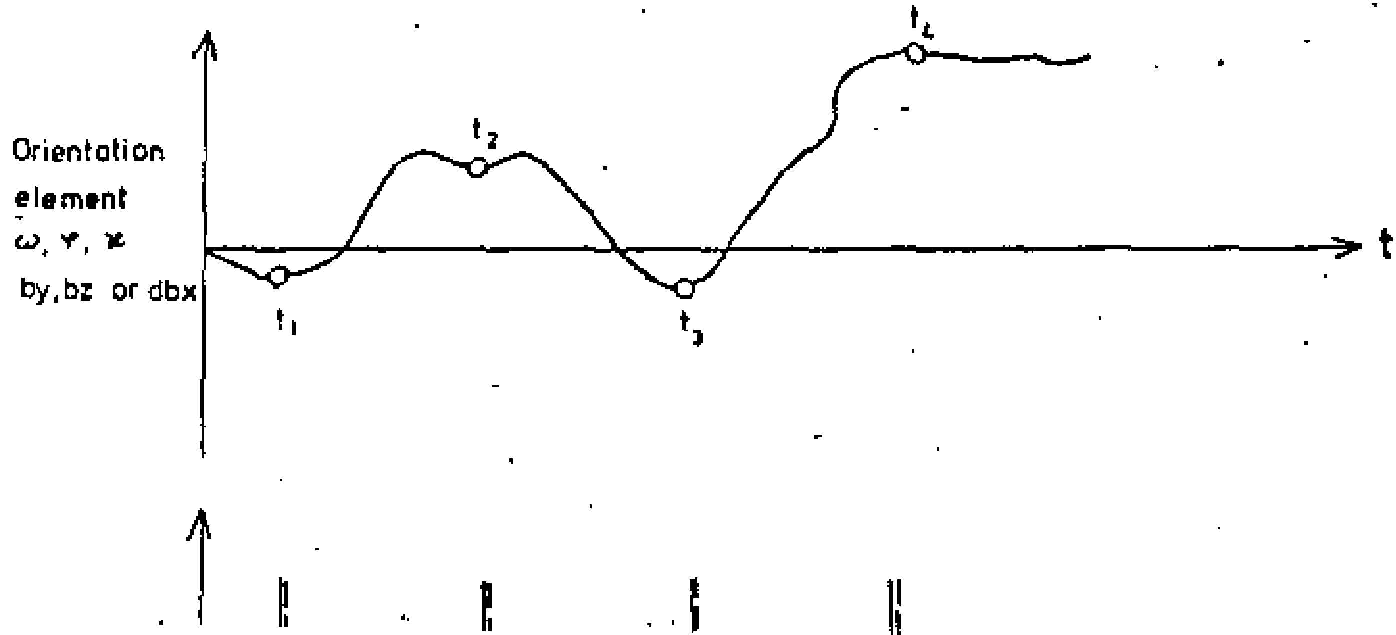
Orientation
element
ω, φ, κ
by, bz or dbx
t
t1
t2
t3
t4

Tab. 1

Parameters of commonly used imaging sensors (Konecny)

Sensor type	Sensor	film size (original)	resolution l.p. mm (original)	angular view in x	angular view in y	angular resolution	ground pulse resolution	Sensor constant c	range of scale factors
photography	frame camera	230x 230mm	60	-60° to +60°	-60° to +60°	0,1mrad ≐ 0,0057°	-	152 mm	1000 to 100 000
	strip camera	230 to 70mm strip	60	strip	-60° to +60°	0,1mrad	-	152 mm	100 to 10 000
	panoramic camera	115x 1140 mm	60	-40° to +40°	-90° to +90°	>0,05mrad (0,015mrad)	-	>300 mm (1000mm)	1 000 to 100 000
satellite imagery	television camera	(25,4x25,4mm) enlarged to 230x230mm	40 in enlargment	-5° to +5°	-5° to +5°	0,02 mrad	-	125 mm (enlarged to 1100 mm)	>1.000 000
	multi-spectral scanner	70 mm strip enlarged to 230 mm	20 in enlargement	strip	-5° to +5°	0,05mrad for visible light		250 mm (enlarged to 1100 mm)	>1 000 000
infrared scanning	I.R. scanner	70 mm strip	20	strip	-60° to +60°	3 mrad	-	30 mm	1 000 to 1 000 000
radiometry	passive radiometer	70mm strip	5	semi-annulus at constant angle		10 mrad	-	-	10 000 to 5 000 000
radar	P.P.I.	circular, r up to 100mm	5	polar coordinate representation α=0° to 360°, θ = 0° to 90°		8 mrad in azimuth	50m	-	10 000 to 1 000 000
	SLAR	70 mm strip	20	strip	0° to 90°	3 mrad in azimuth	15m	-	100 000 to 1 000 000
	coherent SLAR + interferometer	70 mm strip	30	strip	0° to 90°	2 mrad in azimuth	15m	-	100 000 to 1 000 000
sonar	sonar fish	graph paper strip	10	strip	0° to 90°	5 mrad in azimuth	10m	-	10 000 to 100 000 ?

Mission	1 / Jahr / año	Sensor	m_B	Auflösung / resolución	exactitud / Genauigkeit: Lage / plano	Höhe / altura
SKYLAB S190A	435 km 1973	Kamera C=15 mm	1:2900000	29 lp/mm = 100 m	± 40 m - ± 60 m (13 µm - 20 µm)	± 150 m - ± 180 m (0,3 °/oo·h)
SKYLAB S190B	435 km 1973	C=460 mm	1: 950000	25 lp/mm = 38 m	-	-
LANDSAT 1-2	920 km 1972	Abtaster	-	220 m	± 50 m - ± 80 m	-
LANDSAT 3	920 km 1978	Abtaster, RBV	-	220 m 110 m	-	-
SEASAT	790 km 1978	Radar	-	theor. 25 m	-	-
SOJYZ 22-30	250 km seit/desde 1976	MKF-6-Kamera C=125 mm	1:2 Mill.	80 lp/mm = 25 m	-	-
GEMS 1000	12,5 km	Flugzeug-radar	1: 400000	theor.10 m	± 20 m - ± 300 m	-

Comparación de misiones diferentes

Vergleich verschiedener Missionen (Sensoren)

Sensores – resumen

Sensoren Sensors Capteurs-détecteurs Sensores	Typ Type Type Tipo	Strahlungs-Quelle Source Source de rayonnement Fuente de radiación	Empfänger Detector Récepteur Receptor	Spektralbereich Spectral range Gamme spectrale Gama espectral	Ungefähre Auflösung / Approximate resolution / Définition approximative / Resolución aproximada: geometrisch geometric géométrique geométrica	thermisch thermal thermique térmica	Anwendungszeit Time of use Mise en oeuvre Tiempo de aplicación	Primärer Datenspeicher Primary data storage Mémoire primaire Almacén de datos primario
Photographische Systeme Photographic systems Systèmes photographiques Sistemas fotográficos	passiv passive passif pasivo	Sonne Sun Soleil Sol	Photogr. Schichten Photogr. emulsions Émulsions photograph. Emulsiones fotogr.	0.4–0.9 µm	0.1–0.4 mrad	—	Tag Day Le jour Día	Film Film Film Película
Multispektral-Abtaster Multispectral scanner Scanner multispectral Scanner multiespectral	passiv passive passif pasivo	Sonne Sun Soleil Sol	Photodetektoren Photo detectors Photodétecteurs Fotodetectores	0.4–1.5 µm	1–3 mrad	—	Tag Day Le jour Día	Magnetband Magnetic tape Bande magnétique Cinta magnética
	passiv passive passif pasivo	Erde Earth Terre Tierra	Infrarotdetektoren Infrared detectors Détecteurs IR Detectores de infrarr.	1.5–14 µm	1–3 mrad	0.2 °C	Tag, Nacht Day night Jour/nuit Día/noche	Magnetband Magnetic tape Bande magnétique Cinta magnética
Infrarot-Abtaster Infrared scanner Scanner infrarouge Scanner infrarrojo	passiv passive passif pasivo	Erde Earth Terre Tierra	Infrarotdetektoren Infrared detectors Détecteurs IR Detectores de infrarr.	3–14 µm	1–6 mrad	0.2 °C	Tag Nacht Day night Jour/nuit Día/noche	Film Magnetband Film magnetic tape Film bande magnétique Película cinta magnética
Fernsehsysteme Television systems Systèmes de télévision Sistemas de televisión	passiv passive passif pasivo	Sonne Sun Soleil Sol	Bildröhren Image tubes Tubes image Tubos de imagen	0.4–0.8 µm	0.2–2 mrad	—	Tag Day Le jour Día	Magnetband Magnetic tape Bande magnétique Cinta magnética
Mikrowellen-Radiometer Microwave radiometer Radiomètre microondes Radiometro de microonda	passiv passive passif pasivo	Erde Earth Terre Tierra	Antennen Antennas Antennes Antenas	0.5–30 cm	30–100 mrad	0.5–3 °C	Tag Nacht Day-night Jour-nuit Día noche	Magnetband Magnetic tape Bande magnétique Cinta magnética
Radarsysteme (SLAR) Radar systems (SLAR) Systèmes radar (SLAR) Sistemas de radar (SLAR)	aktiv active actif activo	Sender Transmitter Emetteur Transmisor	Antennen Antennas Antennes Antenas	0.8–100 cm	~ 2 mrad	—	Tag Nacht Day-night Jour/nuit Día noche	Film Film Film Película

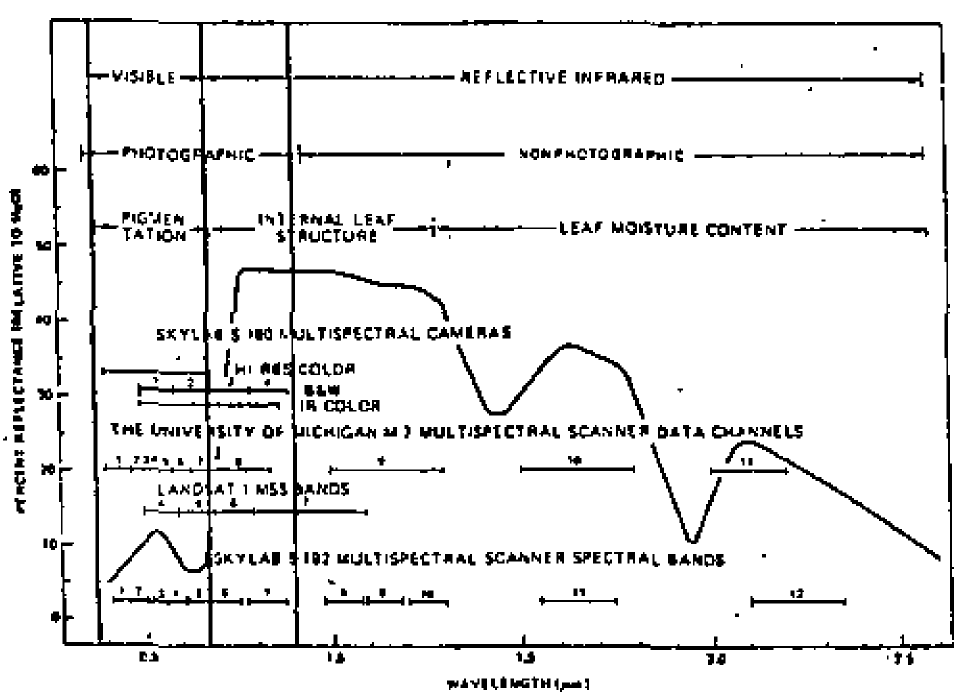

Ejemplo (Swain/Davies)

Leyes de radiación importantes

Kirchhoffsches Gesetz
Kirchhoff's law
Loi de Kirchhoff
Ley de Kirchhoff

$$\varepsilon(T) = \frac{M(T)}{M_s(T)} \qquad \varepsilon(\lambda, T) = \alpha(\lambda, T)$$

Der Emissionsgrad ε eines Körpers ist das Verhältnis seiner spezifischen Ausstrahlung M zur spezifischen Ausstrahlung M_s des Schwarzen Körpers derselben Temperatur T. Der Emissionsgrad eines Körpers ist für beliebige Wellenlängenbereiche stets gleich dem Absorptionsgrad α. Der Schwarze Körper, der jede auf ihn auftreffende Strahlung vollständig absorbiert, hat den größten Emissionsgrad ($\varepsilon = \alpha = 1$).

The emissivity ε of a body is the ratio between its radiant exitance M and the radiant exitance M_s of a full radiator of identical temperature T. The emissivity of a body for certain wavelength regions is always equal to the absorptance α. A full radiator which absorbs all the radiation incident on it has the highest emissivity ($\varepsilon = \alpha = 1$).

Le pouvoir émissif ε d'un corps est le rapport entre son rayonnement spécifique M et le rayonnement spécifique M_s du corps noir à la même température T. Pour des gammes de longueurs d'onde quelconques, le pouvoir émissif d'un corps est toujours égal à son pouvoir d'absorption α. Le corps noir qui absorbe intégralement tout rayonnement reçu par sa surface a le plus grand pouvoir émissif ($\varepsilon = \alpha = 1$).

La emisividad ε de un cuerpo es la relación entre su exitancia radiante M y la exitancia radiante M_s de un radiador completo a la misma temperatura T. La emisividad de un cuerpo para distintas gamas de longitud de onda es siempre igual a la absortancia α. Un radiador completo, que absorbe por completo toda la radiación incidente en él, tiene la máxima emisividad ($\varepsilon = \alpha = 1$).

Stefan-Boltzmannsches Gesetz
Stefan-Boltzmann law
Loi de Stefan-Boltzmann
Ley de Stefan-Boltzmann

$$M = \sigma \cdot T^4$$
$$\sigma = 5.67 \cdot 10^{-8}\ W/m^2 \cdot K^4$$

Die spezifische Ausstrahlung M des Schwarzen Körpers ist proportional der vierten Potenz der absoluten Temperatur T.

The radiant exitance M of a full radiator is proportional to the fourth power of the absolute temperature T.

La puissance totale de rayonnement M du corps noir est proportionnelle à la quatrième puissance de la température absolue T.

La exitancia radiante M de un radiador completo es proporcional a la cuarta potencia de la temperatura absoluta T.

Wiensches Verschiebungsgesetz
Wien's displacement law
Loi de répartition de Wien
Ley de desplazamiento de Wien

$$\lambda_{max} \cdot T = c$$
$$c = 2898\ \mu m \cdot K$$

Die Wellenlänge λ_{max} der maximalen Strahldichte des Schwarzen Körpers ist seiner absoluten Temperatur umgekehrt proportional.

The wavelength λ_{max} of the maximum radiance of a full radiator is inversely proportional to its absolute temperature.

La radiation émise avec le maximum de puissance par le corps noir a une longueur d'onde λ_{max} inversement proportionnelle à sa température absolue.

La longitud de onda λ_{max} de la radiancia máxima de un radiador completo es inversamente proporcional a su temperatura absoluta.

Plancksche Formel
Planck's formula
Formule de Planck
Fórmula de Planck

$$L_\lambda(\lambda, T) = \frac{2c_1}{\lambda^5} \cdot \frac{1}{e^{c_2/\lambda T} - 1}$$

$$c_1 = 5.9544 \cdot 10^{-12}\ W \cdot cm^2 \qquad c_2 = 1.4388\ cm \cdot K$$

Die Plancksche Formel gibt die Abhängigkeit der spektralen Strahldichte L_λ von der Temperatur T des Schwarzen Körpers und der Wellenlänge λ wieder.

Planck's formula defines spectral radiance L_λ as a function of the temperature T of a full radiator and of wavelength λ.

La formule de Planck exprime la variation de la radiance spectrale L_λ en fonction de la température T du corps noir et de la longueur d'onde λ.

La fórmula de Planck indica la radiancia espectral L_λ en función de la temperatura T de un radiador completo y de la longitud de onda λ.

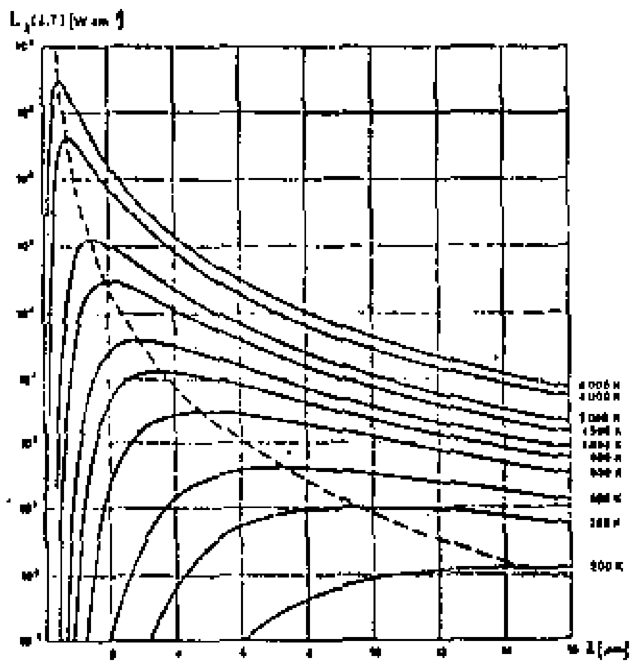

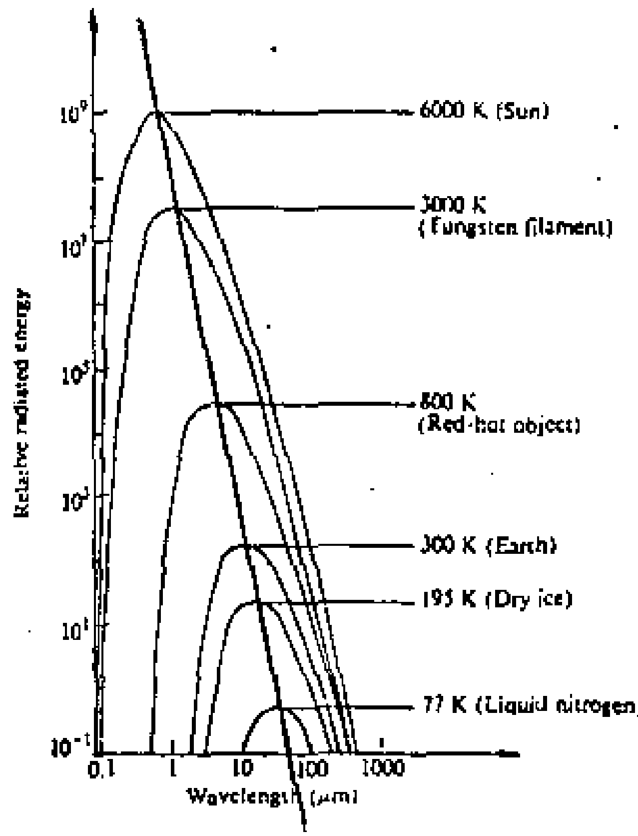

(50)

Radiación solar y atmósfera

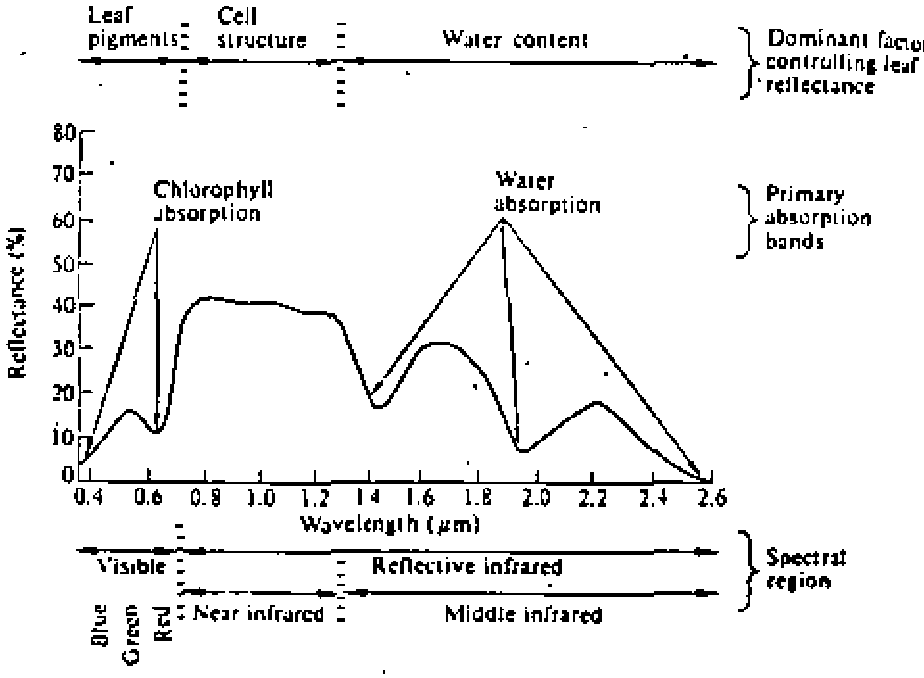

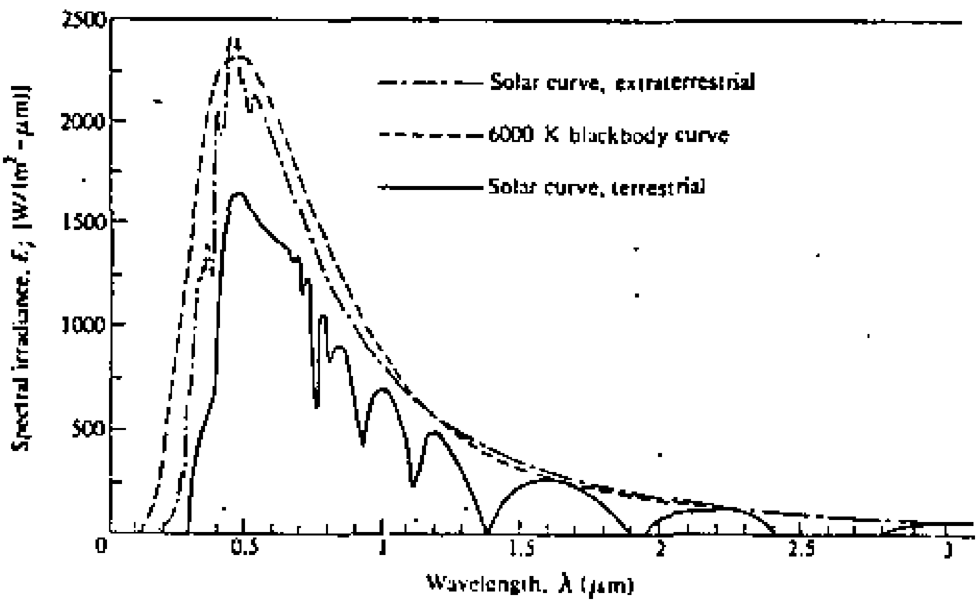

Relative spektrale Energieverteilung in Meereshöhe
Relative spectral energy distribution at sea level
Distribution spectrale relative de l'énergie au niveau de la mer
Distribución espectral relativa de energía al nivel del mar

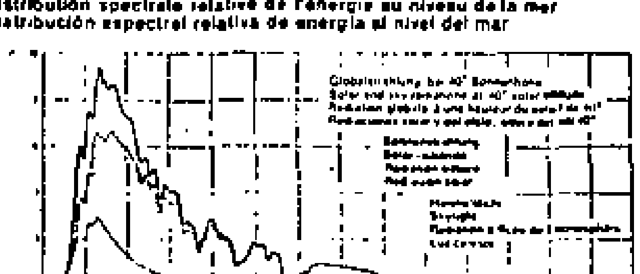

Relative spektrale Energieverteilung der Globalstrahlung
Relative spectral energy distribution of solar and sky radiations
Distribution spectrale relative de l'énergie de la radiation globale
Distribución espectral relativa de energía de las radiaciones solar y del cielo

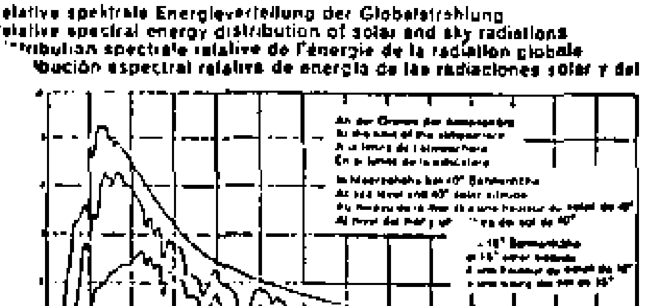

Spektrale Hellempfindlichkeit des Auges
Luminosity curve of the eye
Sensibilité lumineuse de l'oeil
Curva espectral de luminosidad del ojo

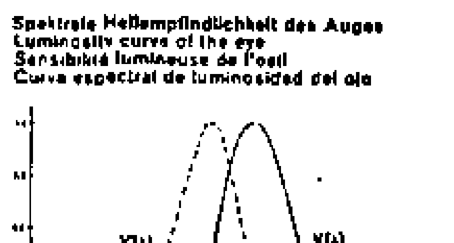

V' (λ) Nachtsehen
Scotopic vision
Vision nocturne
Visión escotópica

V (λ) Tagessehen
Photopic vision
Vision diurne
Visión fotópica

RADIATION

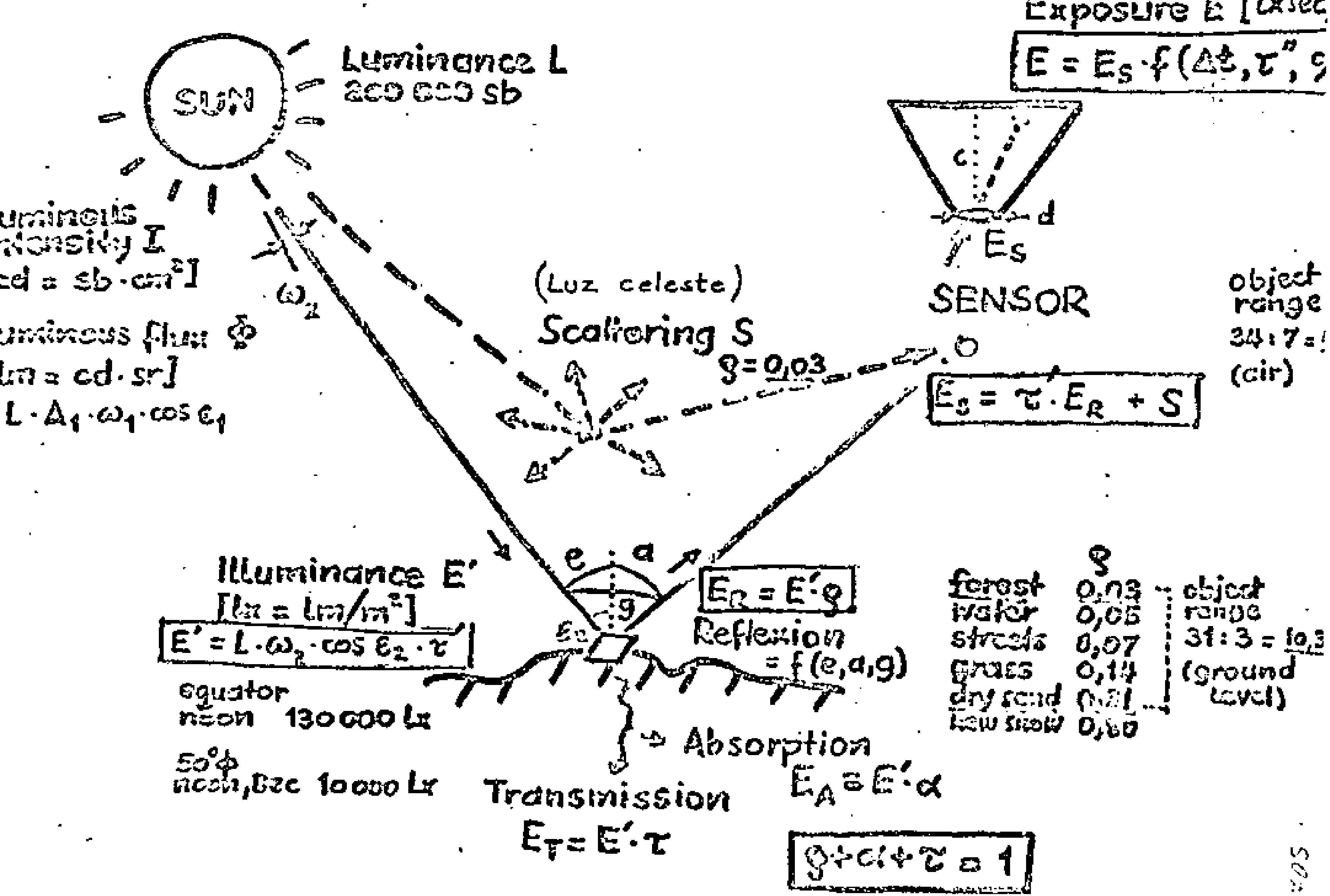

SUN
Luminance L
200 000 sb
(Luz celeste)
Scattering S
ρ = 0,03
SENSOR
E_S
d
c
Exposure E [lx sec
E = E_S · f(Δt, τ'', ρ
E_S = τ · E_R + S
object range
34 : 7
(cir)
Illuminance E'
[lx = lm/m²]
E' = L · ω₂ · cos ε₂ · τ
equator noon 130 000 lx
50° φ noon, Dec 10 000 lx
e
a
g
E_R = E'·ρ
Reflexion = f(e,a,g)
Absorption
E_A = E'·α
Transmission
E_T = E'·τ
ρ + α + τ = 1
ρ
forest 0,03
water 0,05
streets 0,07
grass 0,14
dry sand
new snow 0,80
object range
31 : 3 = 10,3
(ground level)
Luminous flux Φ
[lm = cd · sr]
L · A₁ · ω₁ · cos ε₁
ω₂

Pérdida de luz

Lichtverluste
Light loss
Pertes de lumière
Pérdida de luz

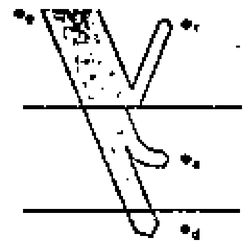

Reflexionsgrad
Reflectance
Réflectance
Reflectancia

$$\rho(\lambda) = \frac{\Phi_r}{\Phi_o}$$

Absorptionsgrad
Absorptance
Absorptance
Absortancia

$$\alpha(\lambda) = \frac{\Phi_a}{\Phi_o}$$

Transmissionsgrad
Transmittance
Transmittance
Transmitancia

$$\tau(\lambda) = \frac{\Phi_d}{\Phi_o}$$

$$\rho + \alpha + \tau = 1$$

Bouguer-Lambertsches Gesetz
Lambert-Bouguer law of absorption
Loi d'absorption de Bouguer-Lambert
Ley de absorción de Bouguer-Lambert

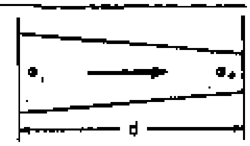

Reinabsorptionsgrad
Internal absorptance
Absorptance interne
Absortancia interna

$$\alpha_i(\lambda) = \frac{\Phi_i - \Phi_e}{\Phi_i} = 1 - \tau_i$$

Reintransmissionsgrad
Internal transmittance
Transmittance interne
Transmitancia interna

$$\tau_i(\lambda) = \frac{\Phi_e}{\Phi_i} = e^{-K \cdot d} = 10^{-m \cdot d}$$

Extinktionsmodul
Linear absorption coefficient
Coefficient d'absorption linéaire
Coeficiente de extinción

$K = 2.718\ m \qquad m = 0.4343\ K$

Von einem Lichtstrom Φ_o verbleibt nach der Reflexion an »r« Grenzflächen und dem Durchgang durch ein absorbierendes Medium der Dicke »d«:

After reflection at »r« boundary faces and passing through an absorbing medium of thickness »d«, a luminous flux Φ_o is reduced to:

Après réflexion sur »r« surfaces limites et passage à travers un milieu absorbant d'épaisseur »d«, un flux lumineux Φ_o est réduit à:

Después de ser reflejado en »r« superficies límite y de pasar por un medio absorbente de espesor »d«, queda de un flujo luminoso Φ_o:

$$\Phi = (1 - \rho)^r \, e^{-K \cdot d} \, \Phi_o \qquad \rho \approx \left(\frac{n-1}{n+1}\right)^2$$

Extinción

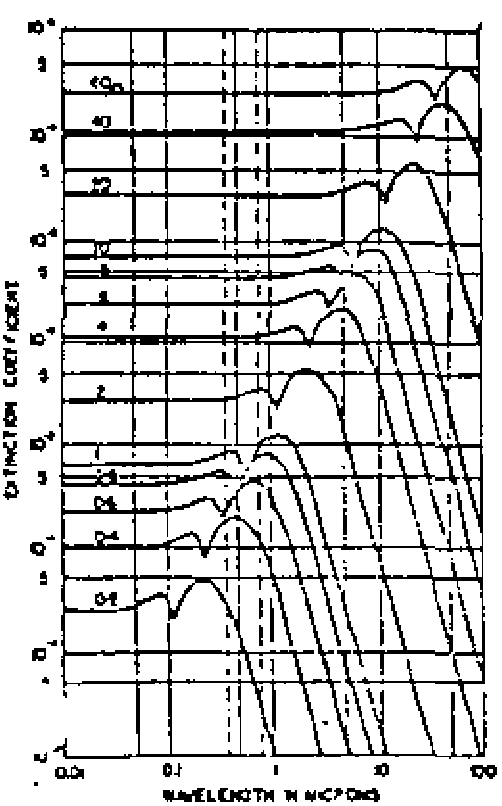

Extinction Coefficient (α)		Visual range for green	"Visual range" for 1.0μ	Ratio
For Green Light	For 1.0μ radiation			
0.0136	0.00101	288 Km.	3,850 Km	13.6
0.0298	0.00782	131	500	3.82
0.0440	0.0154	89	254	2.86
0.129	0.0541	30.4	72.4	2.38
0.298	0.160	13.1	24.5	1.87
0.461	0.275	8.5	14.2	1.67

Iluminancia

Die Beleuchtungsstärke, die eine punktförmige Lichtquelle auf einer Fläche F erzeugt, ist umgekehrt proportional zum Quadrat der Entfernung r und proportional zum Kosinus des Winkels ε, den die Strahlenrichtung mit der Flächennormalen einschließt.

The illuminance produced by a point source on a surface F is inversely proportional to the square of distance r and proportional to the cosine of angle ε made by the direction of radiation and the normal.

L'éclairement produit sur une surface F par une source ponctuelle est inversement proportionnel au carré de la distance r et proportionnel au cosinus de l'angle ε que la direction du rayonnement forme avec la perpendiculaire à la surface.

La iluminancia producida por una fuente de luz puntiforme en una superficie F es inversamente proporcional al cuadrado de la distancia r y proporcional al coseno del ángulo ε formado por la dirección de la radiación y la normal.

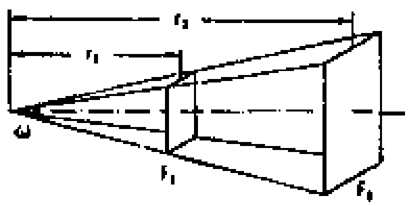

$$E_1 = \frac{\Phi}{\omega \cdot r_1^2} = \frac{1}{r_1^2}$$

$$E_2 = \frac{\Phi}{\omega \cdot r_2^2} = \frac{1}{r_2^2}$$

$$E_1 : E_2 = \frac{1}{r_1^2} : \frac{1}{r_2^2}$$

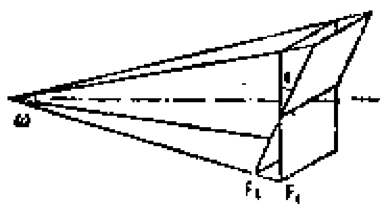

$$E_1 = \frac{\Phi}{\omega \cdot r^2}$$

$$E_2 = \frac{\Phi}{\omega \cdot r^2} \cos \varepsilon$$

$$E_1 : E_2 = 1 : \cos \varepsilon$$

Leuchtende bzw. beleuchtete Fläche
Luminous or illuminated surface
Surface lumineuse ou éclairée
Superficie luminosa o iluminada

A_1 A_2

Raumwinkel ω in Steradiant (sr)
Solid angle ω in steradian (sr)
Angle solide ω dans un stéradiant (sr)
Angulo sólido ω en estereorradianes (sr)

$$\omega_1 = \frac{A_{1\varepsilon}}{r^2} \text{ sr} \approx \frac{A_1}{r^2} \text{ sr}$$

$$\omega_2 = \frac{A_{2\varepsilon}}{r^2} \text{ sr} \approx \frac{A_2}{r^2} \text{ sr}$$

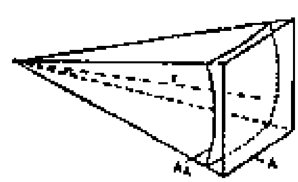

$A_\varepsilon \approx A$

	L	I	Φ	E	H
L =	L	$\frac{I}{A_1 \cdot \cos \varepsilon_1}$	$\frac{\Phi}{A_1 \cdot \omega_1 \cdot \cos \varepsilon_1}$	$\frac{E \cdot r^2}{A_1 \cdot \cos \varepsilon_1}$	$\frac{H}{\omega_2 \cdot t \cdot \cos \varepsilon_1}$
I =	$L \cdot A_1 \cdot \cos \varepsilon_1$	I	$\frac{\Phi}{\omega_1}$	$\frac{E \cdot r^2}{sr \cdot \cos \varepsilon_2}$	$\frac{H \cdot r^2}{t \cdot sr \cdot \cos \varepsilon_2}$
Φ =	$L \cdot A_1 \cdot \omega_1 \cdot \cos \varepsilon_1$	$I \cdot \omega_1$	Φ	$E \cdot A_2$	$\frac{H \cdot A_2}{t}$
E =	$L \cdot \omega_2 \cdot \cos \varepsilon_2$	$\frac{I \cdot \cos \varepsilon_2}{r^2}$	$\frac{\Phi}{A_2}$	E	$\frac{H}{t}$
H =	$L \cdot \omega_2 \cdot t \cdot \cos \varepsilon_2$	$\frac{I \cdot t \cdot \cos \varepsilon_2}{r^2}$ sr	$\frac{\Phi}{A_2} t$	$E \cdot t$	H

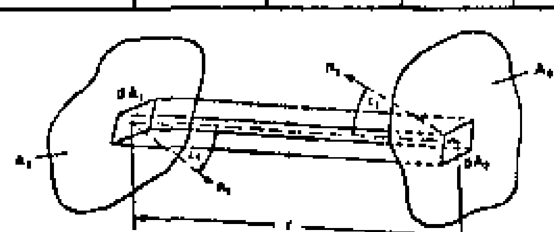

(5?)

Fotometría: unidades de medida importantes

Lichtstärke
Luminous intensity — 1 Candela [cd]
Intensité lumineuse
Intensidad luminosa

1 Candela ist die Lichtstärke, mit der $^1/_{600\,000}$ m² des Schwarzen Strahlers bei der Erstarrungstemperatur des Platins (2042 K) senkrecht zu seiner Oberfläche leuchtet.

1 candela is the luminous intensity of a blackbody of $^1/_{600\,000}$ m² on a plane perpendicular to its surface at the temperature of freezing platinum (2042 K).

1 candela correspond à l'intensité lumineuse produite par une surface de $^1/_{600\,000}$ m² du corps noir perpendiculairement à cette surface, à la température de solidification du platine (2042 K).

1 candela es la intensidad luminosa de un cuerpo negro de $^1/_{600\,000}$ m² a la temperatura de solidificación del platino (2042 K) perpendicularmente a su superficie.

Leuchtdichte
Luminance — L [cd/m²]
Luminance
Luminancia

Die Leuchtdichte ist ein spezifisches Maß für die Helligkeit einer leuchtenden Fläche. Ihre Einheit 1 Candela/Quadratmeter ist $^1/_{600\,000}$ der Leuchtdichte des Schwarzen Strahlers bei der Erstarrungstemperatur des Platins.

Luminance is a specific measure of the brightness of a luminous surface. Its unit of 1 candela/square meter is equivalent to $^1/_{600\,000}$ of the luminance of a blackbody at the temperature of freezing platinum.

La luminance est une unité de mesure spécifique pour l'éclat d'une surface lumineuse. Son unité de 1 candela/m² équivaut à $^1/_{600\,000}$ de la luminance du corps noir à la température de solidification du platine.

La luminancia es una medida específica de la luminosidad de una superficie luminosa. Su unidad de 1 candela/metro cuadrado es equivalente a $^1/_{600\,000}$ de la luminancia de un cuerpo negro a la temperatura de solidificación del platino.

Lichtstrom
Luminous flux — Φ Lumen [lm] — 1 lm = 1 cd · sr
Flux lumineux
Flujo luminoso

Der Lichtstrom Φ ist die von der Lichtquelle ausgestrahlte Leistung, bewertet nach dem spektralen Hellempfindlichkeitsgrad des Auges. Der Lichtstrom 1 Lumen ist die Strahlung von 1 Candela in den Raumwinkel 1.

Luminous flux Φ is the radiation of a source, evaluated according to the spectral response function of the human eye. A luminous flux of 1 lumen is equivalent to a radiation of 1 candela over the solid angle 1.

Le flux lumineux Φ est l'énergie rayonnante d'une source de lumière, appréciée d'après le degré de sensibilité lumineuse de l'oeil. Un flux lumineux de 1 lumen équivaut au rayonnement de 1 candela dans l'angle solide 1.

El flujo luminoso Φ es la energía irradiada por una fuente luminosa, evaluada según la eficiencia luminosa espectral del ojo humano. El flujo luminoso de 1 lumen equivale a la radiación de 1 candela en el ángulo sólido 1.

Beleuchtungsstärke
Illuminance — E Lux [lx] — 1 lx = 1 lm/m²
Éclairement
Iluminancia

Die Beleuchtungsstärke E ist der auf die Fläche bezogene Lichtstrom. Die Einheit 1 Lux ergibt sich, wenn eine 1 m² große Fläche gleichmäßig von einem Lichtstrom von 1 Lumen bestrahlt wird.

Illuminance E is the quotient of the luminous flux incident on a surface. A unit of 1 lux is equivalent to the uniform incidence of a luminous flux of 1 lumen on an area of 1 m².

L'éclairement E est le flux lumineux référé à une unité de surface. Un éclairement de 1 lux équivaut à celui d'une surface de 1 m² qui reçoit un flux lumineux de 1 lumen, uniformément réparti.

La iluminancia E es el flujo luminoso por unidad de superficie iluminada. La unidad de 1 lux es equivalente a la incidencia uniforme de un flujo luminoso de 1 lumen en una superficie de 1 m².

Belichtung
Exposure — H Luxsekunde [lxs]
Exposition
Exposición

Die Belichtung ist das Produkt aus der Beleuchtungsstärke und der Zeit.
Exposure is the product of illuminance and time.
L'exposition est donnée par le produit de l'éclairement et du temps.
La exposición es el producto de la intensidad de iluminación por el tiempo.

---

		cd · m⁻²	cd · in⁻²	sb	asb	L
1 Candela per m²	=	1	6.452 · 10⁻⁴	10⁻⁴	π	π · 10⁻⁴
1 Candela p. sq. in	=	1550	1	0.155	4869	0.4869
1 Stilb	=	10⁴	6.452	1	π · 10⁴	π
1 Apostilb	=	$\frac{1}{\pi}$	2.054 · 10⁻⁴	$\frac{1}{\pi}$ · 10⁻⁴	1	10⁻⁴
1 Lambert	=	$\frac{1}{\pi}$ · 10⁴	2.054	$\frac{1}{\pi}$	10⁴	1

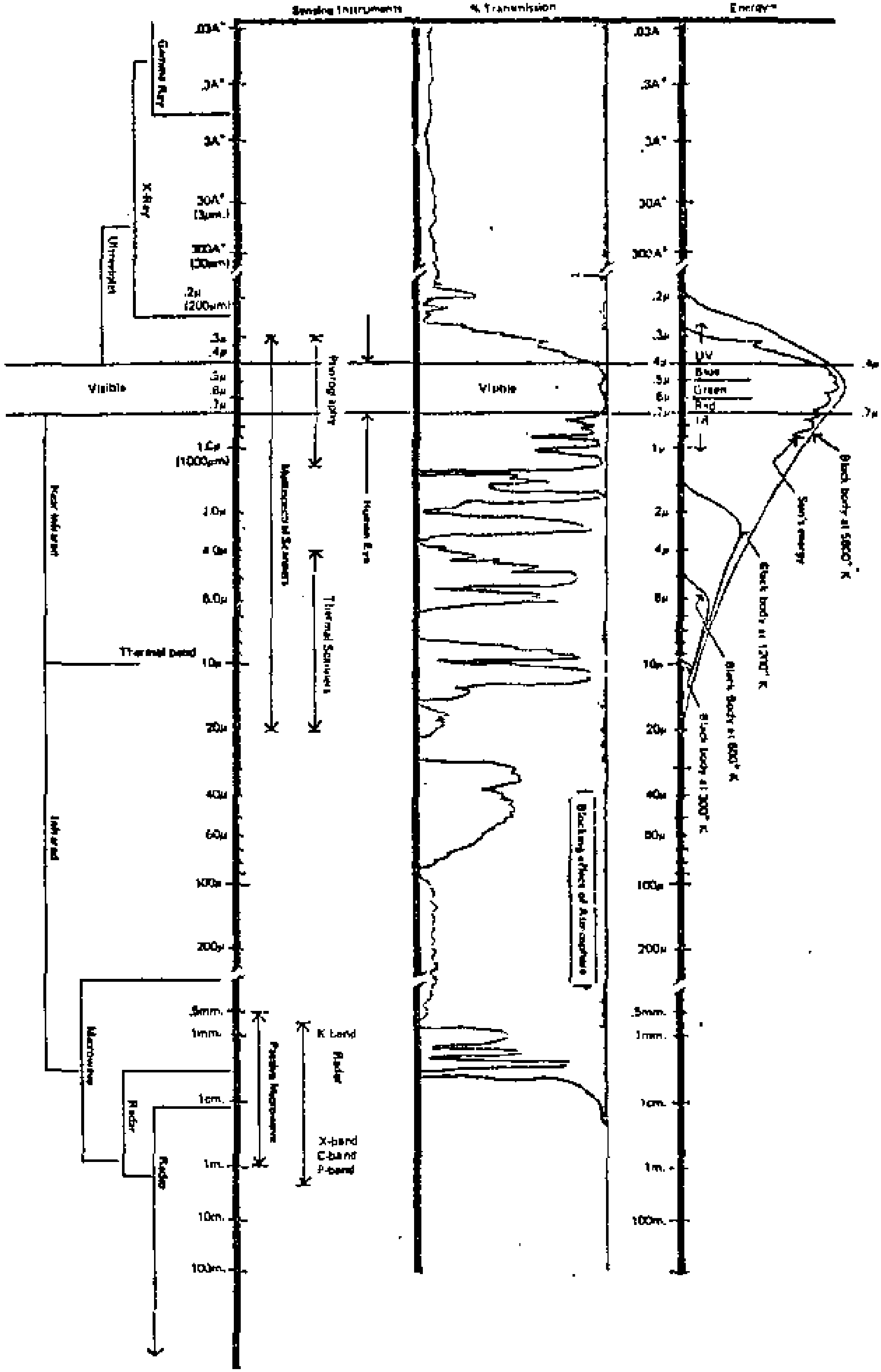
Sensing Instruments
% Transmission
Energy
Gamma Ray
X-Ray
Ultraviolet
Visible
Near Infrared
Thermal band
Infrared
Microwave
Radar
Radar
Photography
Multispectral Scanners
Thermal Scanners
Human Eye
Passive Microwave
K band
Radar
X-band
C-band
P-band
Visible
Blocking effect of Atmosphere
UV
Blue
Green
Red
IR
Sun's energy
Black body at 5800° K
Black body at 1200° K
Black body at 800° K
Black body at 300° K
.03A°
.3A°
3A°
30A°
(3μm.)
300A°
(30μm)
.2μ
(200μm)
.3μ
.4μ
.5μ
.6μ
.7μ
1.0μ
(1000μm)
2.0μ
4.0μ
8.0μ
10μ
20μ
40μ
60μ
100μ
200μ
.5mm.
1mm.
1cm.
1m.
10m.
100m.

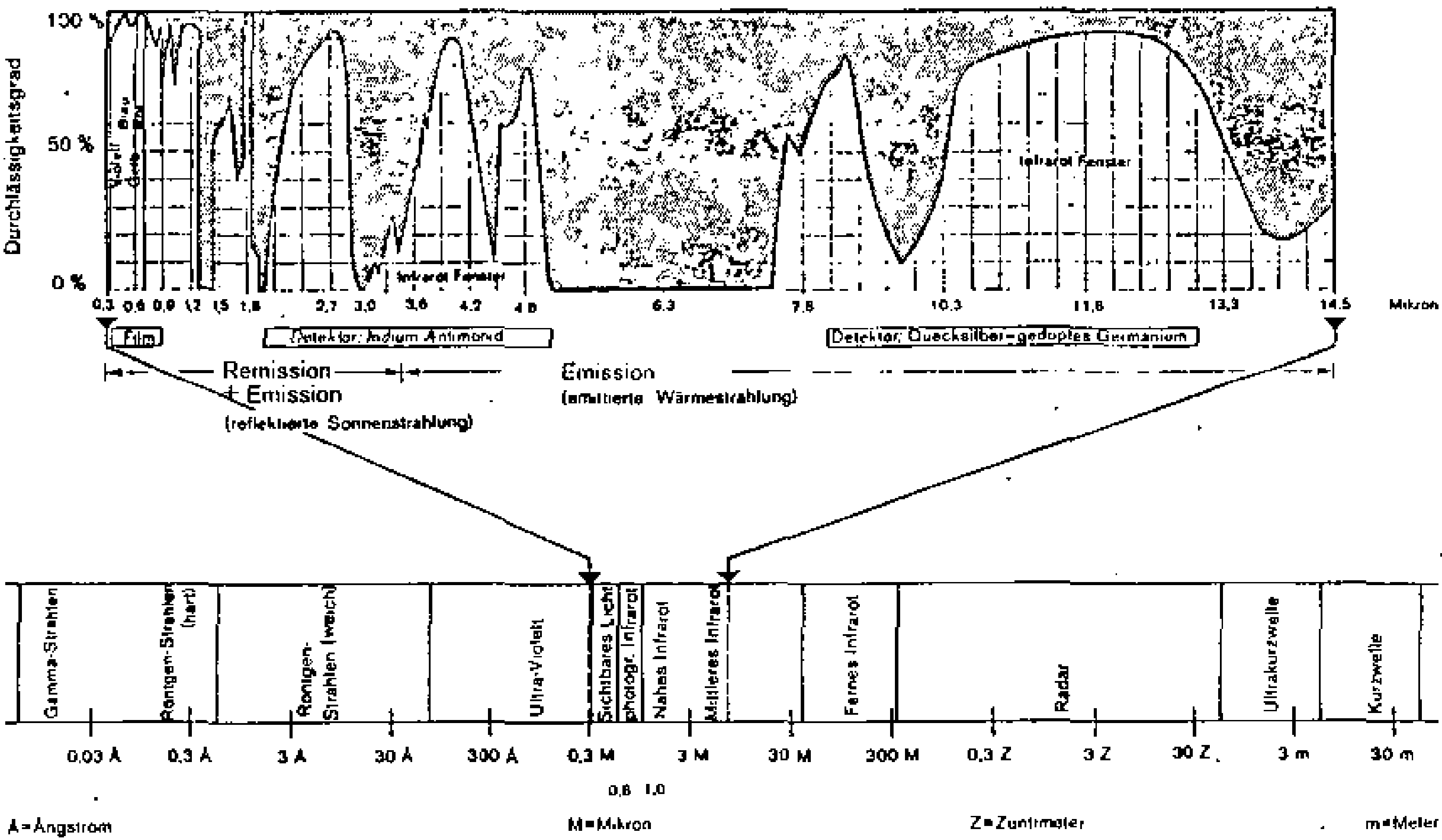

Espectro electromagnético

2.1.1-20

Ondas electromagnéticas

53'2

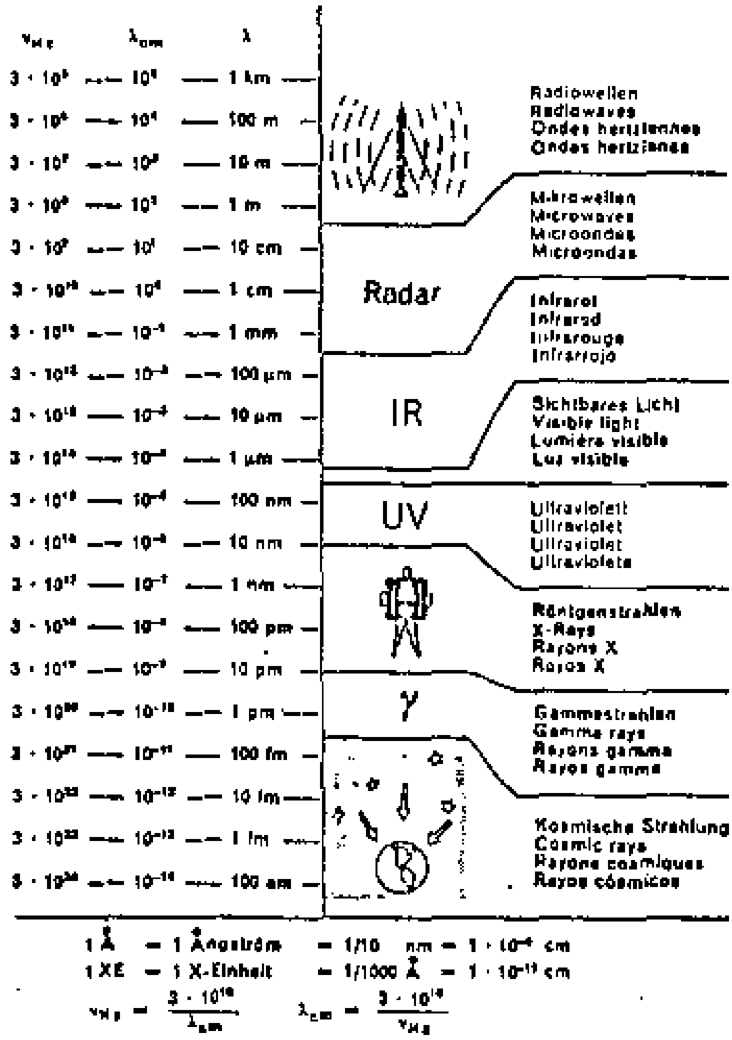

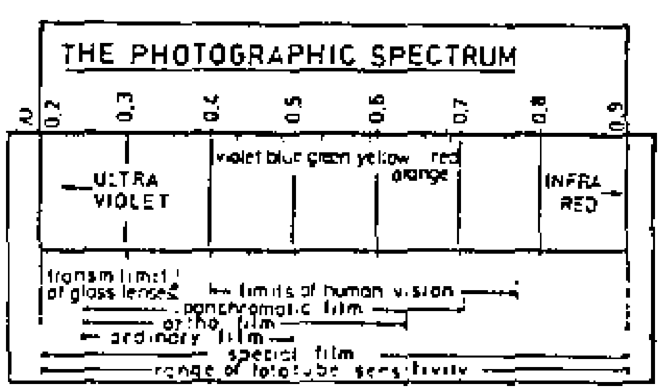

centro de educación continua
división de estudios de posgrado
facultad de ingeniería unam

CURSO: PERCEPCION REMOTA

BIBLIOGRAFIA

DR. HANS PETER BAHR

3-7 MARZO, 1980

Palacio de Minería Calle de Tacuba 5 primer piso México 1, D. F. Tel: 521-40-20

"Acción recíproca entre la fotogrametría y la teledetección"

Bibliografía

Abreviaciones:

BUL	Bildmessung und Luftbildwesen
IGP	Internationale Gesellschaft für Photogrammetrie
ITC	International Training Center, Enschede
Phot.Eng.	Photogrammetric Engineering
ZfV	Zeitschrift für Vermessungswesen

+ diccionario: alemán, inglés, francés y español →

ALBERTZ/KREILING: Photogrammetrisches Taschenbuch. Wichmann Verlag, Karlsruhe

ALBERTZ, J. u. SCHROEDER, M. (Hrsg.): Berichte zum Flugzeugmeßprogramm. Bundesministerium für Forschung und Technologie, Forschungsbericht W78-04, 1978

ALVES, K.: Radiometrische Untersuchung von Farb-Umkehr-Diapositiven. Diplomarbeit TU Hannover, 1976

BÄHR, H.-P.: Ergebnisse vom Erderkundungssatelliten ERTS. BUL 1973

BÄHR, H.-P.: SCHUHR, W.: Versuche zur Ermittlung der geometrischen Genauigkeit von ERTS-Multispektral-Bildern. BUL 1/1974

BÄHR, H.-P.: Interpolation and Filtering of ERTS-Imagery. IGP, Komm. III Symposium, Stuttgart 1974

BÄHR, H.-P.: Erfahrungen mit Methoden der Fernerkundung für Fragen der Küstengewässer. Symposium Erderkundung, DFVLR, Köln 1975

BÄHR, H.-P.: Geometrical Models for Satellite Scanner Imagery. IGP Komm. III, Helsinki 1976 a

BÄHR, H.-P.: Geometrische Modelle für Abtasteraufnahmen von Erderkundungssatelliten. BUL 5/1976 b

BÄHR, H.-P.: Analyse der Geometrie auf Photodetektoren abgetasteter Aufnahmen von Erderkundungssatelliten. Schriftenreihe des Niedersächsischen Landesverwaltungsamtes - Landesvermessung -, Hannover 1976 c

BÄHR, H.-P.: Vom Satellitenbild zur Reihenmeßkammeraufnahme: das Jadegebiet im Vergleich unterschiedlicher Sensoren. Symposium Flugzeugmeßprogramm, Hannover 1977 a; herausgegeben vom BMFT 1978

BÄHR, H.-P.: Digital Image Processing Experience at Hannover Institute for Photogrammetry. Mitteilungen der Geodätischen Institute der Technischen Universität Graz, Folge 29, 1977 b

BÄHR, H.-P.: Design of Large LAMBERT-Type Reflection Standard and Full-Frame Calibration of a Camera Lens. IGP Komm. VII Symposium. Freiburg 1976 a

BÄHR, H.-P.: Digital Rectification of a Facade. IGP Komm. III, Moskau 1978 b

BÄHR, H.-P.: Geometric Analysis and Rectification of LANDSAT MSS Imagery: Comparison of Different Methods. IGP Komm. III, Moskau 1978 c

BÄHR, H.-P.: Analytische Bestimmung und digitale Korrektur des Lichtabfalls in Aufnahmen eines Hochleistungsobjektivs. BUL 1979

BÄHR, H.P. u. DENNERT-MÖLLER, E.: Tidal Land Mapping from LANDSAT. 3ème Colloque international du GDTA, Toulouse 1979

BAUDOIN, A.: Perspectives en cartographie topographique aportées par le satellite SPOT. Colloque International du GDTA, Toulouse 1979

BAUER, F.L. u. GOOS, G.: Informatik. Berlin, Heidelberg, New York, 1971

BERNHARDSEN, T.: Undersøkelse av den geometriske nøyaktighet i ERTS-bilder. Institut for landmåling, Norges landbrukshøgskole, 1975

BERNATH, H.J.: Radiometric Calibration of a Multi-Spectral Aerial Camera. Phot.Eng. 1973, S.939

BERNSTEIN, R. et al.: Digital Processing of Conical Scanner Data. Phot. Eng. 1977, S.155

BOEHNEL, H.-J. et al.: Spectral Field Measurements for the Determination of Reflectance Characteristics of Grown Surfaces. IGP Kommission VII Symposium, Freiburg 1978

BRONSTEIN-SEMENDJAJEW: Taschenbuch der Mathematik. Leipzig 1962

BÜTTNER, H.: Die Bestände des Meydenbauerschen Denkmälerarchivs und ihr Schicksal im und nach dem zweiten Weltkrieg. Landeskonservator Rheinland, Arbeitsheft 18, 1977

CASE, J.B.: The Utilization of Constraints in Analytical Photogrammetry. Phot.Eng. 1961

COLVOCORESSES, A.P.: Multispectral Linear Arrays as an Alternative to LANDSAT D. Phot.Eng. 1979

DENNERT-MÖLLER, E.: Multispectral Classification of Tidal Lands. Mitteilungen der Geodätischen Institute der TU Graz, Folge 29, 1977

DÖHLER, M.: Photogrammetrische Bestandsaufnahme kulturhistorischer Objekte - Erfahrungen und Vorschläge. Landeskonservator Rheinland, Arbeitsheft 18, 1977

DOYLE, F.J.: Kammer-Systeme und Photogrammetrie in der Raumfahrt. Otto v. Gruber Gedächtnisvorlesung, BUL 1971

DOYLE, F.J.: Imaging Sensors for Space Vehicle-. IGP Komm. I, Ottawa 1972

DOYLE, F.J.: Instruments and Techniques for Cartographic Processing of Space Photographs. IGP Komm. II, Ottawa 1972

DOYLE, F.J.: A Large Format Camera for Shuttle. Phot.Eng. 1979

DREWES, H.: Berechnung regionaler Geoidundulationen durch gravimetrisches Nivellement mit Prädiktion der Schwereanomalien. Wiss. Arbeit Lehrst. Geod., Phot. und Kart., TU Hannover Nr. 63, 1976

DUCHER, G., KONECNY, G.: The Spacelab Project. 3e Colloque International du GDTA, Toulouse 1979

ELLENBECK, K.-H. und WROBEL, B.: Zur Leistungssteigerung der terrestrisch-photogrammetrischen Punktbestimmung. BUL 1977

FERNANDEZ, S., SEIDERER, M.: Analog-Digital Picture Processing Using an Extensible, Problem Oriented Single Level Programming System. The Forth Approach. Mitteilungen der Geodätischen Institute der Technischen Universität Graz, Folge 29, 1977

FINSTERWALDER, S.: Zur photogrammetrischen Praxis. Zeitschrift für Vermessungswesen, 1896

FINSTERWALDER-HOFMANN: Photogrammetrie. Berlin 1968

FORAMITTI, H.: Kulturgüterschutz. Empfehlungen zur praktischen Durchführung (3 Bde.). Wien, Köln, Graz 1970

FORREST, R.B.: Geometric Correction of ERTS-1 MSS Images. IGP Kommission III Symposium, Stuttgart 1974

GIZZI, S.: Data Processing Facilities of the TERRA Experiment. In: Remote Sensing of the Environment, London-Boston 1977

GOLD, B. u. RADER, C.M.: Digital Processing of Signals. New York

GROTHENN, D.: Untersuchungen zur Wattvermessung. Schriftenreihe des Niedersächsischen Landesverwaltungsamtes - Landesvermessung -, Hannover 1964

GROSSMANN, W.: Geodätische Rechnungen und Abbildungen in der Landesvermessung. Stuttgart 1964

GRÜN, A.: Photogrammetrische Rekonstruktion von Rotationsflächen aus Einzelbildern. Deutsche Geodätische Kommission, Reihe C, Heft 212, München 1975

GUYOT, G. et al.: Evolution des Indicatrices de Réflectance de Cultures de Blé en Fonction de leurs Stades Phénologiques. IGP Kommission VII Symposium, Freiburg 1978

HABERÄCKER, P.: Untersuchungen zur Klassifizierung multispektraler Bilddaten aus der Fernerkundung. Diss.TU Berlin 1978

HARRIS, G., Jr.: A Low Throughput Digital Image Enhancement System. Mitteilungen der Geodätischen Institute der Technischen Universität Graz, Folge 29, 1977

HARTEN, H., VOLLMERS, H.: Die Ästuarien der deutschen Nordseeküste. In: Die Küste, Heft 32, Heide 1978

HELAVA, U.: Digitale Komponenten in der Photogrammetrie (5. Otto-von-Gruber-Gedächtnis-Vorlesung). In: Symposium über den Einsatz digitaler Komponenten in der Photogrammetrie. Wissenschaftliche Arbeiten der Lehrstühle für Geodäsie, Photogrammetrie und Kartographie an der Technischen Universität Hannover Nr. 84, 1978

HIRVONEN, R.A.: On the Precision of the Gravimetric Determination of the Geoid. American Geophysical Union 36, S.1-8, 1956

HOFMANN, O.: Mikroprozessoren im Kartographischen und photogrammetrischen Instrumentenbau. In: Symposium über den Einsatz digitaler Komponenten in der Photogrammetrie. - Wissenschaftliche Arbeiten der Lehrstühle für Geodäsie, Photogrammetrie und Kartographie an der Technischen Universität Hannover Nr. 84, 1978

JORDAN/EGGERT/KNEISSL: Handbuch der Vermessungskunde Bd.IIIa, Photogrammetrie, Stuttgart 1972

KASPER, H.: Einige Bemerkungen zur photogrammetrischen Aufnahmeoptik. Festschrift C.F.BAESCHLIN, Zürich 1957

KASTEN, F., Raschke, E.: Nomenklatur zur Beschreibung von Strahlungsmessungen und -rechnungen. Bundesministerium für Bildung und Wissenschaft, Forschungsbericht W72-30, 1972

KIESOW, G.: Dokumentation in der denkmalpflegerischen Praxis. Landeskonservator Rheinland, Arbeitsheft 18, 1977

KORTE, H.: Über Messung des Leuchtdichtefaktors an beliebig reflektierenden Proben. Mitteilungen der Physikalisch-Technischen Bundesanstalt Braunschweig in LICHTTECHNIK 11/1967

KONECNY, G., DERENYI, E.E.: Geometry of Infrared Imagery. Canadian Surveyor 1964, S.279-290

KONECNY, G.: Metric Problems in Remote Sensing. IGP Symposium Komm.IV Delft 1971, Veröff. des ITC, Reihe A Nr.50

KONECNY, G.: Orientierungsfragen bei Streifenbildern und Aufnahmen der Infrarotabtastung. BUL 1971

KONECNY, G.: Geometrische Probleme der Fernerkundung, BUL 4/1972

KONECNY, G.: Approach and Status of Geometric Restitution for Remote Sensing Imagery. BUL 1/1975

KONECNY, G.: Digitale Entzerrung der Daten von Zeilenabtastern. BUL 4/1975

KONECNY, G.: Mathematische Modelle und Verfahren zur geometrischen Auswertung von Zeilenabtaster-Aufnahmen. BUL 5/1976

KONECNY, G.: Analytische Auswertegeräte vom Gesichtspunkt des Benutzers. In: Symposium über den Einsatz digitaler Komponenten in der Photogrammetrie. Wissenschaftliche Arbeiten der Lehrstühle für Geodäsie, Photogrammetrie und Kartographie an der Technischen Universität Hannover, Nr.84, 1978

KONECNY, G.: Zum gegenwärtigen Stand der Fernerkundung. In: Berichte zum Symposium Flugzeugmeßprogramm. Forschungsbericht W78-04 des Bundesministeriums für Forschung und Technologie, 1978

KONECNY, G.: Methods and Possibilities for Digital Differential Rectification. Phot.Eng. 1979, S.727

KRATKY, V.: Cartographic Accuracy of ERTS. Phot.Eng. 1974

KRATKY, V.: Geometric Calibration of the Canadian ERTS Photoreproduction System. IGP, Symposium Komm. III, Stuttgart 1974

KRAUS, K.: Interpolation nach kleinsten Quadraten in der Photogrammetrie. ZfV, S.387-389, 1970

KRAUS, K., MIKHAIL, E.M.: Linear Least-Squares Interpolation. IGP Komm. III, Ottawa 1972

KRAUS, K. und TSCHANNERL, J.: Die photographische Entzerrung abwickelbarer Regelflächen. Landeskonservator Rheinland, Arbeitsheft 18, 1977

KREYSZIG, E.: Statistische Methoden und ihre Anwendungen. Göttingen 1965

KRIEBEL, K.T.: Reflection Terminology for Remote Sensing Applications. IGP Komm. VII Symposium, Freiburg 1978

KRISTOF, S.J. und WEISMILLER, R.A.: Computer-Aided Analysis of LANDSAT Data for Surveying Texas Coastal Zone Environments. Mitteilungen der Geodätischen Institute der Technischen Universität Graz, Folge 29, 1977

LACMANN, O.: Die Photogrammetrie in ihrer Anwendung auf nichttopographischen Gebieten. Leipzig 1950

LOSCHNER, F.: Das Internationale Komitee für Architekturphotogrammetrie (CIPA). BUL 1974

LOTJEN, K.: Struktur des bildverarbeitenden Prozessors F.L.I.P. In: Symposium über den Einsatz digitaler Komponenten in der Photogrammetrie. Wissenschaftliche Arbeiten der Lehrstühle für Geodäsie, Photogrammetrie und Kartographie an der Technischen Universität Hannover, Nr. 84, 1978

MEIER, H.K.: Diskussion der Bewegungsunschärfe bei Luftbildern mit Hilfe einer Kontrastübertragungsfunktion. BUL 2/1960

MEIER, H.K.: Verzeichnung, Kammerkonstante und Fokussierung von Luftbildkammern unter dem Einfluß bildflugspezifischer Umweltbedingungen. BUL 1978

MEYDENBAUER, A.: Das photographische Aufnehmen zu wissenschaftlichen Zwecken, insbesondere das Meßbild-Verfahren. Berlin 1892

MEYDENBAUER, A.: Das Denkmäler-Archiv. Ein Rückblick zum zwanzigjährigen Bestehen der Königlichen Meßbild-Anstalt in Berlin. Berlin 1905

MORITZ, H.: Neuere Ausgleichungs- und Prädiktionsverfahren. ZfV 1973

MORITZ, H.: Statistische Methoden in der gravimetrischen Geodäsie. ZfV 1963

NIEMANN, H.: Methoden der Mustererkennung. Frankfurt/M. 1974

OPPENHEIM, A.V., SCHAFER, R.W.: Digital Signal Processing. Englewood Cliffs, 1975

PRATT, W.K.: Digital Image Processing. New York 1978

QUIEL, F.: A Branched Classification System Offering Additional Possibilities in Multispectral Data Analysis. BUL 1976

RHODE, H.: Die Geschichte des deutschen Küstengebietes. In: Die Küste, Heft 32, Heide 1978

ROSENBRUCH, K.-J.: Die Kontrastempfindlichkeit des Auges als Beitrag zur Frage der Gütebewertung optischer Bilder. Optik 16, Heft 3, 1959

ROSENBRUCH, K.-J.: Untersuchungen der Bildgeometrie und Bildqualität von Objektiven an Luftbildkammern. IGP Komm. I, Helsinki 1976

ROSENFELD, A.: Picture Processing by Computer. New York, London 1969

SCHLEIDER, W.: Untersuchungen zur Anwendung des Wasserlinienverfahrens in hydrologisch schwierigen Gebieten. Wissenschaftliche Arbeiten der Lehrstühle für Geodäsie, Photogrammetrie und Kartographie an der Universität Hannover, 1979

SCHLUDE, F.: Ein Experimental-Radargerät zur Erdbeobachtung vom Flugzeug aus. BUL 1978

SCHMID, H.: An Analytical Treatment of the Orientation of a Photogrammetric Camera. Phot.Eng. 1954

SCHNEIDER, S.: Luftbild und Luftbildinterpretation. Berlin, New York 1974

SCHÜLER, H.: Über Photogrammetrische Verzeichnung. IGP Komm.I, Helsinki 1976

SCHOONMAKER, J.W. Jr.: Geometric Evaluation of MSS Images from ERTS-1. ASP Spring Convention 1974, St.Louis

SCHUHR, W.: Digitale Entzerrung multispektraler Bilder. BUL 1976

SCHWIDEFSKY, K.: Grundriß der Photogrammetrie. Stuttgart 1954

SCHWIDEFSKY, K.: Albrecht Meydenbauer - Initiator der Photogrammetrie in Deutschland zur 50. Wiederkehr seines Todestages am 15.11.1971. BUL 1971

SEEGER, E.: Orthophotography in Architectural Photogrammetry. IGP, Helsinki 1976

SHANNON, C.E. u. WEAVER, W.: The Mathematical Theory of Communication. University of Illinois Press, Urbana 1949

SIEVERS, J.: Zusammenhänge zwischen Objektreflexion und Bildschwärzung in Luftbildern. Deutsche Geodätische Kommission, Reihe C, Heft 221, München 1976

SIEVERS, J.: Density Corrections and Directional Reflectances of Terrain Objects from Black- and White Aerial Photos. Photogrammetria 33/1977

SLOAN, D.S., ORTH, R.: Self-Contained LANDSAT Data Reception and Precision Cartographic Image Production System. Mitteilungen der Geodätischen Institute der Technischen Universität Graz, Folge 29, 1977

STEINBUCH, K.: Taschenbuch der Nachrichtenvearbeitung. Berlin Göttingen, Heidelberg 1962

STEINER, D.: Die Jahreszeit als Faktor bei der Landnutzungsinterpretation. Schriftenfolge des Instituts für Landeskunde, Bad Godesberg 1961

STEPHANI, M.: Zur Rolle der Photogrammetrie in der Archäometrie. Landeskonservator Rheinland, Arbeitsheft 18, 1977

THOMPSON, L.L.: Remote Sensing Using Solid-State Array Technology. Phot.Eng. 1979

TOU, J.T., GONZALES, R.C.: Pattern Recognition Principles. London 1974

TRINDER, J.C. und NASCA, S.U.: Test on the Mapping Application of LANDSAT Imagery. IGP Kommission III, Helsinki 1976

WARNE, D.K.: Landsat as an Aid in the Preparation of Hydrographic Charts. Phot.Eng. 1978.

WONG, K.W.: Geometric and Cartographic Accuracy of ERTS-1 Imagery. Phot.Eng.1975

ZIEMANN, H.: Image Geometry and Contributions to its Change. IGP Komm. I, Ottawa 1972

DIBIAS-Handbuch: Deutsche Forschungs- und Versuchsanstalt für Luft- und Raumfahrt, Oberpfaffenhofen, 1976

DIN 5032 "Lichtmessung", Bl.1, S.5, 1966

Manual of Remote Sensing. American Society of Photogrammetry (Hrsg.)

NASA Earth Resources Technology Satellite. Data User's Handbook. Goddard Space Flight Center, Document No. 71SD4249

Proceedings of Symposium on Significant Results obtained from the ERTS-1. NASA Sponsorship, 1973; Library of Congress Catalog Card. No. 73-600115

Directorio de Asistentes al curso Percepción Remota 1980.

1.	ARMANDO AGUAYO ELIZALDE SARH Jefe de la Sección de Programas Atenas 30 Entrepiso México 6, D.F. Tel. 535.17.53	Sta. Ma. la Ribera 22-406 México 4, D.F. Tel. 592.47.45
2.	JORGE M. ALCANTARA DIAZ COMISION FEDERAL DE ELECTRICIDAD Jefe de Proyeco Laguna del Pilar 721 San Felipe 5ta. Etapa Chihuahua, Chih. Tel. 627.22	Saturno 3512 Cda. Satélite, Edo. de Méx. Tel. 546.33.77
3.	SERGIO ARREDONDO G. IIMAS UNAM México 20, D.F. Tel. 548.54.65	Calle D # 14 Manz. XI Col. Educación México 21, D.F. Tel. 544.55.50
4.	JUAN F. BAUMGARTNER FACULTAD DE INGENIERIA UNAM México 20, D.F.	Cincinnati 91-1 Col. Nochebuena México 18, D.F. Tel. 563.75.17
5.	JUAN BONILLA ESCARZAGA CFE Río Atoyac 110 PB Col. Cuauhtémoc Z.P. 5 Tel. 553.72.90	Villa Olímpica Edif. 21-304 México 22, D.F. Tel. 568.35.10
6.	ARTURO CALDERON ACOSTA Depto. de Bosques Universidad Autónoma de Chapingo Estado de Mexico Tel. 585.45.55	Zootecnía 7 G. Palacios Chapingo
7.	GRISELDA D. CORDOBA RENDON SARH Balderas 94 México 1, D.F. Tel. 521.25.84	Priv. M. de Oca 19 G-403 Col. Gral. Anaya México 13, D.F.

8. JORGE DIREROT CHELEN FRANULIC
CIA. MINERA AUTLAN S.A. DE C.V.
Thiers 251-9°
México, D.F.
Tel. 250.19.77

9. JUAN W. ESTRADA BERG WOLF
UNIVERSIDAD AUTONOMA CHAPINCO
Departamento de Suelos
Chapingo, México
Tel. 585.45.55 Ext. 353

10. GERARDO H. GARCIA ESTRADA
C.F.E.
Oklahoma 85-7°
México, D.F.
Tel. 536.93.15

C.3 de Fco. Mena 38
Col. Unidad Vicente Guerrero
México 13, D.F.
Tel. 691.23.72

11. TOMAS GARCIA GOMEZ
ESTUDIOS Y PROYECTOS S.A.
V. M. Alemán 81
México 18, D.F.
Tel. 277.35.99

Géminis 31
B. de Sn. Cristobal
Ecatepec, Edo. Méx.

12. ANTONIO GASPAR BAUTISTA
SARH
Atenas 30 Entrepiso
México, D.F. Z.P.6
Tel. 566.17.12

Xochiatipan 6
Col. Arenal 4ta. Sección
México, D.F.

13. ANTONIO HERNANDEZ NAVARRO
Alejandro Dumas 53
Polanco
México 5, D.F.

14. ROBERTO HERNANDEZ ZUÑIGA
C.F.E.
Oklhaoma 85-7°
Col. Nápoles
México, D.F.
Tel. 536.93.15

Apdo. Postal 75-578
Lindavista
México 14, D.F.

15. JORGE ALBERTO JIMENEZ HERNANDEZ
C. DE AGUAS DEL VALLE DE MEXICO
Victoria 77-3°
México 1, D.F.
Tel. 521.87.25 Ext. 125

Unidad Cuitlahuac Edif. 18-A-404
Col. Nva. Sta. María
México, D.F.
Tel. 556.16.77

16. AIDA LOPEZ HERNANDEZ
C.F.E.
Oklahoma 85-7°
México, D.F.
Tel. 536.93.15

Colima 326
Col. Jacarandas
Estado de México
Tel. 398.45.22

17. HECTOR EULALIO LOPEZ SALAS
SRIA. DE PROGRAMACION Y PRESUPUESTO
DETENAL Secc. Fotointerpretación
Sn. Antonio Abad 124-4°
México 8, D.F.
Tel. 578.62.00 Ext. 124

Ermita Iztapalapa 442 -73
México 13, D.F.
Tel. 581.06.19

18. JAIME MEJIA FLORES
COMISION DEL PLAN NA. HIDRAULICO
Tepic 40
México 7, D.F.

Sur 26 No. 43
Fracc. Nvo. Paseo Sn. A.
Estado de México
Tel. 355.61.74

19. JORGE MORANCHEL PACHECO
Dir. Gral. de Estudios del
Territorio Nacional
Sn. Antonio Abad 124
México 8, D.F.
Tel. 578.62.00 Ext. 191

Av. el Río 49-A-201
Villa Coapa
México 22, D.F.
Tel. 594.45.64

20. VICTOR M. MOZO Y TENORIO
FACULTAD DE INGENIERIA
UNAM
México 20, D.F.

Dr. Nicolás León 45-A-9
México 9, D.F.
Tel. 768.12.37

21. ANGEL NAJERA SANTOS
AGRICULTURA Y RECURSOS H.
Atenas 30
México, D.F.
Tel. 591.09.72

Sn. Juan de Aragón 104
Col. J. Villada
Nezahualtocotl

22. JAIME ALBERTO REY CONTRERAS
U. AUTONOMA DE CHAPINGO
Chapingo, Edo. de Méx.
Tel. 585.45.55

Calle 22 de Feb. #5
Col. Alvaro Obregón
Texcoco, Edo. de Mex.

23. DANIEL REYES BUGARIN
ICATEC S.A.
González de Cossio 24
México 12, D.F.
Tel. 536.85.60

24. GONZALO A. REYES HERRERA
SRIA. DE LA DEFENSA NAL.
DEPTO. CARTOGRAFICO
Lomas de Sotelo, D.F.
México 10, D.F.

Pablo A. de la Garza 23
Col. Huizachal
México 10, D.F.
Tel. 589.14.32

25. JOSE O. REYNA CORTES
CIA. DE LUZ Y FZA. DEL CENTRO S.A.
Tlaloc 90-1°
México 17, D.F.
Tel.592.39.95

Retorno 24 # 5
Av. Cecilio Robelo
México 9, D.F.
Tel.762.34.44

26. CARLOS REYNA RAMIREZ
SARH
Jefe de la Ofi. de Regionalización
y Clasif. Hidrológica
Gómez Farías 2-2°
México 4, D.F.
Tel.546.6786

Calz. de los Misterios 89-25
México 2, D.F.

27. ANTONIO L. RIVERA HERNANDEZ
DIR. GRAL. DE EST. DEL TERRITORIO NACIONAL
Sn. Antonio Abad 124
México 8, D.F.
Tel.578.62.00

I. la Católica 512 Nte.
Toluca, Edo. de Méx.
Tel. 498.32

28. ADRIAN R. RODRIGUEZ PRADO
SARH
Gómez Farías 2-1°
México 4, D.F.
Tel.535.41.20

Valle del Mixteco 157
V. de Aragón
Netza., Edo. de Mex.

29. VIRGILIO RUBIO VAZQUEZ
COMISION NAL. DE SEGURIDAD NUCLEAR Y SALVAGUARDIAS
Av. Insurgentes Sur 1806-4°
México 20, D.F.
Tel.524.78.45

Av. la Hda. Andador 8# 52
V. Coapa
Z P.22
Tel.594.12.15

30. JOSE F. RUIZ FIGUEROA
U. Autónoma de Chapingo
Estado de México
Tel.585.45.55

22 de Feb. # 6
Col. A. Obregón
Chapingo, México

31. OCTAVIO S. SANTAMARIA GALLEGOS
DETENAL
Sn. A. Abad 124-4°
Mexico 8, D.F.

Elena 14-5
México 13, D.F.
Tel.696.25.69

32. FRANCISCO J. SIFUENTES R.
U.A. AGRARIA "ANTONIO NAVARRO"
Buenavista
Saltillo, Coah.

Bravo Sur 457-1
Saltillo, Coah.
Tel.2.88.50

33. ARTURO SOTELO RODRIGUEZ
SAHOP
Supervisor de Est. Geoténcicos
Xola y Av. Universidad
México 12, D.F.
Tel. 519.76.60

Zaragoza 53-4
Col. Guerrero
Mexico 3, D.F.
Tel. 535.17.24

34. RICARDO TORRES COSSIO
ENEP CUAUTILAN
ESTADO DE MEX.
Te. 2-09.97